

Lecture Notes in Mechanical Engineering

Vivek Kumar Singh
Gautam Choubey
S. Suresh *Editors*

Advances in Thermal Sciences

Select Proceedings of ICFAMMT 2022

 Springer

Lecture Notes in Mechanical Engineering


Series Editors

Fakher Chaari, National School of Engineers, University of Sfax, Sfax, Tunisia

Francesco Gherardini , Dipartimento di Ingegneria “Enzo Ferrari”, Università di Modena e Reggio Emilia, Modena, Italy

Vitalii Ivanov, Department of Manufacturing Engineering, Machines and Tools, Sumy State University, Sumy, Ukraine

Editorial Board

Francisco Cavas-Martínez , Departamento de Estructuras, Construcción y Expresión Gráfica Universidad Politécnica de Cartagena, Cartagena, Murcia, Spain

Francesca di Mare, Institute of Energy Technology, Ruhr-Universität Bochum, Bochum, Nordrhein-Westfalen, Germany

Mohamed Haddar, National School of Engineers of Sfax (ENIS), Sfax, Tunisia

Young W. Kwon, Department of Manufacturing Engineering and Aerospace Engineering, Graduate School of Engineering and Applied Science, Monterey, CA, USA

Justyna Trojanowska, Poznan University of Technology, Poznan, Poland

Lecture Notes in Mechanical Engineering (LNME) publishes the latest developments in Mechanical Engineering—quickly, informally and with high quality. Original research reported in proceedings and post-proceedings represents the core of LNME. Volumes published in LNME embrace all aspects, subfields and new challenges of mechanical engineering. Topics in the series include:

- Engineering Design
- Machinery and Machine Elements
- Mechanical Structures and Stress Analysis
- Automotive Engineering
- Engine Technology
- Aerospace Technology and Astronautics
- Nanotechnology and Microengineering
- Control, Robotics, Mechatronics
- MEMS
- Theoretical and Applied Mechanics
- Dynamical Systems, Control
- Fluid Mechanics
- Engineering Thermodynamics, Heat and Mass Transfer
- Manufacturing
- Precision Engineering, Instrumentation, Measurement
- Materials Engineering
- Tribology and Surface Technology

To submit a proposal or request further information, please contact the Springer Editor of your location:

China: Ms. Ella Zhang at ella.zhang@springer.com

India: Priya Vyas at priya.vyas@springer.com

Rest of Asia, Australia, New Zealand: Swati Meherishi at swati.meherishi@springer.com

All other countries: Dr. Leontina Di Cecco at Leontina.dicecco@springer.com

To submit a proposal for a monograph, please check our Springer Tracts in Mechanical Engineering at <https://link.springer.com/bookseries/11693> or contact Leontina.dicecco@springer.com

Indexed by SCOPUS. All books published in the series are submitted for consideration in Web of Science.

Vivek Kumar Singh · Gautam Choubey · S. Suresh
Editors

Advances in Thermal Sciences

Select Proceedings of ICFAMMT 2022

 Springer

Editors

Vivek Kumar Singh
Thermal Engineering Division
Space Applications Centre, ISRO
Ahmedabad, India

Gautam Choubey
Department of Mechanical and Aerospace
Engineering
IITRAM
Ahmedabad, India

S. Suresh
Department of Mechanical Engineering
National Institute of Technology
Tiruchirappalli, India

ISSN 2195-4356

ISSN 2195-4364 (electronic)

Lecture Notes in Mechanical Engineering

ISBN 978-981-19-6472-5

ISBN 978-981-19-6470-1 (eBook)

<https://doi.org/10.1007/978-981-19-6470-1>

© The Editor(s) (if applicable) and The Author(s), under exclusive license to Springer Nature Singapore Pte Ltd. 2023

This work is subject to copyright. All rights are solely and exclusively licensed by the Publisher, whether the whole or part of the material is concerned, specifically the rights of translation, reprinting, reuse of illustrations, recitation, broadcasting, reproduction on microfilms or in any other physical way, and transmission or information storage and retrieval, electronic adaptation, computer software, or by similar or dissimilar methodology now known or hereafter developed.

The use of general descriptive names, registered names, trademarks, service marks, etc. in this publication does not imply, even in the absence of a specific statement, that such names are exempt from the relevant protective laws and regulations and therefore free for general use.

The publisher, the authors, and the editors are safe to assume that the advice and information in this book are believed to be true and accurate at the date of publication. Neither the publisher nor the authors or the editors give a warranty, expressed or implied, with respect to the material contained herein or for any errors or omissions that may have been made. The publisher remains neutral with regard to jurisdictional claims in published maps and institutional affiliations.

This Springer imprint is published by the registered company Springer Nature Singapore Pte Ltd. The registered company address is: 152 Beach Road, #21-01/04 Gateway East, Singapore 189721, Singapore

About This Book

The first International Conference on Futuristic Advancements in Materials, Manufacturing and Thermal Sciences (ICFAMMT-2022) was jointly organized by the Department of Mechanical and Aerospace Engineering, Institute of Infrastructure, Technology, Research and Management (IITRAM), Ahmedabad, India, and the Space Society of Mechanical Engineers (SSME), Space Applications Centre, ISRO, Ahmedabad. This conference aims to provide splendid opportunities for academicians, researchers, industrial persons, and young scientists to address new challenges and discuss futuristic advancements in materials, manufacturing, and thermal sciences.

This book includes select peer-reviewed proceedings of the International Conference on Futuristic Advancements in Materials, Manufacturing and Thermal Sciences (ICFAMMT-2022). The contents of this book provide an overview of the latest research in the area of thermal sciences such as computational and numerical methods in fluid flow and heat transfer, advanced energy systems, optimization of thermal systems, technologies for space, and aerospace applications, supersonic combustion, two-phase/multiphase flows. The book will be a reliable reference for researchers and professionals working in the field of thermal and fluid sciences.

Ahmedabad, India
Ahmedabad, India
Tiruchirappalli, India

Vivek Kumar Singh
Gautam Choubey
S. Suresh

Contents

Wettability Interaction on Two-Phase Flow in Microfluidic Flow-Focusing Geometry	1
Rakesh Majumder and Gautam Choubey	
Impact of Secondary Channel Combined with Different Shaped Cavities and Ribs on Double Layer Microchannel Heat Sink	15
Dipak Debbarma, Krishna Murari Pandey, and Abhishek Paul	
Influence of Geometric Configuration on the Flow and Heat Transfer Characteristics of an Open Microchannel Thermal Sinks	27
Mohammed Anees Sheik, Abhishek Dasore, Bukke Kiran Naik, and Vinit Malik	
Transient Heat Transfer Analysis on Coaxial Surface Junction Thermocouples of Types K, E, and J	41
Chaganti Apoorva Priya and Ravi K. Peetala	
Comparison of Heat Transfer Characteristics of Nanofluids for Electric Vehicle Battery Thermal Management	57
S. G. Sankeeth, S. Kathiresan, J. Harish, D. Srihari, and R. Harish	
Theoretical Investigation of Base Fluid Type in Nanofluids for Heat Transfer Enhancement in Multidisciplinary Engineering Applications	69
N. Brinda, Prem Raj, Amod Yadav, H. P. Monika, and V. Somashekar	
CFD Analysis on Thermal Performance of Nanofluids in Electric Vehicle Battery	79
P. L. Palaniappan, T. T. K. Lokeswar, V. Adhitya, and R. Harish	
Impact of Titanium Oxide-Based (TiO₂) Nanofluid on Parabolic Trough Solar Concentrating Collector	91
Shri Ram Bhardwaj, Surendra Kumar Yadav, and Arvind Kumar	

Effect of Variation of Free Stream Boundary Conditions on Flow Characteristics of Transverse Injection-Based Scramjet Combustor Equipped with Shock Generators	103
Pabbala Monish Yadav, Kavina Bhojani, and Gautam Choubey	
Effect of Divergence Angles on the Performance of a Cavity-Based Scramjet Combustor	115
Malhar Solanki, Tathya Bhatt, G. Kshitij, and Gautam Choubey	
A Review on the Selection of Materials and Heat Transfer Properties in Scramjet Engines	125
Namrata Bordoloi, Krishna Murari Pandey, and Gautam Choubey	
Review on Enhancement of Thermal Capacity in Heat Exchangers with Various Nanofluids	135
Geeta Kumari, Susheel Kumar, K. M. Pandey, and B. R. Ramesh Babu	
A Review on Paraffin Phase Change Material-Based Thermal Management of Li-Ion Battery	149
Durgesh Kumar Mishra, Sumit Bhowmik, and Krishna Murari Pandey	
A Comprehensive Study of an Ejector System and Its Applications: A Review	161
Abhishek Kulkarni, Surendra Kumar Yadav, and Arvind Kumar	
Computational Analysis on the Flow Behavior and Performance Evaluation of Single and Double Offset Butterfly Valves	173
Kushal Saxena, Nivedita Bhadauria, and Vivek Kumar Patel	
Spiral Wound Gasket in a Typical Liquid Engine Convergent-Divergent Nozzle	187
Suman Sharma, Chitaranjan Pany, R. Suresh, Sirajudeen Ahamed, and C. K. Krishnadasan	
Design and Testing of a Liquid Rocket Engine	203
G. Dinesh Kumar, KJ Hari Krishnan, S. Gokulakrishnan, M. Lokeshwar, and S. Rogith	
Thermal Management Challenges in Small Satellites	217
Kamlesh Kumar Baraya	
Piezo-Actuated and Hydraulically Amplified Linear Compressor for Pulse Tube Cryocooler	231
Faisalkhan R. Pathan, Numan Ahmad, Gagan Agrawal, Naimesh R. Patel, Reena R. Trivedi, and Shaunak R. Joshi	
Transient Thermal Modeling of Thermoelectric Coolers	245
Akshat Patel, S. S. Sisodia, Vivek Kumar Singh, Prasanta Das, Rakesh Bhavsar, and V. J. Lakhera	

Feasibility Study on the Development of PGS-Based Flexible Radiator for Deep Space Applications 257
 N. Ashraf Khan, S. S. Sisodia, V. K. Singh, Prasanta Das, R. R. Bhavsar, and A. Elayaperumal

Analysis of Parameters Affecting Effectiveness of Industrial Cooling Towers 269
 Jitendra Hemwani, Raj Kumar Satankar, Yatna Bhagat, and Y. P. Deshmukh

Effect of Magnetic Field on Refrigeration Devices for Improving Its Performance and Refrigerant Properties 281
 Aditya K. Alagatu, Shivam A. Katkar, Rahul A. Dakare, Shantanu M. Darlinge, Sarthak C. Lautawar, Santosh B. Jaju, and Ashish S. Raut

Optimization of Significant Parameters for Ramp Film Cooling Using CFD-Integrated RSM Approach 289
 V. G. Krishna Anand

Enhancing Fuel Efficiency of a Two-Wheeler Based on Taguchi and ANOVA Method and Regression Analysis 299
 J. Kevin Joseph, R. Jeyanthinathan, and Lokavarapu Bhaskara Rao

The Impact of Drying Conditions on Drying Characteristics, Kinetics, and Mass Transfer Parameters of Pumpkin Seeds (Cucurbita Maxima) 317
 Priyanka Dhurve and Vinkel Kumar Arora

Study of Aerodynamic Components on the Rear of the Car and the Effects of Varying Design Parameters 329
 Harshit Dawar, Gurparas Singh, and Himanshu

About the Editors

Vivek Kumar Singh is currently working as Scientist/Engineer at Thermal Engineering Division of Space Application Centre, ISRO, Ahmedabad. He is working in the area of thermal design, analysis and testing of spacecraft payloads. He worked as Project Manager (Payload Thermal) for various spacecraft payloads (RISAT-2B, GSAT-20, GSAT-24, GSAT-30, IDRSS, etc.) of ISRO. He worked at Propulsion Research and Studies Entity of Liquid Propulsion Systems Centre, ISRO, Trivandrum from year 2007 till 2013, where he worked mainly in the area of CFD analyses for engine/stage components and electric propulsion subsystems. He has research interest in the area satellite payload thermal management, heat transportation devices, PCMs, Cryogenics, etc. He has published papers in peer reviewed international journals. He is the recipient of Dr. Wille Memorial Prize for the year 2007, conferred by the National Society of Fluid Mechanics and Fluid Power, India.

Dr. Gautam Choubey is presently working as an Assistant Professor in the Department of Mechanical and Aerospace Engineering at the Institute of Infrastructure Technology Research and Management (IITRAM), Ahmedabad, India. He holds a Ph.D. in the field of supersonic combustion and an M.Tech. in thermal engineering from the National Institute of Technology (NIT) Silchar, India. For the past 8 years, his research has focused on computational fluid dynamics modelling of supersonic compressible flow. Dr. Choubey has authored more than 30 publications in reputed SCI journals. His research interest mainly includes scramjet combustion, supersonic combustion, turbulence modelling in high-speed flows, and shock-boundary layer interaction. He also figured among top 2% researchers and scientists of the world in a report published by Stanford University (US) and Elsevier BV (Netherlands) for the year 2020. He is also serving as an editorial board member of BMC Research Notes (Springer Nature), Mathematical Problems in Engineering (Hindwai; IF: 1.430).

Dr. S. Suresh has worked extensively in the area of nanofluids, nanostructured surfaces, vacuum insulation panels, nano-encapsulated PCM and phase change materials. He has successfully completed several projects funded by the DST, SERI, SERB, UKIERI, CSIR and ISRO. He has collaboration with global universities in UK, Australia, Canada, Singapore, South Korea and Taiwan for research project, knowledge sharing and exchange, patent and paper publications, joint research projects and student exchange programs. From the research outcomes, he has published more than 150 research papers in peer reviewed journals among them about 30 were exclusively in the PCM field, and his articles have citations of 7130 times. He has an h-index of 40 and i-10 index of 101. He has been awarded the prestigious Shastri Mobility Award by the Indo-Canadian Shastri Institute in 2018. In 2019, he has been elected as a fellow of the Institute of Engineers.

Wettability Interaction on Two-Phase Flow in Microfluidic Flow-Focusing Geometry



Rakesh Majumder and Gautam Choubey

Abstract The underlying mechanism related to microfluidic two-phase flow system under the surface wettability conditions is getting more attention for both chemical and biological applications. The current study computationally explores the interaction of physicochemical determinants such as capillarity and surface wettability on the microfluidic behaviors of two immiscible fluids flowing in a flow-focusing apparatus with two types of cross-junction angle arrangements ($\alpha = 90^\circ$ and $\alpha = 60^\circ$) using volume of fluid (VOF) method utilizing OpenFOAM environment. With an aim to investigate the temporal behavior of dispersed phase with its resulting phenomena such as dripping and jetting, three non-wetting scenarios with a combination of three capillary numbers (Ca) are chosen. The findings reveal that the dripping flow behavior lasts for all non-wetting circumstances at lower capillary numbers. However, the dripping transits to jetting flow pattern by the alteration from lower to higher non-wetting scenario (super-hydrophobic) at higher capillary number. Further, various important phenomena such as pinch-off time and pressure field variation for both junction angles are also illustrated in detail. Such findings indicate that surface wettability acts as a crucial governing parameter that may have important implications for the creation of microfluidic droplet-based systems.

Keywords VOF · Two-phase flow · Junction angles · Wettability · Dripping · Jetting · Capillary number (Ca) · OpenFOAM

R. Majumder (✉)

National Institute of Technology, Silchar (NITS), Assam 788010, India

e-mail: majumderrakesh1@gmail.com

G. Choubey

Institute of Infrastructure, Technology, Research and Management (IITRAM), Ahmedabad, Gujarat 380026, India

1 Introduction

The application of multiphase flow system in microfluidic devices has been attracted by the researcher of different branches. The use of microfluidic devices in industrial processes such as nanomaterial synthesis [1], chemical analysis [2], mems cooling system [3] and biomedical approaches such as cancer cell separation [4] and drug delivery [5] has been increasing since last decade. Further, the application of multiphase flow system in microfluidic confinements facilitates generation of droplets. From this perspective, the most frequently applied junction-based microfluidic arrangements to produce droplets are T -junctions [6], co-flowing geometry [7] and flow-focusing devices [8]. Out of many types of flow-focusing configurations, the flow-focusing devices with cross-junction are constructed by the two lateral channels connected at a perpendicular or angular way with central inlet and outlet channel of equal height and width [9–11]. In such devices, the immiscible dispersed and continuous fluids enter through middle and lateral channels, respectively, and their mutual interaction results into droplet generation past junctions in the outlet section. The advancement of two-phase fluids through the flow-focusing device is highly controlled by various internal aspects. Additionally, the majority of research on the droplet production has also focused on examining the effects of crucial physicochemical parameters such capillary number (viscous force to surface tension) [9, 12–14], viscosity ratio [11, 13, 15–17], interfacial tension [18], pressure [19], and wettability [10, 11, 20].

One of the key elements that can affect the flow properties of an immiscible flow system is surface wettability [21–23]. For example, Kang et al. [21, 22] and Schleizer et al. [23] computationally analyzed only on the dynamic characteristics of an immiscible drop transportation under various wettability conditions incorporated with bond number and capillary number, respectively.

It is clear from the above that capillary number along with viscosity ratio are the two main factors that are generally considered in studies of droplet production in two-phase systems. Again, the majority of research on two-phase flow in flow-focusing geometry have taken only one constant wettability setting for the whole study, which suggests that any significant effects that could result from alteration of the wettability are out of consideration. Once more, most of the investigations on two-phase systems flowing in the flow-focusing geometry ignore angular configurations other than right-angle junctions. Addressing those concerns, the present numerical investigation aims to evaluate the outcome of various surface wettability configurations on microfluidic behaviors of two-phase flow for both right angle ($\alpha = 90^\circ$) and one angular ($\alpha = 60^\circ$) junction-based flow-focusing geometry. In light of this, the present study concentrates on the outcome of capillary along with wettability interaction on the flow behaviors of two-phase flow employed in the microfluidic flow-focusing geometry having cross-junction angle of $\alpha = 90^\circ$ and $\alpha = 60^\circ$ via volume of fluid (VOF) approach, with a specific attention on the potentials of the surface wettability.

2 Problem Specification

In order to computationally examine the impact of capillary-wettability interaction on the two-phase flow characteristics, the three-dimensional configuration of a microfluidic flow-focusing with cross-junction angle of $\alpha = 90^\circ$ and $\alpha = 60^\circ$ employed in the present work is shown in details in Figs. 1 and 2. As demonstrated in Fig. 2a, the flow-focusing device is constructed by four channels having a uniform square cross section of $W = 600 \mu\text{m}$. Each of the lateral and central inlet channels for the continuous phase and dispersed phase, respectively, has a length of $3W$, whereas the outlet channel has a length of $10W$. The properties related to the immiscible two-phase liquids taken into consideration for the current investigation are listed in Table 1.

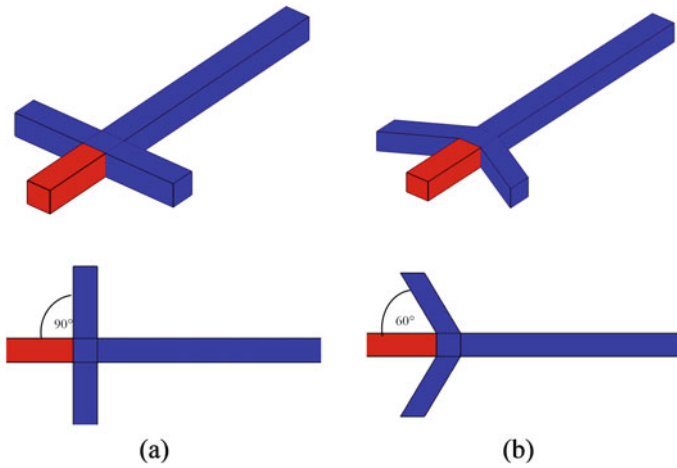


Fig. 1 Schematic representation of flow-focusing device with junction angle **a** $\alpha = 90^\circ$ and **b** $\alpha = 60^\circ$

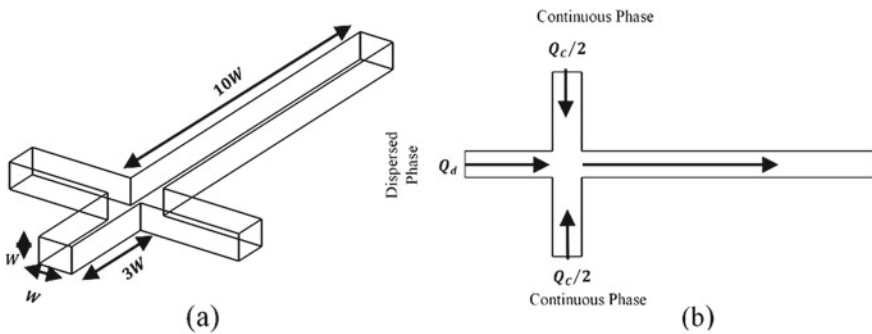


Fig. 2 **a** Dimensions and **b** inlet flow rate direction of the microfluidic flow-focusing geometry

Table 1 Properties of two-phase system

Liquids	Density (Kgm ⁻³)	Dynamic viscosity (mPa s)
Polydimethylsiloxane silicone oil (PDMS)	920	11
Deionized water with 0.5% SDS	1000	0.92

The schematic diagram indicating inlet flow rate direction of two immiscible fluids through the inlets is shown in Fig. 2b. The inlet flow rate of the dispersed fluid is maintained as constant ($Q_d = 300 \mu\text{L}/\text{min}$) throughout the whole study, while the inlet flow rate of the continuous fluid is (Q_c) adjusted according to the capillary number ($Ca = U_c \mu_c / \sigma$), where ($U_c = Q_c / w^2$) and μ_c stand for the continuous medium's inlet velocity and dynamic viscosity, respectively, and σ designates the property of surface tension of two-phase system. It must be added here that the associated flow velocity in the microchannel is laminar for the designated capillary numbers (Ca), and therefore, Reynolds number (Re) stands in a tolerable span of $Re < 100$, where $Re = \rho_c U W / \mu_c$. For the current computational study, the designated capillary numbers are $Ca = 0.007$, $Ca = 0.015$ and $Ca = 0.05$. The various wettability configurations of the channel substrate are imposed in terms of the static contact angle (θ), and Young's equation [24] can be appointed to accurately approximate θ represented as

$$\cos \theta = \frac{\sigma_{wc} - \sigma_{wd}}{\sigma}$$

where σ_{wc} , σ_{wd} and σ stand for interfacial tension where 'w', 'c' and 'd' stands for channel wall surface, continuous and dispersed medium, respectively. The wettability setting of walls of the dispersed or central inlet channel is kept in a neutral setting (i.e., $\theta = 90^\circ$) throughout the whole study, while the wettability setting of rest of the walls is altered from lower to higher non-wetting (super-hydrophobic) configurations, viz. $\theta = 105^\circ$, 120° and 150° . It is essential to note in this context that the side of the length (W) of the square cross section is utilized with a purpose to make all the geometric parameters non-dimensional. Moreover, concerning time (t) related to present investigation is also made non-dimensional by rescaling with total simulation time (τ_{\max}) where non-dimensional time $\tau = t / \tau_{\max}$.

3 Theoretical Formulation

The current time-dependent numerical study of two-phase system via a 3D microfluidic cross-junction-based channel is executed utilizing the VOF method originally introduced by Hirt et al. [25]. The VOF method employs the continuity and Navier-Stokes equations to computationally solve the transport equations associated with two-phase flow-field. Subsequently, the interface tracking factor (α_c) of the VOF method is defined to indicate the interface of the dispersed and continuous phase and

defined as

$$\alpha_c = \begin{cases} 0 & \text{for dispersed phase} \\ 1 & \text{for continuous phase} \\ 0 < \alpha_c < 1 & \text{at the interface} \end{cases}$$

Thus, the properties of the mixed fluid can be defined in terms of α_c and α_d , where volume fraction for the dispersed phase ($\alpha_d = 1 - \alpha_c$). Therefore, density (ρ_b) and viscosity (μ_b) of the mixed fluid can be evaluated as

$$\rho_b = \alpha_d \rho_d + (1 - \alpha_d) \rho_c \quad (1)$$

$$\mu_b = \alpha_d \mu_d + (1 - \alpha_d) \mu_c \quad (2)$$

Here, the dispersed and continuous phase of the fluid are indicated by the subscripts 'd' and 'c'. For an incompressible and Newtonian two-phase system being unsteady and laminar in nature flowing through a three-dimensional domain can be presented as dimensional form in the following manner,

Mass conservation equation:

$$\nabla \cdot \mathbf{U} = 0 \quad (3)$$

Momentum conservation equation:

$$\frac{\partial \rho_b \mathbf{U}}{\partial t} + \nabla \cdot (\rho_b \mathbf{U} \mathbf{U}) = -\nabla p + \nabla \cdot \mu_b (\nabla \mathbf{U} + \nabla \mathbf{U}^T + \rho_b \mathbf{g} + \mathbf{F}_s) \quad (4)$$

Phase fraction equation:

$$\frac{\partial \alpha}{\partial t} + \nabla \cdot (\alpha \mathbf{U}) = 0 \quad (5)$$

where vector \mathbf{U} indicates the two-phase velocity, and p denotes two-phase pressure fields. Further, \mathbf{g} represents the gravitational force. Here, \mathbf{F}_s refers to surface tension force and calculated using CSF model [26] as $F_s = \gamma \kappa \nabla(\alpha)$, where γ depicts the interfacial surface tension, and κ designates interface curvature where $\kappa = \nabla \left(\frac{\nabla \alpha}{|\nabla \alpha|} \right)$.

4 Solution Methodology

The VOF method is implemented due to its advantageous tracking of each phase's volume fraction throughout the chosen domain for computational purpose [27]. A

native two-phase system solver of OpenFoam (V-1912) environment known as InterFoam is executed to solve the transport equations numerically. Integration of velocity and pressure is done using the pressure implicit method for pressure linked equations (PIMPLE algorithm). For the purpose of discretization of convective and diffusive terms in the current numerical model, upwind and linear scheme of Gaussian methods are employed sequentially [28]. Additionally, the Euler's time scheme is utilized. Adaptive time method is applied to the current transient simulation for all the cases. For the purpose of computational accuracy, the iterations are continued until convergence is accomplished by maintaining comparative error between two successive iterations equals 10^{-6} precisely. To have a better computational output, a grid independence study is conducted by comparative analysis of dispersed-phase thread length (D_L) over three sets of hexagonal mesh elements for the highest and the lowest capillary numbers scenario, i.e., $Ca = 0.007$ and $Ca = 0.05$, respectively, for wettability condition of $\theta = 150^\circ$. The measured D_L for a particular time period is compared for each grid system showed in Table 2. It can be observed that with the increasing number of cells, the D_L has also been increased. However, the variation in D_L is the least for the cell number D_L has also been increased. However, the variation in D_L is the least for the cell number of 5,68,800 and 7,02,075. Taking both numerical precisions and computation cost into account, the optimum hexagonal mesh elements of 5,68,800 are appointed in the current numerical investigation. Further, the validation of the current numerical analysis has been carried out by comparing the experimental results exhibited by Fu et al. [11]. The variation in dispersed thread length (L_t) over time found numerically has been set against the experimental outcome shown by Fu et al. [11]. As seen in Fig. 3, the experimental findings of [11] are well supported by the current VOF method-based solver. Thus, the findings in our current investigation validate the precision of the present solver.

5 Results and Discussion

The primary objective of the current computational work is to explore the effect of surface wettability integrated with capillary number (Ca) on flow physics of micro-scale two-phase flow employed in a flow-focusing geometry by taking two cross-junction angles, viz. $\alpha = 90^\circ$ and $\alpha = 60^\circ$ into account using VOF approach. The effect of the combined action of capillary and wettability under dripping and jetting regime results in displacement behavior of dispersed phase associated with various phenomena such as necking, droplet formation, droplet morphology, pinch-off time and pressure variation that are comprehensive explanations are provided in the following sections.

Table 2 Grid independence test

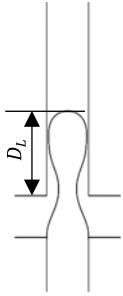
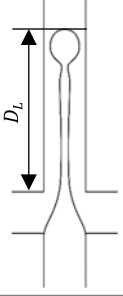
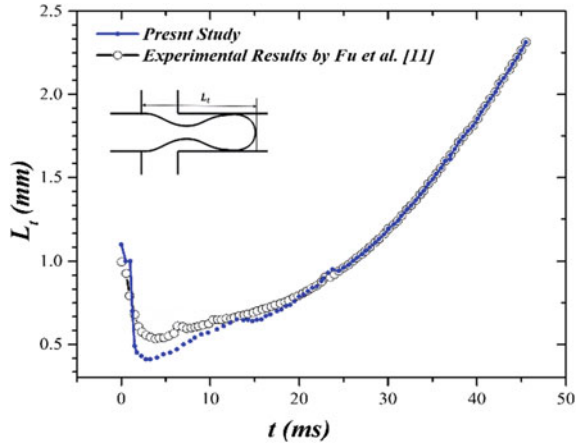
No. of cells	$Ca = 0.007$		$Ca = 0.05$	
	D_L (μm)	Error (%)	D_L (μm)	Error (%)
4,82,400	1.81	2.16	3.01	22.16
5,68,800	1.84	0.54	3.334	4.16
7,02,075	1.85	0	3.42	0
	 <p style="text-align: center;">$Ca = 0.007$</p>		 <p style="text-align: center;">$Ca = 0.05$</p>	

Fig. 3 Comparison of the variation in length of the dispersed liquid thread over time with Fu et al. [11]



5.1 Temporal Study of Microfluidic Characteristics of Dispersed Thread

The time-dependent variation related to flow behaviors of the two-phase system in the both $\alpha = 90^\circ$ and $\alpha = 60^\circ$ cross-junction angle with respect to the displacement characteristics concerning dispersed medium thread for three non-wetting ($\theta = 105^\circ, 120^\circ$ and 150°) settings for a fixed viscosity ratio ($\mu_r = 12$) at several capillary numbers ($Ca = 0.007, 0.015$ and 0.05) is displayed in Figs. 4, 5, 6 and 7.

It can be easily identified from Figs. 4 and 5 that at the both $Ca = 0.007$ and 0.015 , the dispersed fluid first progresses through the junction with higher expansion to the radial direction forming a concave neck induced by dispersed medium’s inertia at $\tau = 0.024$ for both $\alpha = 90^\circ$ and $\alpha = 60^\circ$ under all non-wetting circumstances. Simultaneously, as dispersed thread passes through the junction while flowing toward outlet section, the continuous medium from the sidewise inlet channels starts to interact with the dispersed thread. As the time advances, at $\tau = 0.047$, the dispersed

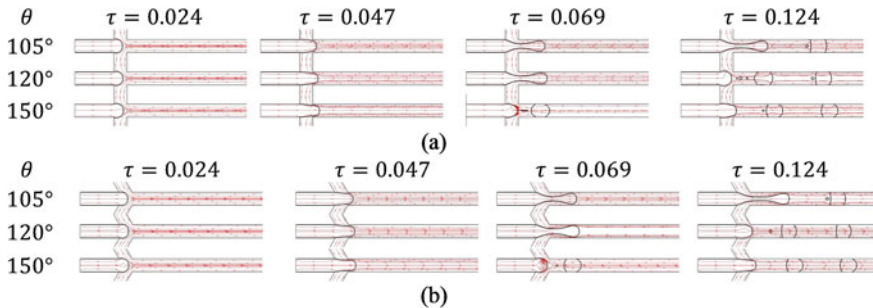


Fig. 4 Temporal evolution of dispersed phase at $Ca = 0.007$ for **a** $\alpha = 90^\circ$ and **b** $\alpha = 60^\circ$

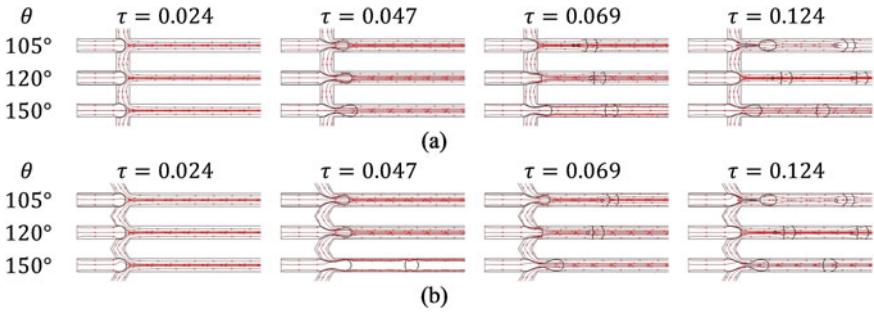


Fig. 5 Temporal evolution of dispersed phase at $Ca = 0.015$ for **a** $\alpha = 90^\circ$ and **b** $\alpha = 60^\circ$

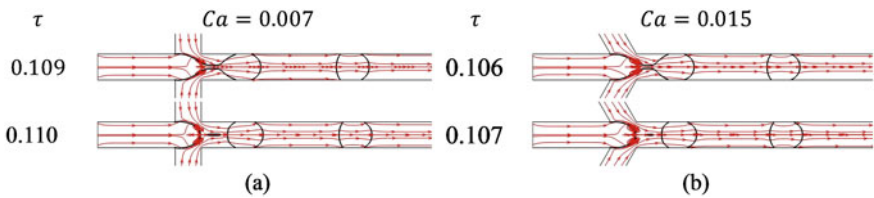


Fig. 6 Vorticity generation under $Ca = 0.007$ and $Ca = 0.015$ for **a** $\alpha = 90^\circ$ and **b** $\alpha = 60^\circ$

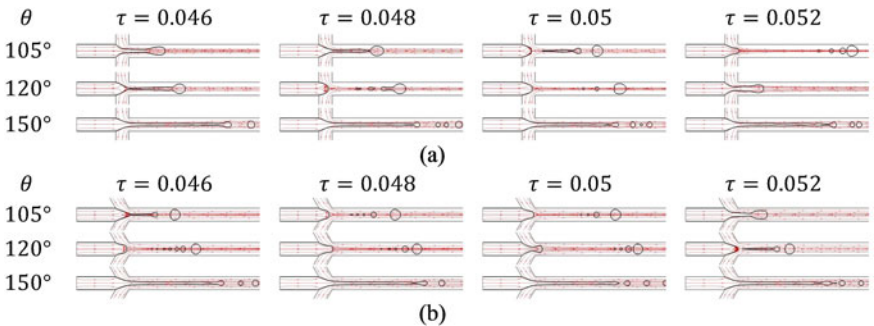


Fig. 7 Temporal evolution of dispersed phase at $Ca = 0.05$ for **a** $\alpha = 90^\circ$ and **b** $\alpha = 60^\circ$

thread restricts the continuous fluid flow in the lateral channels which propels the inertia of the continuous medium to come into the action and starts to shrink the concave interface to form convex interface. As a result, the radius of the convex interface increases with simultaneous axial elongation of the dispersed column; in other words, the dispersed thread begins to experience necking. This variation in the radius of interface curvature over time is relied on the axial imbalance of interfacial tension force of the dispersed medium, shearing action induced by the continuous medium and the surrounding pressure differential around dispersed medium. This convex interface ultimately evolves into a concave tip which gets dislodged

or pinched-off from the dispersed thread as mother droplet with thin thread which breaks into multiple satellite drops which may catch to the mother droplet with time [9, 11]. It can be seen that recirculation vortexes are generated due to retraction caused by interfacial tension immediately before and shortly after pinch-off phenomena shown in Fig. 6. Thus, for both $\alpha = 90^\circ$ and $\alpha = 60^\circ$, the dripping flow pattern is spotted in close proximity to the outlet channel at $Ca = 0.007$ and $Ca = 0.015$ under all wettability scenario. It is also evident from Figs. 4 and 5 that the interfacial concave or almost planer meniscus of dislodged droplets at lower non-wetting circumstances ($\theta = 105^\circ$) switches to convex meniscus at higher non-wetting ($\theta = 150^\circ$) circumstance. It can be also distinguished that droplet generation frequency becomes higher with the alteration from lower to higher non-wetting condition as the detached droplets adhere to the channel surface for a less period of time.

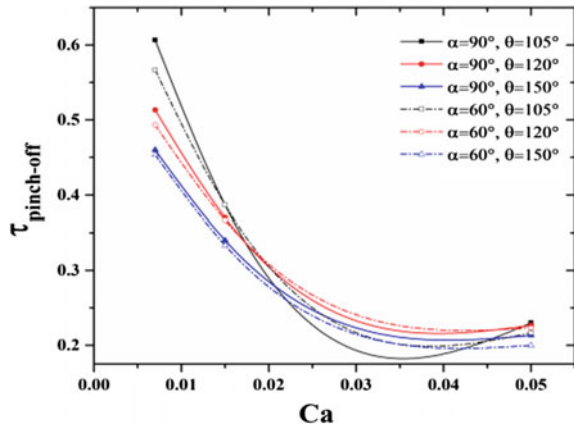
Figure 7 illustrates the time-dependent displacement of dispersed liquid column for various non-wetting circumstances at the higher capillary number of $Ca = 0.05$. It is incredibly intriguing to witness how the dynamics of dispersed column changes over time for both $\alpha = 90^\circ$ and $\alpha = 60^\circ$ at $Ca = 0.05$. At $Ca = 0.05$, it can be noticed here that the dispersed column traverses into central outlet channel without blocking or adhering to lateral channels irrespective of wetting conditions. However, wettability controls the manner or fashion in which the detachment of liquid fragments from dispersed thread occurs.

For lower non-wetting cases, i.e., $\theta = 105^\circ$ and $\theta = 120^\circ$, it is found that the dispersed thread still exhibits dripping flow pattern by stretching toward outlet direction up to a specific length before necking. Hence, mother droplets having length smaller than the channel width with satellite droplets are generated. It is seen that mother droplet with many satellite droplets is created more often at $Ca = 0.05$. It is due to the highly deformed dispersed thread results in multiple breakup sequences at $Ca = 0.05$. Additionally, the wettability condition of $\theta = 150^\circ$ (super-hydrophobic surface) results into the lowest solid-liquid attraction force which allows the dispersed phase to proceed as a steady and prolonged downstream thread as opposed to the dripping phenomena seen at $\theta = 105^\circ$ and $\theta = 120^\circ$. Additionally, for higher capillary number ($Ca = 0.05$), two different types of fluids flow side by side to one another which finally produces jetting flow pattern with prolonged downstream thread. As the shearing action of the continuous medium exceeds the interfacial tension force at greater non-wetting circumstance ($\theta = 150^\circ$), the jet's interface loses its stability after reaching its utmost expansion along the downstream or outlet direction and begins to form secondary droplets.

5.2 Variation in Pinch-Off Time

The combined impact of both wettability and capillarity on the microfluidic characteristics of the dispersed column can be estimated by time ($\tau_{\text{pinch-off}}$) as the variation in non-dimensional pinch-off while two mediums with immiscible properties appointed

Fig. 8 Variation in pinch-off time ($\tau_{\text{pinch-off}}$) at various capillary number



in the cross-junction apparatus for Ca at surface wettability settings for both $\alpha = 90^\circ$ and $\alpha = 60^\circ$ are shown in Fig. 8. The $\tau_{\text{pinch-off}}$ is highly varied depending upon the wettability. It is evident that the overall pinch-off time for both $\alpha = 90^\circ$ and $\alpha = 60^\circ$ is reduced at higher non-wetting condition, i.e., $\theta = 150^\circ$. It can be attributed to the decrement in solid–fluid affinity at $\theta = 150^\circ$ which causes to dispersed thread to adhere to the channel surface for a shorter period of time, and thus, earlier destabilization occurs and results in reduction of pinch-off time. However, for the individual context, the pinch-off time is lower for $\alpha = 60^\circ$ compared to $\alpha = 90^\circ$. This is due to the less resistance experienced by the continuous phase at junction for $\alpha = 60^\circ$ which results in earlier formation of concave tip as well as faster pinch-off under all capillary number.

5.3 Variation in Pressure Field

Another critical case evaluated corresponding to the flow behavior of the dispersed medium employed in microfluidic flow-focusing apparatus is pressure field variation. In order to visualize the pressure field, we demonstrate the change of pressure field along center line of the channel at $Ca = 0.007$ and $Ca = 0.05$ under various non-wettability scenarios for both $\alpha = 90^\circ$ and $\alpha = 60^\circ$ illustrated in Fig. 9. It is worthy to mention that pressure variation along centerline of the channel is shown at an instant of time when maximum number of droplets are present in the channel before passing through outlet. It is evident from the illustration of Fig. 9 that the pressure field up to the droplet pinch-off point is almost constant with less fluctuations. After that, significant variation in pressure is observed due to interactions between two-phase fluids. According to [29], the dissimilarity of the radius of interface curvature from back to front of a droplet causes a pressure contrast over the droplet, and thus, in any pressure profile, each droplet location and shape are identified by a

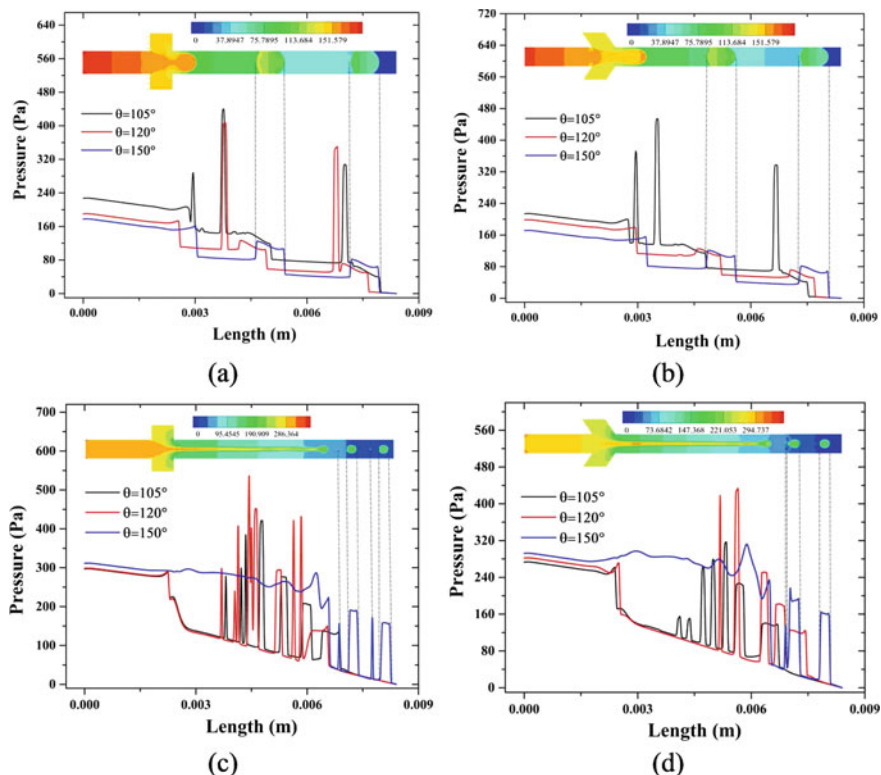


Fig. 9 Variation in pressure field at different capillary number **a** $\alpha = 90^\circ$ and **b** $\alpha = 60^\circ$ at $Ca = 0.007$, **c** $\alpha = 90^\circ$ and **d** $\alpha = 60^\circ$ at $Ca = 0.05$

peak with its width, respectively. Consequently, it is observed that higher the overall droplet generation higher the pressure fluctuation. As such, the higher number of droplets in jetting regime compared to dripping regime causes more fluctuations at higher capillary number, i.e., $Ca = 0.05$ when the surface is maintained at higher non-wetting condition, i.e., $\theta = 150^\circ$.

6 Conclusion

The current work computationally evaluates the microfluidic behavior of a two-phase system employed in the flow-focusing device with junction angles of $\alpha = 90^\circ$ and $\alpha = 60^\circ$. The impact of the interaction between capillary and wettability on the microfluidic behavior of the dispersed medium resulting into dripping as well as jetting flow pattern have been explored. The following important conclusion can be drawn from the present study:

- i. At lower capillary number ($Ca = 0.007$ and $Ca = 0.015$), dripping phenomena are observed in all non-wetting scenarios ranging from lower to super-hydrophobic condition. In this dripping regimen, the droplet interface changes from concave or almost planar meniscus to convex meniscus with shifting of lower to higher non-wetting substrate scenario.
- ii. At higher capillary number ($Ca = 0.05$), dripping phenomena are observed for lower hydrophobic surface, i.e., $\theta = 105^\circ$ and $\theta = 120^\circ$, whereas jetting phenomena with longer downstream length are observed only for the higher non-wetting surface (i.e., $\theta = 150^\circ$). This longer and more stable downstream length before pinch-off is caused by the substrate's weak solid-fluid attraction at super-hydrophobicity (i.e., $\theta = 150^\circ$).
- iii. As a whole, the pinch-off time regarding droplet formation decreases higher non-wetting scenario for all capillary number. It is evident that though droplet detachment process is same for both junction angles, the less resistance of junction angle of $\alpha = 60^\circ$ causes faster necking and subsequently, faster pinching-off from droplet from the dispersed column. Consequently, lower pinch-off time is observed for junction angle of $\alpha = 60^\circ$ compared to $\alpha = 90^\circ$.
- iv. The pressure variation along centerline of the flow-focusing device is highly dependent on the presence of droplet numbers at a time. The higher the number of droplets the higher the pressure fluctuations. As a result, jetting regime due to super-hydrophobicity at $Ca = 0.05$ shows higher fluctuations in pressure for both types of flow-focusing devices compared to dripping regime.

References

1. Chan E, Alivisatos A, Mathies R (2005) High-temperature microfluidic synthesis of CdSe nanocrystals in nanoliter droplets. *J Am Chem Soc* 127:13854–13861
2. Song H, Chen D, Ismagilov R (2006) Reactions in droplets in microfluidic channels. *Angew Chem Int Ed* 45:7336–7356
3. Abdelgawad M, Wheeler A (2009) The digital revolution: a new paradigm for microfluidics. *Adv Mater* 21:920–925
4. Lee M, Shin J, Bae C, Choi S, Park J (2013) Label-free cancer cell separation from human whole blood using inertial microfluidics at low shear stress. *Anal Chem* 85:6213–6218
5. Shembekar N, Chaipan C, Utharala R, Merten C (2016) Droplet-based microfluidics in drug discovery, transcriptomics and high-throughput molecular genetics. *Lab Chip* 16:1314–1331
6. Sivasamy J, Wong T, Nguyen N, Kao L (2011) An investigation on the mechanism of droplet formation in a microfluidic T-junction. *Microfluid Nanofluid* 11:1–10
7. Umbanhowar P, Prasad V, Weitz D (1999) Monodisperse emulsion generation via drop break off in a coflowing stream. *Langmuir* 16:347–351
8. Teh S, Lin R, Hung L, Lee A (2008) Droplet microfluidics. *Lab Chip* 8:198
9. Cubaud T, Mason T (2008) Capillary threads and viscous droplets in square microchannels. *Phys Fluids* 20:053302
10. Sontti S, Atta A (2019) numerical insights on controlled droplet formation in a microfluidic flow-focusing device. *Ind Eng Chem Res* 59:3702–3716
11. Fu T, Wu Y, Ma Y, Li H (2012) Droplet formation and breakup dynamics in microfluidic flow-focusing devices: From dripping to jetting. *Chem Eng Sci* 84:207–217

12. Yobas L, Martens S, Ong W, Ranganathan N (2006) High-performance flow-focusing geometry for spontaneous generation of monodispersed droplets. *Lab Chip* 6:1073
13. Chen X, Glawdel T, Cui N, Ren C (2014) Model of droplet generation in flow focusing generators operating in the squeezing regime. *Microfluid Nanofluid* 18:1341–1353
14. Lee W, Walker L, Anna S (2009) Role of geometry and fluid properties in droplet and thread formation processes in planar flow focusing. *Phys Fluids* 21:032103
15. Liu Z, Chai M, Chen X, Hejazi S, Li Y (2021) Emulsification in a microfluidic flow-focusing device: effect of the dispersed phase viscosity. *Fuel* 283:119229
16. Du W, Fu T, Zhu C, Ma Y, Li H (2015) Breakup dynamics for high-viscosity droplet formation in a flow-focusing device: symmetrical and asymmetrical ruptures. *AIChE J* 62:325–337
17. Ngo I, Woo Joo S, Byon C (2016) Effects of junction angle and viscosity ratio on droplet formation in microfluidic cross-junction. *J Fluids Eng* 138
18. Peng L, Yang M, Guo S, Liu W, Zhao X (2011) The effect of interfacial tension on droplet formation in flow-focusing microfluidic device. *Biomed Microdevice* 13:559–564
19. Ward T, Faivre M, Abkarian M, Stone H (2005) Microfluidic flow focusing: drop size and scaling in pressure versus flow-rate-driven pumping. *Electrophoresis* 26:3716–3724
20. Nagayama G, Cheng P (2004) Effects of interface wettability on microscale flow by molecular dynamics simulation. *Int J Heat Mass Transf* 47:501–513
21. Kang Q, Zhang D, Chen S (2002) Displacement of a two-dimensional immiscible droplet in a channel. *Phys Fluids* 14:3203–3214
22. Kang Q, Zhang D, Chen S (2005) Displacement of a three-dimensional immiscible droplet in a duct. *J Fluid Mech* 545:41
23. Schleizer A, Bonnecaze R (1999) Displacement of a two-dimensional immiscible droplet adhering to a wall in shear and pressure-driven flows. *J Fluid Mech* 383:29–54
24. III (1805) An essay on the cohesion of fluids. *Philos Trans Royal Soc London* 95:65–87
25. Hirt C, Nichols B (1981) Volume of fluid (VOF) method for the dynamics of free boundaries. *J Comput Phys* 39:201–225
26. Brackbill J, Kothe D, Zemach C (1992) A continuum method for modeling surface tension. *J Comput Phys* 100:335–354
27. Gao D, Morley N, Dhir V (2003) Numerical simulation of wavy falling film flow using VOF method. *J Comput Phys* 192:624–642
28. Boruah M, Sarker A, Randive P, Pati S, Chakraborty S (2018) Wettability-mediated dynamics of two-phase flow in microfluidic T-junction. *Phys Fluids* 30:122106
29. Abiev R (2017) Analysis of local pressure gradient inversion and form of bubbles in Taylor flow in microchannels. *Chem Eng Sci* 174:403–412

Impact of Secondary Channel Combined with Different Shaped Cavities and Ribs on Double Layer Microchannel Heat Sink



Dipak Debbarma, Krishna Murari Pandey, and Abhishek Paul

Abstract Double layer microchannel heat sink is the convenient heat sink in respect of its low temperature gradient causing lesser thermal stress and other benefits. Advantage of secondary sub-channel observed in single layered sink is the motivation for the present study. Double layer microsinks with secondary sub-channel, different shaped cavities and ribs in their flow channels are investigated. The parameters such as wall or fluid temperatures, Nusselt number ratio (Nu/Nu_o) and thermal performance factor (η) have been numerically evaluated. All cases of such microchannel design investigated in this study are observed beneficial except the case having vertical secondary sub-channel without rib. Horizontal secondary sub-channel along with cavities and ribs brings proper fluid mixing into the channel so that better temperature uniformity is obtained in the substrate and fluid layers as well. The average 24% reduction in ΔT_b would help such heat sinks to recover from the thermal stresses. Although higher Re suggests higher heat transfer coefficient (h) and larger Nu , medium range of Re leads to optimum pumping power and η . It has been realized that the model having secondary sub-channel along with triangular cavity and diamond-shaped rib offers higher heat transfer coefficient, maximum Nu and the best overall performance among the cases studied. This heat sink exhibits optimum Nu/Nu_o of 1.43 at $Re = 346$ and η of 1.26 at $Re = 593$, respectively.

Keywords Double layered microchannel heat sink · Secondary sub-channel · Maximum bottom wall temperature difference · Nusselt number ratio · Thermal performance factor

1 Introduction

The heat flux generated in the circuits of micro-electro-mechanical system in today's technology is simultaneously increasing with the trend of modern evolution. After the introduction of concept of microchannel heat sink by Tuckerman and Pease [1] in

D. Debbarma · K. M. Pandey (✉) · A. Paul
Mechanical Engineering Department, National Institute of Technology, Silchar, India
e-mail: kmpandey2001@yahoo.com

1981, researchers were attracted by the concept. Thus, the researchers started more investigations in this domain due to the advantages of microchannel. Karayiannis and Mahmoud [2] indicated heat flux of high intensity in the future computers. Such prediction drew attention of several investigators which led to identification of innovative and improved techniques.

Employing cavities and ribs into flow channel are some of the potential concepts. Xia et al. [3, 4] applied cavity of different shapes in single layered microchannel and observed superiority in the performance parameters. The researchers through their works [5–9] have articulated that microchannel with combination of cavities and ribs creates chaotic advection and flow mixing into the channel. Employment of dimple and protrusions also helps to enhance performance. Wei et al. [10] performed study of microchannel with the row of dimples at its bottom surface with air as coolant. Lan et al. [11], Li et al. [12, 13] investigated the influences of dimple as well as the protrusions on performance. The secondary flow through adding secondary sub-channel in single layered microchannel has received wide attention recently. The prospect of secondary flow through secondary small channel was well demonstrated by Steinke and Kandlikar [14]. The single layer microchannel sink with oblique sub-channels was proposed by Ghani et al. [15]. More elaborate investigations were carried out by Japar et al. [16] for the models with rectangular rib, triangular cavity and combination of rectangular rib, triangular cavity and secondary channel. Vafai and Zhu [17], in 1997, unveiled the concept of double layer microchannel heat sink and suggested more reliability in it. Vafai and khaled [18], Chong et al. [19], Xie et al. [20, 21] had reported the significant better performances in double layer sink. In similar investigation, Xie et al. [22] studied the influence of counter and parallel flow for wavy channel. Shen et al. [23, 24] took novel structures having staggered flow alternation. Performance variation with different width ratio, aspect ratio and flow rate was studied by Wu et al. [25] and Wei et al. [26]. Levac et al. [27] highlighted benefits of double layered sink.

Exploration of secondary channel, cavities and ribs on double layer microchannel heat sink (DL-MCHS) is the main objective of the present study. Use of secondary channel, cavities and ribs are found to be beneficial in single layer microchannel heat sink (SL-MCHS). But their influence on performances in the DL-MCHS is not studied by the researchers as per the knowledge of present authors. Therefore, this work has been taken up in regard to enhancement of DL-MCHS. The performance parameters for different shaped cavities combined with ribs and secondary channel are investigated in present study.

2 Design and Model Description

2.1 Heat Sink

Double layer microchannel heat sinks (DL-MCHS) of total width, $W = 10$ mm and total length, $L = 10$ mm are considered in present study. Figure 1 depicts schematic diagram of a double layer microchannel heat sink (DL-MCHS). The heat sinks bear channel height (H_c) of $400 \mu\text{m}$, width (W_c) of $100 \mu\text{m}$ and base height (H_b) of $150 \mu\text{m}$. Total five cases of DL-MCHS as shown in Table 1 are investigated in the study. Water as coolant is flown through the silicon channel substrate. Counter flow is arranged for the study. The thickness of wall between bottom and top channel (t_m) is $50 \mu\text{m}$, kept unchanged for all cases. Channel wall thickness (W_w) of $200 \mu\text{m}$ and channel total length (L) of 10 mm are also constant for all cases. Same channel height (H_c) is considered for both bottom and top layers in all cases. Case 0 is the microchannel heat sinks with smooth channel. The secondary sub-channels are introduced in Case 1, Case 2, Case 3 and Case 4. Circular cavity and vertical secondary channel, rectangular cavity and rectangular rib with secondary channel, triangular cavity and diamond-shaped rib with secondary channel and circular cavity and circular rib with secondary channel are the parts of flow channels of Case 1, Case 2, Case 3 and Case 4, respectively, as shown in Fig. 2.

Figure 3 portrays 2D views of single computational domain of Case 0 and Case 4. Table 1 depicts dimensions of channel parameters. Table 2 shows dimensions of cavity and rib parameters. Cavity width (C_1), cavity depth (C_2) and rib width (W_r)

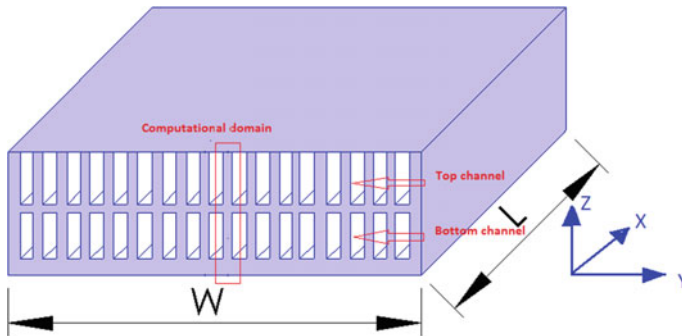


Fig. 1 Schematic of double layer microchannel heat sink (DL-MCHS)

Table 1 Dimensions of channel parameters

Sl. No.	Channel parameters	
1	W_c	$100 \mu\text{m}$
2	W_w	$200 \mu\text{m}$
3	L	10 mm

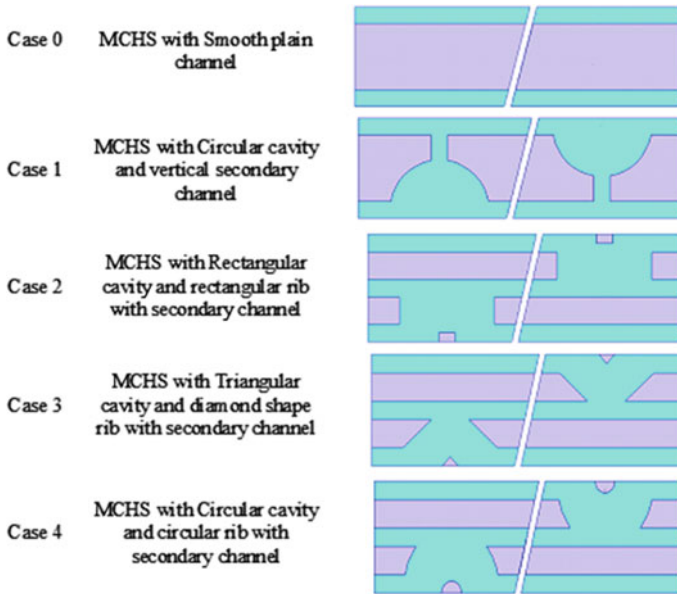
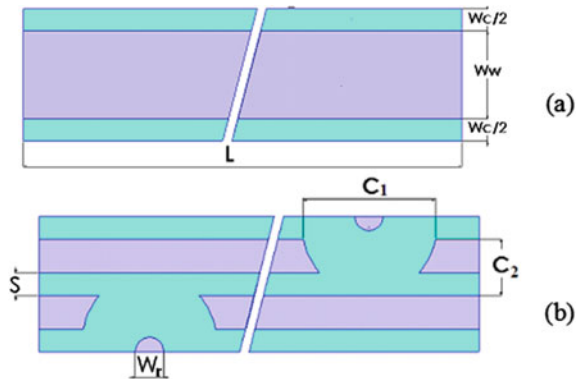


Fig. 2 Descriptions of heat sink channels

Fig. 3 a 2D view of single computational domain of Case 0 and b 2D view of single computational domain of Case 4



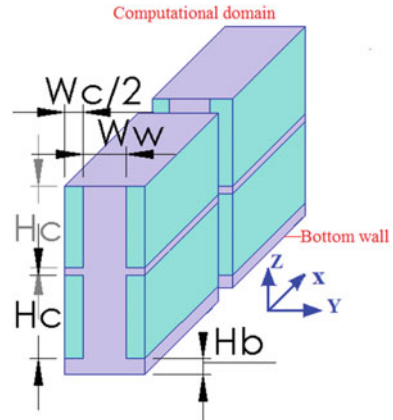
are considered identical for all cases. The secondary channel possesses its width (S) as $50 \mu\text{m}$.

2.2 Computational Model

A single computational domain as shown in Fig. 4 represents conjugate unit of symmetrical geometry of the heat sink. This single domain has channel height H_c ,

Table 2 Dimensions of cavity and rib parameters

Sl. No.	Cavity and rib parameters	
1	C_1	300 μm
2	C_2	125 μm
3	W_r	50 μm
4	S	50 μm

Fig. 4 Schematic of computational model of DL-MCHS

substrate wall thickness W_w and base height H_b . Half of channel width, $W_c/2$, is selected as the domain channel width. The t_m denotes thin solid layer between two fluid channel layers.

2.3 Mathematical Equation and Computation

The coolant fluid flow in the microchannel heat sink is generally assumed as incompressible, laminar and steady in order to make the problem formulation simplified.

The general forms of continuity equation, momentum equation and energy equations are the governing equation for the present problem. At inlet of lower layer ($x = 0$): $u = u_{in}$, $v = 0$, $\omega = 0$ and $T_{in} = 293$ K; at upper layer ($x = 0$ for parallel flow, $x = L$ for counter flow): $u = u_{in}$ (parallel), $u = -u_{in}$ (counter), $v = 0$, $\omega = 0$ and $T_{in} = 293$ K. The SIMPLEC method is adopted for numerical solution in Fluent solver. Fluid viscosity is taken as piecewise-linearly variable with temperature. The inlet fluid velocity (u_{in}) is ranged from 0.5 m/s to 4 m/s, and uniform heat flux (q) applied at bottom surface is 10^6 W/m².

Followings are some other associated equations and performance parameters for microchannel domain:

The Reynolds number (Re) and hydraulic diameter (D_h) are given as

$$\text{Re} = \rho u D_h / \mu \quad (1)$$

$$D_h = (2H_c W_c) / (H_c + W_c) \quad (2)$$

where ρ , u , μ , H_c and W_c are fluid density, flow velocity, fluid viscosity, channel height and channel width, respectively.

Fanning's friction factor (f), Nusselt number (Nu) and heat transfer coefficient (h) are computed as

$$f = (\Delta p D_h) / (2\rho u^2 L) \quad (3)$$

$$\text{Nu} = h D_h / k \quad (4)$$

$$h = Q_{b,\text{total}} / [A_{\text{con}} (T_{b,\text{av}} - T_{\text{av}})] \quad (5)$$

where Δp , L and k are representing pressure drop, channel length and thermal conductivity of fluid. $Q_{b,\text{total}}$, A_{con} , $T_{b,\text{av}}$, T_{av} stand for total heat applied at bottom wall, convection heat removal area, average temperature of bottom wall and average fluid temperature of channel.

The thermal performance factor or heat transfer enhancement factor (η) is defined as

$$\eta = \text{Nu} / \text{Nu}_0 / (f / f_0)^{(1/3)} \quad (6)$$

where Nu_0 and f_0 stand for Nusselt number and friction factor of the base microchannel, respectively.

Thermal resistance (R) is expressed as

$$R = \Delta T_b / Q_{b,\text{total}} \quad (7)$$

$$\Delta T_b = T_{b,\text{max}} - T_{b,\text{min}} \quad (8)$$

ΔT_b , $T_{b,\text{max}}$, $T_{b,\text{min}}$, are maximum bottom wall temperature difference, maximum bottom wall temperature and minimum bottom wall temperature, respectively.

2.4 Validation and Grid Independence Check

The present study is compared with experiential results of Wei et al. [26] to verify the reliability of the computational work. For same dimensional geometry and uniform heat flux, the verification is carried out. The comparison is represented in Fig. 5,

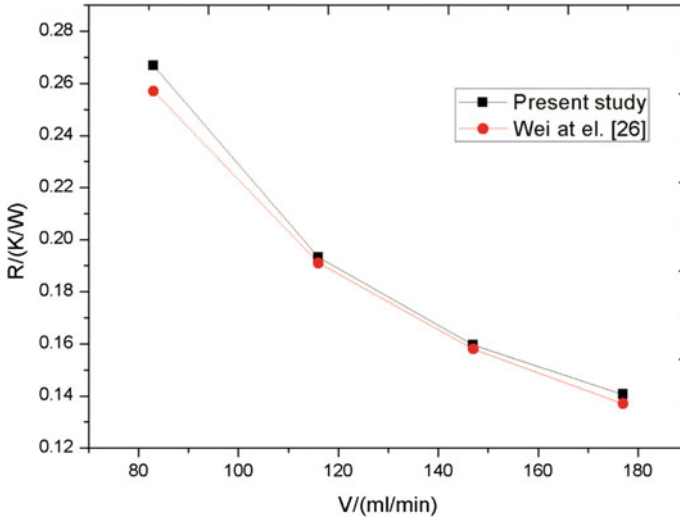


Fig. 5 Comparison of present study with experiential results of Wei et al. [26]

where 3.80% is observed as the maximum variation in thermal resistance justifying the agreement of present work with experiential results.

The computational domain including fluid region has been discretized into hexahedral elements. Independence of grid is checked to confirm the accuracy of numerical solution. As such, three different meshed models of Case 1 comprising Mesh (a) 249,250, Mesh (b) 414,270 and Mesh (c) 801,356 elements give negligible differences in thermal resistance and bottom wall temperature readings. Likewise, Mesh (a) and Mesh (b) show the deviation of only 0.81% and 0.64%, respectively, from Mesh (c) in terms of thermal resistance. Therefore, similar mesh of Mesh (b) is utilized for all other cases.

3 Results and Discussion

The influences of secondary channel and different shaped cavities and ribs in double layer microchannel heat sinks have been estimated in the numerical method. The thermal characteristics along with the hydraulic characteristics of five cases are assessed. Improved results are obtained by virtue of embodiment of these types of secondary channel, cavities and ribs inside the channel. The calculation of ratios of Nusselt number and friction factor and finally determination of heat transfer enhancement factor in the study deliberately helped to come out with several perceptions.

Figure 6 describes temperature distributions for bottom channel of Case 1, Case 2, Case 3 and Case 4 at middle of bottom layer at sectional plane $p-p$. It helps to

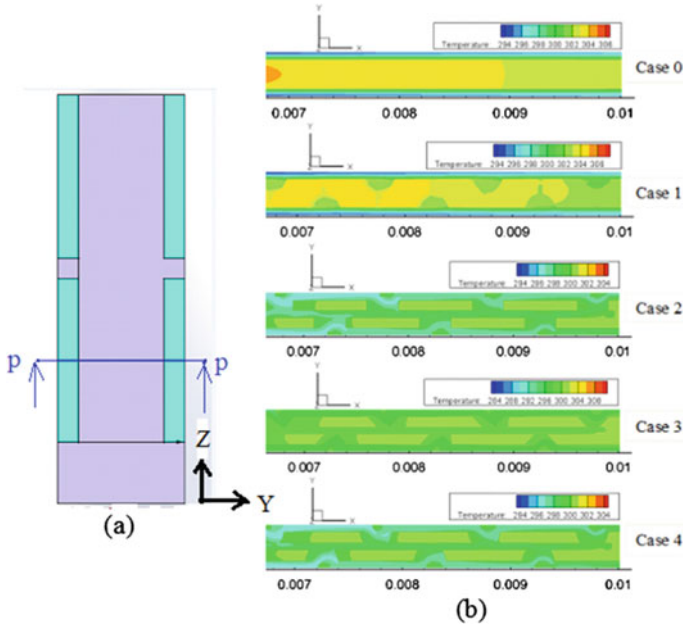


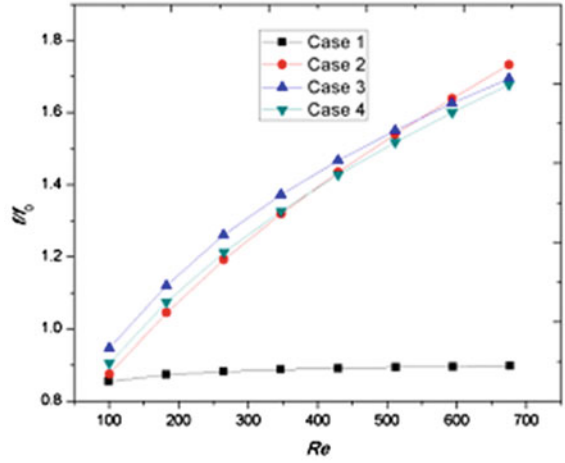
Fig. 6 **a** 2D view of computational domain in z - y axis with the sectional plane p - p at middle of bottom layer and **b** temperature distributions for bottom channel of Case 1, Case 2, Case 3 and Case 4 at the sectional plane p - p at middle of bottom layer at $u_{in} = 2$ m/s

know the property changes in the selected channel local domain. The y - x plane of conjugate domain at middle of bottom layer states how temperature is varying for all cases. The contours of Case 1 and Case 2 have clear differences from Case 3 and Case 4. It shows that substrates of Case 3 and Case 4 are cooled down in better way than Case 1 and Case 2. At this section of heat sinks, better temperature uniformity between substrate and liquid is observed in Case 3 and Case 4 than Case 1 and Case 2.

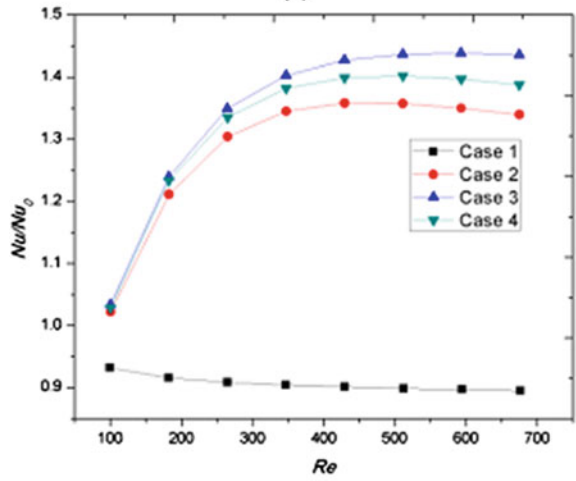
In the analysis of f and f/f_0 data, it has been observed that friction loss occurs as per the expectation. It hikes as the Reynolds number increases. As observed in Fig. 7a, the higher inlet velocities or larger Re brings more friction causing bigger f and f/f_0 . Introduction of ribs is always associated with larger friction, and thus, it causes more pumping power. This is how the Case 1 in absence of rib absorbs less pumping power.

In the study of Nu/Nu_0 and η , interesting results are found. The dimensional number $Re = 346$ leads to the best η of 1.26 in Case 3. Simulation at slightly below $Re = 400$ is predicted as the optimum Re for the best η for all cases. The range of Re from 400 to 700 is subject to higher friction and more pressure drop which in turn causes reduction in heat transfer enhancement factor. As shown in Figs. 7b and 8, Case 1 deteriorates both Nu/Nu_0 and η due to lesser Nu. The reason is vertical secondary sub-channel which does not contribute in transferring heat.

Fig. 7 Comparison of performance parameters for Case 1, Case 2, Case 3 and Case 4: **a** variation of f/f_0 with Re and **b** variation of Nu/Nu_0 with Re



(a)



(b)

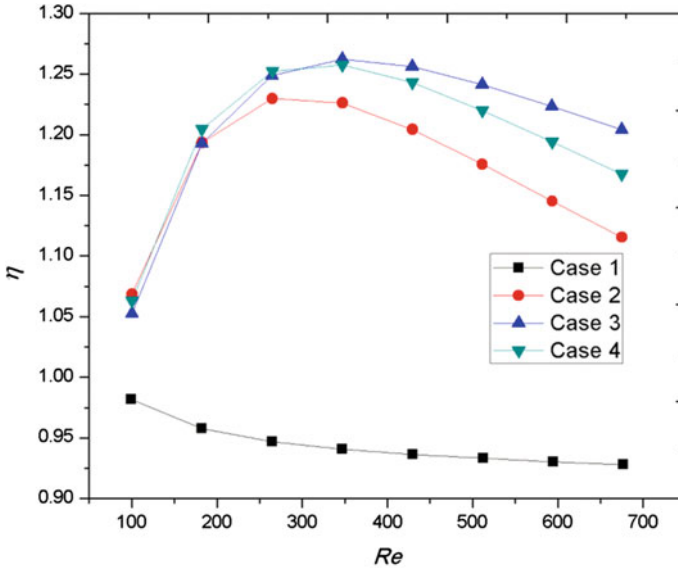


Fig. 8 Variation of thermal performance factor η with Re for Case 1, Case 2, Case 3 and Case 4

4 Conclusion

Investigation using numerical method is carried out on double layer microchannel heat sink to explore the influences of secondary channel, cavities and ribs. Hence, the variation in flow and thermal characteristics for different shaped cavities combined with ribs and secondary channel are assessed in present study. Improved results are obtained by virtue of embodiment of these types of secondary channel, cavities and ribs inside the channel. Followings are the findings observed in the study. In the study of Nu/Nu_0 and η , interesting results are found. Both Nu/Nu_0 and η increase with the increase of Re , but the larger Re after certain value does not provide better output. There is an optimum limit of Re which shows the best results. Hence, whereas $Re = 593$ gives the highest Nu/Nu_0 , $Re = 346$ leads to the best η of 1.26 in Case 3. Simulation at slightly below $Re = 400$ is predicted as the optimum Re for the best η for all cases. The range of Re from 400 to 700 is subject to higher friction and more pressure drop which in turn causes reduction in heat transfer enhancement factor.

References

1. Tuckerman DB, Pease RFW (1981) High-performance heat sinking for VLSI. IEEE Electron Device Lett 2(5):126–129
2. Karayiannis TG, Mahmoud MM (2017) Flow boiling in microchannels: fundamentals and applications. Appl Therm Eng 115:1372–1397

3. Xia GD, Chai L, Zhou M, Wang H (2011) Effects of structural parameters on fluid flow and heat transfer in a microchannel with aligned fan-shaped reentrant cavities. *J Therm Sci Eng* 50:411–419
4. Xia GD, Chai L, Wang H, Zhou M, Cui Z (2011) Optimum thermal design of microchannel heat sink with triangular reentrant cavities. *Appl Therm Eng* 31:1208–1219
5. Esmaili Q, Ranjbar AA, Porkhia S (2018) Experimental analysis of heat transfer in ribbed microchannel. *J Therm Sci Eng* 130:140–147
6. Wang R, Wang J, Lijin B, Zhu Z (2018) Parameterization investigation on the microchannel heat sink with slant rectangular ribs by numerical simulation. *Appl Therm Eng*
7. Xia GD, Zhai Y, Cui Z (2013) Numerical investigation of thermal enhancement in a micro heat sink with fan-shaped reentrant cavities and internal ribs. *Appl Therm Eng* 58:52–60
8. Zhai YL, Xia GD, Liu XF, Li YF (2014) Heat transfer in the microchannels with fan-shaped reentrant cavities and different ribs based on field synergy principle and entropy generation analysis. *Int J Heat Mass Transf* 68:224–233
9. Zhai YL, Xia GD, Liu XF, Li YF (2015) Exergy analysis and performance evaluation of flow and heat transfer in different micro heat sinks with complex structure. *Int J Heat Mass Transf* 84:293–303
10. Wei XJ, Joshi YK, Ligrani PM (2007) Numerical simulation of lamina flow and heat transfer inside a microchannel with one dimpled surface. *J Electron Packag ASME* 129:63–70
11. Lan J, Xie Y, Zhang D (2012) Flow and heat transfer in microchannels with dimples and protrusions. *J Heat Transf ASME* 134:021901
12. Li P, Zhang D, Xie Y (2014) Heat transfer and flow analysis of Al_2O_3 –water nanofluids in microchannel with dimple and protrusion. *Int J Heat Mass Transf* 73:456–467
13. Li P, Xie Y, Zhang D (2016) Laminar flow and forced convective heat transfer of shear-thinning power-law fluids in dimpled and protruded microchannels. *Int J Heat Mass Transf* 99:372–382
14. Steinke ME, Kandlikar SG (2004) Single-phase heat transfer enhancement techniques in microchannel and minichannel flows. In: *Proceedings of ICMM2004, the 2nd international conference on microchannels and minichannels, Rochester, New York, USA*
15. Ghani IA, Sidik NAC, Mamat R, Najafi G, Ken TL, Asako Y, Japar WMAA (2017) Heat transfer enhancement in microchannel heat sink using hybrid technique of ribs and secondary channels. *Int J Heat Mass Transf* 114:640–655
16. Japar WMAA, Sidik NAC, Mat S (2018) A comprehensive study on heat transfer enhancement in microchannel heat sink with secondary channel. *Int Commun Heat Mass Transf* 99:62–81
17. Vafai K, Zhu L (1999) Analysis of two layered microchannel heat sink concept in electronic cooling. *Int J Heat Mass Transf* 42:2287–2297
18. Vafai K, Khaled ARA (2005) Analysis of flexible microchannel heat sink systems. *Int J Heat Mass Transf* 48:1739–1746
19. Chong SH, Ooi KT, Wong TN (2002) Optimisation of single and double layer counter flow microchannel heat sinks. *Appl Therm Eng* 22:1569–1585
20. Xie G, Liu Y, Sunden B, Zhang W (2013) Computational study and optimization of laminar heat transfer and pressure loss of double-layer microchannels for chip liquid cooling. *J Therm Sci Eng Appl* 5:011004
21. Xie G, Chen Z, Sunden B, Zhang W (2013) Numerical predictions of the flow and thermal performance of water-cooled single-layer and double-layer wavy microchannel heat sinks. *Numer Heat Transf Part A* 63:201–225.
22. Xie G, Chen Z, Sunden B, Zhang W (2013) Comparative study of the flow and thermal performance of liquid-cooling parallel-flow and counter-flow double-layer wavy microchannel heat sinks. *Numer Heat Transf Part A* 64:30–55
23. Shen H, Xie G, Wang CC (2019) Heat transfer and thermodynamic analysis by introducing multiple alternation structures into double-layer microchannel heat sinks. *Int J Therm Sci* 145:105975
24. Shen H, Xie G, Wang CC (2019) The numerical simulation with staggered alternation locations and multiflow directions on the thermal performance of double-layer microchannel heat sinks. *Appl Therm Eng* 163:114332

25. Wu JM, Zhao JY, Tseng KJ (2014) Parametric study on the performance of double layered microchannels heat sink. *Energy Convers Manage* 80:550–560
26. Wei X, Joshi Y, Patterson MK (2007) Experimental and numerical study of a stacked microchannel heat sink for liquid cooling of microelectronic devices. *J Heat Transf* 129:1432–1444
27. Levac MLJ, Soliman HM, Ormiston SJ (2011) Three-dimensional analysis of fluid flow and heat transfer in single- and two-layered micro-channel heat sinks. *Heat Mass Transf* 47:1375–1383

Influence of Geometric Configuration on the Flow and Heat Transfer Characteristics of an Open Microchannel Thermal Sinks



Mohammed Anees Sheik, Abhishek Dasore , Bukke Kiran Naik , and Vinit Malik

Abstract Numerical analysis has been carried out to assess the effects of geometrical configuration on fluid flow and heat transfer properties of open microchannel thermal sinks. Varying the fin heights induces an open configuration of microchannel with an open space between the fin top and top wall of the thermal sink. Numerical investigation has been conducted among seven various thermal sinks by considering circular geometric configuration fins and by changing fin heights ranging between 0.5 and 2.0 mm. Conventional configuration, viz., closed microchannel thermal sink with fin height 2.0 mm is also considered in present work to compare with open heat sink performances. Finite volume method (FVM) technique is adopted in the present work to solve governing equations and 3D steady-state conjugate heat transfer problem. Water with $Re < 1000$ is considered to flow through these microchannels. Uniform heat flux of 75 kW/m^2 is maintained in these microchannels. Overall thermal performance is compared and presented to choose the best configuration of the heat sink in the prevailing range of operating conditions. The results indicated that increasing pin fin height in thermal sink enhances the heat transfer rate up to 1.75 mm and beyond that heat dissipation capacity of thermal sink drops. Further, thermal sinks of shorter fins (0.5–1.0 mm) depicted lower thermal performance and pressure drops in comparison with thermal sink having fin height 1.75 and 2.0 mm. The attained results are found to be in good accordance with the experimental data from literature. From the present work, it is inferred that availability of open space and net convective surface area favors better flow behavior which in turn facilitates better heat transfer characteristics of thermal sinks.

M. A. Sheik · A. Dasore

Department of Mechanical Engineering, RGM College of Engineering and Technology, Nandyal, Andhra Pradesh 518501, India

B. K. Naik (✉)

Department of Mechanical Engineering, National Institute of Technology Rourkela, Odisha 769008, India

e-mail: k.bukke@gmail.com

V. Malik

Sustainable Thermal Energy Systems Laboratory (STESL), Department of Mechanical Engineering, National Institute of Technology Rourkela, Odisha 769008, India

Keywords Open microchannel thermal sinks · Pressure drop · Temperature · Nusselt number · Heat transfer coefficient

1 Introduction

Technical equipment such as electronic chips and microelectromechanical systems require excellent thermal management in order to operate in a steady and sustained manner. The compact and slim architecture of such equipment has often intrigued consumers, who need to be miniaturized. The combination of large size reductions and higher transistor density results in considerable increases in heat production per unit volume. It is almost probable that it will reach over 1000 W/cm^2 in future [1]. The dissipation of a great quantity of heat from a confined space has to be arranged more effectively, given the restricted capacity of traditional cooling system that use natural and artificial air (by fans and fins) [2].

The researchers have been particularly interested in microchannel heat sinks, which incorporate a variety of novel heat dissipation strategies such as microchannel cooling, spray cooling, thermoelectric cooling, jet impingement cooling, microchannel, and carbon nanotube cooling [3]. As a consequence, the volume to surface ratio is increased [4], as is the simplicity of application, which is an inherent feature. One of the recent developments [5] is the construction of an inlet/outlet plenum that makes it possible to consistently distribute the cooling mechanism through each channel, reducing the microchannel fluid flow imbalance. Inadequate intake/outlet plenum configuration results in an unpredictable temperatures distribution in the thermal sink that can result in a non-uniform coolant flow during the transition flow [6].

In order to enhance heat transmission via the heat exchanger, researchers first modified the geometry of the channel to allow for more heat dissipation and then improved the properties of coolants to allow for increased heat transfer. Various fluid forms coolant including water, phase-changing material, nanofluid, etc., have been tested for cooling. There is no surprise, however, that water is used most often as coolant, and these days nanofluids are also particularly important because it is rich in nanoparticles that are known as high-heat carriers [7]. However, nanofluid has some disadvantages including sedimentation, higher pressures drop, and corrosion of the pipe wall due to particulate suspension [8]. These problems and the use of nanofluid in microchannels are being solved with considerable efforts. It should be noted that it is still ideal and always has a good reach to provide an appropriate coolant with good heat transfer capability.

Siu-Ho et al. [9] investigated at stagnant rectangular pin fins in the thermal sink and discovered that the efficiency of heat transfer is highest near the inlet and decreases as the flow direction changes.

Yadav et al. [10] with three separate configurations partly located the cylinder micro fins in a rectangular microchannel. The up straight microchannel performed more effectively on low Reynolds number (Re), while the high Re finned

microchannel performs more effectively. The surface roughness and pin fin's relative importance are evaluated by Khalili Sadaghiani et al. [11]. The effect of pin fin forms decreases with an increasing ruggedness of the surface. The experimental work was conducted on the staggered micro-squared pin fine heat sink by Liu et al. [12]. They found that both pressures drop and average Nu rise with the increase in Reynold numbers. Zhao et al. [13] discovered two criteria for increasing the efficiency of pin fins: the permeability of the pin fins and the inclination at which the pin fins are rotated. The finding was that porosity should be 0.75 for improved results and a rotating angle of 30° .

Kadam et al. [14] showed the open microchannel heat sink's potential in comparison with the closed design. It is worth noting that the open microchannel has, however, shown that there are very small works done in single phase coolant flow and boiling flow. In addition, it has rarely been researched on an open microchannel with pin fin setup. Bhandari et al. [15] investigated the heat transfer and fluid flow properties of open microchannel heat sinks with square pin fins numerically. Researcher evaluated seven different heat sinks with fin heights ranging from 0.5 to 2.0 mm. The results show that increasing the fin height increases heat transfer rate, but only up to 1.5 mm fin height. The heat sink's heat dissipation capability decreases at 1.75 and 2.0 mm of fin height, and it is found that heat sink with 1.5 mm fin height has superior thermal performance factor.

The objective of the present work is to consider the heat transfer capacity of the open microchannel heat sinks and to equate them with the effects of the closed microchannel. In addition, a full comparative study of circular micro fin with varying the fins height from open to closed microchannel is performed. Seven individual thermal sinks were investigated with 2, 1.75, 1.5, 1.25, 1.0, 0.75, and 0.5 mm. The 2 mm thermal heat sink is a standard design totally closed without an opening. A comparison was made between the results of the open and closed microchannel heat sinks of circular pin fins in order to determine their relative thermal efficiency. Therefore, a total of 7 geometries were thoroughly studied. In this numerical investigation, the optimal design value that provides the best heat transfer and fluid flow characteristics is predicted.

2 Geometrical Modeling

2.1 *Physical Model and Computational Domain*

Figure 1. illustrates the proposed open microchannel with circular shape fin heat sink. It shows clearly the aspect that an open heat sink has developed in relation to channel height as a result of a shorter fine height. As a result, an open space exists among the fin's top surface and the heat sink's surface. It is widely recognized that the lower the fin's height, the more open space is accessible, and vice versa. Coolant flow occurs through the channel and open space in this arrangement. In this arrangement, fins

are entirely immersed in coolant, which often has heated transfer on the top surface of the fins also. This flow is different from the fully closed microchannel, which regulates fluid to flow only along the channel paths.

The current study analyzes the 3D geometry of the heat sinks numerically. The computational domain's dimension is $L \times W \times H = 27 \text{ mm} \times 10 \text{ mm} \times 3 \text{ mm}$ [15] as shown in Fig. 2. It comprises a set of circular pin fin setup of varying height. As indicated in the figure, 4 rows of fins with 12 fins in per row are used in the arrangement. Therefore, a total of 48 fins of the same size with a base of circular fin setup of 1 mm in diameter are mounted 1 mm away on both sides. As already mentioned, pin fin height was varied to locate the optimal setup for the microchannel heat sink.

ANSYS Fluent V19.0 commercial code generation software is used to create geometry and simulations for the fluent module. Copper material used as the heat sink and liquid water was utilized as a coolant during analysis. The combined heat transfer solution is then used to resolve the problem. In this work, the following assumptions have been taken into account in steady-state analyzes. The fluid used is Newtonian and incompressible, flow is laminar and steady, and walls of the heat sink hold the adiabatic condition and no-slip at wall surface.

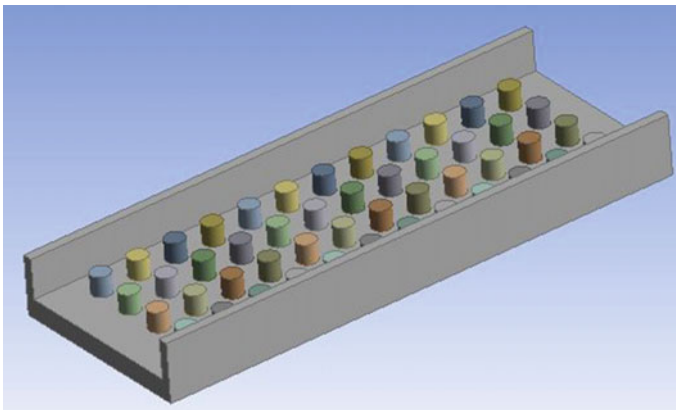


Fig. 1 3D geometry of circular pin fin heat sink

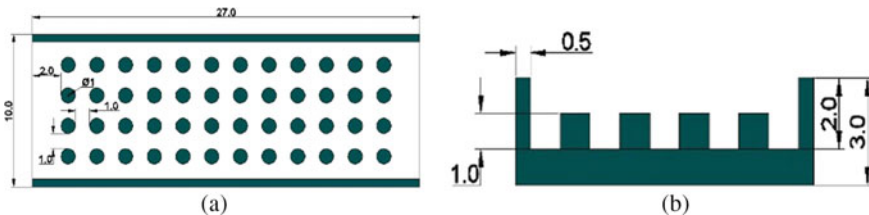


Fig. 2 Detailed 2D sketch of circular pin fin a top view b side view

2.2 Governing Equations

The assumptions listed above make it much easier to comprehend the straightforward fluid flow and heat transfer equations. The following are

$$\text{Continuity equation} \quad \nabla \cdot V = 0 \tag{1}$$

$$\text{Momentum equation} \quad \rho_w(V \cdot \nabla V) = -\nabla P + \nabla \cdot (\mu_w \nabla V) \tag{2}$$

$$\text{Energy equation} \quad \rho_w C_p (V \cdot \nabla T) = K_w \nabla^2 T \tag{3}$$

In the above equations, V denotes the velocity, P denotes pressure, T denotes temperature, and C_p , ρ_w , μ_w , and K_w are specific heat, density, viscosity, and thermal conductivity of liquid water, respectively.

2.3 Boundary Condition and Mesh Independence

The uniform heat flow of 75 kW/m² on the bottom surface of all thermal sinks was taken into account. Adiabatic conditions are taken into account while designing the outside walls of a heat sink. For the microchannel’s intake, a uniform velocity profile and constant coolant inlet temperature of 300 K are assumed. At the microchannel’s exit, a pressure boundary is utilized. Laminar flow simulations have been conducted due to the maximum value of Reynolds number (Re) being 800. ANSYS Fluent and a feasible finite volume program were used to perform the simulations. The momentum and energy equations are discrete in the 2nd order upwind scheme. To address the pressure velocity coupling, the SIMPLE algorithm has been implemented. Gauss Seidal iterative technique is utilized to resolve the resultant algebraic equations scheme. The entire computational domain has been discretized into hexahedral volume components using standardized grids. In Fig. 3, a heat sink with a final meshing of 0.075 mm is shown.

The detailed mesh representations of the fluid region and solid surface suggest that a well-organized mesh was utilized for simulation. The grid independence test

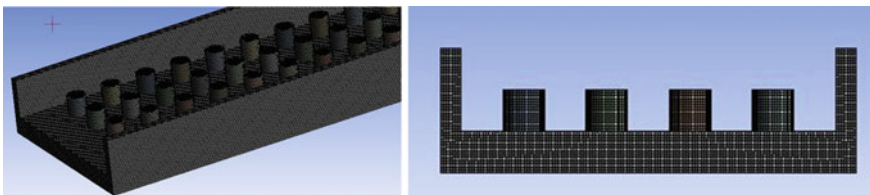
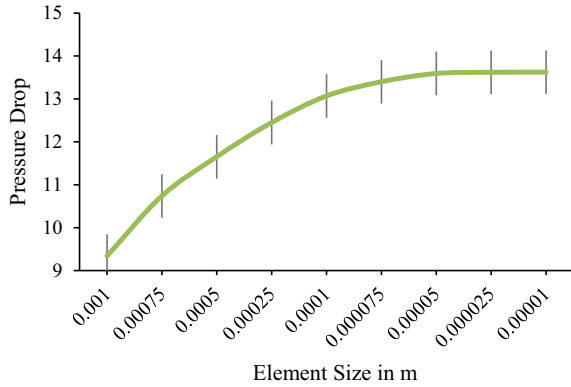


Fig. 3 Heat sink meshing for 1.0 mm of fin height

Table 1 Mesh size that was utilized in the grid independence test is presented below

Element size in mm	Number of elements
1	17,972
2	37,194
0.5	53,457
0.25	139,573
0.1	457,584
0.075	1,049,472
0.05	2,592,000
0.025	4,563,754

Fig. 4 Pressure drop variation with element size



was used to identify the optimal mesh environment. Table 1 contains comprehensive information on meshing the whole computer domain, for both solid and fluid regimes. In addition, Fig. 4 describes the variations in pressure values with reduction element sizes for fin height of 1.0 mm, Re of 200, and heat flux of 75 kW/m². The consequence variation is extremely nominal for the last three sets of grids. In addition to the 0.075 mm grid scale, the pressure variation is just 1–2%. For all the setups of the microchannel heat sink, the 0.075 mm grid size was chosen.

2.4 Data Reduction

A uniform velocity was given at the entrance to the inlet. Reynolds number (Re) at inlet measured with Eq. 4, depending on the coolant's entrance velocity and physical properties.

$$\text{Re} = \frac{\rho u_{\max} D_h}{\mu} \quad (4)$$

where D_h is the hydraulic inlet plenum diameter measured with the following term

$$D_h = \frac{4A_s}{P} \quad (5)$$

where A_s and P denote the intake plenum's cross-sectional area and perimeter, respectively. In this study, D_h is kept constant at 3.27 mm for all heat sink configurations. The following expression is used to calculate avg. heat transfer co-efficient.

$$h = \frac{Q}{T_w - T_{vol}} \quad (6)$$

where Q , T_w , and T_{vol} are effective heat flux, solid–liquid avg contact surface temperature of fluid, and fluid avg. volume temperature, respectively. The effective heat flow is computed using the equations below.

$$Q = q \cdot \frac{A}{A_w} \quad (7)$$

where q , A , and A_w denote the total heat flux provided, the heat sink's bottom wall surface area, and the solid–liquid interface region area, respectively. Avg. Nusselt number (Nu) is calculated by following Eq. 8.

$$Nu = \frac{hD_h}{k_w} \quad (8)$$

2.5 Model Validation

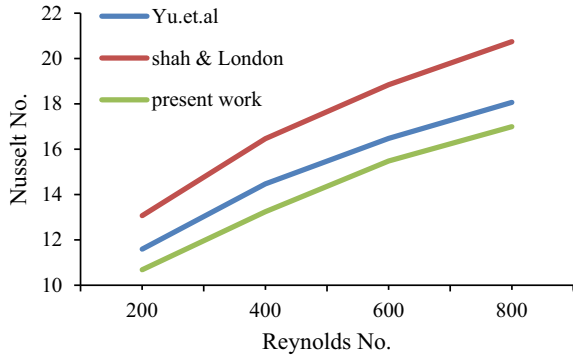
The current numerical model was validated using Yu et al. [16] and Shah et al. [17] Nu correlations. This correlation is intended to be used on a flat surface. Thus, a heat sink's extra flat surface shape was simulated, i.e., without a fin to keep other parameters within the correlations' operating limits. The average value of the Nusselt number was calculated, taking the whole flow domain into account based on the correlations (including developing and developed flow).

$$Nu_{Yu \text{ et al.}} = 2.1219 Re^{0.3204} \quad (9)$$

$$Nu_{Shah \text{ et al.}} = 2.2348 Re^{0.3333} \quad (10)$$

Figure 5 shows a relationship between the average Nu and the different Reynold numbers and at heat flux values of 75 kW/m². The above-mentioned parallels with

Fig. 5 Average Nu for plane microchannel



Eq. 10 in particular were seen as a good agreement. But this model predicts that the Nu value would be approximately 17–20% in line with the Shah et al. [17].

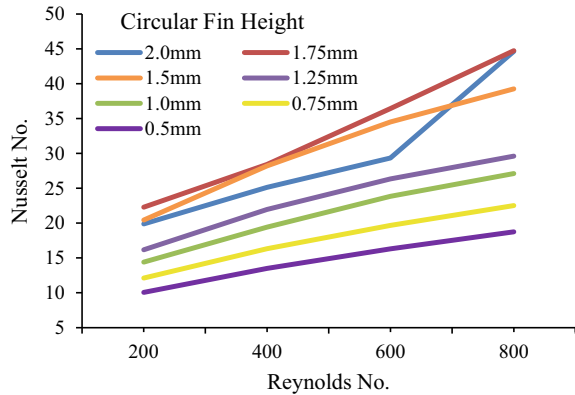
3 Results and Discussion

The study has been proposed with two different fin configuration circular pin fins with varying operational parameters such as Reynolds number. It has dealt with 4 values of Re, i.e., 200, 400, 600, and 800. Four separate setups for the heat sink comprising seven fine height configurations such as 0.5, 0.75, 1.0, 1.25, 1.5, 1.75, and 2.0 mm have been deliberated. The operational factors examined are based on a commonly used selection in the literature and therefore satisfy current heat sink microchannel criteria [5, 16].

3.1 Heat Transfer Performance

To determine the heat transfer performance of different designs of circular fin microchannel heat sinks, Fig. 6 plots the average Nu against Re for a 75 kW/m^2 heat flux. Two significant observations have been made about this figure. To begin, a rise in Re leads in an increase in the average Nusselt number. It is worth noting that the heat sink's coolant flow is disrupted by the fins. Additionally, when Re decreases, the wake created by the trailing edge of the fins accelerates coolant flow via inter-connecting channels, resulting in substantial coolant mixing inside the heat sink and perhaps an early transition to turbulent flow at lower Re. The widespread occurrence of this kind of coolant flow behavior in heat sinks argues for increasing the average Nusselt number with Re. This is self-evident, since the coolant flow rate increases proportionally as Re increases; the coolant transmits more heat.

Fig. 6 Average variation of Nu with Re for various pin fin heights



Close examination shows that the slope of the curves increases as the fin height increases. This tendency is maintained, however, only up to the fin height of 1.25 mm. The increased slope of the curves shows that longer fins can dissipate more heat at higher Re . It is worth noting that heat sinks with fin heights of 1.5 mm and 1.75 mm exhibit exaggerated performance across all Re , whereas heat sinks with 2.0 mm exhibit a significant increase in Nu at Re numbers of 800, indicating some remarkable influence of coolant flow behavior that undoubtedly facilitates favorable heat transfer conditions. However, at 200, 400, and 600 Re , heat transmission increases steadily. Nu reaches a maximum value of 44.7 for heat sinks of 1.75 mm and 2.0 mm at Re 800, but drops to 20, 12, and 8% for fully closed heat sinks of 2.0 mm at Re 600, 400, and 200.

3.2 Overall Pressure Drops

Pressure drop measurements are important for determining the amount of energy required to pump coolant through the microchannel heat sink. Additionally, the thermal performance of the heat sink must be forecasted. The graphic depicts the pressure decrease over the different heat sinks. The pressure drop is the change in pressures at the input and output. It is identified that the pressure differential rises as the Re rises, as does the fin height. The reason for the increased pressure loss is due to the increased blockage to the coolant flow produced by the increased fin height. It is observed that the 1.75 and 2.0 mm of heat sink are having similar flow behavior up to 400 Re ; further for 600 and 800 Re , there is gradually rise in pressure drop such as 7% and 13% respectively, as shown in Fig. 7. Open microchannel 1.75 mm fin height is having higher pressure drop when compared to closed microchannel heat sink of 2.0 mm fin height.

Figure 8 illustrates the pressure drop pattern in the microchannel heat sink using pressure contours. The contours are presented for three fin heights of 1.0, 1.5, and

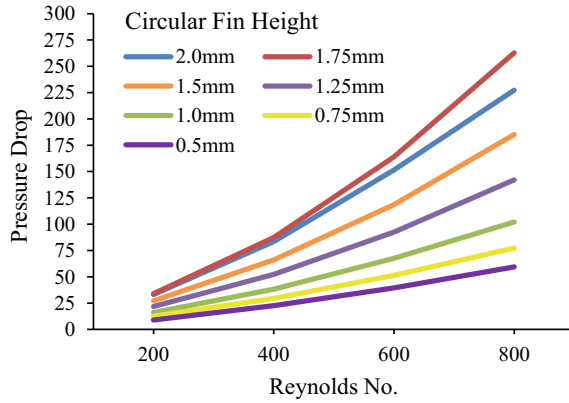


Fig. 7 Average variation of pressure drop with Re for various pin fin heights

2.0 mm at a Re 600 and a heat flux of 75 kW/m². All graphs are in the ZX plane at a distance of 2 mm in the Y direction, with coolant flowing left to right and blue to red color indicating low to high pressure. Pressure drops may be seen throughout the flow path. From the contours, it is noted that there is rise in pressure drop with increase in fin height.

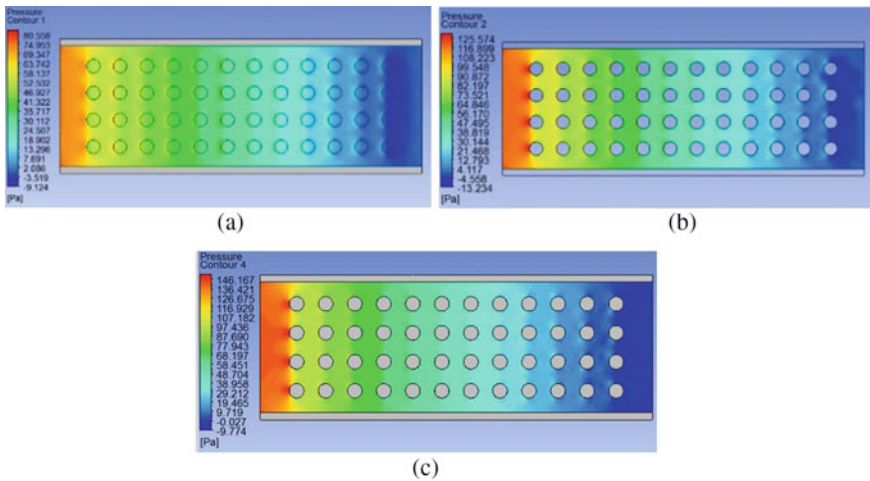


Fig. 8 Pressure contours at Y = 2 mm at 1, 1.5, and 2.0 mm fin heights

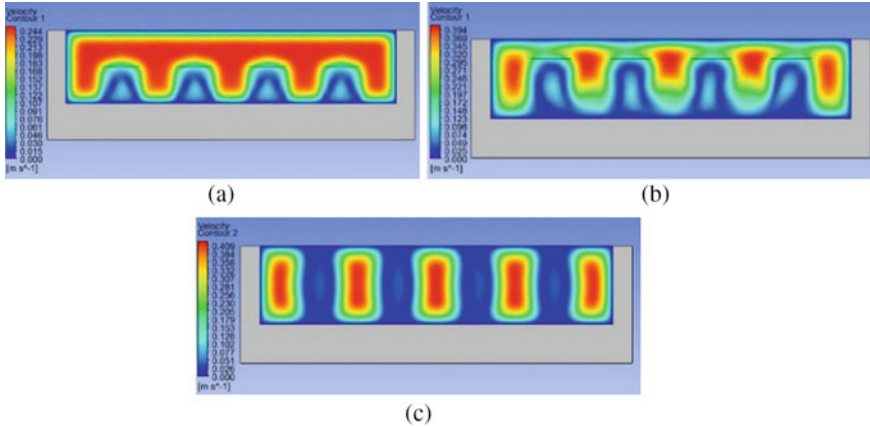


Fig. 9 Velocity contours at mid of plane in X-direction at 1, 1.5, and 2.0 mm fin heights

3.3 Fluid Flow Characteristics

Fluid flow characteristics are mainly necessary to identify the coolant flow route, its flow pattern, and its interaction throughout the fine, primary, and secondary flow path. Figure 9 shows the velocity contour at the mid of x direction in ZY plane for fin height of 1.0, 1.5, and 2.0 mm at 600 Re and 75 kW/m² heat flux. As can be observed, coolant enters the heat sink at a uniform velocity. As that when coolant enters passage between two successive fins (secondary passage), a considerable rise in velocity of coolant is found with increase in fin height.

As the velocity increases, wakes or recirculating vortices develop at the trailing edge of the fins, as shown in Fig. 10. The fins serve as barriers to the coolant flow, causing the vortices to evolve on the trailing edge. When the coolant travels via the secondary path, it is trapped and recirculates near the edge of the fine. It has been observed that increasing the height of the fins slows the flow of coolant through the channel and reduces the amount of free space available in the channel.

3.4 Temperature Contour

To determine the heat transfer properties of a heat sink, the temperature distribution across the base is needed. Figure 11 illustrates the average temperature variation along the bottom wall of a microchannel heat sink. It is self-evident that raising the R_e leads in increased coolant velocity and mass flow rate, resulting in increased heat transfer rate in the heat sink. It is found that 1.75 mm of fin height heat sink is having higher contact surface area of 652.6 mm² and leads to higher heat transfer rate capacity comparative to the other open and closed microchannel heat sinks. Moreover, heat

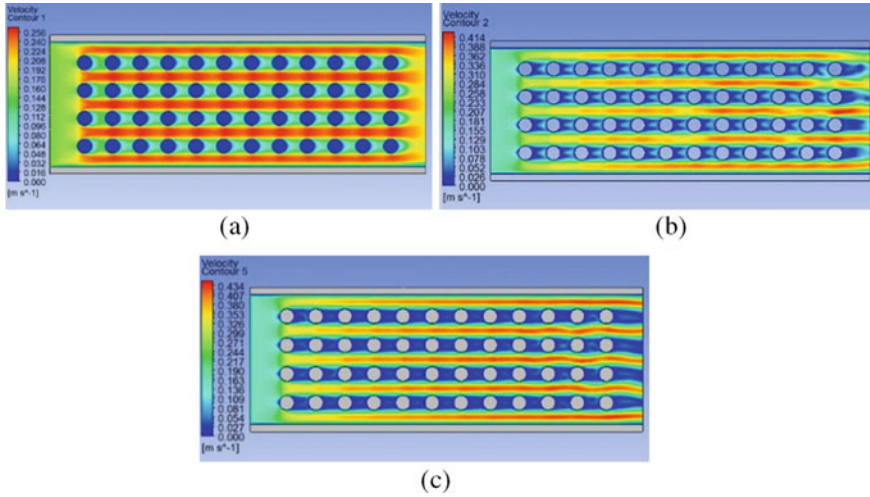
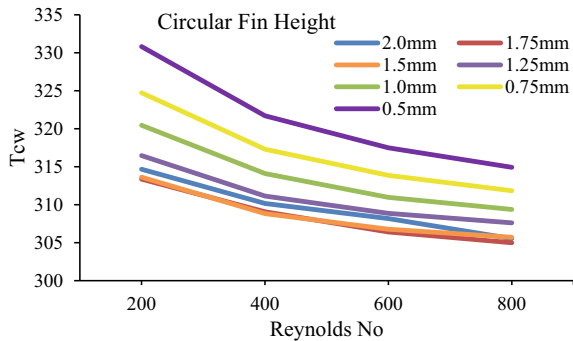


Fig. 10 Velocity contours at $Y = 2$ mm at 1, 1.5, and 2.0 mm fin heights

Fig. 11 Average variation of bottom wall temperature of heat sink (T_{cw}) with Re

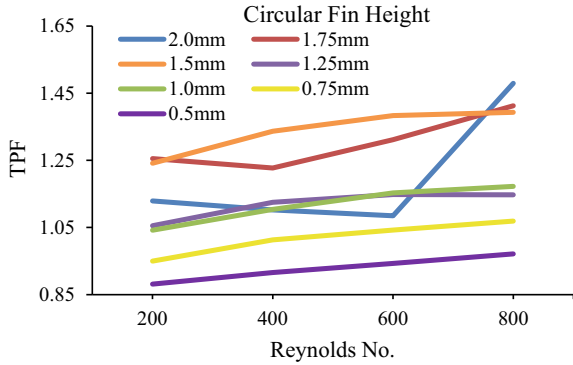


sink with 0.5 mm of fin height is having high-bottom wall temperature irrespective of Re.

3.5 Thermal Performance Factor

Thermal performance factor (TPF) is a parameter used to determine the effectiveness of the microchannel heat sink. The thermal performance factor (TPF) is the ratio of increased heat transfer to pressure decrease. Equation 11 provides the expression for TPF, which was utilized in an empirical research by Zhao et al. [13] for the purpose of evaluating the aggregate performance of all instances, the TPF is determined.

Fig. 12 Average variation of Re with TPF



$$TPF = \frac{Nu/Nu_i}{(\Delta P/\Delta P_i)^{\frac{1}{3}}} \tag{11}$$

where ΔP , ΔP_i , and Nu_p represent the pressure drop over the plain heat sink and Nusselt number in the microchannel. Figure 12 illustrates the thermal performance factor changes with Reynolds number for all microchannel heat sink configurations.

It is noted that the 1.75 mm of heat sink is having higher TPF at 200 Re and is dropped at 400 Re, and it is seen that there is increase in TPF with increase in Re. For the 2.0 mm of heat sink, it is found that there is drastically increase in TPF for 800 Re. When it comes to average, TPF for all the Re 1.5 mm of heat sink is better when compared to other heat sinks.

4 Conclusions

A comparative analysis of open and closed microchannel heat sink is performed, to determine the optimal design value that provides the best heat transfer and fluid flow characteristics. Seven circular shape heat sinks of varying heights were studied. The 2 mm thermal heat sink is a closed microchannel heat sink, and some of the findings are given below.

1. Nu reaches a maximum value of 44.7 for heat sinks of 1.75 and 2.0 mm at 800 Re but drops by 20, 12, and 8% for closed heat sinks 2.0 mm at 600, 400, and 200 Re. Longer fins can dissipate more heat at higher Re.
2. The pressure drop grows with Re, as does the fin height increases. Up to 400 Re, the 1.75 and 2.0 mm heat sinks pressure drop is similar, but at 600 and 800 Re, the pressure drops increased by 7 and 13% when compared with closed heat sink.
3. It is found that 1.75 mm heat sink is higher heat transfer rate capacity comparative to the other open and closed microchannel heat sinks. Moreover, heat sink with 0.5 mm of fin height is having high-bottom wall temperature irrespective of Re.

4. The average TPF for all the Re, 1.5 mm of heat sink is better when compared to other heat sinks.

References

1. Lee J, Mudawar I (2009) Low-temperature two-phase microchannel cooling for high-heat flux thermal management of defense electronics. *IEEE Trans Components Packag Tech* 32(2):453–465
2. Madhuri CR, Ramakrishna K, Abhishek D (2019) Heat transfer enhancement using hybrid nanofluids in spiral plate heat exchangers. *Heat Transf Asian Res* 48:3128–3143
3. Ahmed HE, Salman BH, Kherbeet AS, Ahmed MI (2018) Optimization of thermal design of heat sinks: a review. *Int J Heat Mass Transf* 118:129–153
4. Metta VR, Ramakrishna K, Abhishek D (2018) Thermal design of spiral plate heat exchanger through numerical modeling. *Int J Mech Eng Tech* 9(7):736–745
5. Yadav V, Kumar R, Narain A (2019) Mitigation of flow maldistribution in parallel microchannel heat sink. *IEEE Trans Compon Packag Manuf Technol* 9(2):247–261
6. Zhang S, Tang Y, Yuan W, Zeng J, Xie Y (2016) A comparative study of flow boiling performance in the interconnected microchannel net and rectangular microchannels. *Int J Heat Mass Transf* 98:814–823
7. Chamkha AJ, Molana M, Rahnama A, Ghadami F (2018) On the nanofluids applications in microchannels: a comprehensive review. *Powder Technol* 332:287–322
8. Kumar N, Singh P, Redhewal AK, Bhandari P (2015) A review on nanofluids applications for heat transfer in micro-channels. *Procedia Eng* 127:1197–1202
9. Siu-Ho A, Qu W, Pfefferkorn F (2007) Experimental study of pressure drop and heat transfer in a single-phase micropin-fin heatsink. *J Electron Packag* 129(4):479–487
10. Yadav V, Baghel K, Kumar R, Kadam ST (2016) Numerical investigation of heat transfer in extended surface microchannels. *Int J Heat Mass Transf* 93:612–622
11. Khalili SA, Koşar A (2018) Numerical investigations on the effect of fin shape and surface roughness on hydrothermal characteristics of slip flows in microchannels with pin fins. *Int J Therm Sci* 124:375–386
12. Liu M, Liu D, Xu S, Chen Y (2011) Experimental study on liquid flow and heat transfer in micro square pin fin heat sink. *Int J Heat Mass Transf* 54(25–26):5602–5611
13. Zhao J, Huang S, Gong L, Huang Z (2016) Numerical study and optimizing on micro square pin-fin heat sink for electronic cooling. *Appl Therm Eng* 93:1347–1359
14. Kadam ST, Kumar R, Abiev R (2019) Performance augmentation of single-phase heat transfer in open-type microchannel heat sink Vol 33, No 2, pp 416–424
15. Bhandari P, Prajapati YK (2021) Thermal performance of open microchannel heat sink with variable pin fin height. *Int J Therm Sci* 159:106609
16. Yu X, Woodcock C, Plawsky J, Peles Y (2016) An investigation of convective heat transfer in microchannel with Piranha Pin Fin. *Int J Heat Mass Transf* 103:1125–1132
17. Shah RK, London AL (2014) *Laminar flow forced convection in ducts: a source book for compact heat exchanger analytical data*. Academic press

Transient Heat Transfer Analysis on Coaxial Surface Junction Thermocouples of Types K, E, and J



Chaganti Apoorva Priya and Ravi K. Peetala

Abstract Heat transfer is paramount in the design of hypersonic vehicles. For a vehicle at hypersonic flight, it is arduous to precisely estimate the surface convective heat flux. A need has emerged, for fast responses in the measurement of transient temperature data, in such hostile hypersonic conditions, thus paving way for the development of thermal sensors like thin film temperature detectors and coaxial surface junction thermocouples, for various aerospace applications. Owing to the presence of high temperatures, the surface heat flux and temperatures cannot directly be measured at the surface. Inverse analysis is used to detect the heat flux, from the temperature measurements given by the sensors, placed beneath the surface. In this study, the transient temperature data is acquired from the models of coaxial surface junction thermocouples, of types K, E, and J, from thermal simulation. This data is suitably discretized and is subsequently used in recovering the convective heat flux. Validation of the numerical models of the thermocouples, is done using analytical methods, by retracting the heat flux supplied during the simulation. The obtained heat flux histories from the analytical methods are observed to be in close approximation to the given input heat load of 1000 and 5000 W/m². The transient temperature histories generated from the numerical simulation, are found to be in-line with the experimental outcomes.

Keywords Hypersonic vehicles · Convective heat flux · Transient temperature data · Coaxial surface junction thermocouples

1 Introduction

Advancements in the aerospace applications, have caused studies on hypersonic flows to come into prominence. Hypersonic flow being high energy flow, with Mach numbers of about 5 or greater, establish significant high-temperature phenomena in

C. A. Priya (✉) · R. K. Peetala

Department of Mechanical Engineering, Visvesvaraya National Institute of Technology,
Nagpur 440010, India

e-mail: ch.apoorvapriya@gmail.com

the gas. The boundary layers possess high temperatures, due to the viscous dissipation of the flow's kinetic energy. The enormous temperatures excite vibrational energy internally within the molecules, causing dissociation and ionization of the gas. Aerothermodynamic heating, wherein the heat is transferred from the fluid flow to the surface of the vehicle, is crucial in hypersonic flow, as it is linearly dependent on the kinetic energy of the vehicle [1], and generates requirement for usage of appropriate thermal protection systems. Hence it becomes necessary to ensure accurate measurement of heat flux distribution over the vehicle's surface, in a hypersonic flight. The estimation of surface heat flux is done by temperature measurement, in short test durations. The high total enthalpy of hypersonic freestream in the facilities makes it inevitable to have short test durations, for feasible thermal survival [2].

In this work, Coaxial Surface Junction Thermocouples (CSJTs), based on the Seebeck effect, have been studied. Coaxial Surface Junction Thermocouples feature a unique design, where one thermocouple element is swaged over the other, with a thin layer of electrical insulation in between, having a thickness of about 10 μm . The design of coaxial thermal gauge was first proposed by Bendersky, which was made up of a small wire, consisting one thermoelement, coated with a layer of 12 μm thick aluminium oxide insulation [3]. Due to the presence of smaller dimensions and tube thicknesses in the CSJT, ample precision is required in its fabrication. The steps involved in the fabrication process consist of preparation of the external and internal elements, and preparation of the sensing end of the assembly.

The junction of the thermocouple is formed by plastic deformation when one thermocouple element is abraded over the other, with an abrasive blade or a sandpaper. This allows the CSJT to be perfectly fit into any curved wall, with no gaps between the thermocouple and the wall surface, hence leaving the temperature measurement undisturbed. The micro-scratches generated in the junction formation, represent small amounts of active masses and form an active part of the junction, leading to short response times. The formation of the thermocouple junction in this way, makes the gauge very robust and suitable for the application in hostile hypervelocity conditions.

Numerous research activities have been performed in the study of CSJTs over the last few decades. Charles et al. [4] developed a quick response high temperature and high pressure- resistant thermocouple. The thermocouple was made up of two thin wires, implanted in fused alumina. A thin film of molybdenum provided the electrical contact at the surface junction of the thermocouple. Mohammed et al. [5, 6] demonstrated the design technique of K-type CSJT and associated fabrication difficulties. In addition, the microstructural analysis and the chemical characterization which included SEM and EDX analysis, were carried out. These were used to verify the surface morphology and to evaluate the material composition of CSJT, qualitatively. The EDX analysis showed that the entire surface of the CSJT, comprised alumel and chromel distributed throughout. The ability of developed sensor to measure the transient surface temperatures, was demonstrated using UNITEN's shock-tube facility. The obtained results have shown a time response of the order of microseconds and confirmed the suitability for making the transient heat transfer measurement.

The use of CSJTs in hypervelocity flows is apt, as it provides important advantages of rugged design, faster response time, higher calibration stability, and an ability to be contoured to model surface, in transient heat transfer measurements [5]. As the thermal inertia of the junction so formed is low, temperatures close to the surface of interest, could be gauged well [3].

In this work, numerical modelling and transient thermal analyses of CSJTs of types K, E and J are done, using ANSYS. The temperature-time history obtained from the analytical analysis, is discretized using the cubic-spline fitting with constant thermal properties, to obtain heat flux in order to validate the given input heat flux during simulation. Also, for the known wattage of an input heat flux, a study is done to compare the transient temperature histories obtained by numerical simulations of CSJT models with the ones resulting from the experiments [7].

2 Materials and Methods

2.1 Theoretical Modelling of Coaxial Surface Junction Thermocouples

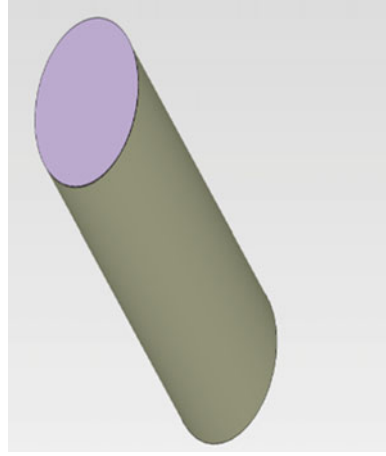
The principle of application of coaxial surface thermocouple for heat flux rate estimation, is temperature measurement of the surface of a body which could be considered as semi-infinite. A semi-infinite body is one which extends to infinity in all directions but one. It is characterized by a single identifiable surface. If sudden changes are imposed at this surface, one-dimensional, transient heat conduction would occur within the body. This semi-infinite consideration provides us with a useful idealization for approximating the transient response of a thermocouple. CSJTs are usually formed from inner wire of negative elements with an outer annulus of the positive element, with both elements being electrically insulated by a layer of epoxy-resin along the length of the element. The artificially created micro-scratches, during the formation of surface junction, help in quickly responding, during short duration timescale of application [8].

The principle on which thermal sensors work, have been systematically studied by Schultz and Jones [9]. Firstly, transient temperature histories are measured by the sensors, and in turn, heat flux is estimated. Considering the model to be transferring heat in one-dimension and the heat flow to be unsteady, the system could be thought of as a semi-infinite solid.

$$\rho c \frac{\partial T}{\partial t} = \frac{\partial}{\partial x} \left[k \frac{\partial T}{\partial x} \right] \quad (1)$$

In order to have uniform initial conditions, if a heat load of $q_s(t)$ is applied instantly, the CSJT would sense a transient temperature of $T_s(t)$. The thermocouple wires are 10 mm long, the outer wire has a diameter 3.25 mm, and the sensing surface junction

Fig. 1 Computational model of CSJT



is 20 μm thick [10]. Initial condition for the simulation is: At $t = 0$ and $0 \leq y \leq 10.02$ mm; $T(y, 0) = 300$ K; at the top wall, $y = 0$, $t > 0$, $q(0, t) = q_s(t)$; at interface, $y = 0.02$ mm. $t > 0$, $T_1 = T_2 = T_s(t)$; at the bottom wall; $y = 10.02$ mm, $t > 0$; $T(10.02, t) = 300$ K. A computational model is shown in Fig. 1. Solving the above equations, whilst treating the thermal properties of the coaxial sensors as constant, Duhamel's superposition integral is put to use, to calculate the heat flux, $q_s(t)$, passing through the surface [11];

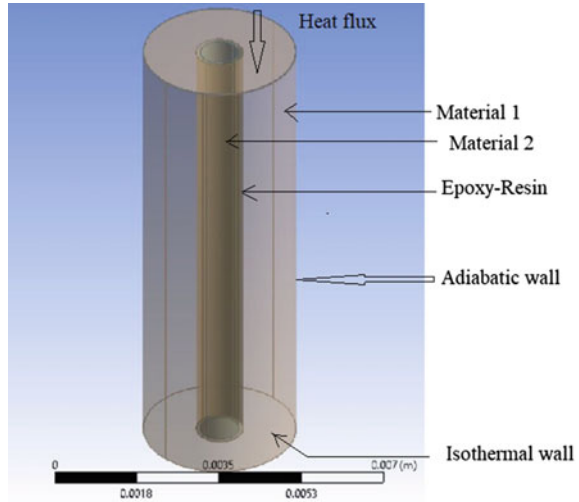
$$q_s(t) = \frac{\beta}{\sqrt{\pi}} \int_0^t \frac{1}{\sqrt{t-\tau}} (dT_s(\tau)/d\tau) d\tau \quad (2)$$

where $\beta = \sqrt{\rho c k}$ is the thermal product of the sensor.

2.2 Numerical Simulation of the Coaxial Surface Junction Thermocouple

Numerical analysis is done in ANSYS APDL (Transient Thermal) v 16.0, by the finite element simulation method, for a known wattage of input step heat loads. The schematic model of the CSJT is shown in Fig. 2. A transient thermal simulation is performed for a duration of 1 s with constant heat flux of 1000 W/m^2 , applied at the surface junction of the thermal probe. The side walls/surface were considered adiabatic, the bottom wall/surface was assumed isothermal with temperature equal to room temperature of 300 K. Subsequently heat load is increased to 5000 W/m^2 and observed. A geometric arrangement of coaxial elements and the boundary conditions to which the thermocouple is subjected to, is shown in the figure.

Fig. 2 Schematic of model of CSJT



The properties of the thermocouple elements are tabulated in Table 1. The properties of the surface junction are considered to be average of those of the thermocouple elements (Table 2). The thermophysical properties selection of temperature sensor elements was taken from Caldwell [12]. As per the investigation performed by Caldwell [12], the approximate analysis of temperature sensors’ elements is as follows,

- (i) alumel constituents are: 94–96% Ni, 1–1.5% Si, 1.3–2.5% Al, 1.8–3.25% Mn, and iron and other constituents in smaller quantities;

Table 1 Properties of thermocouple elements [12]

Material	Density	Specific heat	Thermal conductivity
Alumel	8600	523.336	27.463
Chromel	8730	447.83	17.846
Constantan	8900	390	19.5
Iron	7870	450	80.4
Epoxy	1150	1100	0.15

Table 2 Properties of thermocouple sensors [12]

Type	Density	Specific heat	Thermal conductivity
K (alumel-chromel)	8665	486	22.65
E (chromel-constantan)	8815	419	18.67
J (iron-constantan)	8385	420	49.75

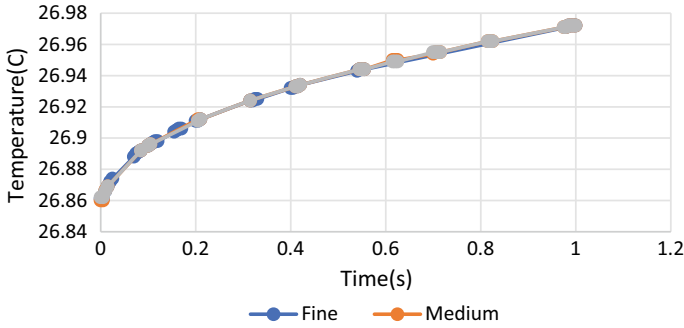


Fig. 3 Grid- independence test using fine, medium, and coarse grid

- (ii) chromel constituents are: 89–90% Ni, 9–9.5% Cr, up to 0.5% Si, 0.02–0.65% Fe, and 0.01–0.8% Mn;
- (iii) constantan constituents are: 55% Cu, 45% Ni

A grid-independence test was performed for coarse, medium, and fine mesh structures, selecting a K-type CSJT and subjecting to a transient thermal load of 1000 W/m^2 for a duration of 1 s. It was observed that the choice of grid-size does not influence the final solution, for the simulations so performed (Fig. 3).

3 Results and Discussion

Thermal simulations are performed on the model of the coaxial thermocouples by imposing sudden changes at the surface junction, thereby one-dimensional, transient heat conduction would occur within the body, as per the semi-infinite slab assumption. This approximation is useful in short duration transient studies, during which, temperatures further below the surface junction are essentially uninfluenced by changes in the surface conditions. The numerical modelling of the three-dimensional sensor configurations by supplying instantaneous heat loads, is done to estimate the gauge dimensions, and directionality of heat flow. The thermal sensor must account for the rapidly varying flow environment and should have very fast response characteristics. As there are no direct means for estimation of surface heat flux, the measured transient temperature data is processed and heat flux based on one-dimensional transient heat conduction theory is recovered, using cubic-spline method.

3.1 Transient Thermal Simulation

A transient simulation has been performed for a duration of 1 s with constant input heat flux of 1000 W/m^2 , applied on the surface junction of the thermal probe, and

the variation of temperature along the length of the thermocouple is depicted in the following figures. Figure 4 shows the transient temperature history for the thermocouples and an appreciable change in temperature is observed till a length of around 6 mm, measuring from the surface junction, in the longitudinal direction, which is the thermal penetration depth of the sensor. Hence it can be shown that the heat transfer is one-dimensional, and can be asserted that the chosen length of the substrate does not violate the assumption of heat conduction for semi-infinite geometry.

Under the same initial and boundary conditions, with a heat supply of 1000 W/m², the thermocouples are then studied to observe the variation along the radius of the surface junction (hot junction). It is noted from Fig. 5, that the lateral variation of temperature is observed to be negligible, owing to the fact that the assumption of adiabatic conditions along the walls, is considered. Thus, the substrate of the sensor does not undergo any lateral heat conduction and the heat is only transferred in the normal direction of the substrate, satisfying the conditions required for assumption of semi-infinite condition.

The thermocouples are further studied by increasing the heat load to 5000 W/m², and temperature contours are generated as shown in Fig. 6.

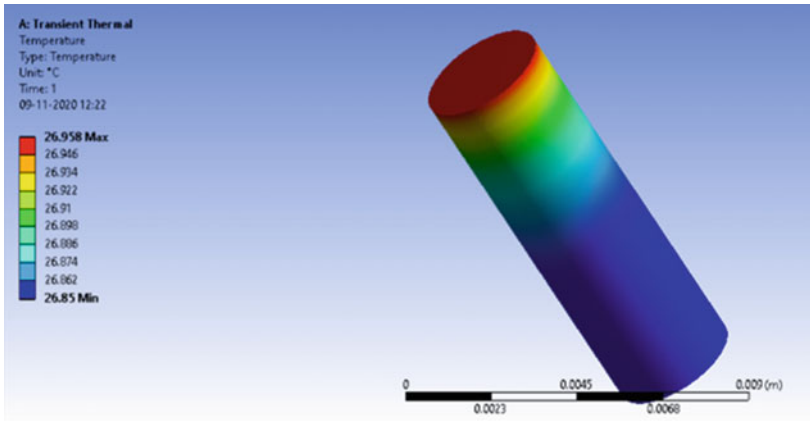
3.2 Validation of Heat Flux Obtained with Numerical Algorithm

The Eq. (2) is one of the most effective forms of temperature data analysis in transient heat transfer applications. Practically, the function in the Eq. (2) cannot be described by a simple expression, making it essential to perform numerical integration by discretizing the temperature data. The obtained temperature–time history of the sensors is discretized using a cubic-spline technique, and the surface heat flux equation is then in the following form;

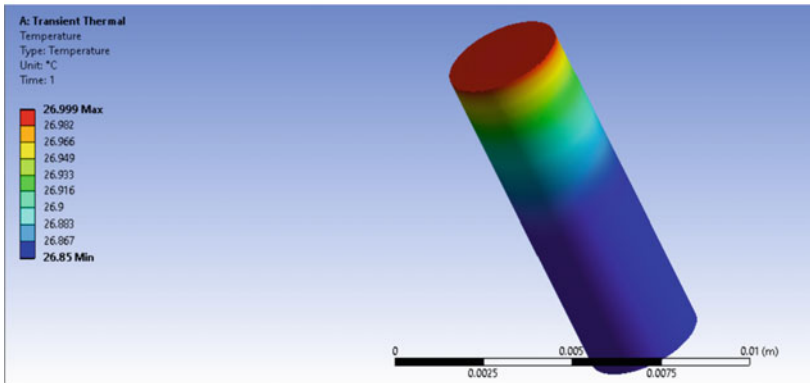
$$\begin{aligned} \{q_s(t)\}_{\text{spline}} = & \left\{ \left[2((\rho_2 C_2 k_2)/\pi)^{1/2} \sum_{(i=1)}^{(M-1)} \left\{ V_i \left(P_i^{1/2} - R_i^{1/2} \right) \right. \right. \right. \\ & - \left(W_i \left(P_i^{3/2} - R_i^{3/2} \right) \right) / 3 \\ & + \left. \left. \left(a_{4,i} \left(P_i^{5/2} - R_i^{5/2} \right) \right) / 10 \right\} \right. \\ & + 2((\rho_2 C_2 k_2)/\pi)^{1/2} \left(V_M - P_M^{1/2} - \left(W_M P_M^{3/2} \right) \right) / 3 \\ & \left. \left. + \left(a_{4,i} P_M^{5/2} \right) / 10 \right] \right\} \sqrt{S_t} \end{aligned} \tag{3}$$

where S_t , is the time scaling factor; constants P , R and W are embedded with the transient surface temperature history.

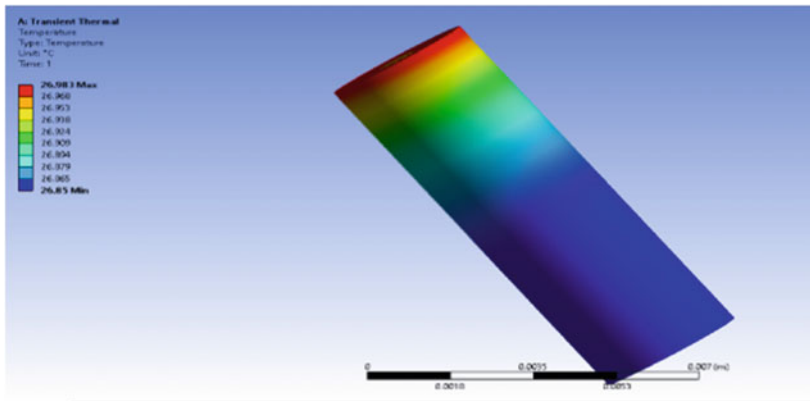
A numerical algorithm developed in MATLAB, is used for retracting the surface heat flux [incorporating Eq. (3)] from the discretized transient temperature. The heat



(a)



(b)



(c)

Fig. 4 Temperature contours of types K, E, and J thermocouples, along their length for an input heat load of 1000 W/m^2

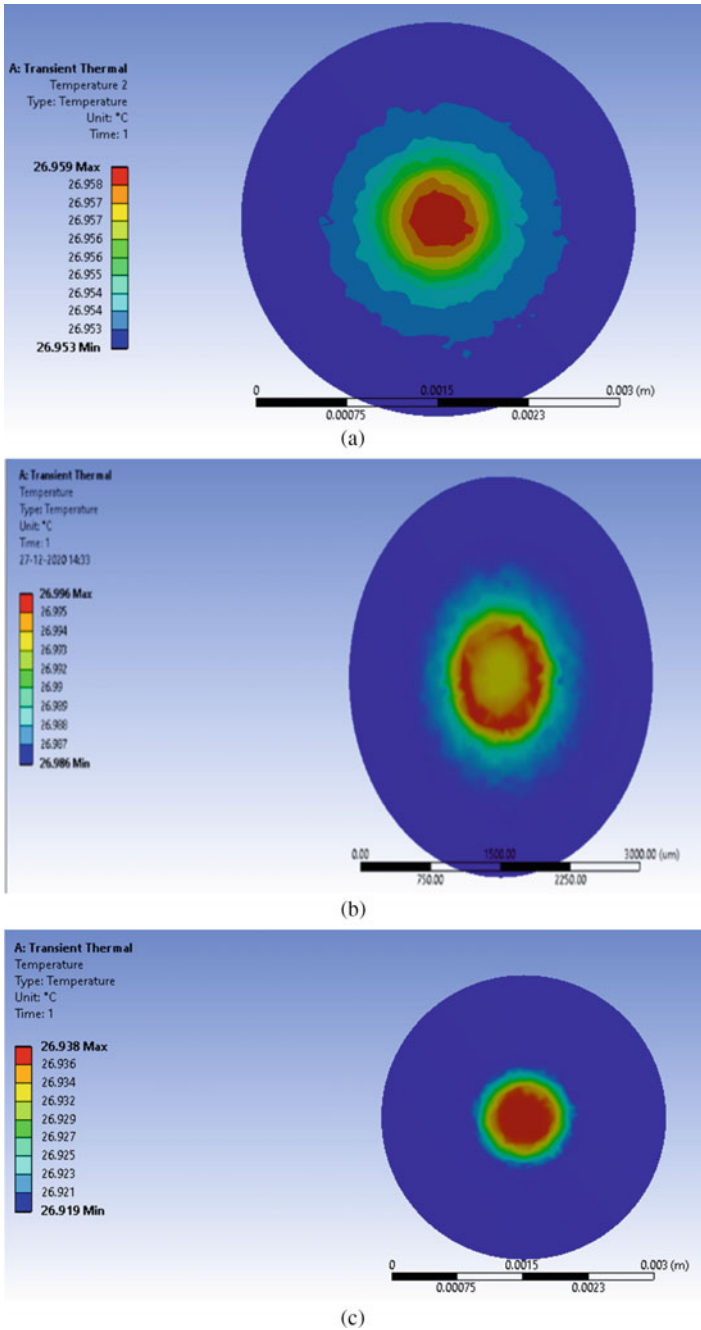


Fig. 5 Temperature contours of the surface junctions of types K, E, and J, showing temperature along the radial direction

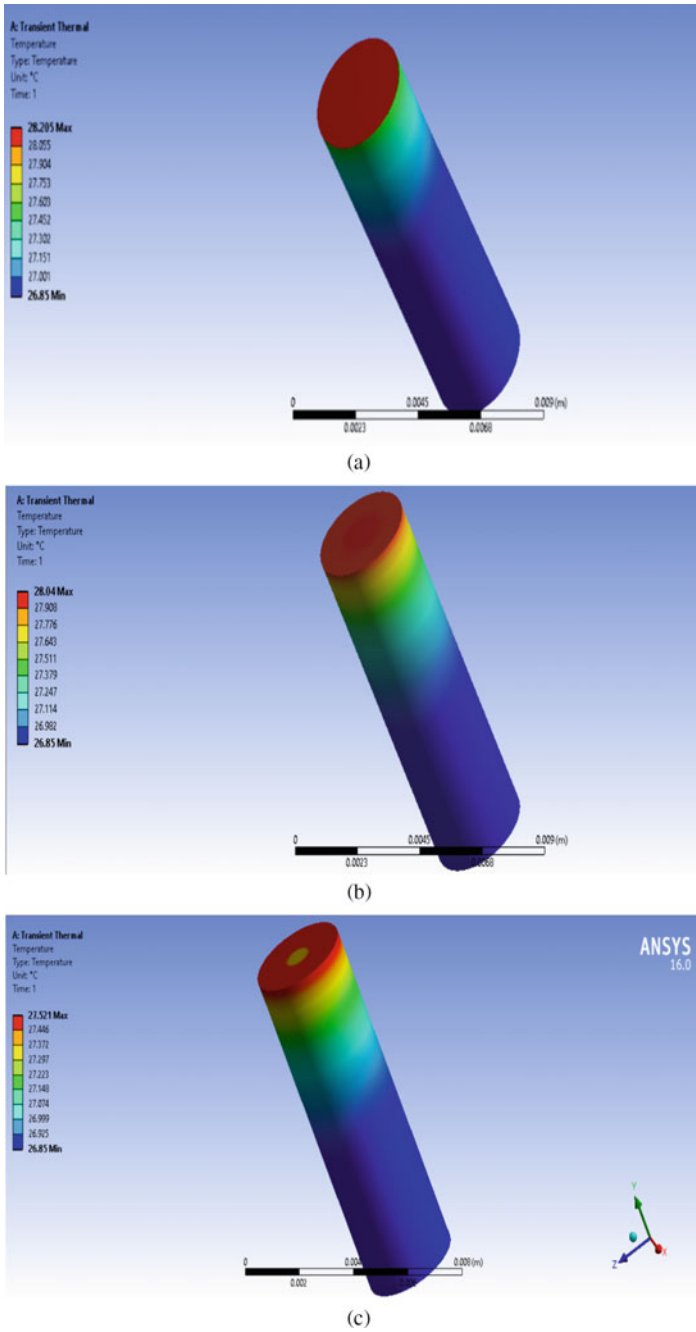


Fig. 6 Temperature contours of the types K, E, and J CSJTs, along their lengths, for an input heat load of 5000 W/m^2

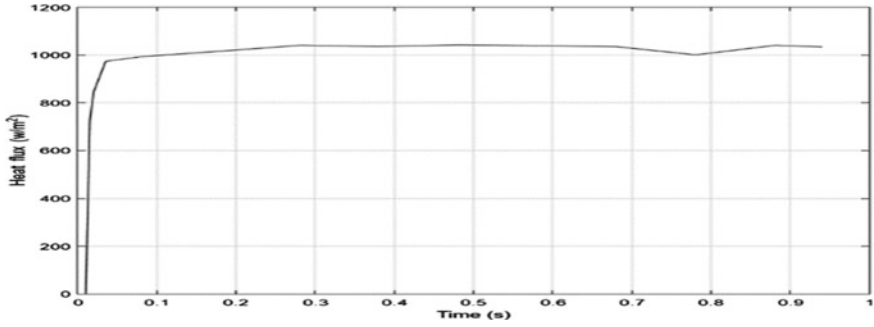


Fig. 7 Heat flux-time plot generated, for the K-type CSJT, with input load 1000 W/m^2

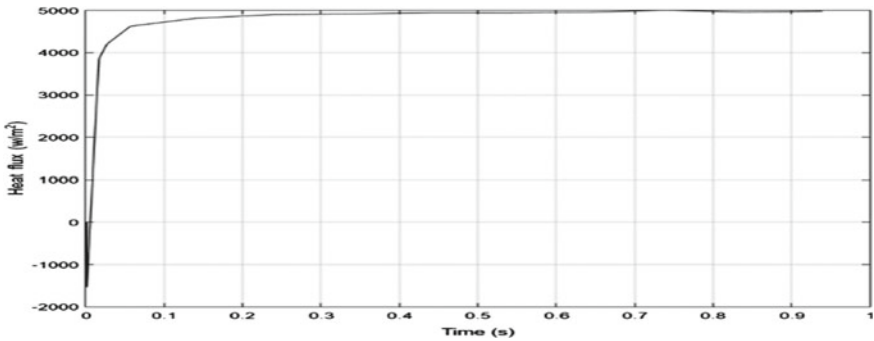


Fig. 8 Heat flux-time plot generated, for the K-type CSJT, with input load 5000 W/m^2

fluxes computed from analytical methods, are shown in Figs. 7, 8, 9, 10, 11 and 12, for K, E and J types of CSJTs, with input heat loads given numerically as 1000 W/m^2 and 5000 W/m^2 . The results produced a mean heat flux value, which estimate to 1000 W/m^2 and 5000 W/m^2 , respectively, same as the input value given. The correctness of simulation is thus verified from the obtained heat flux histories.

3.3 Comparison of Simulation Results with Experimental Data

The simulation results generated, are compared with the ones obtained in an experimental study done, by researchers at ISM Dhanbad [7]. A unit developed for experimental studies of K, E, and J types of, fast response coaxial probes for transient measurements, had the probes' sensing surfaces subjected to step heat loads, to capture transient temperatures for a duration of 1.50 s. The experimental unit consisted of a continuous-wave type infrared diode laser heat source. The transient

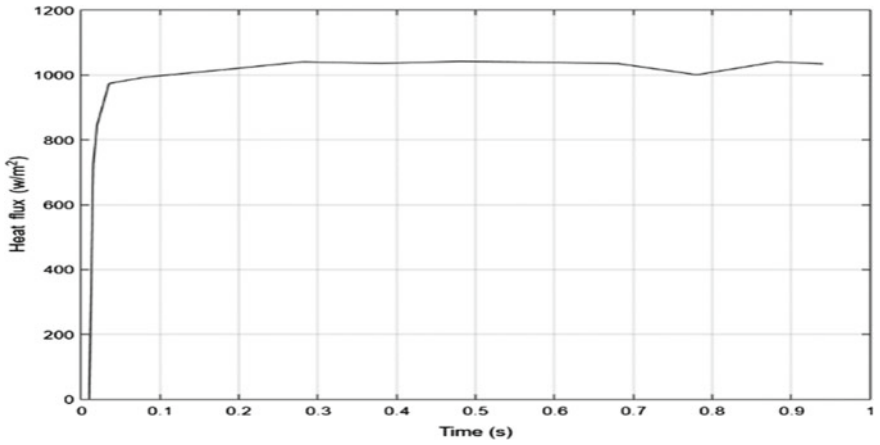


Fig. 9 Heat flux-time plot generated, for the E-type CSJT, with input load 1000 W/m^2

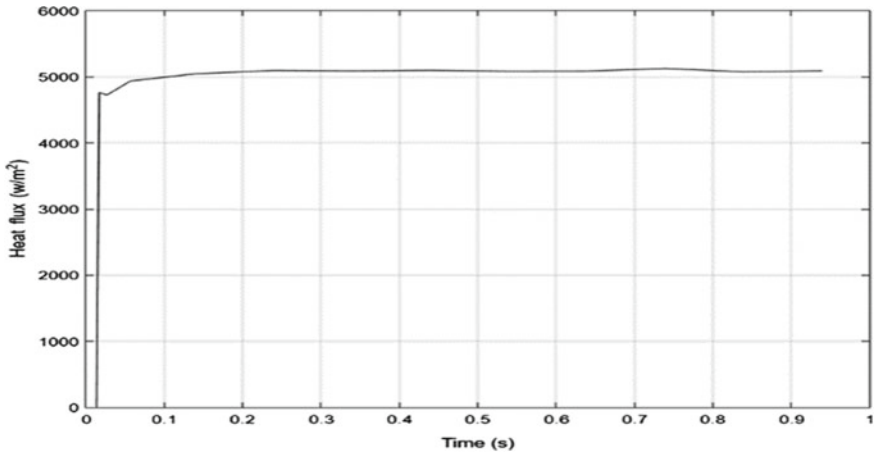


Fig. 10 Heat flux-time plot generated, for the E-type CSJT, with input load 5000 W/m^2

temperatures from the experimental approach, and numerical analysis for K, E, and J types of coaxial probes with 5 kW/m^2 input heat load, are generated as shown in Fig. 13. The percentage error of the numerical results compared to the experimental results are found to be 0.132%, 0.06%, and 0.089%, respectively.

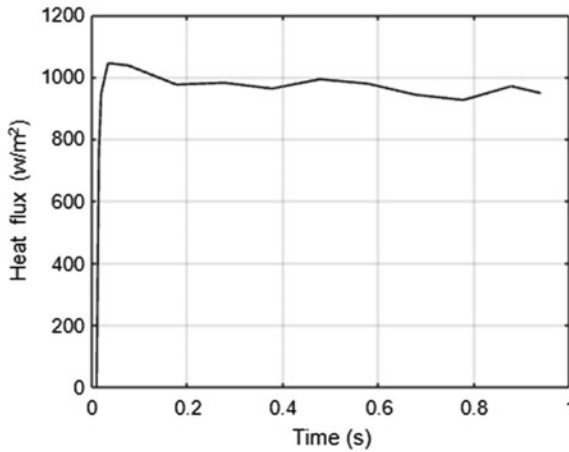


Fig. 11 Heat flux-time plot generated, for the J type CSJT, with input load 1000 W/m²

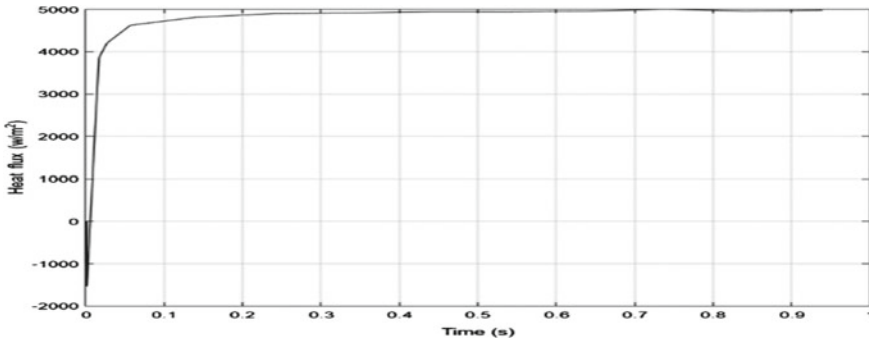


Fig. 12 Heat flux-time plot generated, for the J type CSJT, with input load 5000 W/m²

4 Conclusions

The numerical simulations on K, E, and J types of thermocouples are done to find the required dimension of the thermal sensor for which the semi-infinite assumption holds good. An estimate of the thermal penetration depth of the sensor is done. Transient thermal simulations in ANSYS are conducted to obtain temperature histories of the sensor, for short durations. It can be concluded that there is no significant variation in the lateral direction and a gradual decrement in the temperature is observed along the length of the sensor, thus in-line with the assumptions considered. It is found that the mean heat flux recovered from the analytical methods, approximates quantitatively to the input heat flux in the numerical simulation, and thus the dimension of the model is validated. The transient temperature histories obtained numerically are found to be consistent with those obtained from the experiments.

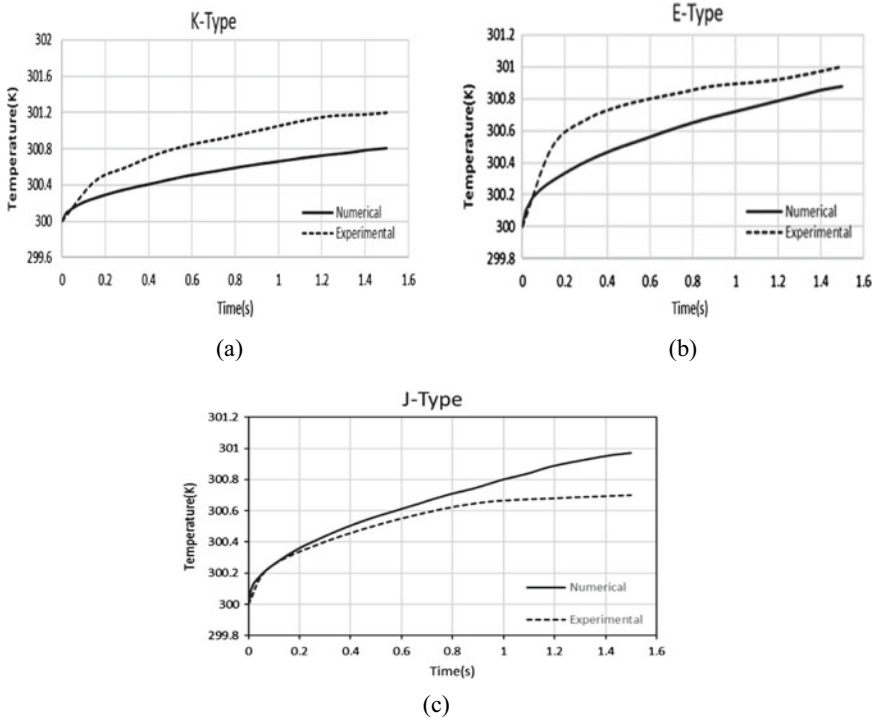


Fig. 13 The transient temperature histories for 1.5 s, of CSJTs of types K, E, and J, with 5 kW/m^2 input heat load

References

1. Fletcher DG, Fundamental of hypersonic flow, aerothermodynamics. Von Karman Institute, Belgium
2. Menezesa V, Bhat S (2010) A coaxial thermocouple for shock tunnel applications. Department of Aerospace Engineering, Indian Institute of Technology Bombay, Powai, Mumbai 400-076, India
3. Mohammed H, Salleh H, Yusoff MZ (2008) Design and fabrication of coaxial surface junction thermocouples for transient heat transfer measurements. Universiti Tenaga Nasional, Malaysia, College of Engineering
4. Charles E, Lorival R, Boyer A, Malbrunot P (1984) A fast-response, high-temperature high-pressure surface thermocouple. *Sens Actuat* 6(2):135–142
5. Mohammed H, Salleh H, Yusoff MZ (2010) Fast response surface temperature sensor for hypersonic vehicles. *Instr Experim Techniq* 53(1):153–159
6. Mohammed H, Salleh H, Yusoff MZ (2008) Design and fabrication of coaxial surface junction thermocouples for transient heat transfer measurements. *Int Commun Heat Mass Transfer* 35(7):853–859
7. Manjhi SK, Kumar R (2020) Comparative performance of K, E, and J-type, fast response coaxial probes for short-period transient measurements
8. Buttsworth DR (2001) Assessment of effective thermal product of surface junction thermocouples on millisecond and microsecond time scales. *Exp Thermal Fluid Sci* 25(6):409–420

9. Schultz DL, Jones TV (1973) Heat transfer measurements in short duration hypersonic facilities. AGARD-AG-165
10. Agarwal S, Sahoo N, Singh RK (2016) Experimental techniques for thermal product determination of coaxial surface junction thermocouples during short duration transient measurements. *Int J Heat Mass Transf* 103:327–335
11. Cook WJ, Felderman EJ (1966) Reduction of data from thin film heat transfer gauge: a concise numerical technique. *AIAA J* 4(3):561–562
12. Caldwell FR (1962) Applied methods and instrument; temperature: its measurement and control in science and industry, thermocouple materials. In: Herzfeld CW (ed) Reinhold, Vol 3, No 2. New York, pp 81–134

Comparison of Heat Transfer Characteristics of Nanofluids for Electric Vehicle Battery Thermal Management



S. G. Sankeeth, S. Kathiresan, J. Harish, D. Srihari, and R. Harish

Abstract The efficiency and performance of electric vehicle batteries are affected due to the high working temperature and operating conditions. Thus, in this study, a novel battery thermal management system using nanofluids is being designed and evaluated. The heat transfer characteristics are numerically investigated using commercial Finite volume solver Ansys Fluent. The CAD model of the battery pack is generated using Design Modular geometry in Ansys. The base fluid is considered as water into which monodispersed nanoparticles of uniform size are dispersed to enhance the overall thermal performance. The nanoparticles considered in the present study are made of metals, metal oxides, carbides, carbon nanotubes, etc. The parametric study is performed using different nanoparticles such as aluminum, aluminum oxide, and single-walled carbon nanotubes (SWNCT). Further investigations are performed by varying the battery temperature and volume concentration of nanoparticles. It is found that the system achieved a considerable drop in temperature, compared to the conventional cooling methods. It was also found that there is a drastic change in the coolant performance on varying the volume fraction of the nanoparticles in the base medium.

Keywords Conventional cooling methods · Nanofluids · Volume fraction

1 Introduction

The main objective is to numerically analyze the battery thermal management of electric vehicles using nanofluids. The lithium-ion batteries which are being widely used in electric vehicles and many other upcoming fields have optimal working temperature which ranges from $-20\text{ }^{\circ}\text{C}$ to $60\text{ }^{\circ}\text{C}$, above which the battery will not perform effectively due to thermal runaway effect which may lead fatal problems. The battery pack is the backbone of any electrical system such as electric vehicles (EVs). The batteries are closely packed which results in the increase of temperature

S. G. Sankeeth · S. Kathiresan · J. Harish · D. Srihari · R. Harish (✉)
School of Mechanical Engineering, Vellore Institute of Technology, Chennai,
Tamil Nadu 600127, India
e-mail: harish.r@vit.ac.in

thereby leading to heat accumulation which in turn affects the entire performance and efficiency of the battery. The rise in temperature in each module of the cell will affect the other modules internally in the battery pack. Although electric vehicles have become popular due to their zero emission and Low Maintenance, still few factors limit the development, performance, cost, lifetime, and safety of the battery. The effective thermal management in batteries is highly important, and various cooling methods such as active cooling method and passive cooling method are applied to make the battery pack work more effectively. The study is based on active cooling in which the coolant liquid or mixture liquid comprising of a base fluid and nanoparticles are in direct contact with the battery cells. The active cooling method plays a vital role in thermal management of battery which results in the temperature distribution along with the nanofluid. The cooling performance of nanofluids as coolant reduces the maximum temperature compared to other conventional cooling methods. Nanofluids have high value in this new type of cooling with high thermal conductivity to the thermal management system of power battery packs for electric vehicles.

Xu et al. [1] investigates the heat performance rates by using nanofluids as coolants. There are two main constrains which have been used namely cylindrical and squared cross-section battery packs. The conclusions were made, and the best-suited nanofluid in case of cylindrical cross-section is CuO-EG and Al_2O_3 -EG in case of squared cross-section. Mondal et al. [2] explores the ways of thermal management for a lithium-ion battery using nanofluids. A proper thermal management has to be done to increase the performance and life of the battery. As we use the battery, they get heated up and to reduce the dissipated heat, the cooling methods such as nanofluids which is a mixture of a base fluid and nanoparticle are used. The temperature variation is also seen by using different nanofluids. The final study on heat dissipation rates in high discharge rates and design considerations is also done. Arora et al. [3] states that the backbone for a E-vehicles is its batteries. The most optimum and adequate battery to be used is lithium-ion battery packs. Now, these can be placed in many different ways to get more efficiency and performance of the automobile. These placements are to be made such that vibrations, vehicle impact, etc.; these things are drastically reduced, thereby not affecting the battery. Many mechanisms and designs are innovated which makes sure that there is no development of high-pressure events in battery. A proper conclusion is made by placing the battery in the center of the chassis of the vehicle in the most preferred and the optimum place for the battery to be present. Jilte et al. [4] investigated on the safety factors for better efficiency in E-vehicles and identified that the cooling components could be replaced with liquid circulated battery cooling system. As the names suggest, the meaning can be understood easily as in one case the battery is submerged and the other is implemented in a way that the battery is surrounded by the nanofluid. Each has its own advantages and disadvantages based on the usage of both the methods. Therefore, both are very much adequate in case of E-vehicles. So, any of the methods can be used. Harish et al. [5] uses a 2-phase mixture model, and a numerical simulation is performed on a transient, 3D model by considering the nanoparticles such as aluminum oxide, copper, and silver as well as the base fluid to be water. The results are withdrawn by varying the diameter of the nanoparticle and volume fraction. Outcomes from

this are the heat transfer increases linearly with volume fraction. Also, the Brownian motion boosts the rate of energy interchange between the fluid and phase particle. Better results are found in turbulent flows than laminar flows by increasing the heat transfer rate and reducing the nanoparticle or particle size.

Rohit et al. [6] studied the effects of phase change materials on thermal cooling of lithium-ion battery. It is observed that graphene acts as an effective temperature management agent than paraffin and capric acid. Wiriyasart et al. [7] studied about the nanofluid thermal management system for electric vehicle battery cooling modules. It is observed that the battery surface temperature reduces up to 27.6% when using nanofluids compared to that of conventional battery cooling modules, and it was also observed that the cooling effect would be more effective as the concentration of nanofluids suspended is higher in the coolant. Abdullh et al. [8] studied the effects of liquid-cooled copper plate with oblique fins for thermal management in electric vehicle. It is observed that the oblique fins significantly enhanced the liquid cold plate performance and the flow rate improves the heat transfer performance and the battery surface temperature was maintained at less than 50 °C which is a nominal battery operating temperature.

Hsuan et al. [9] analyzed the feasibility of using nanofluids with various concentrations as thermal management system in green power sources. It is observed that in the lower concentration condition and minimal flow rate, the efficiency of the nanofluid inside the heat exchangers was better as a coolant system. Syazana et al. [10]. studied about the various types of nanotubes by evaluating the Magnetohydrodynamic (MHD) on a 2D mixed convection. There are two nanofluids considered in the case which are water and kerosene performed on single-walled and multi-walled carbon nanotubes. The results were evaluated and discussed based on the properties such as volume fraction and heat transfer rate. The optimum software used here is MATLAB, to acquire the best results.

Kiani et al. [11] studied a hybrid thermal management passive cooling system, constructed by saturating the copper foam and implemented paraffin as the phase-changing material. Alumina nanofluids were the coolant fluids. Nanofluids were simulated to pass through the surface of the battery, the maximum temperature difference was observed at Reynolds number 420, and time taken was 13s. Arshad et al. [12] conducted review with a system of graphene nanoparticles suspended in various base fluids. Base fluids include water, red wine, acetone, etc., various parameters were computed and contrasted, and the authors concluded that more work is needed in the domain of graphene nanofluids. Huo et al. [13] studied a system employed with Al₂O₃-Water nanofluid as the coolant and lattice Boltzmann (LB) model for the Battery Thermal Management (BTM). This system provided as considerable decrease in average battery temperature, close to 7% for the volume fraction of 0.04. Omiddezyani et al. [14] studied and experimented a system consisting of Al₂O₃-Water nanofluid as well as copper foam filled with paraffin as the phase change material. The results concluded that for the volume fraction of 0.02 of the nanofluid, the system recorded a temperature difference of 4.1 K and the temperature difference dropped close to 77%, assisted with copper foam with/without phase change material. Liu et al. [15] conducted a study on thermal performances of cooling system

with different base fluids mixed with nanoparticles. It was found that the addition of nanoparticles with fluids with less thermal conductivity (engine oil) provided a remarkable result compared to water. It was also observed that with the increase in the volume fraction of nanoparticle, the thermal performance increased. Similar investigations are performed in literature to understand the flow and thermal performance of nanofluids in stepped lid-driven cavity [16], cubical enclosure [17] and ventilated enclosures [18, 19].

So, from most of the research papers reviewed it is evident that most of the papers have tried various materials and fluids in order to create a complete thermal management system for a battery in an electric vehicle but most of them faced many issues due to various factors such as its natural state or its unpredictable behavior at intense testing conditions and in most cases circular battery packs were tested but in actual practice cuboidal battery packs are used in EVs. So, a cuboidal battery design was prioritized and addition of various nanoparticles at different concentrations was added to a base fluid (water), and various factors such as thermal heat transfer coefficient and surface Nusselt number are to be calculated and identifying the best performing nanofluid at precise volume fraction is the primary aim.

2 Methodology

Many types of battery packs are available. They are cylindrical and cubical battery surfaces. The problem methodology incorporated is three-dimensional steady-state heat convection over a turbulent flow. The battery enclosure encompasses a cubical battery pack. As the current chosen method of cooling is the active method, the nanofluid is placed in the void which is found in between the battery and the enclosure's inner surface thereby having direct contact with the battery. We know that the nanofluid is a combination of base fluid and nanoparticles. According to the problem statement, the chosen base fluid is water along with different nanoparticles such as aluminum, aluminum oxide, and single-walled carbon nanotubes. The necessary boundary conditions are also maintained such as the acceleration due to gravity acting on the negative y-axis direction. K-omega shear stress transport [SST] model is used to compute the problem. The wall boundary condition of the six surrounding wall faces are specified with a constant wall temperature maintained at a temperature of 293 K. The wall temperature of the Cubical battery surface is set as 333 K and the enclosure. The thermophysical properties are kept constant based on the temperature. The energy equation is solved using second-order upwind scheme. The convergence criteria were fixed at 10^{-6} .

2.1 Governing Equations

The Mass conservation (1), momentum conservation (2), energy conservation (3), turbulent kinetic energy (4), and specific dissipation rate (5) equations for the fluid are discussed below:

$$\nabla \cdot (\rho_f u) = 0 \quad (1)$$

$$\frac{\partial(\rho_f u)}{\partial t} + \nabla \cdot (\rho_f u u) = -\nabla \cdot p + \nabla \cdot (\mu_f \nabla u) \quad (2)$$

$$\frac{\partial(\rho_f C_p f T)}{\partial t} + \nabla \cdot (p f C_p f T u) = \nabla \cdot (k_f \nabla T) \quad (3)$$

$$\frac{\partial k}{\partial t} + U_j \frac{\partial k}{\partial x_j} = [P_k] + \frac{\partial}{\partial x_j} \left[(v + \sigma_k v_T) \frac{\partial k}{\partial x_j} \right] \quad (4)$$

$$\frac{\partial \omega}{\partial t} + U_j \frac{\partial \omega}{\partial x_j} = \frac{\partial}{\partial x_j} \left[(v + \sigma_\omega v_T) \frac{\partial \omega}{\partial x_j} \right] + 2(1 - F_1) \sigma_{\omega 2} \frac{1}{\omega} \frac{\partial k}{\partial x_i} \frac{\partial \omega}{\partial x_i} \quad (5)$$

2.2 Thermophysical Properties

Based on the boundary conditions implied, the necessary requirements prevailing in the study are nanofluid density, heat capacitance, thermal conductivity, and temperature. The absolute viscosities of the nanofluids were quantified with different volume fraction values using current empirical formulae available. The resultant values are depicted in Table 1.

$$\rho_{nf} = (1 - \emptyset) \rho_f + \emptyset \rho_p \quad (6)$$

$$(\rho C_p)_{nf} = (1 - \emptyset) (\rho C_p)_f + \emptyset (\rho C_p)_p \quad (7)$$

$$\frac{k_{nf}}{k_f} = \frac{(k_p + 2k_f) - 2\emptyset(k_f - k_p)}{(k_p + 2k_f) + \emptyset(k_f - k_p)} \quad (8)$$

$$\mu_{nf} = \frac{\mu_f}{(1 - \emptyset)^{2.5}} \quad (9)$$

$$(\rho \beta)_{nf} = (1 - \emptyset) (\rho \beta)_f + (\emptyset) (\rho \beta)_p \quad (10)$$

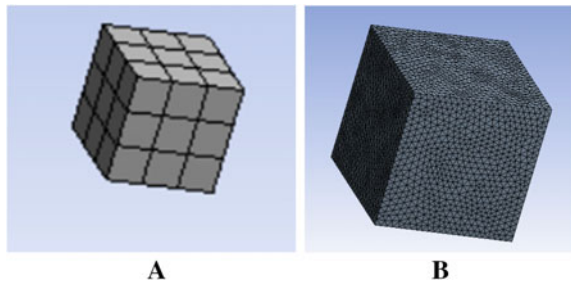
Table 1 Thermophysical properties of nanofluids

Nanoparticles	(ϕ)	(ρ) (kg/m ³)	(C_p) (J/Kg.K)	(k) (W/m.K)	(μ) (N.s/m ³)
Al	0.02	1034	4015.02	0.6428	9.36×10^{-4}
Al	0.04	1068	3855.40	0.6811	9.86×10^{-4}
Al	0.06	1102	3705.61	0.7210	10.39×10^{-4}
Al	0.08	1136	3564.82	0.7626	10.96×10^{-4}
Al ₂ O ₃	0.02	1059	3938.91	0.6412	9.36×10^{-4}
Al ₂ O ₃	0.04	1118	3718.35	0.6778	9.86×10^{-4}
Al ₂ O ₃	0.06	1177	3519.91	0.7159	10.40×10^{-4}
Al ₂ O ₃	0.08	1236	3340.40	0.7555	10.96×10^{-4}
SWCNT	0.02	1032	4102.94	0.6344	10.54×10^{-4}
SWCNT	0.04	1064	4027.88	0.6725	11.10×10^{-4}
SWCNT	0.06	1096	3952.82	0.7122	11.70×10^{-4}
SWCNT	0.08	1128	3877.76	0.7537	12.34×10^{-4}

3 Modeling and Meshing

The modeling and simulation were carried out in ANSYS fluent 20 software. This software is used to simulate computer models of structures, electronics, machine components for analyzing strength, toughness, elasticity, temperature distribution, electromagnetism, fluid flow, etc. Ansys determines the functioning of a product with different specifications, without building test products or conducting crash tests. The battery model was designed using Ansys design modular geometry with dimensions 26 mm × 26 mm × 26 mm; similarly, the enclosure was designed with dimensions 100 mm × 100 mm × 100 mm. The two solids are Boolean subtracted, and the properties are preserved. The meshing is done with an element size of 0.01 m. The respective nodes and elements are 11890 and 60434. Under sizing, the curvature minimum size was set at 1.9752×10^{-4} m and the curvature normal angle is at 18°. Medium smoothing was carried out for meshing in Fig. 1.

Fig. 1 Depicts meshing of **a** Battery pack **b** enclosure



4 Results and Discussions

As per the methodology followed, with the help of Ansys fluent many contours were plotted for various nanofluids such as aluminum-water, aluminum oxide–water, and single-walled carbon nanotubes–water. Variations such as heat transfer coefficient and Nusselt number were established for volume fractions varying from 2 to 8%. Also, percentage increase of heat transfer coefficient was also found and plotted. With comparison of 3 nanofluids considered, aluminum-water showcased better results than compared to other nanofluids. Also, comparisons of these nanofluids with water were computed and plotted.

Considering the temperature distribution contour, convection patterns are visible in Fig. 2. This shows that the maximum value of the temperature is observed at the surface of the battery pack, and as we move away from the surface, the temperature gradient is observed, and the minimum temperature is observed at the wall of the enclosure. When we take into the considerations of velocity, we see that the distribution is random and is found to be low at the edges of the battery pack. Figs. 3 and 4 depict the pressure distribution contour, where the pressure varies from minimum to maximum as we go from bottom surface of the enclosure to the top surface of the enclosure.

Fig. 5 represents the variation of heat transfer coefficient for various volume fractions for aluminum-water nanofluid. The heat transfer coefficient values were found out to be 29.267616, 31.010925, 32.827723, and 34.722755 (W/m²K) for volume fractions of 2%, 4%, 6%, and 8%, respectively. Increase in the heat transfer coefficient for increase in the volume fraction is observed.

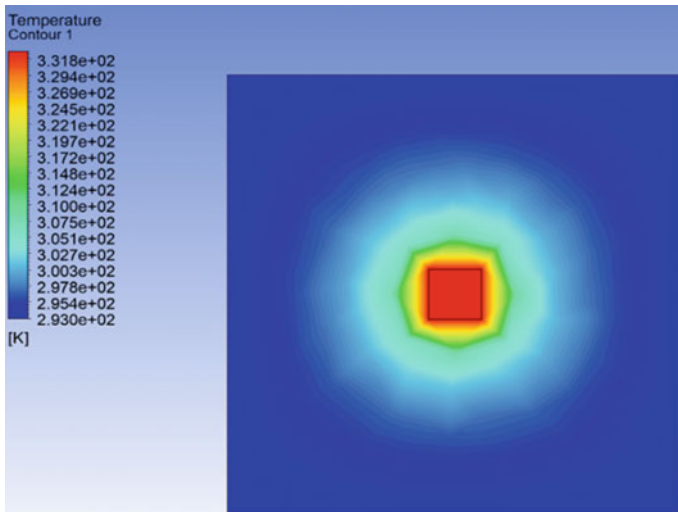


Fig. 2 Temperature distribution of nanofluid (aluminum–water) with $\phi = 8\%$

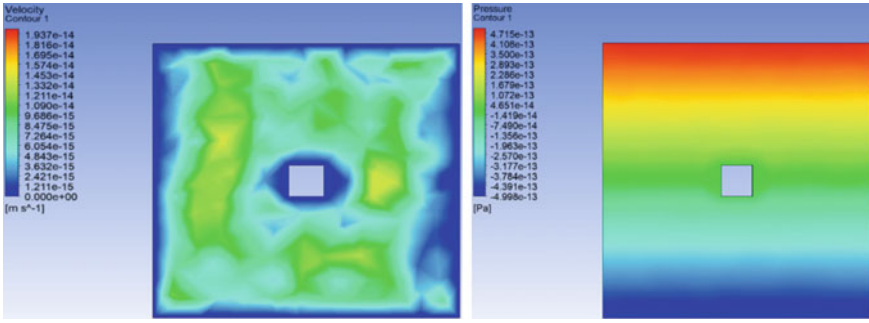


Fig. 3 Velocity distribution of nanofluid (aluminum–water) with $\phi = 8\%$, Pressure distribution of nanofluid (aluminum–water) with $\phi = 8\%$, respectively

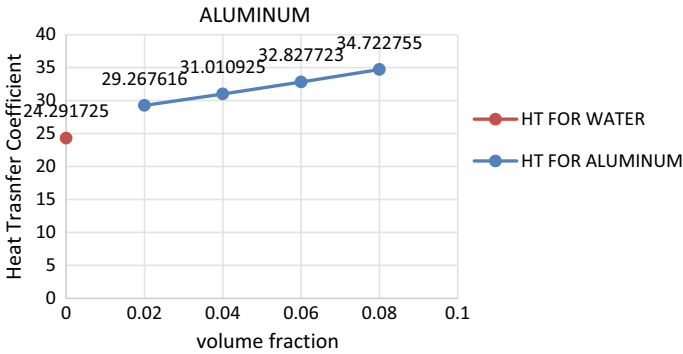


Fig. 4 Volume fraction versus heat transfer coefficient (W/m^2K) for aluminum–water at various volume fractions

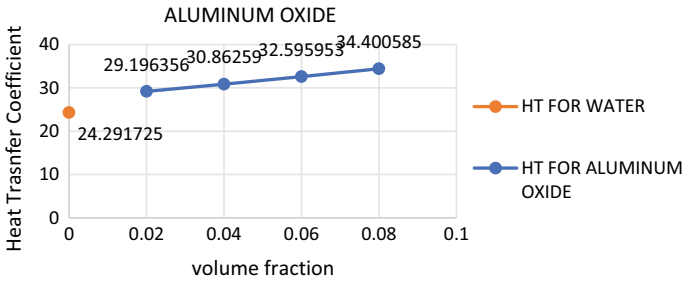


Fig. 5 Volume fraction versus heat transfer coefficient (W/m^2K) for aluminum oxide–water at various volume fractions

Figure 6 represents the variation of heat transfer coefficient for various volume fractions for aluminum-oxide-water nanofluid. The heat transfer coefficient values were found out to be 29.196356, 30.86259, 32.595953, and 34.400585 (W/m²K) for volume fractions of 2%, 4%, 6%, and 8%, respectively. Increase in the heat transfer coefficient for increase in the volume fraction is observed.

Figure 7 represents the variation of heat transfer coefficient for various volume fractions for SWCNT-water nanofluid. The heat transfer coefficient values were found out to be 28.886567, 30.621396, 32.429078, and 34.318721 (W/m²K) for volume fractions of 2%, 4%, 6%, and 8%, respectively. Increase in the heat transfer coefficient for increase in the volume fraction is observed.

For aluminum-induced nanofluid, the heat transfer coefficient increased by 18.63% when compared with 2% and 8% volume fractions. Considering aluminum

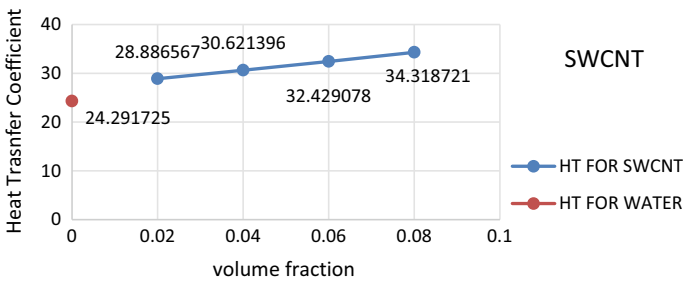


Fig. 6 Volume fraction versus heat transfer coefficient (W/m²K) for SWCNT-water at various volume fractions

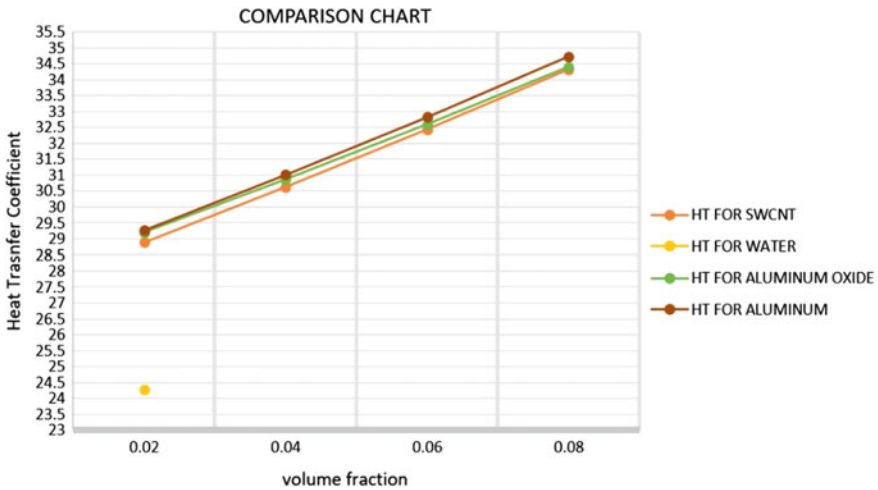


Fig. 7 Comparison chart of volume fraction versus heat transfer coefficient (W/m²K) for different nanofluids at various volume fractions

Table 2 Observation (represents the various nanofluids and their corresponding percentage change for each nanofluid with respect to value for volume fraction of 0.02)

Nanofluid	Volume fraction	Thermal heat transfer coefficient (W/m ² K)	Nusselt number
SWCNT	0.02	28.886567	45.53368
	0.04	30.621396	45.533674
	0.06	32.4229078	45.533668
	0.08	34.318721	45.533662
Al ₂ O ₃	0.02	29.196356	45.533696
	0.04	30.86259	45.533668
	0.06	32.595953	45.533681
	0.08	34.400585	45.533675
Al	0.02	29.267616	45.533683
	0.04	31.010925	45.53684
	0.06	32.827723	45.533676
	0.08	34.722755	45.533668

oxide induced nanofluid 17.83% when compared with 2% and 8% volume fractions. Finally, considering SWCNT-induced nanofluids the heat transfer coefficient increased by 18.80% when compared with 2% and 8% volume fractions. The maximum value of heat transfer coefficient was observed for aluminum-water nanofluid with corresponding volume fraction of 8%, and the value was found as 34.722755 W/m²K. On comparing this with water, a drastic increase of 35.61% was observed and shown in Table 2.

5 Conclusion

From the simulations performed, the following conclusions were drawn. All three nanofluids had similar temperature contours and similar convection patterns were also observed. The nanofluid-induced coolants showed better rate of convection than standard water. Further, higher the concentration of nanofluid minimal was the velocity of the nanofluid particles during convection. From the temperature contour, it is observed that, as battery heat source gets heated up thermal convection patterns are visualized, similarly the velocity contour is also noted. Because of the thermal convection, the flow propagation takes place near the walls of the enclosure so that the cold nanofluid present near the battery pack gets heated and it tries to diffuse toward the walls with higher velocity. The nanofluid closer to the heat source gets heated up and because of thermal buoyancy force thereby the pressure distribution is very high toward the upper half of the enclosure. The cold nanofluid that is present inside the enclosure is at higher density and as it settles down the pressure distribution is reduced in the lower half of the enclosure. Perhaps, aluminum-water nanofluid

with 0.08 volume fraction provides better heat transfer coefficient and can be used as an active cooling system for thermal management of battery in E-vehicles. Thus, as the efficiency and the power of the battery increase a proper thermal management system for the same in the future has a huge scope in terms of a viable market and as the world is moving toward EVs, making the battery more efficient is of huge interest.

Nomenclature

The annotations mentioned in the above formulae are:

u	flow velocity (m/s)
t	time (s)
T	temperature (K)
k	kinetic energy (J)
σ	empirical constants
ω	turbulent dissipation rate (m^2/s^3)
ν	kinematic viscosity (m^2/s)
U	velocity in the domain (m/s)
P	pressure gradient (Pa/m)
ϕ	volume fraction of the nanoparticle
ρ	density (kg/m^3)
K	thermal conductivity (W/m K)
C_p	heat capacity (J/Kg K)
β	thermal expansion coefficient (K^{-1})
μ	dynamic viscosity ($\text{N}\cdot\text{s}/\text{m}^2$)
α	thermal diffusivity (m^2/s)
Q	heat generated by the battery during the process of discharging (J)

The subscripts $p, f, nf, b,$ and k represent the nanoparticle, fluid, nanofluid, battery, and kinetic energy, respectively.

References

1. Xu X, Xiao T, Chen S, Lin S (2019) Exploring the heat transfer performance of nanofluid as a coolant for power battery pack. *Heat Transf* 48(7):2974–2988
2. Mondal B, Lopez FC, Mukherjee PP (2017) Exploring the efficacy of nanofluids for lithium-ion battery thermal management. *Int J Heat Mass Transf* 112:779–794
3. Arora S, Shen W, Kapoor A (2018) Review of mechanical design and strategic placement technique of a robust battery pack for electric vehicles. *Renew Sustain Energy Rev* 60:1319–1331
4. Jilte D, Kumar R, Mohammad H (2019) Cooling performance of nanofluid submerged versus nanofluid circulated battery thermal management systems. *J Cleaner Prod* 240:118131
5. Harish R, Sivakumar R (2018) Turbulent thermal convection of nanofluids in cubical enclosure using two-phase mixture model. *Int J Mech Sci* 190:106033

6. Kumar KR, Sharan V, Harish R, Kumar MS (2020) Numerical study of thermal cooling for Lithium-ion battery pack using phase change material. In: IOP conference series: earth and environmental science vol 573, p 012018
7. Wiriyasart S, Hommalee C, Sirikasemsuk S, Prurapark R, Naphon P (2020) Thermal management system with nanofluids for electric vehicle battery cooling modules. *Case Stud Thermal Eng* 18:100583
8. Aldosry AM, Mansur A, Zulkifli R, Ghopa WW (2021) Heat transfer enhancement of liquid cooled copper plate with oblique fins for electric vehicles battery thermal management. *World Electr Veh J* 12(2):55
9. Hung YH, Chen JH, Teng TP (2013) Feasibility assessment of thermal management system for green power sources using nanofluid. *J Nanomater* 93:93
10. Anuar NS, Bachok N, Turkyilmazoglu M, Arifin NM, Rosali H (2020) Analytical and stability analysis of MHD flow past a nonlinearly deforming vertical surface in carbon nanotubes. *Alex Eng J* 59(1):497–507
11. Kiani M, Ansari M, Arshadi AA, Houshfar E, Ashjaee M (2020) Hybrid thermal management of lithium-ion batteries using nanofluid, metal foam, and phase change material: an integrated numerical–experimental approach. *J Therm Anal Calorim* 141(5):1703–1715
12. Arshad A, Jabbal M, Yan Y, Reay D (2019) A review on graphene based nanofluids: preparation, characterization and applications. *J Mol Liq* 279:444–484
13. Yutao H, Rao Z (2015) The numerical investigation of nanofluid based cylinder battery thermal management using lattice Boltzmann method. *Int J Heat Mass Transf* 91:374–384
14. Kiani M, Omiddezyani S, Houshfar E, Miremadi SR, Ashjaee M, Nejad AM (2020) Lithium-ion battery thermal management system with $\text{Al}_2\text{O}_3/\text{AgO}/\text{CuO}$ nanofluids and phase change material. *Appl Therm Eng* 180:115840
15. Liu H, Chika E, Zhao J (2018) Investigation into the effectiveness of nanofluids on the mini-channel thermal management for high power lithium ion battery. *Appl Therm Eng* 142:511–523
16. Janjanam N, Nimmagadda R, Asirvatham LG, Harish R, Wongwises S (2021) Conjugate heat transfer performance of stepped lid-driven cavity with $\text{Al}_2\text{O}_3/\text{water}$ nanofluid under forced and mixed convection. *SN Appl Sci* 6:1–13
17. Harish R, Sivakumar R (2021) Effects of nanoparticle dispersion on turbulent mixed convection flows in cubical enclosure considering Brownian motion and thermophoresis. *Powder Technol* 378:303–316
18. Harish R (2018) Buoyancy driven turbulent plume induced by protruding heat source in vented enclosure. *Int J Mech Sci* 148:209–222
19. Harish R (2018) Effect of heat source aspect ratio on turbulent thermal stratification in a naturally ventilated enclosure. *Build Environ* 143:473–486

Theoretical Investigation of Base Fluid Type in Nanofluids for Heat Transfer Enhancement in Multidisciplinary Engineering Applications



N. Brinda, Prem Raj, Amod Yadav, H. P. Monika, and V. Somashekar

Abstract The effect of using various types of nanofluids as coolant fluids in CPU cooling, microtubes, solar parabolic trough collector, and distributor transformer on the enhancement of heat transfer was studied theoretically. Identifying the suitable base fluid and nanoparticles is challenging in multidisciplinary engineering applications. Through theoretical study, we made an attempt to identify a suitable base fluid for multidisciplinary engineering applications through this work. Four different cases are considered in this work. Case 1 is a cooling system for a central processing unit. Case 2 is a microtubes. Case 3 is a solar parabolic trough collector. Case 4 is a distributor transformer. For both CPUs and distributor transformers, the Reynolds number is considered to be in the 5000 to 15,000 range. The range of Reynolds numbers is considered to be 10 to 140 for microtubes. Similarly, the Reynolds number range for a solar parabolic through collector is considered to be 50,000 to 250,000. From the theoretical results for CPU, the recorded maximum Nusselt number for glycerine base fluid is 1458.9 at Reynolds number 15000. For microtubes, the recorded maximum Nusselt number for glycerine base fluid is 140 at Reynolds number 140. For a distributor transformer, the recorded maximum Nusselt number for glycerine base fluid is 1609.2 at Reynolds number 15,000. Similarly, for the solar parabolic trough collector, the recorded maximum Nusselt number for glycerine base fluid is 9913 at 250,000. It can be concluded that the optimal parameter setting resulted in the greatest increase in heat transfer in engineering applications.

Keywords Nanofluids · Heat transfer · CPU · Microtubes · Solar collector · Transformer

1 Introduction

Fluids containing nanometer-scale materials (droplets, nanosheets, nanorods, and nanoparticles) are called “nanofluids”. They are two-phase systems in which one

N. Brinda · P. Raj · A. Yadav · H. P. Monika · V. Somashekar (✉)
Department of Aeronautical Engineering, Acharya Institute of Technology, Bengaluru,
Karnataka 560107, India
e-mail: somashekar.v@acharya.ac.in

© The Author(s), under exclusive license to Springer Nature Singapore Pte Ltd. 2023
V. K. Singh et al. (eds.), *Advances in Thermal Sciences*, Lecture Notes
in Mechanical Engineering, https://doi.org/10.1007/978-981-19-6470-1_6

phase (the solid phase) is contained within the other (the liquid phase). Nanofluids exhibit improved thermo-physical properties such as convective heat transfer coefficients, thermal conductivity, thermal diffusivity, and viscosity when compared to base fluids such as water or oil. It has shown significant application potential in a variety of fields [1].

Nanotechnology is concerned with the manufacture and application of nanoscale materials as well as the integration of the resulting nanostructures into larger systems. Nanotechnology is expected to have a significant impact on our daily lives in the coming decades, according to trends [2].

Nanofluids have gained increasing attention in recent years. The primary motivation for nanofluids research is the breadth of their applications. Although several review articles on the progress of nanofluid investigation have been published in the last few years [3–8], the majority of reviews focus on experimental and theoretical studies of nanofluids' thermo-physical properties or convective heat transfer.

By combining different types of nanoparticles with different types of base fluids, nanofluids can be created. Copper oxide (CuO), alumina oxide (Al_2O_3), silica oxide (SiO_2), and zinc oxide (ZrO_2) are used most frequently, but silver, copper, and copper oxide (CuO) also show up frequently. De-ionized water, oil, and ethylene glycol are the most widely used base fluids for nanofluids [9].

As a result, the way to suspend liquid-borne particles for heat transfer improvement was known, but it was never utilized. For those conventional fluids with less heat transfer, using active and passive techniques to improve heat transfer rates is a common technique. Using external energy sources, active flow control changes the flow; it is contrasted with passive flow control, which does not need additional energy sources to modify the flow. Nanofluids consist of suspended nanoparticles. Nanosized particles are more dispersed because of their large surface area and mobility [9].

Researchers have conducted many studies to improve base fluid heat transfer rates by using nanofluids. Trisaksri [10] demonstrates how additives are implemented to improve base fluid heat transfer. A new technology in heat transfer is using nanometer-sized particles in suspension in traditional fluids. The nonmetallic or suspended metallic nanoparticles influence the properties of the base fluid that control how heat is transferred and the transfer of material in the system. According to Eastman et al., [11] 10 nm copper particles (40% increased conductivity) in ethylene glycol achieve higher conductivity with a small particle loading fraction. To get the volume fraction to 4%, users have to use a percentage improvement of 20% with cupric oxide. Clearly, particle size has an effect on conductivity enhancement. Al_2O_3 and TiO_2 nanoparticles in water were found to have 12% less convective heat transfer coefficient than pure water in the 3% volume fraction, as reported by Pak and Cho [12].

As a result of this widespread interest, numerous research projects have been launched in heat transfer. Three possibilities were discovered regarding heat transfer improvement. They are making the flow more erratic and creating more turbulence in the fluid. In some fluid-based heat transfer systems, small particles can be beneficial. In order to address the above-mentioned voids, the current research aims to outline

the best base fluids with nanoparticles using a theoretical approach. The purpose of this paper is to discover suitable base fluids for multidisciplinary engineering applications (considered central processing unit (CPU), microtubes, solar parabolic trough collector, and distributor transformer). Using empirical relations, we predicted non-dimensional quantities such as heat transfer coefficient, Nusselt number, and Prandtl number using a theoretical approach. The theoretical data obtained is compared with previously published numerical data.

2 Nanofluids Thermo-Physical Properties

Numerous theoretical and empirical models for predicting the effective thermal conductivity, density, effective viscosity, Prandtl number, specific heat of nanofluid, convective heat transfer coefficient, and average Nusselt number of nanofluids have been proposed. The following are the most frequently used models, along with their formulas.

The dynamic viscosity, density, thermal conductivity, and heat capacity of various base fluids and SiO₂ nanoparticles are listed in Table 1. The following equations are used to calculate these properties:

Density of Nanofluid [13]:

$$\rho_{nf} = (1 - \varnothing)\rho_f + \varnothing\rho_{np}. \quad (1)$$

The mass densities of the base fluid and the solid nanoparticles are ρ_f and ρ_{np} , respectively.

Effective Thermal Conductivity [14]:

$$K_{\text{eff}} = K_{\text{static}} + K_{\text{Brownian}} \quad (2)$$

$$K_{\text{static}} = K_f \left[\frac{(k_{np} + 2k_f) - 2\varnothing(k_f - k_{np})}{(k_{np} + 2k_f) + \varnothing(k_f + k_{np})} \right]. \quad (3)$$

where k_s denotes the thermal conductivity of the solid particles, and k_f denotes the thermal conductivity of the base fluid, respectively.

According to [15], thermal conductivity due to Brownian motion is as follows:

$$K_{\text{Brownian}} = 5 \cdot 10^4 \beta \varnothing \rho_f C_{pf} \sqrt{\frac{KT}{2R_{np}}} f(T, \varnothing). \quad (4)$$

$$f(T, \varnothing) = (2.8217 \cdot 10^{-2} \varnothing + 3.917 \cdot 10^{-3}) \left(\frac{T}{T_o} \right) + (-3.0669 \cdot 10^{-2} \varnothing - 3.3991123 \cdot 10^{-3}). \quad (5)$$

Table 1 Base fluid’s thermo-physical properties

Thermo-physical properties	Glycerin	Engine oil	Ethylene glycol
Density, $\rho(\text{Kg/m}^3)$	1259.9	884.1	1114.4
Dynamic viscosity, $\mu(\text{Kg/ms})$	0.799	0.486	0.0157
Thermal conductivity, $k(\text{W/mK})$	0.286	0.145	0.252
Specific heat, $C_p (\text{J/Kg. K})$	2427	1909	2415
	<i>Water</i>	<i>Ethanol</i>	<i>Transformer Oil</i>
Density, $\rho(\text{Kg/m}^3)$	998.203	789.45	880
Dynamic viscosity, $\mu(\text{Kg/ms})$	0.00101	0.001095	0.01432
Thermal conductivity, $k(\text{W/mK})$	0.613	0.171	0.126
Specific heat, $C_p (\text{J/Kg. K})$	4182	2.46	1860
	<i>PropyleneGylcol</i>	<i>Ammonia</i>	<i>Kerosene</i>
Density, $\rho(\text{Kg/m}^3)$	1036	730	786
Dynamic viscosity, $\mu(\text{Kg/ms})$	0.042	0.01	0.00164
Thermal conductivity, $k(\text{W/mK})$	0.34	0.022	0.145
Specific heat, $C_p (\text{J/Kg. K})$	3.474	4.744	2.01
	<i>Hydrofluoric acid</i>	<i>Nitric acid</i>	<i>Medical Paraffin</i>
Density, $\rho(\text{Kg/m}^3)$	1.15	1.51	0.85
Dynamic viscosity, $\mu(\text{Kg/ms})$	0.981	3.5	0.00198
Thermal conductivity, $k(\text{W/mK})$	2.33	0.26	0.127
Specific heat, $C_p (\text{J/Kg. K})$	2.66	1.72	2.13

where K denotes the Boltzman constant, T denotes thfluid temperature, and T_0 denotes the reference temperature, the β values for the SiO_2 pticle are as follows [15]:

$$1.9526(100\emptyset)^{-1.4594} \text{ for } 1\% \leq \emptyset 10\% \text{ at } 298k \leq T \leq 363k \quad (6)$$

The following mean empirical correlation can be used to determine the effective viscosity [13]:

$$\mu_{\text{eff}} = \mu_f * \left(\frac{1}{1 - 34.87 \left(\frac{d_p}{d_f}\right)^{-0.3} * \emptyset^{1.03}} \right) \quad (7)$$

$$d_f = \left[\frac{6M}{N\pi\rho f_0} \right]^{1/3} \quad (8)$$

The following is the effective specific heat [13]:

$$C_{nf} = \frac{(1 - \emptyset)(\rho C_p)_f + \emptyset(\rho C_p)_{np}}{\rho_{nf}} \quad (9)$$

The heat capacities of the based fluid and the solid nanoparticles are $(\rho C_p)_f$ and $(\rho C_p)_{np}$, respectively.

Prandtl Number:

$$Pr = \frac{\mu C_p}{k} \quad (10)$$

Average Nusselt Number:

$$0.3 + \frac{0.62 Re^{1/2} Pr^{1/2}}{\left[1 + \left(\frac{0.4}{Pr}\right)^{2/3}\right]^{1/4}} \left[1 + \left(\frac{Re}{282000}\right)^{5/8}\right]^{4/5} \quad (11)$$

Convective Heat Transfer Coefficient

$$h = \left(\frac{Nu k}{L}\right) \quad (12)$$

3 Results and Discussion

The effect of twelve different types of base fluids which are ethylene glycol (EG), glycerine, engine oil, water, ethanol, transformer oil, propylene glycol, ammonia, kerosene, hydrofluoric acid, nitric acid, and medicinal paraffin with SiO₂ as nanoparticles is used in this section.

Case 1: Central Processing Unit (CPU) Cooling System

Investigate different Reynolds numbers of different base fluids to see how they affect CPU cooling heat transfer enhancement (i.e., 5000, 7500, 10,000, 12,500, and 15,000), all other parameters of the CPU must be consistent with Husam Abdulrasool Hasan et al. (2018) [16] numerical results. Twelve different types of base fluids are illustrated in Fig. 1 to show how Nusselt number changes with Reynolds number. From the theoretical results, the recorded maximum Nusselt numbers for glycerine and engine.

Oil base fluid are 1609.2 and 1578.4 at Reynolds number 15000, respectively. Similarly, the recorded minimum Nusselt number for kerosene base fluids is 14.71.

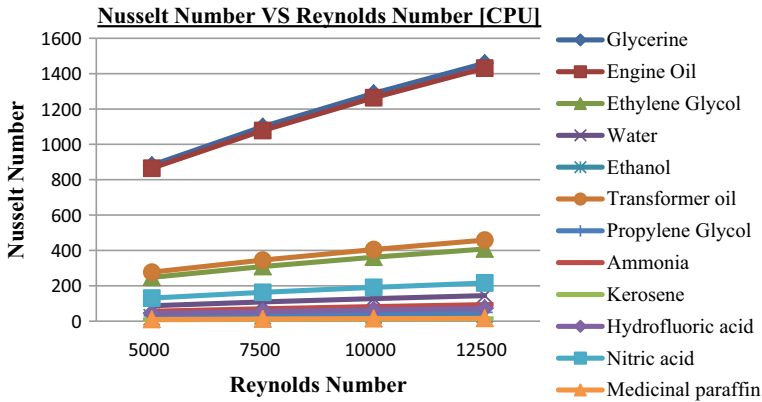


Fig. 1 Average Nu number versus Re number for CPU

The maximum Nusselt number variation between the glycerine and kerosene base fluids is 99.08% at Reynolds number 15000.

Case 2: Microtubes

From the results, glycerin-SiO₂ nanofluids have the highest Nusselt number when compared to other types of nanofluids. For the purpose of determining how different base fluids affect heat transfer in the microtubes cooling system at different Reynolds numbers (i.e., 10, 40, 80, 140), all other parameters of the microtubes must be consistent with Salman et al. (2014) [17] numerical results. The average Nusselt number for various Reynolds numbers is shown in Fig. 2 (i.e., 10, 40, 80, 140). From the graph, glycerin-SiO₂ nanofluids have the highest Nusselt number when compared to other types of nanofluids. From the theoretical results, the recorded maximum Nusselt number for glycerine base fluid is 140 at Reynolds number 140, respectively. Similarly, the recorded minimum Nusselt number for kerosene base fluids is 1.54. The maximum Nusselt number variation between the glycerine and kerosene base fluids is 98.9% at Reynolds number 140. In this case, it is because the glycerine base fluid has the highest viscosity, which causes the nanofluids' velocity to increase as a result, since velocity is directly proportional to the viscosity of the base fluid in question. In that order of viscosity, engine oil is the second most important base fluid, followed by EG and then water.

Case 3: Solar Parabolic Trough Collector

For the purpose of studying the effect of various base fluids on the improvement of heat transfer in the solar parabolic trough collector at different Reynolds numbers (i.e., 50,000, 100,000, 150,000, 200,000, and 250,000), all other parameters of the solar parabolic trough collector must be consistent with Ghasemi and Ranjbar [17] numerical results. With twelve different types of base fluids, the variation in Nusselt numbers can be seen in Fig. 3. From the theoretical results, the recorded maximum Nusselt numbers for glycerine and engine oil base fluid are 9913 and 9724 at Reynolds

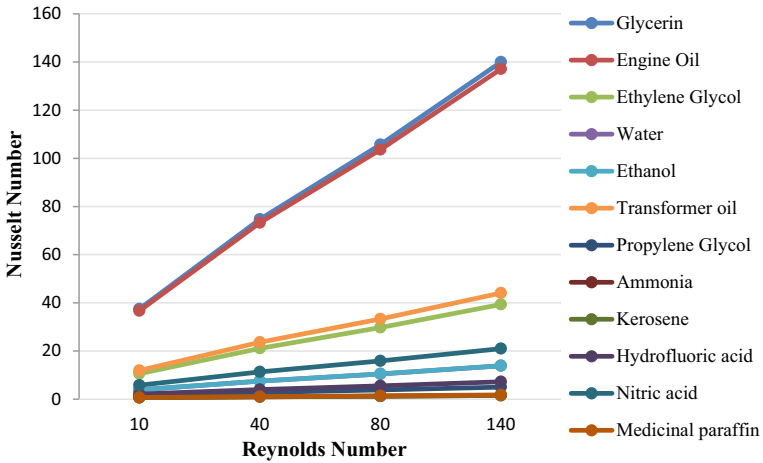


Fig. 2 Average Nu number vs Re number for microtubes

number 250000, respectively. Similarly, the recorded minimum Nusselt number for kerosene base fluids is 89.17. The maximum Nusselt number variation between the glycerine and kerosene base fluids is 99.10% at Reynolds number 250000.

Case 4: Distributor Transformer

For the purpose of studying the effect of various base fluids on the enhancement of heat transfer in the distributor transformer at different Reynolds numbers (i.e., 5000,

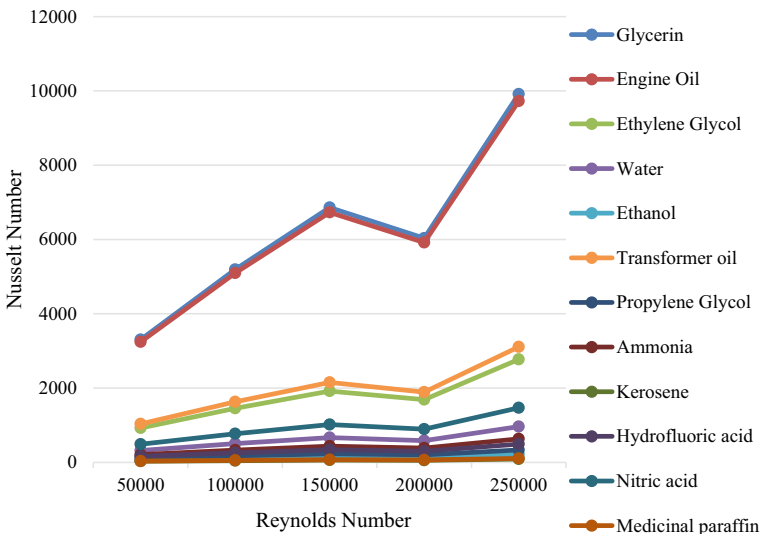


Fig. 3 Average Nu number versus Re number for solar parabolic trough collector

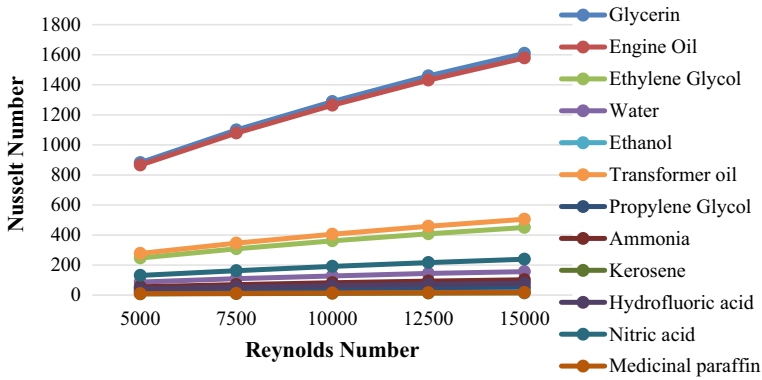


Fig. 4 Average Nu number versus Re number for distributor transformer

7500, 10,000, 12,500, and 15,000), all other parameters of the distributor transformer must be consistent with Pendyala et al. [18] numerical results. Based on twelve types of base fluids, the variation in Nusselt number as a function of Reynolds number is shown in Fig. 4. From the theoretical results, the recorded maximum Nusselt numbers for glycerine and engine oil base fluid are 1609.2 and 1578.4 at Reynolds number 15000, respectively. Similarly, the recorded minimum Nusselt number for kerosene base fluids is 14.71. The maximum Nusselt number variation between the glycerine and kerosene base fluids is 99.08% at Reynolds number 15000.

The Nusselt number increases as the Reynolds number increases because of the intensification of the nanofluid mixing fluctuation. It is clear from theoretical studies that glycerine and engine oil base fluids, as well as other base fluids, show the greatest heat transfer enhancement in cases 1 to 4.

4 Validation

In our theoretical study, for validation purposes, we used glycerine base fluid with SiO₂ nanoparticles for heat transfer enhancement in microtubes at different Reynolds numbers, i.e., 10, 40, 80, 140 to be consistent with Salman et al. (2014) [19] numerical results. Glycerin-SiO₂ has the highest Nusselt number, smallest axial velocity along tube radius, and coldest axial and wall temperatures, according to the findings of this study [19]. When compared with the numerical data, our study showed good results for the Nusselt number. The theoretical results agree quite well with the corresponding numerical results for different Reynolds numbers. The maximum difference in the Nusselt number between theoretical and numerical [19] results at various Reynolds numbers is illustrated in Fig. 5 and summarized in Table 2.

Theoretical value refers to the value that a scientist anticipates from an equation under ideal or near-optimal conditions. On the other hand, numerical/experimental

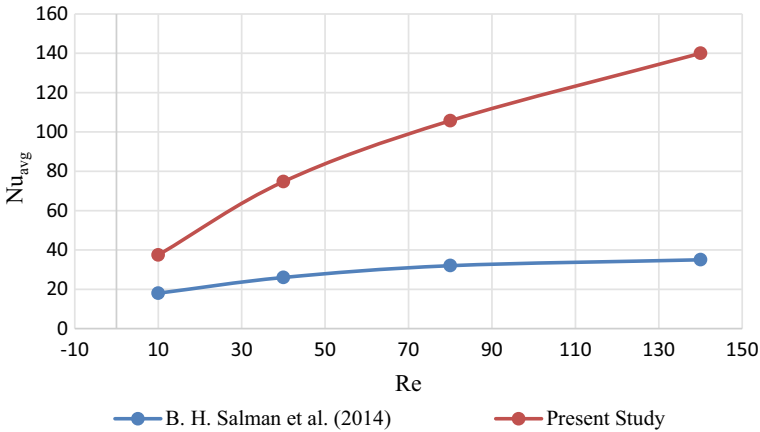


Fig. 5 Average Nu number versus Re number for glycerine base fluid

Table 2 Nusselt number for numerical and theoretical study at different Reynolds number

Salman et al. (2014) [17]		Present study	
Reynolds number	Nusselt number	Nusselt number	% variations
10	18	37.44	51.92
40	26	74.71	65.20
80	32	105.71	69.73
140	35	140	75.00

value refers to what is actually measured during a numerical/experiment. These numbers are rarely identical.

5 Conclusions

Investigating the effect of various base fluids on the enhancement of heat transfer in the central processing unit (CPU), microtube, solar parabolic trough collector, and distributor transformer at different Reynolds numbers was carried out using empirical relations and theoretically. For theoretical calculations considered the most available/utilizing various base fluids (i.e., ethylene glycol (EG), glycerine, water, engine oil, ethanol, transformer oil, propylene glycol, ammonia, kerosene, hydrofluoric acid, nitric acid, medicinal paraffin) for the central processing unit (CPU), microtube, solar parabolic trough collector, and distributor transformer were theoretically studied. According to the results, glycerine base fluid has the highest Nusselt number in all of the above cases. It can be concluded that the optimal parameter setting resulted in the greatest increase in heat transfer in engineering applications. This research proves

that the best base fluid for multidisciplinary engineering applications is glycerine for enhancement of heat transfer.

Acknowledgements “Thanks to **ICFAMMT 2022** Professors in other Institutions for their insight and helpful feedback provided at conference discussions”.

References

1. Yu W, Xie H (2012) A review on nanofluids: preparation, stability mechanisms, and applications. *J Nanomaterials*, Article ID 435873, 17
2. Bhushan B (2004) Springer handbook of nanotechnology, 2nd edn. Springer, New York
3. Trisaksri V, Wongwiset S (2007) Critical review of heat transfer characteristics of nanofluids. *Renew Sustain Energy Rev* 11(3):512–523
4. Özerinc S, Kakac S, Yazıcıoğlu AG (2010) Enhanced thermal conductivity of nanofluids: a state-of-the-art review. *Microfluid Nanofluid* 8(2):145–170
5. Wang XQ, Mujumdar AS (2007) Heat transfer characteristics of nanofluids: a review. *Int J Therm Sci* 46(1):1–19
6. Wang XQ, Mujumdar AS (2008) A review on nanofluids-part I: theoretical and numerical investigations. *Braz J Chem Eng* 25(4):613–630
7. Li Y, Zhou J, Tung S, Schneider E, Xi S (2009) A review on development of nanofluid preparation and characterization. *Powder Technol* 196(2):89–101
8. Kakac S, Pramuanjaroenkij A (2009) Review of convective heat transfer enhancement with nanofluids. *Int J Heat Mass Transf* 52(13–14):3187–3196
9. Anbazhagan VN, Rejikumar R (2013) TeshomeBekeleKotu: analysis of heat transfer coefficient of nanofluids. *Int J Eng Res Technol (IJERT)* 2(6)
10. Trisaksri V, Wongwiset S (2007) Critical review of heat transfer characteristics of nanofluids. *Renew Sustain Energy Rev* 11:512–523
11. Eatman JA, Choi SUS, Li S, Yu W, Thompson LJ (2001) Anomalous increased effective thermal conductivities of ethylene glycol based nanofluids containing copper nanoparticles. *Appl Phys Lett* 78:718–720
12. Pak B, Andcho YI (1998) Hydro dynamic and heat transfer study of dispersed fluids with sub micro metallic oxide particle. *Exp Heat Transf* 11:151–170
13. Corcione M (2010) Heat transfer features of buoyancy-driven nanofluids inside rectangular enclosures differentially heated at the sidewalls. *Therm Sci* 49:1536–1546
14. Ghasemi B, Aminossadati S (2010) Brownian motion of nanoparticles in a triangular enclosure with natural convection. *Therm Sci* 49:931–940
15. Vajjha RS, Das DK (2009) Experimental determination of thermal conductivity of three nanofluids and development of new correlations. *Heat Mass Transf* 52:4675–4682
16. Hasan HA, Alquziweeni Z, Sopian K (2018) Heat transfer enhancement using nanofluids for cooling a central processing unit (CPU) system. *J Adv Res Fluid Mech Therm Sci* 51(2):145–157
17. Ghasemi SE, Ranjbar A (2016) Effect of nanoparticles in working fluid on thermal performance of solar parabolic trough collector. *J Mol Liq* S0167–7322(16):30738–3
18. Pendyalaa R, Ilyasa SU, Lima LR, Marnenic N (2016) CFD analysis of heat transfer performance of nanofluids in distributor transformer. 4th international conference on process engineering and advanced materials, procedia engineering vol 148, pp 1162–1169
19. Salman BH, Mohammed HA, Kherbeet AS (2016) The effect of base fluid type in nanofluids for heat transfer enhancement in microtubes. In: *Applied mechanics and materials* vol 818. Trans Tech Publications, Ltd, pp 12–22

CFD Analysis on Thermal Performance of Nanofluids in Electric Vehicle Battery



P. L. Palaniappan, T. T. K. Lokeswar, V. Adhitya, and R. Harish

Abstract As electric vehicles are becoming more popular, thermal management systems for batteries have become an important aspect of keeping the temperature and performance of the batteries under check. Exposure to extreme or higher temperatures might lead to the reduction in maximum voltage and the durability of the battery. Thus, an efficient way of thermal management is required for good performance. This research paper deals with the modelling and simulation of a thermal management system of batteries, which makes use of nanofluids as a cooling medium. The battery is modelled as a cylindrical body with isothermal temperature surrounded by nanofluid as cooling medium. Water is considered as a base fluid and parametric study is conducted using different nanoparticles such as aluminium, aluminium oxide and graphene. The volume fraction of the nanofluid is varied between 2 and 8%. Monodispersed spherical particles of uniform size are referred to as nanoparticles. By taking into account the impacts of natural convection, the problem is treated as a three-dimensional incompressible unstable flow. The problem is investigated by plotting the streamline, temperature, velocity and pressure contours. The findings show that the type of nanofluid used and its volume percentage can have a substantial impact on the flow and heat transfer characteristics of batteries. The findings of this study will aid in determining the ideal nanofluid combination for increasing heat transfer rate.

Keywords Battery · Nanofluids · Enhancement

1 Introduction

Batteries have now become an inevitable part of our day-to-day life. They have their applicability in a wide range of fields from consumer electronics to electrical vehicles. The most widely used batteries in the present-day world are lithium-ion batteries. Lithium-ion batteries have profound use because of their rechargeable capabilities.

P. L. Palaniappan · T. T. K. Lokeswar · V. Adhitya · R. Harish (✉)
School of Mechanical Engineering, Vellore Institute of Technology, Chennai,
Tamil Nadu 600127, India
e-mail: harish.r@vit.ac.in

During both periods of charging and discharging, there is dissipation of heat from their surfaces which exposes the battery continuously to high temperatures. This may affect the operating conditions and efficiency of the battery. Constant operation at excessive temperatures dwindles the performance of the batteries and also fast tracks the deterioration process thus reducing the battery's lifespan. Additionally, there is a possibility of the heat generation value of the battery exceeding the amount of heat dissipation to the surroundings. This phenomenon known as thermal runaway can create a domino effect with the internal battery temperature rising exponentially bringing about a rise in battery current. This hike in temperature in any single battery can set about affecting other batteries in the close vicinity. Besides the excessive temperature, the large disparity in the temperatures inside the battery package could potentially lead to irregular current densities and battery decay. All these issues arise the need for a proper thermal management system of a battery to transmit the excess heat to the surroundings and maintain the battery at optimal temperatures.

Ahmed et al. [1] used a single-phase model in an inclined square enclosure with buoyancy-driven flow to examine the utilization of CuH_2O nanofluid. The two surfaces under consideration are a cold obstacle and a circular cylinder with unsteady state convection taking place between the surfaces. Jilte et al. [2] investigated two techniques of cooling component arrangement: liquid filled battery cooling systems and liquid circulated battery cooling systems. The two-cooling mediums considered are water and alumina-water nanofluid and inspect the improvement in cooling performance by addition of nanoparticles. Harish and Sivakumar [3] examined the turbulent thermal convection flow with the heat and cold sources attached to the walls of the cubical enclosure using nanofluids. A transient, three-dimensional, two-phase mixture model was developed with the values of Grashof numbers varied to compute the results. Karimi et al. [4] investigated the use of phase change composites to increase the heat transfer rate of cylindrical lithium-ion batteries. The different phase change material (PCM) used were copper, silver and iron oxide, and the computed results were weighed up with metal matrix of PCM. Alipanah et al. [5] studied the outcome of various geometrical and operating conditions on the battery surface temperature which is the vital aspect of BTMS. The cooling media considered were octadecane and gallium and aluminium foams with different porosities were saturated with these mediums to determine the increase in the thermal conductivity values.

Jilte et al. [6] studied the characteristics of a thermal management system which uses nano-enhanced phase change materials for better heat transfer. In this study on addition of nanoparticles to phase change materials, it was observed that after a certain time, the addition of nanoparticles enhanced the heat absorption characteristics of the material. Huo et al. [7] using lattice Boltzmann method investigated the thermal management system which was based on nanofluid medium. He used aluminium oxide as the nanoparticles suspended in water as the cooling medium and conducted the analysis on a cylinder with uniformly distributed constant heat source. Mondal et al. [8] worked on the thermal management system and investigated on the efficacy of nanoparticles. In this study, different nanoparticles were tested on the battery with different flow configurations. Kiani et al. [9] looked into pure water and nanofluid battery thermal control systems. The system was used in conjunction with phase

change material (copper foam filled with paraffin wax). Singh et al. [10] looked at the thermal conductivity of various nanofluids to see how diverse their applications are.

Liu et al. [11] studied about the effectiveness of nanofluid on the mini-channel thermal management in lithium-ion battery. It is observed in this paper that the addition of nanofluid shows great influence on cooling effect in fluids with lower thermal heat conductivity especially on engine oil. The addition of nanoparticle to base fluid shows a very good thermal management performance as they control the maximum cell temperature. Kiani et al. [12] investigated the use of nanofluid, metal foam and phase change material in the hybrid thermal control of lithium-ion batteries. In this paper, the authors have shown that nanofluid cooling system is very much effective in thermal management when compared to that of water-cooling system during stressful operating conditions of the battery. It is observed in this paper that nanofluid cooling system extends the battery's operation time. Nasir et al. [13] studied about the nanofluid heat pipe in managing the temperature of electric vehicle lithium-ion battery. When aluminium oxide nanofluid with a volume fraction of roughly 0.015 is used as a working fluid in a heat pipe, the overall thermal resistance is reduced by 15% when compared to water filled heat pipes. Wiriyasart et al. [14] investigated the nanofluid thermal management system for battery cooling modules in electric vehicles. It is observed that the battery surface temperature reduces up to 27.6% when compared to that of conventional battery cooling modules. It is also found that the cooling effect of the coolant would increase drastically if the concentration of the nanoparticles suspended in the coolant is higher. Wu et al. [15] investigated the nanofluid-based battery thermal management system using lattice Boltzmann method. The authors have observed 6.5% decrease in the temperature of the battery if we use nanofluid with 0.06 volume fraction.

Majority of the earlier papers involves the investigation of effects of usage of nanofluids in distinct shapes. To the best of authors' knowledge, there is a lack of study on the comparison of different nanofluids' utilization in battery thermal systems and singling out the best ones. Thus, this paper studies the use of aluminium, Al_2O_3 and graphene in a simulated battery thermal environment and figuring out the most efficient nanofluid particle. A three-dimensional model is developed in an unsteady state environment to determine the different required characteristics. Through the alteration of different volume fraction values, the heat transfer characteristics of various nanofluids are investigated. Similar investigations were performed in [3, 16–19].

2 Methodology

The designed model of the presented problem comprises of an unsteady state flow of nanofluids enclosed in an enclosure. The nanofluids are considered to be incompressible and viscous. The base fluid to be used is water with the nanoparticles suspended in them. The three different nanoparticles under consideration are aluminium, alumina and graphene. The battery is in cylindrical shape with a diameter of 14 mm and

height of 50 mm. This cylindrical battery surface generates heat uniformly over its surface. Thus, the boundary condition is set to be constant wall temperature of 85 °C at the outer surface of the cylinder. The acceleration due to gravity is taken in the conventional direction and is set as 9.81 m/s². The thermophysical properties are presumed to be constant.

2.1 Governing Equations

The conservation equations for mass, momentum and energy equations of the fluid are as follows:

$$\frac{\partial \rho_f}{\partial t} + \nabla \cdot (\rho_f u) = 0 \quad (1)$$

$$\frac{\partial (\rho_f u)}{\partial t} + \nabla \cdot (\rho_f u u) = \nabla \cdot p + \nabla \cdot (\mu_f \nabla u) \quad (2)$$

$$\frac{\partial (\rho_f C_{pf} T)}{\partial t} + \nabla \cdot (p_f C_{pf} T u) = \nabla \cdot (k_f \nabla T) \quad (3)$$

where ρ_f represents the density of fluid, μ_f indicates the dynamic viscosity, C_{pf} depicts the specific heat of the fluid and k_f represents the thermal conductivity of the fluid. The other parameters like the velocity, time and temperature are denoted by u , t and T , respectively. The assumptions taken under this study are incompressible fluid flow and steady state heat transfer.

$$\frac{\partial k}{\partial t} + U_j \frac{\partial k}{\partial x_j} = P_k \frac{\partial}{\partial x_j} \left[(v + \sigma_k v_T) \frac{\partial k}{\partial x_j} \right] \quad (4)$$

$$\frac{\partial \omega}{\partial t} + U_j \frac{\partial \omega}{\partial x_j} = \frac{\partial}{\partial x_j} \left[(v + \sigma_\omega v_T) \frac{\partial \omega}{\partial x_j} \right] + 2(1 - F_1) \sigma_{\omega 2} \frac{1}{\omega} \frac{\partial k}{\partial x_i} \frac{\partial \omega}{\partial x_i} \quad (5)$$

Equation (4) and (5) denote the turbulent kinetic energy equation and diffusion equation, respectively, where K is the kinetic energy, v represents the kinematic viscosity of the nanofluid, v_T represents the turbulent viscosity and U_j indicates the velocity in the domain.

σ_w denotes the empirical constants. ω and P_k variables in the equation are the turbulent dissipation rate and production of turbulent kinetic energy, respectively.

2.2 Thermophysical Properties

According to the requirements pertaining to the required study, the effective density, heat capacitance. Thermal conductivity and absolute viscosities of the nanofluids were computed based on the following formulas with different volume fraction values under consideration. The values are computed using the formulas and presented in Table 1

$$\rho_{nf} = (1 - \emptyset)\rho_f + \emptyset\rho_p \quad (6)$$

$$(\rho C_p)_{nf} = (1 - \emptyset)(\rho C_p)_f + \emptyset(\rho C_p)_p \quad (7)$$

$$\frac{k_{nf}}{k_f} = \frac{(k_p + 2k_f) - 2\emptyset(k_f - k_p)}{(k_p + 2k_f) + \emptyset(k_f - k_p)} \quad (8)$$

$$\mu_{nf} = \frac{\mu_f}{(1 - \emptyset)^{2.5}} \quad (9)$$

$$(\rho\beta)_{nf} = (1 - \emptyset)(\rho\beta)_f + (\emptyset)(\rho\beta)_p \quad (10)$$

$$\alpha_{nf} = \frac{k_{nf}}{(\rho C_p)_{nf}} \quad (11)$$

Table 1 Property values of different nanofluids

Nanofluids	Volume fraction	Density (Kg/m ³)	Viscosity (Pa. s)	Heat capacity (J/kgK)	Thermal conductivity (W/mK)
Aluminium	0.02	1034	0.000936	4015.016673	0.642768328
	0.04	1068	0.00099	3855.38809	0.681054605
	0.06	1102	0.00104	3705.609546	0.720954813
	0.08	1136	0.0011	3564.79662	0.762573202
Aluminium oxide	0.02	1059	0.00094	3938.91407	0.641203288
	0.04	1118	0.00099	3718.354204	0.677796832
	0.06	1177	0.00104	3519.906542	0.715864647
	0.08	1236	0.0011	3340.404531	0.755497657
Graphene	0.02	1025.4	0.00094	4031.178077	0.643056194
	0.04	1050.8	0.00099	3884.316711	0.681654448
	0.06	1076.2	0.00104	3744.38766	0.721893065
	0.08	1101.6	0.0011	3610.911402	0.763878884

where φ refers to the volume fraction of the nanoparticle. The subscripts in the equation p , f and nf represent the thermal capacity, μ represents the dynamic viscosity, β means the thermal expansion coefficient and α depicting the thermal diffusivity. Table 1 represents the thermophysical properties of three different nanofluids under different volume fraction.

2.3 Simulation Modelling

Fluent in Ansys software was used to run the simulation. We created a cylinder 15 mm in diameter and 50 mm in length. It was enclosed in an enclosure of 100 mm in all six directions. The created model was meshed further with the default size. Further, all the sides of the enclosure and cylinder was named using the named selection. Next step was carried on the Fluent environment. The enclosure fluid was defined here using the nanofluid properties taken from Table 1. The surface of the cylinder is defined with a constant wall temperature of 333 K (60 °C), and the fluid is taken to be at 293 K (20 °C). All the residuals of velocity, momentum and energy are set to values of 1e-06. Calculations were carried out for a total of 1000 iterations. The flow in this simulation is considered to be incompressible and turbulent. Further, the values of convective heat transfer coefficients, surface heat flux values are taken from the reports. Contours for temperature pressure and velocity are plotted with the count of contours to be 1000. The maximum temperature was taken from the contour plotted in Fig. 1.

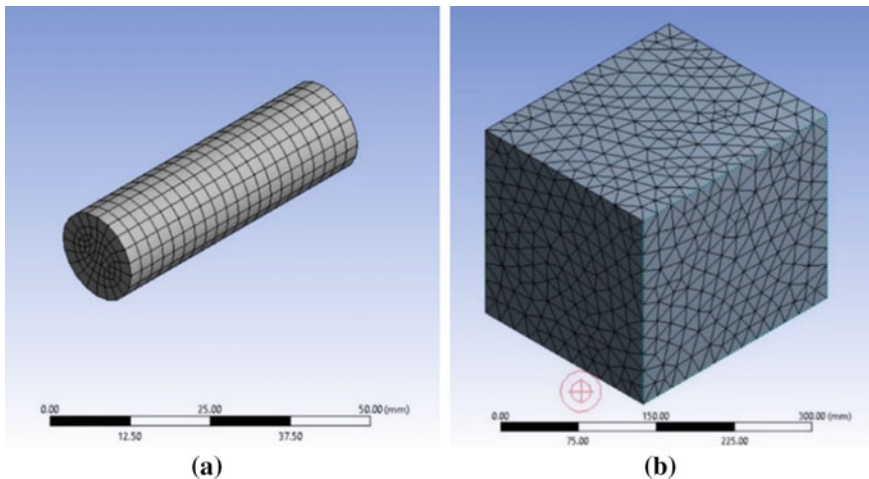


Fig. 1 Meshing of **a** cylinder in the enclosure **b** the enclosure

3 Result and Discussions

Temperature, velocity and pressure contours of all the 12 simulations are calculated. Figure 2a represents one such temperature distribution contour of aluminium-water nanofluid with a volume fraction of 6%. In this scenario, the temperature decreases as the distance from the battery increases, forming a concentric rings pattern. The temperature varies from a maximum temperature of 333 k on the surroundings with a temperature of 293 K. The temperature is conducted in the initial stage from the solid cylinder to surrounding fluids whereby afterwards the convection takes over and the temperature near the fluid is convected to the low temperature surroundings. Figure 2b represents the velocity distribution of the same case. Due to convection, the particles near the fluid get the energy and diffuse towards the walls of the enclosure which can be seen in the visualization as small patches. Figure 3 represents the pressure distribution of the same case. All other values' temperature, velocity, and pressure contours were found to be similar to Figs. 2a, b and 3 accordingly.

The velocities of the nanofluids are highest near the heat source, which is the cylindrical battery, in the early periods. These high-energy particles propagate towards the wall surfaces as the transient heat transfer continues. Thus, after a period of time, the higher velocities are seen to be concentrated towards the enclosure fences as seen in Fig. 2b. As observed from Fig. 3, the pressures are spotted to be maximal near the vicinity of the top surfaces. This is a result of the buoyancy forces acting

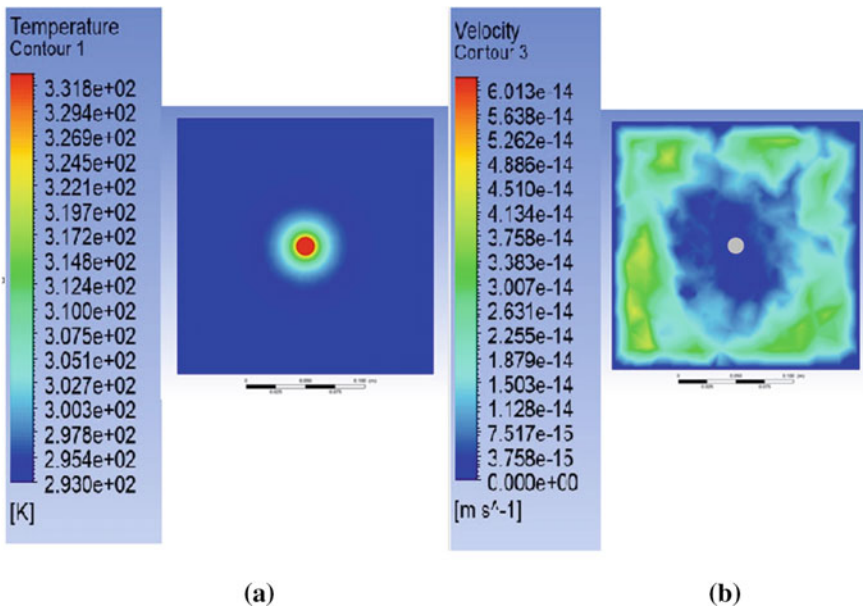


Fig. 2 a Temperature distribution contour of (aluminium–water) with $\phi = 6\%$ b Velocity distribution of (aluminium–water) with $\phi = 6\%$ at the base of the cylinder

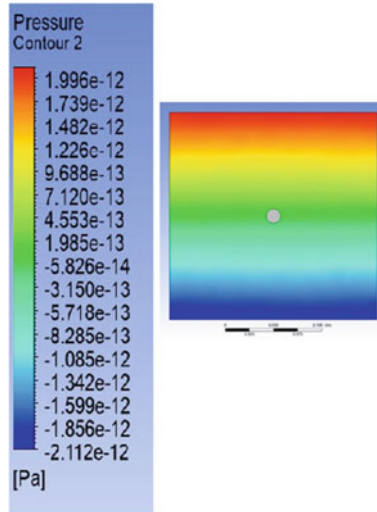


Fig. 3 Pressure distribution contour of (aluminium–water) with $\phi = 6\%$

on the nanofluid molecules. The particles absorb this heat and grow lighter as the temperature of the molecules rises due to the heat generated. As a result, a significant concentration of molecules may be found near the upper parts, resulting in higher-pressure results. Similarly, lower pressures are seen in the lower surface where a lesser concentration of nanofluids can be identified.

The fluctuation of the heat transfer coefficient with volume fraction is depicted in Fig. 4a. It is observed that the line graph for the variation is found to be increasing linearly with the addition of nanoparticles. When the volume percentage was increased from 2 to 4%, the heat transfer coefficient increased by 4.67 per cent. Subsequently, there was an increase of 4.3% and 4.52% increase in h value from 4 to 6% and 6% to 8%. Figure 4b represents the total heat flux variation with volume fraction. The pattern found here is that the value of surface heat flux increases momentarily as the volume fraction of nanoparticles in nanofluids increases, implying that more heat is transported per unit area as the volume fraction of nanoparticles grows.

The fluctuation of the heat transfer coefficient with the volume fraction for alumina-water nanofluid is shown in Fig. 5a. An exact increasing trend was observed in the case of heat transfer coefficient with the value jumping from $63.75 \text{ W/m}^2\text{K}$ to $72.46 \text{ W/m}^2\text{K}$ on varying the volume fraction from 2 to 8%. Similarly, a positive slope is observed in case of total surface heat flux in Fig. 5b varying from 2858.501 W/m^2 to 3249.34 W/m^2 on addition of nanoparticles. Figure 6 indicates that the heat transfer coefficient and total surface heat flux increases with increase in volume fraction for graphene-water nanofluid.

Simulation of graphene-water nanofluid was carried out with different nanoparticles concentration, and the results were plotted on a graph. An increasing slope is

Fig. 4 Variation of **a** heat transfer coefficient (W/m^2K) and **b** total surface heat flux (W/m^2) with volume fraction of aluminium-water nanofluid

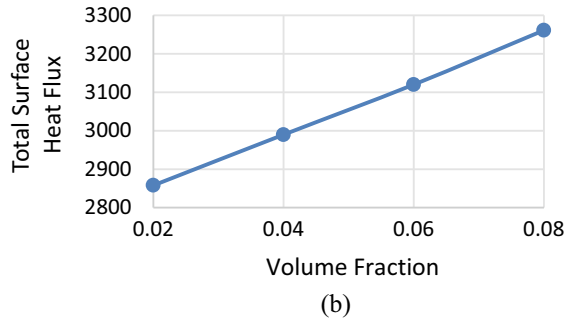
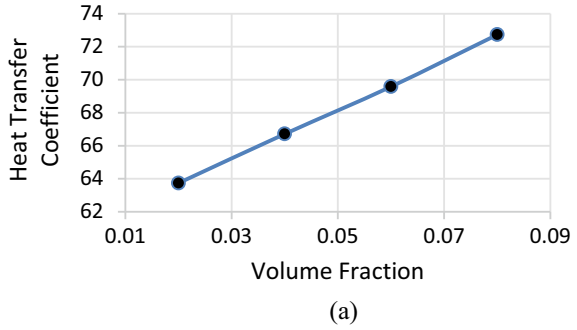


Fig. 5 Variation of **a** heat transfer coefficient (W/m^2K) and **b** total surface heat flux (W/m^2) with volume fraction of alumina-water nanofluid

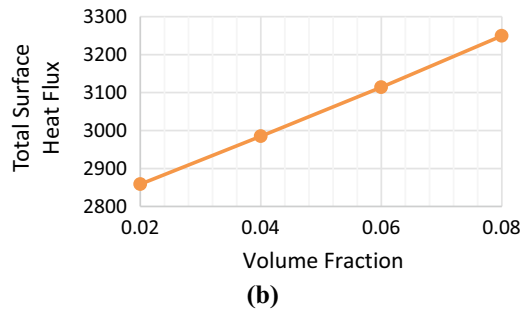
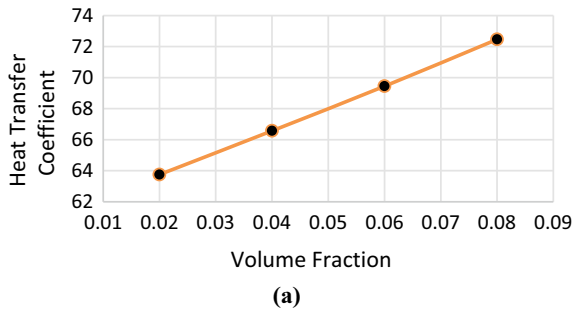
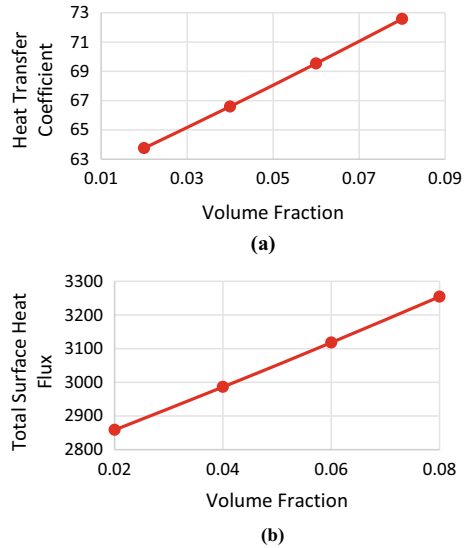


Fig. 6 Variation of **a** heat transfer coefficient ($\text{W}/\text{m}^2\text{K}$) and **b** total surface heat flux (W/m^2) with volume fraction of graphene-water nanofluid



observed in case of heat transfer coefficient on increasing the nanoparticle concentration. On the other hand, the total surface heat flux increases on increasing the nanoparticle concentration. On average the heat transfer coefficient increases by a percentage of 4.41% for 2% increase in nanoparticle concentration. In case of total surface heat flux, it increases by an average of 4.25% on rise of 2% rise in the nanoparticle concentration. Figure 7 represents the comparison aluminium-water, alumina-water and graphene-water nanofluids combination's fluctuation in the coefficient of heat transfer with the increase in nanoparticle concentration. On comparing on all the values obtained in the simulation, it can be noted that aluminium has the highest coefficient of heat transfer comparing to aluminium oxide and graphene. Aluminium with a volume fraction of 8% exhibited the highest of all heat transfer coefficients with a value of $72.73 \text{ W}/\text{m}^2\text{K}$. It can also be noted from the line graphs that the value of h increases with the rise in nanoparticle concentration for all the three cases. Figure 8 depicts the increase in the coefficient of convective heat transfer on increasing the volume fraction by 2 percentage. It was observed that a change of 4.5% on average increase on increasing the volume fraction by 2%.

4 Conclusion

- This work establishes a lithium-ion battery model of a nanofluid-based battery thermal management system to keep the battery temperature within safe limits. On a cylinder with a constant wall temperature, the validation is carried out.

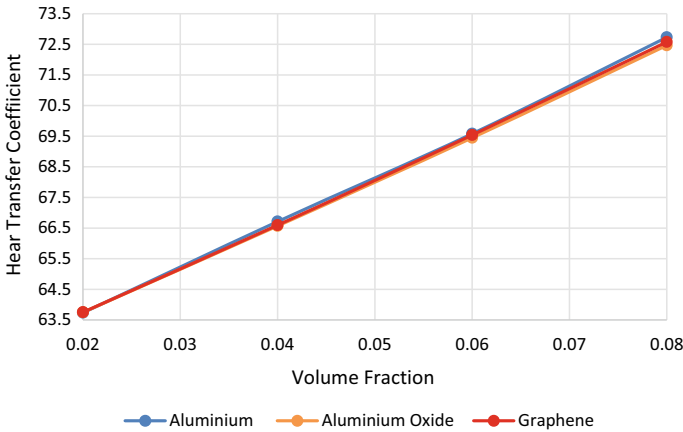


Fig. 7 Comparison of all the above mentioned nanofluids

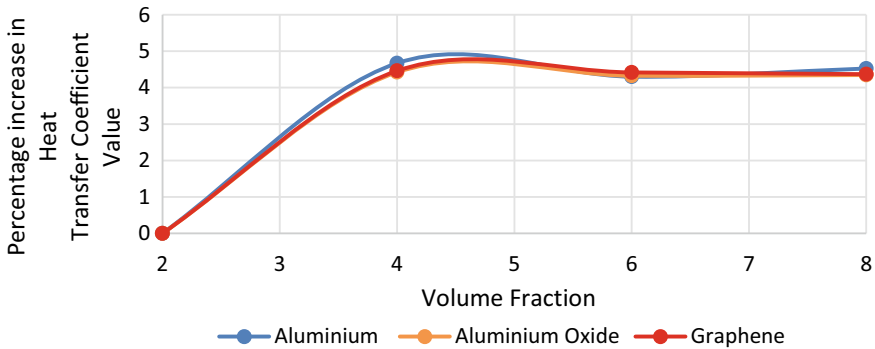


Fig. 8 Percentage increase of heat transfer coefficient on increasing the value of nanoparticle concentration

- The cooling qualities have been investigated, and it has been discovered that the cooling features improve as the percentage of nanoparticles in the nanofluid increases.
- Out of the three nanofluids, aluminium-water nanofluid exhibited a higher convective heat transfer coefficient. The highest heat transfer coefficient of $72.73 \text{ W/m}^2\text{K}$ is observed on the Al-water nanofluid with 8% volume fraction of aluminium which signifies its better ability of cooling and maintaining a lower temperature on the surface of a battery.
- In the variation of total surface heat flux with volume fraction of nanoparticles, it is concluded that with the increase of nanoparticle concentration, the amount of heat transferred per unit area has increased on the surface which shows its ability to be added along with base fluid to enhance the cooling capacity.

- Similarly, a maximum heat flux of 3261.166 W/m^2 was observed in case of aluminium–water nanofluid with a nanoparticle concentration of 8%. Thus, the nanofluids can be used in order to increase the rate of heat transfer to the surroundings from the surface of the battery to maintain it at optimal temperatures.

References

1. Ahmed E, Elshehaby H (2018) Buoyancy-driven flow of nanofluids in an inclined enclosure containing an adiabatic obstacle with heat generation/absorption: effects of periodic thermal conditions. *Int J Heat Mass Transf* 124:58–73
2. Jilte D, Kumar R, Mohammad H (2019) Cooling performance of nanofluid submerged versus nanofluid circulated battery thermal management systems. *J Cleaner Prod* 240:118131
3. Harish R, Sivakumar R (2021) Turbulent thermal convection of nanofluids in cubical enclosure using two-phase mixture model. *Int J Mech Sci* 190:106033
4. Karimi G, Azizi M, Babapoor A (2016) Experimental study of a cylindrical lithium-ion battery thermal management using phase change material composites. *J Energy Storage* 8:168–174
5. Alipanah M, Xianglin L (2016) Numerical studies of lithium-ion battery thermal management systems using phase change materials and metal foams. *Int J Heat Mass Transf* 102:1159–1168
6. Jilte R, Asif A, Satyam P (2021) A novel battery thermal management system using nano-enhanced phase change materials. *Energy* 219:119564
7. Huo Y, Rao Z (2015) The numerical investigation of nanofluid based cylinder battery thermal management using lattice Boltzmann method. *Int J Heat Mass Transf* 91:374–384
8. Mondal B, Lopez CF, Mukherjee PP (2017) Exploring the efficacy of nanofluids for lithium-ion battery thermal management. *Int J Heat Mass Transf* 112:779–794
9. Kiani M, Omiddezyani S, Houshfar E, Miremadi SR, Ashjaee M, Nejad AM (2020) Lithium-ion battery thermal management system with $\text{Al}_2\text{O}_3/\text{AgO}/\text{CuO}$ nanofluids and phase change material. *Appl Therm Eng* 180:115840
10. Singh AK (2008) Thermal conductivity of nanofluids. *Def Sci J* 58(5):600
11. Liu H, Chika E, Zhao J (2018) Investigation into the effectiveness of nanofluids on the mini-channel thermal management for high power lithium-ion battery. *Appl Therm Eng* 142:511–523
12. Kiani M, Ansari M, Arshadi AA, Houshfar E, Ashjaee M (2020) Hybrid thermal management of lithium-ion batteries using nanofluid, metal foam, and phase change material: an integrated numerical–experimental approach. *J Therm Anal Calorim* 141(5):1703–1715
13. Nasir FM (2019) Nanofluid-filled heat pipes in managing the temperature of EV lithium-ion batteries. *J Phys: Conf Ser* 1349(1). IOP Publishing
14. Wiriyasart S, Hommalee C, Sirikasemsuk S, Prurapark R, Naphon P (2020) Thermal management system with nanofluids for electric vehicle battery cooling modules. *Case Stud Therm Eng* 18:100583
15. Wu F, Rao Z (2017) The lattice Boltzmann investigation of natural convection for nanofluid based battery thermal management. *Appl Therm Eng* 115:659–669
16. Janjanam N, Nimmagadda R, Asirvatham LG, Harish R, Wongwises S (2021) Conjugate heat transfer performance of stepped lid-driven cavity with $\text{Al}_2\text{O}_3/\text{water}$ nanofluid under forced and mixed convection. *SN Appl Sci* 3(6):1–13
17. Harish R, Sivakumar R (2021) Effects of nanoparticle dispersion on turbulent mixed convection flows in cubical enclosure considering Brownian motion and thermophoresis. *Powder Technol* 378:303–316
18. Harish R (2018) Buoyancy driven turbulent plume induced by protruding heat source in vented enclosure. *Int J Mech Sci* 148:209–222
19. Harish R (2018) Effect of heat source aspect ratio on turbulent thermal stratification in a naturally ventilated enclosure. *Build Environ* 143:473–486

Impact of Titanium Oxide-Based (TiO₂) Nanofluid on Parabolic Trough Solar Concentrating Collector



Shri Ram Bhardwaj, Surendra Kumar Yadav, and Arvind Kumar

Abstract Parabolic trough solar concentrating collector (PTSC) system is proficient in all solar applications such as power generation, steam, water heating, and air heating. This work was conceded for the study of nanofluids which are nascent fluid that has given away the growth in the thermal properties over the past decade. Nanofluids have made great potential in the field of nanotechnology for thermal engineers. The present work investigates the effects of variation of titanium oxide nanoparticles concentration on the efficiency of a nanofluid-based parabolic trough solar concentrating collector with the usage of high-reflective mirror trough. Nanofluids blend primarily the base fluid (water, in this study) with the nanoparticles of the size micro or millimeter and display characteristic features than that of conservative fluids employed. At 110 lph mass flow rate, the percentage change in overall thermal efficiency was found to be increasing with increase in concentration of nanoparticle, i.e., 42.5% at 0.01% of TiO₂, 59.17% at 0.1% of TiO₂, and 62.28% at 0.15% of TiO₂ in comparison to the water. On the other hand, with an increase in mass flow rate (i.e., 160 lph), the percentage variation in overall thermal efficiency was found to be 26.47%, 41.06%, and 66.37% at 0.01%, 0.1%, and 0.15% of TiO₂ nanoparticles, respectively, when it is compared to the water being used as working fluid. The study indicated that the overall performance of the PTSC improves with an enhancement of mass flow rate and nanoparticle concentration.

Keywords PTSC · Nanofluid · Titanium oxide · Solar energy

1 Introduction

In this experiment, the characteristics of parabolic trough solar concentrating collector at different concentrations of nanofluid were investigated. The parabolic trough solar collector was employed here, which has a reflector of parabolic shape, made by using typically a mirror or an aluminum sheet as per required performance

S. R. Bhardwaj · S. K. Yadav (✉) · A. Kumar
Department of Mechanical Engineering, K. R. Mangalam University, Gurugram 122001, India
e-mail: surendra.yadav@krmangalam.edu.in

to reflect and focus the solar radiations in the direction of a receiver tube positioned at the focal length of the parabola. The absorber tube is prepared of copper or mild steel and tarnished with heat resilient black paint in order to increase the absorbing capacity of the absorber tube. The receiver engrosses the entering radiations and converts them into heat energy that is conveyed and composed by a fluid medium flowing inside the receiver tube. The heat transport fluid streams throughout the absorber tube get heated and hence transmits heat. The fluid temperature was found to be stretched up to 400 °C.

Depending upon the heat transfer characteristics, various heat transfer fluids can be used. Nanofluid is one of those heat transportation fluids which are formed by blending of nanoparticles and base fluid. Nanofluids are a new challenge as well as a new opportunity in the field of thermal engineering. These have distinctive characteristics altered from conservative solid–liquid mixtures in which they are in millimeter or micrometers-sized particles of metals and non-metals scattered onto it. Due to their excellent characteristics, nanofluids have discovered extensive applications in enhancing heat transfer (Fig. 1).

The knowledge behind the employment of nanofluids as thermo-fluids in heat exchangers is the enrichment of heat transfer coefficient and to minimize the measurement of heat transfer equipment’s dimensions. The characteristics of nanofluid, which are viscosity, density, thermal conductivity, and specific heat, are supported for saving of heat energy and material necessary for the heat exchanger. The essential parameters influencing the heat transfer with its properties are primarily dependent on the operating temperature of nanofluids. Heat transfer fluids usually use oil, water, and ethylene glycol, which have comparatively less thermal conductivities than the

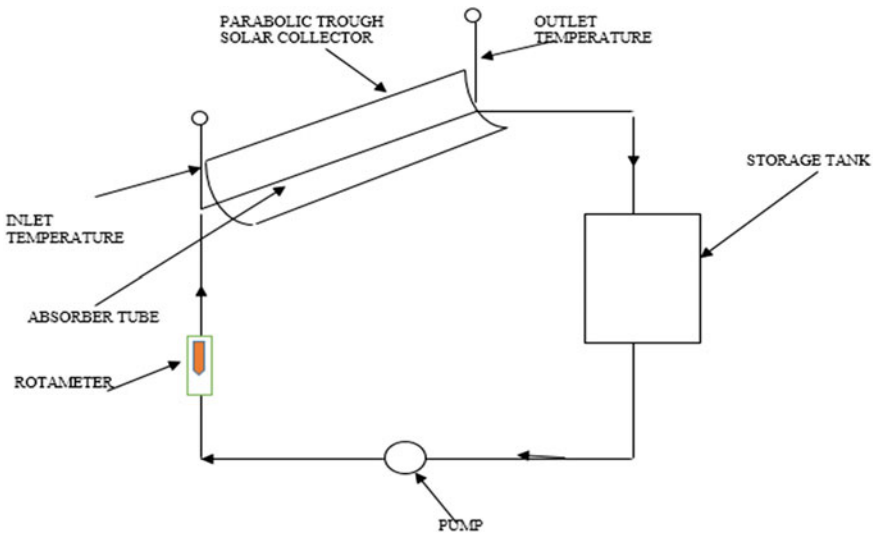


Fig. 1 Flow diagram of a parabolic trough solar collector

thermal conductivity of solids. The solids (metals) have higher thermal conductivity and can upturn the thermal conductivity by accumulating a small quantity of solid elements to that of fluid. The development in optical loss features in the linear type of concentrating solar collectors for practice heat application was explained by Heimsath et al. [1] and witnessed that the energy generation practice was extra operational in temperature range 423–573 K. The model investigation of solar thermal damages of PTSC in Malaysia employing computational fluid dynamics (CFD) was described by Tijani et al. [2]. The convection and radiation heat losses were scrutinized by means of the ensuing temperature of the glass cover from the model. Cau et al. [3] performed a contrast of medium-sized concentrating solar power (CSP) plants established on parabolic and linear collectors. The maximum specific energy creation was found to be 55–60 kWh/y per m² square land engaged with solar multiples in the range of 1.74–2.5 in 4–12 h.

Prinsloo et al. [4] studied electrical power generation using concentrated solar radiation as a temperature heat radiation source. It proposed a 12 square meter parabolic frame design, including modifications to lightweight solar concentrating collectors. Khullar and Tyagi [5] performed the speculative & mathematical examination concerning the usage of nanofluid as working fluid in parabolic trough solar concentrating collector devices. It was shown from the results that the collector performance with the help of nanofluid as a functioning liquid has an enhanced enactment than the conventional collectors in similar circumstances of thermal and optical effectiveness and greater exit temperatures. The results also concluded that the accumulation of aluminum nanoparticles into the base fluid (water) considerably advances its absorption features. Torrecilla et al. [6] proposed mathematical scheming of wind loads over solar collectors. The results were validated for fixed no. of points and variables. It was observed that the accurate assessment of results permits optimization of the configuration, growing consistency, and decreasing cost, which can result in substantial savings in security in the plant. Oukili et al. [7] conducted a Moroccan power grid adequacy evaluation process with CSP by the solar tower and parabolic trough glass technology. It was found that with an increase in load, there was an increase in the risk of load non-recovery. Nagarajan et al. [8] mentioned nanofluid application in parabolic through solar accumulators and revealed that nanofluid enriches the solar system's usefulness when utilized in solar accumulators. It was perceived that the friction factor didn't show any part in refining heat transfer. Some researchers observed that the rate of concentration yields no or very little influence on heat transfer rate. Nanofluids as an advanced knowledge for heat transfer augmentation were described by Dharmalingam et al. [9] and precised the heat transfer in nanofluids. It was shown that nanoparticles developed the thermal conductivity and convective heat transfer of liquids mixed with various base fluids. The temperature absorption was established to be greater with the high density of nanofluid compared to water.

Jilte et al. [10] probed the convective heat transfer damages from solar openings in the wind circumstances and in the changed forms such as conical, cylindrical, cone-cylindrical, dome-cylindrical, and hetero-conical. The comprehensive Nusselt number was offered based on convective heat transfer damages from altered shapes

and magnitudes with or without obstacles under face-to-face wind situations. The viscosity and thermal conductivity of nanofluid by retaining the hypothetical and investigational revisions was studied by Murshed et al. [11] study. The volume fraction of the nanoparticles was taken from 1 to 5%, and different graphs demonstrated the results indicating a direct intensification in the effective thermal conductivity with the temperatures. Wang et al. [12] presented a brief assessment associated with the depiction of heat transfer in a nanofluid. The factors connected with the heat transfer, commonly thermal conductivity, viscosity, convective heat transfer, boiling heat transfer of the nanofluid by quantifying, and their study examinations were essentially established on the existing conductivity additional equitably than on the heat transfer feature. Other studies also focused on role of nanofluid in solar collectors [13–17].

The primary aim of this study was to check the performance of solar collectors by using mirror strips as a reflector material. Using empirical formulas, we also aim to calculate nanofluid's thermophysical properties (density, specific heat, viscosity, & thermal conductivity). The nanoparticle concentration was varied (0.01%, 0.1%, and 0.15%) with base fluid water at two mass flow rates (110, 160 lph). The variation of efficiency in parabolic trough solar collectors using nanofluids at varying mass flow rates and concentrations of the nanofluid was studied and demonstrated in the later sections.

2 Design Methodology

The primary importance is to make parabolic trough solar collector (PTSC) with different materials which are easily accessible and have a low cost without compromising the feature of the material and hence enactment of the system. The trough should be prepared proficient in surviving different loads like wind load and stress loads. So, these things are set aside in mind during the fabrication of the PTSC system. The general made-up PTSC system is displayed as shown in Fig. 2. The PTSC has a reflector of parabolic shape to replicate the direct solar radiation and focused them on top of the focal line of the parabola. A receiver tube is employed on this focal axis to absorb the focused solar radiation flux. It is prepared with stainless steel, iron, or copper and coated with a careful coating on the outside surface.

The coating has a high absorption power for entering radiations but a low emitting ability for the infrared radiations in the solar energy spectrum to decrease the thermal radiation losses. Inside the receiver tube, heat transfer fluid (HTF) flows, which is nanofluid ($\text{TiO}_2 + \text{water}$) here in this study, takes up the focused radiation which drops on the tube and changes the solar radiation into thermal energy. The receiver tube is surrounded by a Pyrex glass cover to decrease the thermal losses to the surroundings. The space between the glass cover and the tube is evacuated to sustain the vacuum which has low thermal conductivity and high viscosity as heat transfer takes place through radiation in this region. Figure 2 below shows the flow diagram of PTSC. Titanium oxide + water nanofluid was used as the working fluid in different



Fig. 2 Fabricated parabolic trough solar collector

concentrations with different mass flow rates. The experiment comprises circulating nanofluid from the storage tank through the collector inlet to the receiver tube, where it catches the heat and then streams back to the storage tank. A pump is used for the circulation of the working fluid in the system. Two digital thermometers are used on the inlet and outlet separately to measure the increase in the temperature. By the use of a solar power meter and anemometer, solar intensity and wind speed were repetitively measured during the experiment. The PTSC is slanted in the southeast direction to track the sun. The investigation is performed by taking different mass flow rates with changing concentrations of nanofluid. The detailed geometrical parameters of fabricated parabolic trough solar collector (PTSC) as shown in Table 1.

2.1 Nanofluid Preparation

The quantity of nanoparticles to be used in the nanofluid depends upon the concentration of nanofluid [refer Fig.3a]. This can be easily calculated by using the following expression (Table 2):

$$M = \frac{M_{\text{nano}} \times 100}{M_{\text{sol}}} \quad (1)$$

The measured nanoparticle is now mixed with the base fluid. This mixing is accomplished with the help of a magnetic stirrer [refer Fig. 3b]. Stirring is required

Table 1 Collector specification

Parameters	Specifications
Aperture area	2.45 m ²
Collector length	2.1 m
Collector breadth	1.2 m
Rim angle	90°
Absorber inner diameter	0.0286 m
Absorber outer diameter	0.0305 m
Glass envelope inner diameter	0.039 m
Glass envelope outer diameter	0.041 m
Concentration ratio	12.17
Circulating pump	40 W
Storage tank material	Plastic
Nanoparticle	TiO ₂
Base fluid	Distilled water
Collector material	Mirror strips
Absorber material	Copper



(a)



(b)



(c)

Fig. 3 a Weighing b Stirring c Sonication

Table 2 Mass of TiO₂ nanoparticles in water to make nanofluids at three different concentrations

Concentration	Mass of TiO ₂ (g)
0.01	2.96
0.1	29.6
0.15	44.4

to be done to disperse the nanoparticles in the base fluid to prevent particle agglomeration. The stirring is done for approximately 30 min. Lastly, the sonication process was performed for nanoparticle stability, as illustrated in Fig. 3c. Finally, sonication of the nanofluid is done to stabilize the nanoparticles for approximately 2 to 3 h. After preparing the nanofluid, the thermophysical properties were calculated using the various empirical relations [refer Appendix A].

3 Results and Discussion

Performance analysis of parabolic solar collector using TiO₂-H₂O based nanofluid considered in this study. The variation in thermal efficiency with time for TiO₂ and water-based nanofluid was investigated in this study. The variation in the thermal efficiency with time at different flow rates (110 and 160 l/hr) for 0.01, 0.1, and 0.15% concentration, respectively, is shown in Fig. 4a–c below. The graph shows that the maximum thermal efficiency was obtained at the beginning of the experiment because the working fluid exhibited maximum temperature rises during this course of time. Nagarajan et al. [8] also show the same trends where the performance of the PTSC was found to be improved with the application of nanofluids.

The efficiency variation at 110 lph and 160 lph with 0.01% concentration of nanoparticles in comparison to the water is shown below in Fig. 5a, b and witnessed that the efficiency is much greater when we use the titanium oxide + water as nanofluid than using only water as a working fluid. These trends were also indicated by Nagarajan et al. [8]. The variation in useful heat gain at 110 lph & 160 lph revealed that the heat gain was observed maximum in peak time of the sunshine where the temperature difference was found to be maximum, as shown in Fig. 6a–d.

It was also identified that the useful heat gain increases with increase in flow rates (110 lph to 160 lph) alongside an increase in nanoparticle (TiO₂) concentration (0.01%, 0.1%, and 0.15%) in the base fluid (water).

The results displayed that the maximum observed intensity was 745.35, 785.58, 810.56, 762.48, 825.06, and 879.45 W/m². The maximum outlet temperatures observed were 43, 42.9, 49.7, 42.7, 45.9, and 44.6 °C, respectively. The maximum temperature difference observed at 0.01, 0.1, and 0.15% nanoparticle concentration at a flow rate of 110lph was 3.2, 5.9, and 6.4, respectively, and at 160 lph was 4, 4.4, and 6.6, respectively. The maximum useful heat gains at 160 and 110 lph were observed around 575.65 and 494.72 W with 0.01%, 586.96 and 517.64 W with 0.1%, and 708.84 and 472.58 W with 0.15% concentration of nanoparticles

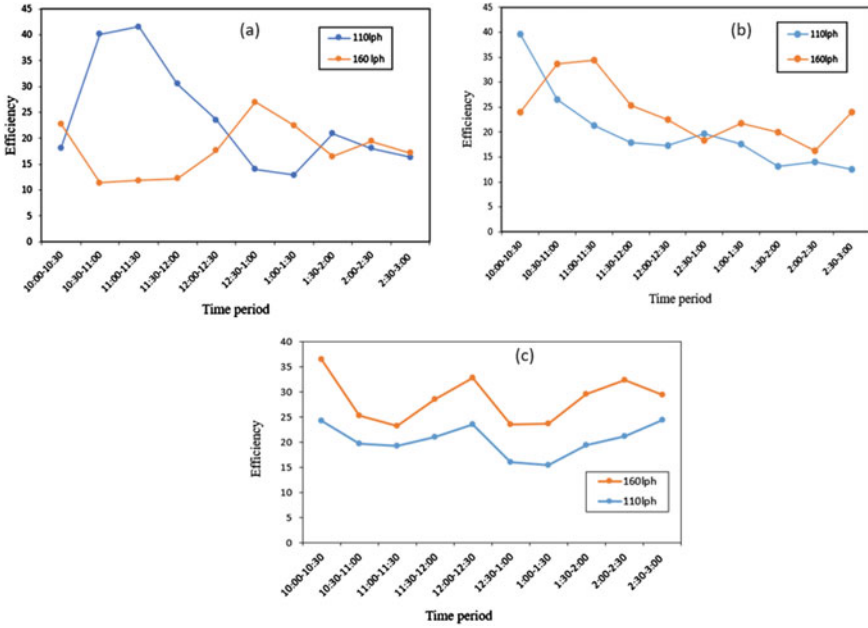


Fig. 4 a, b, c Variation in the thermal efficiency with time at different flow rates

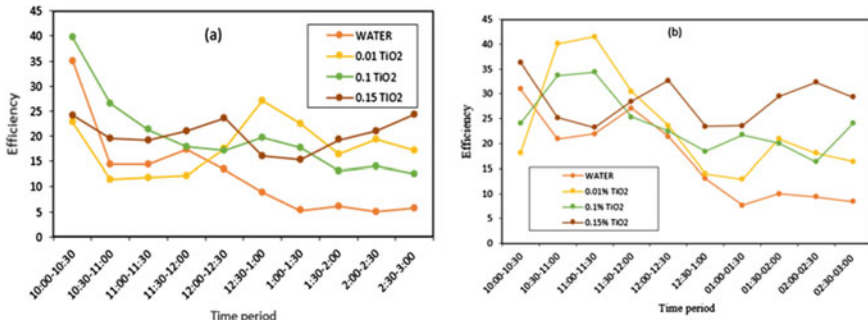


Fig. 5 a, b Variation in thermal efficiency for with 0.01%, 0.1%, and 0.15% TiO₂-H₂O-based nanofluid at vol. flow rate of 110 lph, 160 lph in comparison to water

in the working fluid. The overall thermal efficiency was observed 17.87, 19.96, and 20.53% at 110 lph and 21.59, 24.08, and 28.04% at 160 lph with 0.01, 0.1, and 0.15% concentration of nanoparticles, respectively (Table 3).

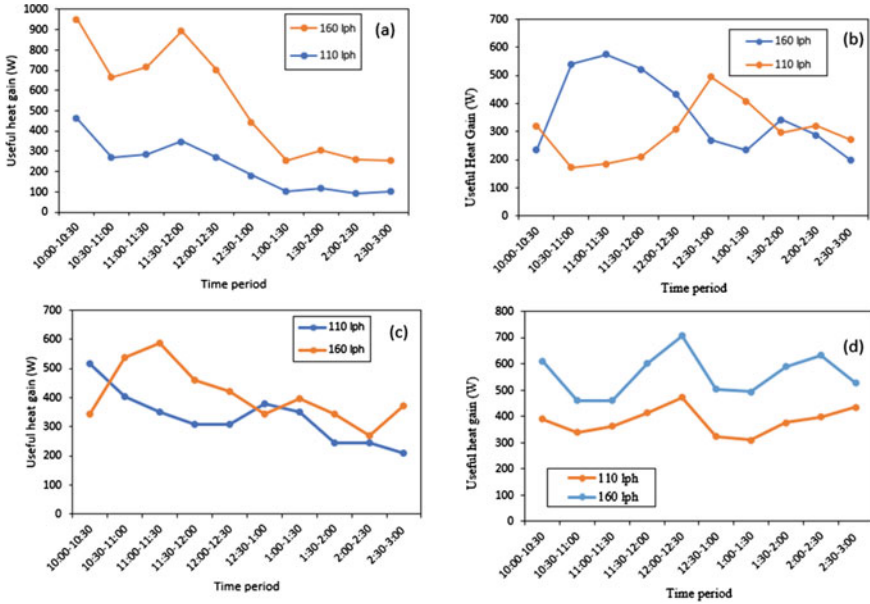


Fig. 6 Variation of useful heat gain at different flow rates

Table 3 Results of experimental observations

Parameters	Water		Nanofluid Concentration					
	110 lph	160 lph	0.01%		0.1%		0.15%	
			110 lph	160 lph	110 lph	160 lph	110 lph	160 lph
Max. temperature difference (°C)	3.6	2.9	3.2	4	5.9	4.4	6.4	6.6
Max. useful heat gain (W)	543.98	464.26	575.65	494.72	586.96	517.64	708.84	472.58
Maximum thermal efficiency	30.99%	35.01%	27.01%	41.52%	39.69%	34.35	24.29%	36.37%
Overall thermal efficiency	12.54%	17.01%	17.87%	21.59%	19.96%	24.08%	20.53%	28.04%

4 Conclusion and Future Scope

The investigation has been performed to investigate the performance of parabolic trough solar concentrating collector using TiO₂-H₂O-based nanofluids and water. The

results were obtained from the experimental analysis of $\text{TiO}_2\text{-H}_2\text{O}$ -based nanofluids and water compared. The study was examined with different volume concentrations (i.e., 0.01, 0.1, and 0.15% of TiO_2) and various mass flow rates (110 and 160 lph). Based on the outcomes of the experimental work, the following conclusions can be made:

- The maximum temperature difference was observed at 160 lph volume flow rate, and the minimum temperature difference was observed at 110 lph. The maximum useful heat gain was observed at a volume flow rate of 160 lph and a minimum useful heat gain at 110 lph of volume flow rate.
- The maximum thermal efficiency with 0.01, 0.1, and 0.15% concentration of TiO_2 was found to be 27.01, 39.69, and 24.29% at 110 lph and 41.52, 34.35 and 36.37%, respectively.
- The overall thermal efficiency was observed to be 17.87, 19.96, and 20.53% at 110 lph and 21.59, 24.08, and 28.04% at 160 lph with 0.01, 0.1, and 0.15% concentration of nanoparticles, respectively.
- The overall thermal efficiency of the PTSC was found to be greater when TiO_2 -based nanofluid was employed as working fluid in comparison to water being used as working fluid.
- It was also observed that the overall efficiency of the solar system goes on increasing with an increase in volume flow rate.

Some of the modifications possible in the future are listed as follows:

- Instead of using a number of mirror strips, a reflector can be fabricated to reflect the maximum amount of solar radiation onto the receiver using a single mirror piece.
- The absorber tube here used was of copper. Instead of using the copper tube, aluminum tubes can also be used as absorber tubes. The diameter of the absorber tube and the glass cover used can be varied to prevent heat losses during the experiment.
- In this experimental investigation, we have taken three concentrations and two volume flow rates of nanoparticles as 0.01, 0.1, and 0.15% of TiO_2 & 110 and 160 lph, respectively. The certain other concentrations and volume flow rates can be used to check the effect of change in concentration on the performance of the solar collector.

Appendix A

Calculations of thermophysical properties and performance evaluation parameters of solar collector: To study the properties of nanofluid and performance of nanofluid using parabolic trough solar collector, following relations are used:

Thermal conductivity: Chandrasekar et al. [18] expressed thermal conductivity as follows:

$$\frac{K_{nf}}{K_{dw}} = \left[\frac{Q_{nf}}{Q_{dw}} \right]^{1.358} \left[\frac{C_{pnf}}{C_{pdw}} \right]^{-0.023} \left[\frac{\mu_{dw}}{\mu_{nf}} \right]^{0.126} \quad (2)$$

Viscosity: Viscosity of nanofluid is calculated by involving the following equation [19]:

$$\mu_{nf} = \frac{\mu_{dw}}{(1 - \varphi_p)^{2.5}} \quad (3)$$

Density: It is also calculated by relating the following equation [19]:

$$\rho_{nf} = (1 - \varphi_p)\rho_{dw} + \varphi_p\rho_p \quad (4)$$

Specific heat: Specific heat also calculated by relating the following equation [19]:

$$C_{eff} = [(1 - p)_f C_{f\ eff}] \quad (5)$$

Useful heat gain: It is calculated under steady-state condition from the following relation:

$$Q_u =_{eff} C_{eff}(T_0 - T_i) \quad (6)$$

Thermal efficiency: The hourly efficiency of the PTSC under steady-state conditions can be obtained from following equation:

$$\eta_{th} = \frac{m_{eff} c_{pnf} (T_o - T_i)}{A_{aper} G_B} \quad (7)$$

Overall thermal efficiency: The overall thermal efficiency under the steady-state conditions is calculated as:

$$\eta = F_R(\tau\alpha) - F_R U_L \left(\frac{T_i - T_a}{G_B} \right) \quad (8)$$

References

1. Heimsatha A, Berna G, Rooyena DV, Nitza P (2014) Quantifying optical loss factors of small linear concentrating collectors for process heat application. International conference on solar heating and cooling for buildings and industry, vol 48, pp 77–86
2. Tijania S, Bin Roslanb AMS (2014) Simulation analysis of thermal losses of parabolic trough solar collector in Malaysia using computational fluid dynamics. 2nd International conference on system-integrated intelligence: challenges for product and production engineering, vol 15, pp 842–849

3. Cau G, Cocco D (2014) Comparison of medium-size concentrating solar power plants based on parabolic trough and linear Fresnel collectors. 68th Conference of the Italian thermal machines engineering association, vol 45, pp 101–110
4. Prinsloo G, Dobson R, Schrevey K (2014) Mechatronic platform with 12m² solar thermal concentrator for rural power generation in Africa. Proceedings of the solar PACES 2013 international conference, vol 49, pp 1470–1480
5. Khullar V, Tyagi H (2010) Application of nanofluids as the working fluid in concentrating parabolic solar collectors. 37th national & 4th international conference on fluid mechanics & fluid power, IIT Madras, Chennai, India, Dec 16–18, paper no. FMFP 2010–179
6. Mier-Torrecilla M, Doblare M (2014) numerical calculation of wind loads over solar collectors. Energy Procedia 49:163–173
7. Oukili M, Zouggar S, Seddik M, Vallee F, Hafyani ME, Ouchbel T (2014) Evaluation of the Moroccan power grid adequacy with introduction of concentrating solar power (CSP) using solar tower and parabolic trough mirrors technology. Mediterranean green energy forum 2013: proceedings of an international conference, vol 42, pp 113–122
8. Nagarajan PK, Subramani J, Suyambazhahan S, Sathyamurthy R (2014) Nanofluids for solar collector applications. International conference of applied energy, vol 61, pp 2416–2434
9. Dharmalingama R, Sivagnanaprabhu KK, Kumarc BS, Thirumalaid R (2014) Nano materials and nanofluids: an innovative technology study for new paradigms for technology enhancement. 12th global congress on manufacturing and management, vol 97, pp 1434–1441
10. Jiltea RD, Kedarea SB, Nayaka JK (2014) Investigation on convective heat losses from solar cavities under wind conditions. 2013 ISES solar world congress, vol 57, pp 437–446
11. Murshed SMS, Leong KC, Yang C (2008) Investigations of thermal conductivity and viscosity of nanofluids. Int J Therm Sci 47(5):560–568
12. Wang XQ, Mujumdar AS (2007) Heat transfer characteristics of nanofluids. Int J Therm Sci 46(1):1–19
13. Ram S, Mishra AK, Jawney K, Prakash C (May 2017) Comparison of performance of parabolic trough solar collector (PTSC) using water and nanofluid (TiO₂ + water). Int J Adv Sci Res Manag 2(4):24–33. ISSN 2455-6378
14. Prakash C, Ram S, Sharma K, Singh P (April 2015) To study the behaviour of nanofluids in heat transfer applications: a review. Int J Res Eng Technol. 4(4):653–6558. ISSN: 2321-7308
15. Meena AS, Mishra AK, Ram S (July 2017) Performance enhancement of solar water heater by twisted tape insert. Int J Eng Technol, Manag Sci. 5(7). ISSN: 2349-4476
16. Kumar A, Kumar V, Subbarao PMV, Yadav SK, Singhal G (2021) Numerical assessment on the performance of variable area single-and two-stage ejectors: a comparative study. Proc Ins Mech Eng, Part E: J Process Mech Eng 09544089211033129
17. Ram S, Mishra AK, Jawney K. Nanofluid application in solar collectors. (ISBN: 978-3-330-32676-7) Lambert Academic Publishing GmbH & Co. KG, Germany
18. Chandrasekar M, Suresh S, Bose AC (2010) Experimental investigations and theoretical determination of thermal conductivity and viscosity of Al₂O₃/water nanofluid. Exp Therm Fluid Sci 34(2):210–216. <https://doi.org/10.1016/j.expthermflusci.2009.10.022>
19. Khanafer K, Vafai K (2011) A critical synthesis of thermophysical characteristics of nanofluids. Int J Heat Mass Trans 54(19-20):4410–4428. <https://doi.org/10.1016/j.ijheatmasstransfer.2011.04.048>

Effect of Variation of Free Stream Boundary Conditions on Flow Characteristics of Transverse Injection-Based Scramjet Combustor Equipped with Shock Generators



Pabbala Monish Yadav, Kavina Bhojani, and Gautam Choubey

Abstract Scramjets are very useful, in clocking supersonic speeds or greater and, as a superior alternative for turbo engines due to the absence of moving parts in them. Current work involves the study of the effect of variation in Mach number and temperature of inlet air stream on the flow dynamics and working of the scramjet combustor enhanced with dual shock generator. This is a numerical study conducted using Ansys Fluent software for executing the simulations. The 2D study involves a solver setup based on 2D coupled implicit RANS equations and standard k- ϵ turbulence model for a better comprehension of the flow characteristics and interactions between the air and the fuel. Due to its wide flammability characteristics and efficient combustion, hydrogen was chosen as fuel for the current study. By the research done previously on the usage of shock generators in the combustor of a scramjet engine, a 2D geometry with dual shock generators suggested by the study was used for the current work due to the merits in mixing and penetration of fuel. To justify the credibility of the solver, simulations were performed of the experimental work conducted by Weidner and Drummond and compared, and it was observed that the results from the simulations were in proper concurrence with experimental findings.

Keywords Scramjet combustor · Shock generators · Boundary parameters variation

1 Introduction

Scramjets amassed ample enthusiasm from both the academic community and industry interested in research regarding supersonic and hypersonic flights [1]. Rocket-based combined cycle systems or turbine-based combined cycle systems [2], which are an example of dual-mode ramjets and combined cycle propulsion systems [3], use scramjets as a supportive engine module. Thus, making this appropriate equipment for supersonic and hypersonic vehicles. These air-breathing propulsion

P. M. Yadav · K. Bhojani · G. Choubey (✉)

Department of Mechanical and Aerospace Engineering, Institute of Infrastructure Technology Research and Management (IITRAM), Ahmedabad, Gujarat 380026, India
e-mail: gautamnits19@gmail.com

systems occupy a prominent place in the defense as well as nondefense utilizations, however, have low combustion and mixing timescales due to brief duration of residence of the fuel in the flow in the combustion chamber, thus requiring vast amounts of research in high-speed combustion for the design and advancement of scramjet engines [3–5]. As supersonic mixing and combustion stand as the most essential concerns at present, injection strategies that enable surface contact enhancement of fuel and air accomplish the task of improved mixing [4–6]. Consequently, diverse injection strategies such as transverse injection [6–8], swept ramp injection [9], cantilevered ramp injection [10, 11], cavity-based injection [12–14], and strut injection [15, 16] were devised to address the mixing and combustion concerns, albeit these strategies were not able to solve the issues completely yet.

It has been proved by Cao et al. [17], a numerical study, that the mixing efficiency of fuel in the combustor was greatly improved by the existence of shock waves. Additionally, to find the effect of shock waves induced by shock generators on mixing of fuel and air in scramjet combustor, computational work was conducted by Choubey et al. [18] where they concluded that mixing efficiency and flame stability are improved due to shocks produced by the shock generators and also they suggested a geometric model with dual shock generators due to its profound capability and superiority over the other models including the one without any shock generator. Hence from the above-stated literature, it can be pronounced that the existence of shock waves boosts mixing efficiency and augments flame stability.

It is very crucial to study the effect of variation of free stream conditions on mixing of fuel and air and consequent combustion process for the provision of greater stability and plausibility of the scramjet during its utilization as the air conditions vary extremely with altitudes.

Based on the literature review presented and to the best of the author's knowledge, there are not any computational studies determining the optimum inlet conditions of air for the scramjet combustor equipped with shock generators, rather than the existing works which involve the study of variation of inlet air conditions for the scramjet combustors without shock generators. Hence, it is essential to evaluate the influence of various free stream conditions on the mixing efficiency of the scramjet combustor equipped with shock generators. In the present work, the study is performed with varying free stream Mach numbers and temperatures, separately, keeping the rest of the parameters the same as in the case of Choubey et al. [18].

2 Numerical Formulation

The 2D coupled implicit RANS equations are used to replicate the attributes and nature of the flow. Moreover, the conventional $k-\varepsilon$ model is used for the simulation of the interaction between free stream and helium. The conventional $k-\varepsilon$ model is selected in computational fluid dynamics models due to its resilience and capability to fit the iterations, design lectotype, and parametric investigation [19]. In addition,

the no-slip criteria are chosen for the walls of the channel, and the conventional wall functions are provided to represent the near-wall area flow.

The other equations which are used for the computation of different elements are equations of standard $k-\epsilon$ turbulent model, equation of species transport, equation of mass diffusion in turbulent flows, and equations of eddy-dissipation model.

3 Geometry and Mesh Data

3.1 Geometry

The geometry for the validation purpose as shown in Fig. 1 has been adapted from the experiment performed by Weidner and Drummond [20], where helium is injected transversely at $Ma = 1$ from a 0.0559 cm diameter port on the lower wall of the combustor which is a 2D rectangle like channel of 25.4 cm length and 7.62 cm height. Here, the helium is injected into supersonic air stream entering the rectangular channel from the left at $Ma = 2.9$ with stagnation pressure (P) and stagnation temperature (T) as 0.0663 MPa and 108 K, respectively.

For the purpose of studying the effect of variation of inlet air conditions, the geometry is chosen from Choubey et al. [18] in which it is titled as geometry 3 (shown in Fig. 1). This geometry is also a rectangular shaped channel but with the dimensions 25.5 cm (length) \times 8 cm (height) and includes two shock generators with each on the upper and bottom walls of the channel at 12.7 cm and 7 cm, respectively, downstream the air inlet (left). The shock generators are 1.8 cm long and 0.5 cm high, and the fuel is injected from a 0.3 cm slot situated at 17.8 cm downstream of the channel's air inlet.

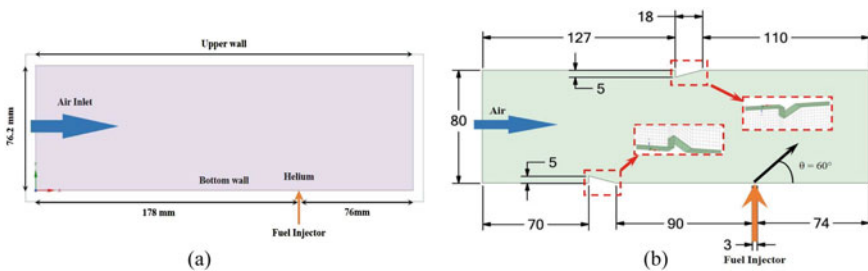


Fig. 1 a Geometry of the model used for validation and b investigated model (all dimensions are in mm)

3.2 Mesh Generation and Grid Independence Test

It is crucial to develop a potential grid for capturing dynamics of compressible flow, and the interaction regions require dense cell distributions for credible results. Thus, keeping in mind, the boundary layers and interaction regions a structural mesh as shown in Fig. 2 were produced by using the Ansys software (commercial) [19]. The mesh contains highly dense cells in the proximity of the wall and the injector, to keep the errors to a minimum with the first cell's height being 0.001 mm and with the tolerable value of y^+ being < 2.5 .

To test the grid independence of the solution, three different meshes, namely coarse, moderate, and refined with total cell quantity as 360,202, 502,304, and 721,345, respectively, were created, and a simulation was performed using all three grids. Results for simulations using all the three grids are compared and as shown in Fig. 3 which proves the independence of solution over the grid.

4 Validation

The validation is based on data from Weidner and Drummond's experimental work [20]. There are certain inconsistencies relating to underestimating of static pressure spike proximal to the upstream area of the injector by the $k-\epsilon$ turbulent model's, due to its limitations, consistent flow presumption at fuel departure, and the complications of the flow. Apart from these minor differences, the experimental outcomes and the values produced from the simulation, as depicted in Fig. 4a, are quite similar. It can be seen that the interaction of the bow shock wave, boundary layer, and bottom wall shock wave causes high pressures in both the separation and reattachment zones close to the injector, resulting in the creation of a powerful shock wave. The pressure is likewise lowered downstream of the injection slot, and the boundary layer and shock wave intermesh to form separation areas on each side of fuel injection zone. The shock wave is found to perish in the combustor at a point situated at 3.81 cm downstream the fuel injector.

For both the experiment and the simulation work, helium mass fractions plotted on a line to inlet of the combustor at a distance of 3.81 cm from the injector are

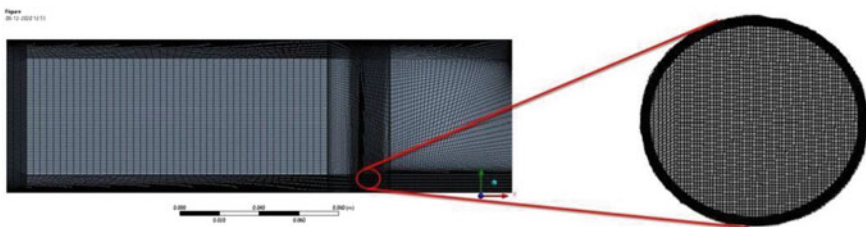


Fig. 2 Image depicting mesh generation across the combustion chamber

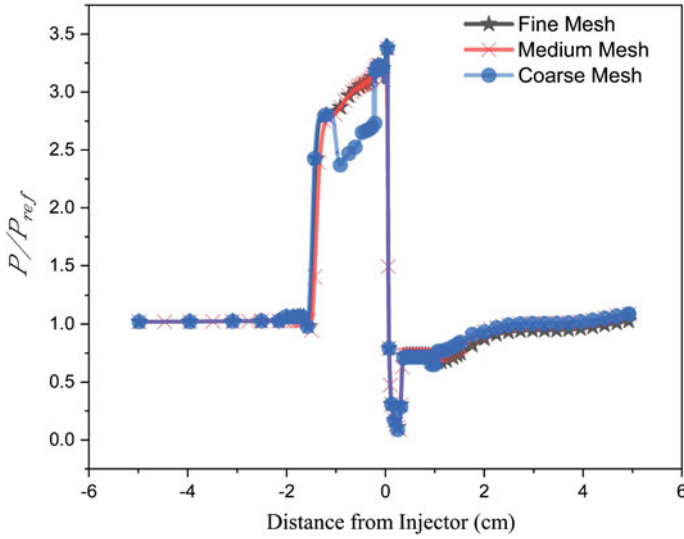


Fig. 3 Static pressure distribution along the bottom wall of combustor for various grid sizes (grid independence test)

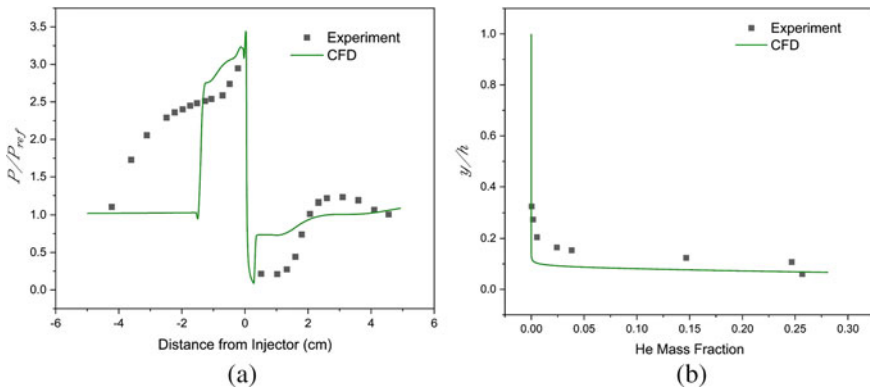


Fig. 4 Comparison of computational results and experimental results from Weidner and Drummond [20] **a** pressure distribution on bottom wall, **b** static pressure at 3.81 cm downstream of the injector

evaluated and presented as normalized height vs helium mass fraction graphs and compared as shown in Fig. 4b. The nature of the graphs is almost the similar for experimental work and the simulations performed, and the values of both are near to each other, despite the simulation work’s underestimate.

It can be inferred from Fig. 4a and b that simulated models can be used to replicate free stream and fuel mixing, as well as the detection, study, and prediction of shock waves. Thus, computational and numerical simulations can be utilized to investigate

the effects of variation in free stream conditions on the flow characteristics of a shock generator equipped transverse injection-based scramjet combustor.

5 Results and Discussion

Subsequent to the fact that the validation results are in concurrence with experimental results, the effect of change in free stream Mach number and temperature on the flow field and mixing efficiency fuel of the combustor is studied. The geometry of the combustor is as described in Sect. 3.1. Firstly, the effect of variation of free stream Mach number is examined by using three different Mach numbers 2.5, 3.0, and 3.5, respectively, at a constant temperature of 800 K. Secondly, the effect of variation of free stream temperature is investigated by changing it from 700 to 900 K at constant free stream Mach number ($Ma = 3.0$).

5.1 Effect of Variation of Inlet Mach Number

Computational simulations with free stream Mach numbers 2.5, 3.0, and 3.5 are performed in the combustor model (Fig. 1b) with a stagnation temperature of 800 K. The second simulation performed in this study, i.e., the one with free stream Mach number as 3.0 is the exact same simulation which has been performed by Choubey et al. [18].

Figure 5 shows the Mach number contours of the combustor for various free stream Mach numbers. It can be observed that Fig. 5b is closely similar to the result indicated in Choubey et al. [18].

From Fig. 5a–c, by interpolating the oblique shock wave (produced by upper wall shock generator) and separation shock (produced downstream of the bottom wall shock generator), we can find the intercepts (X_1 for oblique shock on bottom wall, X_2 for separation shock on upper wall) of the shocks on both the walls. By looking at the intercepts for all the values of the Mach numbers, it can be interpreted that by an increment in inlet air Mach number, there is a shift in intercepts toward further downstream in the combustor. Thus, with an increase in inlet air Mach number, the flow dynamics tend to shift toward the right or downstream of the combustor. This downstream shift causes a decrease in the size of separation zones in the combustor.

The decrease in the size of the separation zone may indicate reduction in the size of the vortices formed in the zone. It can also be noticed from Fig. 6 that with an increase in free stream Mach number, there is a decrease in the size of the separation zone formed downstream of the injector slot as well as in the recirculation zone which may cause degradation in flame holding capacity of the combustor.

Velocity streamlines for all the cases were plotted and are shown in Fig. 6. The effect of an increase in Mach number as predicted above can be clearly seen in Fig. 6. For the simulation with free stream $Ma = 2.5$, there is counter-rotating vortex pair

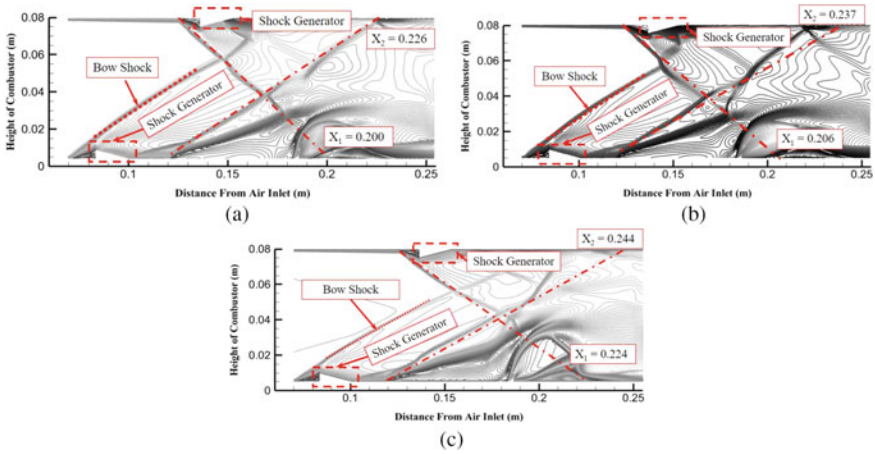


Fig. 5 Mach number of contour lines of the combustor **a** with free stream $Ma = 2.5$ **b** with free stream $Ma = 3.0$, **c** with free stream $Ma = 3.5$

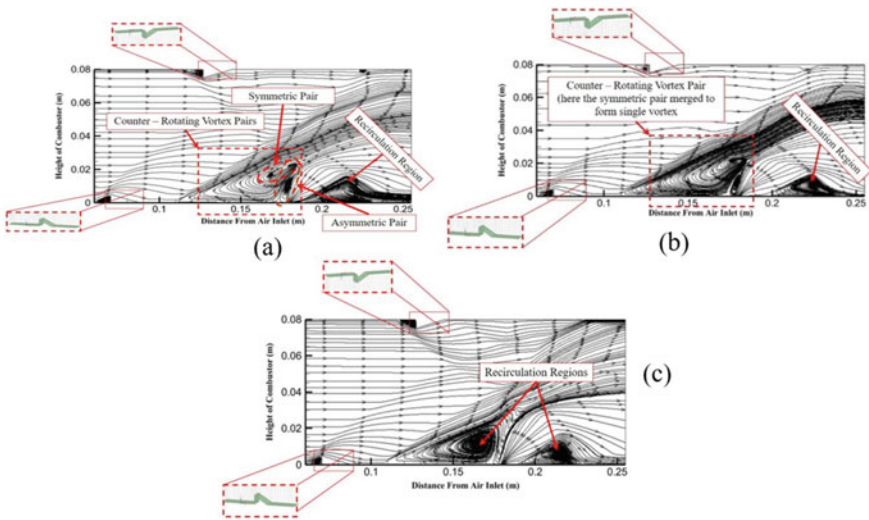


Fig. 6 Computed streamlines distribution along the combustor for **a** free stream $Ma = 2.5$, **b** free stream $Ma = 3.0$, **c** free stream $Ma = 3.5$

along with a larger vortex in the separation upstream of the injector; later when the free stream Mach number is increased to $Ma = 3.0$, we can notice the counter-rotating vortex pair merging into a single vortex resulting in only single pair of counter-rotating vortices in the whole separation region due to increase in the influence of separation shock on the separation zone. As the free stream Mach number is further increased to $Ma = 3.5$, there is clear evidence of the strong influence of the shock over

the zone due to which the vortices disappear and the whole region gets occupied by a recirculation zone ahead of the injector, this clearly illustrates the effect of variation of free stream Mach number on the flow field of the combustor. The vortex pairs which are generated in the proximity of the fuel injection zone promote mixing of free stream with fuel than the recirculation zone formed upstream of the injection slot as it does not increase any surface area of fuel and air.

From the provided velocity streamlines images, it can be deduced that there will be an effect on mixing efficiency of the combustor from the variation of free stream Mach number, which is evident from the elements of the flow dynamics like vortices and recirculation zones. We can also notice that with an advancement in free stream Mach number, there is a decrement in the size of the recirculation zone formed downstream of the injector, thus decreasing the flame holding capacity of the combustor.

The comparison of mixing efficiencies of the combustor from all the simulations was made and depicted in Fig. 7. We can see that the mixing efficiency of a combustor with free stream $Ma = 2.5$ has the highest efficiency than any other initially and then takes second place as we proceed toward the right side of the combustor. The combustor with a free stream $Ma = 3.5$ has the least mixing efficiency of all the cases throughout the combustor.

The higher mixing efficiency of the combustor with free stream $Ma = 2.5$, by a very low margin, than the combustor with free stream $Ma = 3.0$ in spite of almost same upstream separation zone volume is due to the presence of additional counter-rotating vortex pair in the combustor with free stream $Ma = 3.0$ which increases the contact surface area of fuel and air promoting higher mixing efficiency. The rise

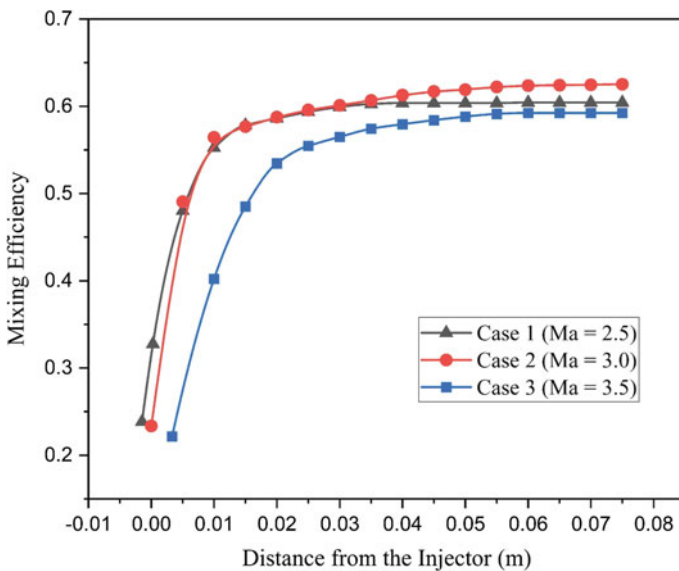


Fig. 7 Mixing efficiency comparison for all the cases with varying free stream Mach number

in mixing efficiency in a combustor with free stream $Ma = 3.0$ than the combustor with free stream $Ma = 2.5$, as we proceed toward the right side of the combustor, is due to high downstream mixing caused by an increase in Mach number of the inlet air. The reason for low mixing efficiency of the combustor with free stream $Ma = 3.5$ is because of the absence of any vortex in the upstream region of the injector, even though there is a huge recirculation zone, it cannot cater to the capability of a counter-rotating vortex in terms of mixing ability, but we can observe the rise in mixing efficiency as we approach toward the outlet due to high downstream mixing rate because of high free stream Mach number.

5.2 Effect of Variation of Stagnation Temperature of Inlet Air

In this section, three cases are compared and the variation among them is in the free stream temperatures. The free stream temperatures studied are 700 K, 800 K, and 900 K with a constant $Ma = 3.0$. Here, the case with free stream temperature as 800 K is nothing but the same case as in the 2nd case in the previously done study (i.e., the effect of variation of free stream Mach number—Sect. 5.1) and also the same simulation as performed by Choubey and Pandey [21].

The separation shock formed downstream the bottom wall shock generator in the combustor with inlet air temperature as 700 K is closer to the shock generator and further from the injector in comparison with the other two cases (Fig. 8a–c). In the other two instances (i.e., in combustor with inlet air temperatures as 800 K and 900 K), there is not much difference in the location of separation shock/region formation. This early formation of separation shock/region in the first case ($T = 700$ K) allows for the formation of a huge separation region. The flow dynamics for the cases with inlet air temperatures of 800 K and 900 K are a lot similar to each other.

The combustor case with 700 K as free stream temperature has a very large counter-rotating vortex pair in the upstream of the injector which has a great deal of influence over the mixing efficiency of the combustor as shown in Fig. 9a. The separation zone housing the counter-rotating vortex pair starts very ahead in the combustor slightly prior 0.1 m downstream the air inlet of the combustor. Whereas in other cases, the zone starts at around 0.11 m downstream of the air inlet. The smallest recirculation zone formed downstream the injector is in the case with the free stream temperature of 800 K.

The highest mixing efficiency [21] is achieved by the combustor with free stream temperature of 700 K (Fig. 10) due to the formation of a very large counter-rotating vortex pair, which increases the contact surface area of air and fuel staggeringly. The second case combustor ($T = 800$ K) has a very slight advantage over the last simulation (i.e., combustor with $T = 900$ K) due to slightly more contact surface area due to the merged vortex present in it, thus providing a minor upper hand in mixing efficiency over the other.

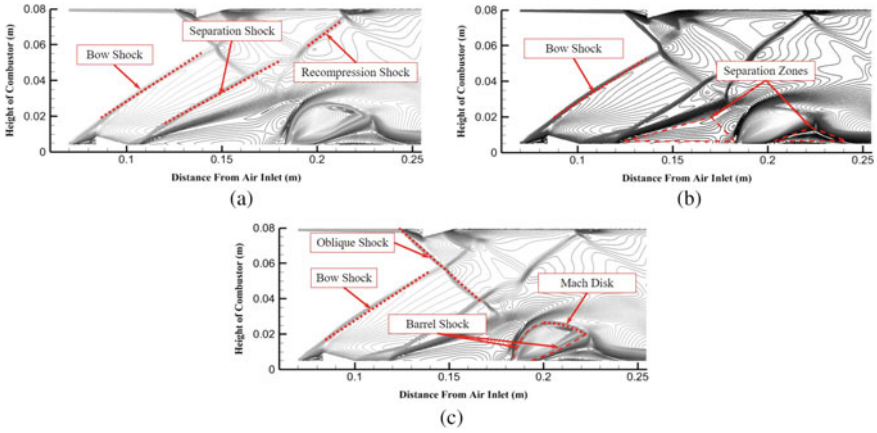


Fig. 8 Mach numbers contours of the combustor **a** with free stream $T = 700$ K **b** with free stream $T = 800$ K **c** with free stream $T = 900$ K

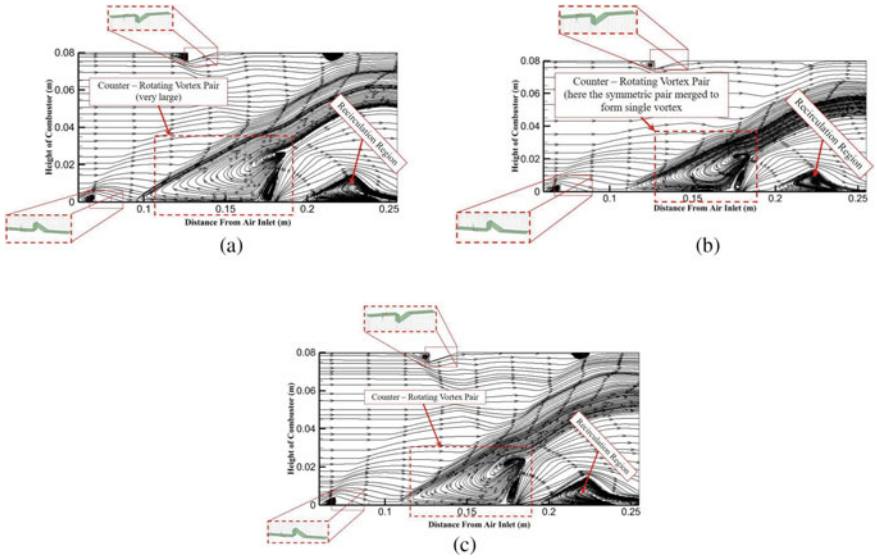
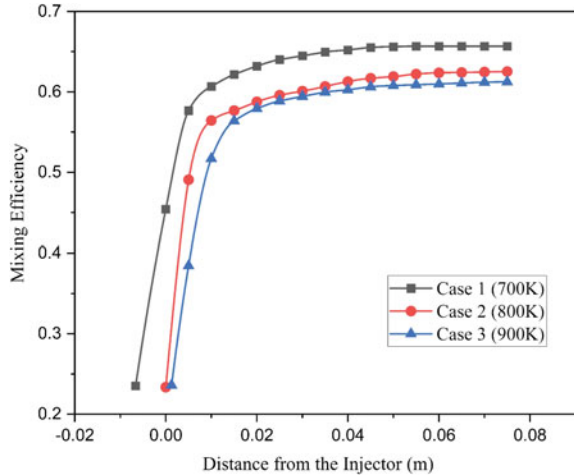


Fig. 9 Computed streamlines distribution along the combustor for **a** free stream $T = 700$ K, **b** free stream $T = 800$ K, **c** free stream $T = 900$ K

6 Conclusions

The effect of variation of inlet air Mach number and temperature on the flow dynamics and mixing ability of a scramjet combustor equipped with dual shock generators is studied, and the following outcomes are.

Fig. 10 Mixing efficiency comparison for all the cases with varying free stream temperature



- The mixing efficiency of the combustor with inlet air Mach value of $Ma = 2.5$ was the highest initially due to the presence of more vortices and was overcome by the combustor with inlet air Mach value of $Ma = 3.0$ because of high downstream mixing due to high velocity.
- Combustor with $Ma = 2.5$ has the largest recirculation zone downstream the injector making it the best in terms of flame holding capacity, and the combustor with $Ma = 3.5$ is the worst due to its smallest recirculation zone, downstream the injector, of all because of high velocity.
- Simulation with inlet air stagnation temperature $T = 700$ K has the highest mixing efficiency due to the presence of the largest counter-rotating vortex pair of all the cases. The cases with inlet air stagnation temperatures of 800 K and 900 K are similar.

References

1. Musielak, DE et al (2015) Busy year of scramjet research, 53–53
2. Wei B et al (2017) Propulsion performance research and status of TRRE engine experiment. In: 21st AIAA International Space Planes and Hypersonics Technologies Conference 2017, p 2351. Xiamen
3. Segal C (2009) The scramjet engine: processes and characteristics, Vol 25, 1st edn. Cambridge University Press, New York
4. Aso S et al (2009) A study on supersonic mixing by circular nozzle with various injection angles for air breathing engine. Acta Astronaut 65(5–6):687–695
5. Choubey G, Pandey KM (2017) Numerical studies on the performance of scramjet combustor with alternating wedge-shaped strut injector. Int J Turbo Jet-Engines 34(1):11–22
6. Zhang Y et al (2015) Effects of oblique and transverse injection on the characteristics of jet in supersonic crossflow. Acta Astronaut 115:356–366

7. Huang W, Yan L (2013) Progress in research on mixing techniques for transverse injection flow fields in supersonic crossflows. *J Zhejiang Univ, Sci, A* 14(8):554–564
8. Huang W et al (2012) Influences of the turbulence model and the slot width on the transverse slot injection flow field in supersonic flows. *Acta Astronaut* 73:1–9
9. Donohue JM et al (1994) Experimental and numerical study of swept ramp injection into a supersonic flowfield. *AIAA J* 32(9):1860–1867
10. Parent B et al (2002) Numerical investigation of the turbulent mixing performance of a cantilevered ramp injector. *AIAA J* 40(8):1559–1566
11. Huang W et al (2013) Performance evaluation and parametric analysis on cantilevered ramp injector in supersonic flows. *Acta Astronaut* 84:141–152
12. Ben A, Hanson RK (2001) Cavity flame-holders for ignition and flame stabilization in scramjets: an overview. *J Propul Power* 17(4):869–877
13. Kim KM et al (2004) Numerical study on supersonic combustion with cavity-based fuel injection. *Int J Heat Mass Transf* 47(2):271–286
14. Huang W et al (2012) Numerical validation and parametric investigation on the cold flow field of a typical cavity-based scramjet combustor. *Acta Astronaut* 80:132–140
15. Fureby C et al (2015) A computational study of supersonic combustion in strut injector and hypermixer flow fields. *Proc Combust Inst* 35(2):2127–2135
16. Huang W (2015) Investigation on the effect of strut configurations and locations on the combustion performance of a typical scramjet combustor. *J Mech Sci Technol* 29(12):5485–5496
17. Cao D et al (2017) LES study on flow features of the supersonic mixing layer affected by shock waves. *Int Commun Heat Mass Transfer* 85:114–123
18. Choubey G et al (2021) Numerical investigation on mixing improvement mechanism of transverse injection based scramjet combustor. *Acta Astronaut* 188:426–437
19. ANSYS, Inc. (2016) ANSYS fluent user's guide, Release 17 (2016) 2
20. Weidner EH, Drummond JP (1981) A parametric study of staged fuel injector configurations for scramjet applications. In: *Proceedings of the AAS/AIAA Astrodynamics Conference 1981*, pp 3–5. American Institute of Aeronautics and Astronautics (AIAA), Nevada (1981)
21. Choubey G, Pandey KM (2016) Effect of variation of angle of attack on the performance of two-strut scramjet combustor. *Int J Hydrogen Energy* 41(26):11455–11470

Effect of Divergence Angles on the Performance of a Cavity-Based Scramjet Combustor



Malhar Solanki, Tathya Bhatt, G. Kshitij, and Gautam Choubey

Abstract Supersonic combustion is a work-in-progress field primarily dealing with difficulties in mixing fuel with the free stream air coming into the engine leading to difficulties of inefficient combustion and thus inefficient thrust production. Such new generation engines require unique fluid mechanisms to achieve good mixing. One such approach is changing the shape of the space surrounding the fuel injector yields generates vortices that aids in mixing fuel with air by increasing the residence time of the combustible mixture. In addition to the bespoke shape of the cavity, a diverging cross-sectional area is provided to reduce if not prevent thermal choking. It was found that the trapezoidal shape cavity provided the best metrics with diverging angles.

Keywords Supersonic combustion · Trapezoidal cavity fuel injection · Divergence angle · Mixing efficiency

1 Introduction

Scramjet engines offer greater capabilities for propelling aircrafts and missiles. These engines are light weight as compared to their counterparts (traditional jet engines) because of fewer number of mechanical components. Contributions from across the world have led to development of geometrical modifications of the combustion domain. The primary objective of making a geometric contraction of hot gases is to provide constant source of ignition which in turn provides sustained combustion. The cavity flows are segregated mainly into open type ($L/D < 10$) and closed type ($L/D > 10$). In open type flows, the shear layer formed at the separation corner spans the entire cavity length and reattaches somewhere along the cavity back face. These cavities generally have low values of drag, but also relatively small levels of entrainment from the main flow. Closed cavity flows occur when the shear layer is unable to span the entire length of the cavity and reattaches on the cavity floor. Closed

M. Solanki · T. Bhatt · G. Kshitij · G. Choubey (✉)
Department of Mechanical and Aerospace Engineering, Institute of Infrastructure Technology
Research and Management (IITRAM), Ahmedabad, Gujarat 380026, India
e-mail: gautamnits19@gmail.com

cavities are characterized by larger drag coefficients compared with open cavities. Thus, open cavities are more desired in scramjet combustors due to their lower drag coefficients.

Sustained combustion is difficult to achieve because of the sonic velocity of air at inlet. Thus, the complete combustion lasts no more than few milliseconds, therefore, effective combustion is a critical factor in increasing the efficiency of the engine. Since the velocity of fuel injected is very high, mixing efficiency is the key factor contributing to optimize fuel combustion.

This topic of mixing efficiency due to various geometrical entrapments is widely researched upon; Huang et al. [1] have investigated the ram-to-scram mode transition induced by jet-to-crossflow pressure ratio, while Huang et al. [2] extensively worked on transient combustion flow for the hypermixer in a Hyshot scramjet combustor. Prominent works of Gruber et al. [3] have provided comprehensive literature on improving the fundamental understanding of cavity-based flame holders. On contrary, researchers have also tried to incorporate dual-cavity injection; Lu et al. [4] concluded that the interaction of fuel injection and cavity flow gave rise to the formation of two sizes of vortexes in the upstream cavity. Ali et al. [5] comprehended the effects of microjet generated oblique shocks (multiple parallel and coalescing shocks) on the flow field. To use fuel-mixing capabilities to its potential, various geometrical constrictions aiding fuel mixing and their combustion are studied with the help of CFD. Recently, Choubey and his fellow researchers also [6–16] conducted some important simulation on scramjet combustor. A survey was conducted by Seiner et al. [17] on numerous concepts previously investigated on mixing augmentation of scramjet for future consideration.

The rate of the enhancement was controlled by cavity shape and velocity of the inlet air. The flow field entrapped in the cavity recirculates flow increasing the residence time of fluid in the cavity leading to proper mixing of fuel with air. Streamline patterns are compared for different divergence angles to show its influence. It shall be noted that circulations are main results of the cavity in the supersonic flow patterns. The injection of the hydrogen divides the main circulation, and role of the cavity shape is prominent for the formation of the circulations inside the cavity.

From the above literature review, it can be easily noticed that the effect of divergence angle of the upper wall of the combustor has rarely been analyzed, and it might have an impact on the combustion performance inside the scramjet engine. Therefore, this information needs to be explored further.

Numerous experiments with unique approaches and geometries were developed by scientists to enhance the mixing efficiency. Roos et al. [18] in their work investigated the effect of a cavity placed directly upstream of an injector on the performance of generic scramjet combustor while in this work, we have primarily focused on the trapezoidal cavity-based fuel injection (injector placed inside the cavity).

Among different types of cavities, we have comprehensively analyzed the mass distribution of H_2O inside the trapezoidal chamber which is the most valuable parameter effecting the mixing efficiency. Moreover, our studies also consider the effects on mixing efficiency with change in divergence angle of the upper wall.

2 Flow Modeling and Simulation

2.1 Geometry and Grid Generation

A two-dimensional model is developed with dimensions of 300 mm and 50 mm in horizontal and vertical directions, respectively. The geometric model of the cavity flow domain used in this work is from Moradi, et al. [19] for extensive investigation. This geometry has been further changed for performing different investigations. A divergence angle of 1.5° and 3° is provided on the upper wall as a part of this study. A high-resolution structured mesh grid is generated inside the cavity. To reduce the numerical diffusion, the generated high-resolution grid in the model is essential. The grid generated is very uniform throughout to eliminate any type of discontinuity in the results (Fig. 1).

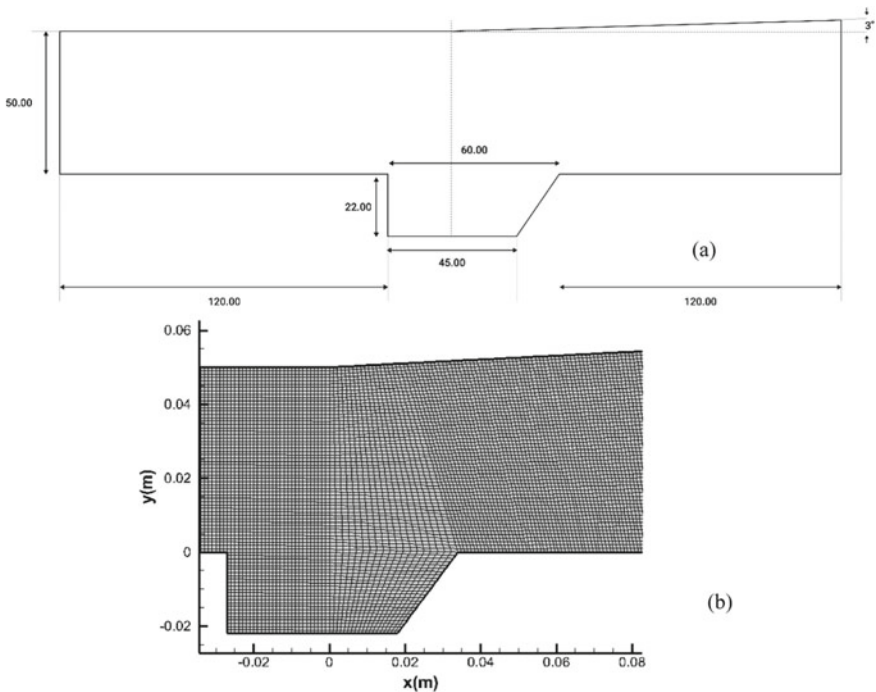


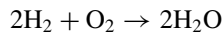
Fig. 1 a Schematic diagram of trapezoidal cavity (*All dimensions are in mm) b Grid generation

2.2 Numerical Setup

In this research, the use of implicit solver has been made with a finite volume cell center method and with help of that we have performed the computational investigation at Mach numbers 1.5, 2, 2.5 and temperature 300 K and studied each parameter at two different divergence angles. Several boundary conditions were imposed to make sure we get a robust solution. To obtain a higher accuracy solution, k-omega shear stress transport turbulence model [20] was used with an inclusion of energy balance and species transport equations. For this study, 2-D Navier–Stokes equation has been used to describe the flow of the fluid.

While k-omega model is used for low Reynolds number and near wall treatment, SST k-omega is used for high Re and free stream flow. Thus, SST model is preferred for high turbulent flows. To find relevant diffusion data using trapezoidal cavity, species transport equation is necessary, which helps in determining mass fraction of hydrogen, oxygen and water present in the combustion chamber.

Species transport solver with mixture as hydrogen and air was employed with single step reaction option enabled.

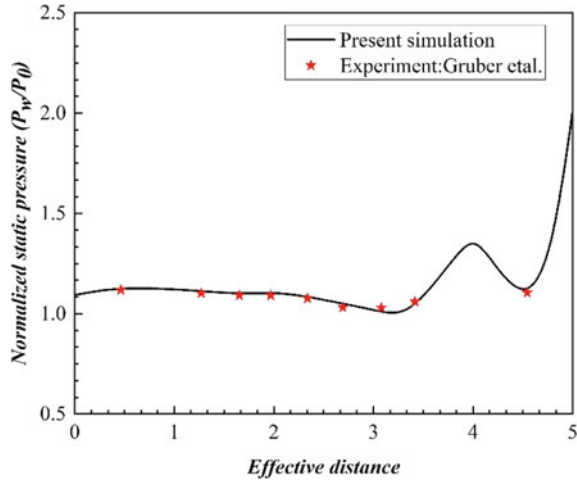


3 Results and Discussions

This section presents the results of our numerical simulations in terms of the performance parameter. Our previous studies concluded that trapezoidal cavity is best suited for preserving the ignition zone, thus trapezoidal cavity is considered for this study; as it was already verified from Moradi et al. [19] work.

3.1 Simulation Validation

The curve in Fig. 2 represents the static pressure distribution with respect to the distance along cavity wall. The distance is measured upstream from the separation corner, the cavity floor and the cavity rear face. Based on Gruber's experimental results, the current study shows good agreement with his experimental data.

Fig. 2 Validation study

3.2 Effect of Variation of Mach Number

Combustion simulations using species transport equations were performed on trapezoidal cavity geometry work having divergence angle for this study. Running the simulations at different Mach numbers ($M = 1.5, 2, 2.5$), it was observed that Mach number $M = 2.5$ yielded better results than the other Mach numbers. The Mach number contours of the performed simulations are shown in the Figs. 3, 4, and 5. Two prominent factors; shock waves and flow separation were examined during this study. At $M = 1.5$, the flow velocity is pretty non-uniform while at $M = 2$, bow shocks started to emerge in the geometry with 3° divergence angle but in the geometry with 1.5° divergence angle there are irregularities in the flow velocity. It is evident from the Mach contours (Figs. 3, 4, and 5) that $M = 2.5$ is a favorable condition for profound shock generation. It has also been observed that the shockwaves generated in the geometry with 1.5° divergence angle are much less sustained downstream than those obtained in the geometry with 3° divergence angle. Secondly, there is an abrupt change in flow velocity downstream in the geometry with 1.5° divergence angle while the flow velocity transition is subtle in the geometry with 3° divergence angle. In the latter, geometry flow separation is delayed thus pronouncing the effect of bow shocks.

3.3 Effect on Mole Fraction of H₂O

Further, investigation on the flow of H₂O shows that the hydrogen-rich flow is very perturbed at low Mach numbers (i.e., $M = 1.5$ and 2) (Figs. 6 and 7). The flow is having uniform distribution of H₂O at $M = 2.5$ with 3° of divergence angle, with

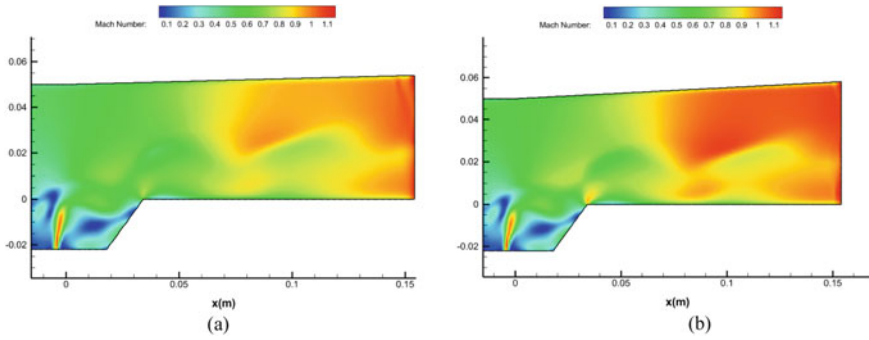


Fig. 3 Mach number contours for a 1.5° and b 3° divergence angle at M = 1.5

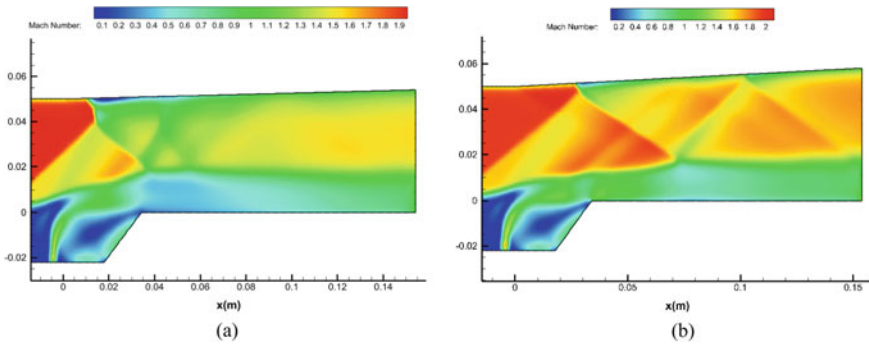


Fig. 4 Mach number contours for a 1.5° and b 3° divergence angle at M = 2

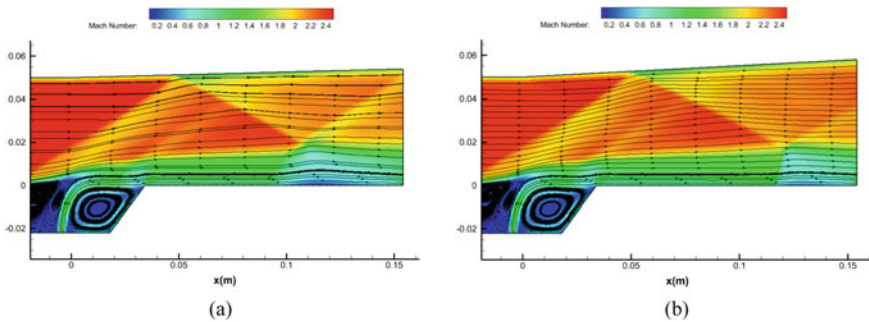


Fig. 5 Mach number contours for a 1.5° and b 3° divergence angle at M = 2.5

less flow turbulence as compared to 1.5° divergence angle. Geometry with 3° of divergence angle also gives more profound combustion when compared with 1.5° divergence angle as evident by mixing efficiency (Fig. 8).

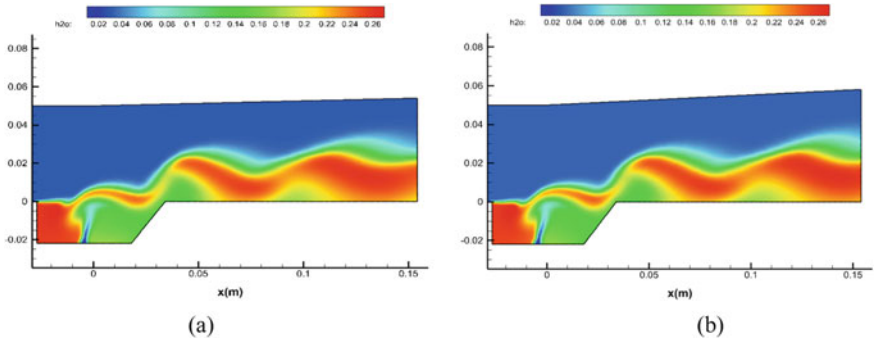


Fig. 6 Mole fraction of H₂O contours for a 1.5° and b 3° divergence angle at M = 1.5

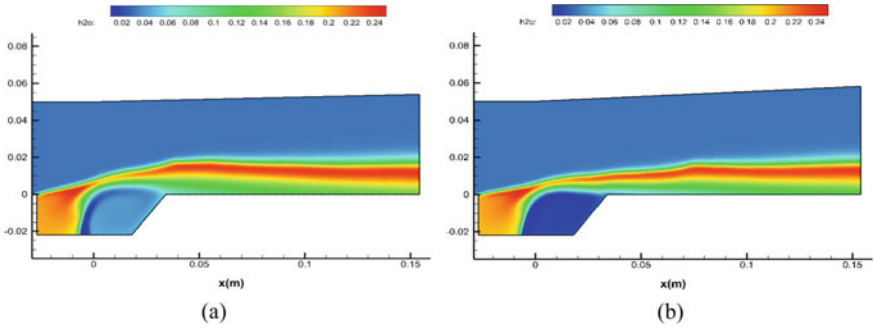


Fig. 7 Mole fraction of H₂O contours for a 1.5° and b 3° divergence angle at M = 2

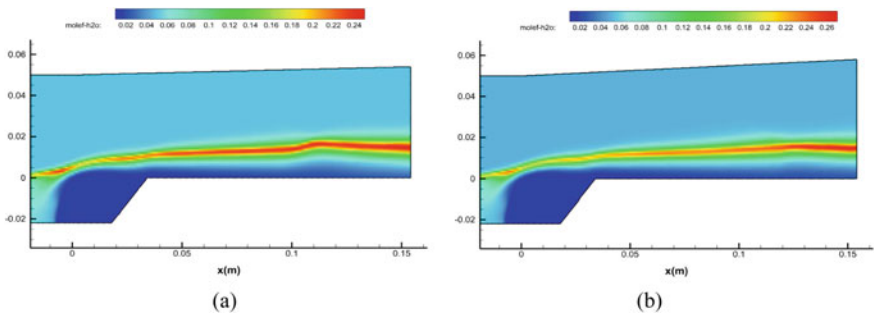


Fig. 8 Mole fraction of H₂O contours for a 1.5° and b 3° divergence angle at M = 2.5

3.4 Mixing Efficiency

Mixing efficiency is a measure of the level of mixing of fuel taking place in the combustor, which can be calculated as [15].

$$\eta_{\text{mixing}} = \frac{\int \alpha \cdot \rho_{\text{gas}} \cdot \chi_{\text{H}_2} \cdot u \cdot dA}{\dot{m}_{\text{H}_2}}$$

α = stoichiometric ratio for hydrogen.

ρ_{gas} = density of gas (combustion products).

χ_{H_2} = mass fraction of fuel available for combustion.

u = axial velocity.

\dot{m}_{H_2} = the mass flow rate of fuel at the fuel inlet.

It gives us an idea of potential combustion performance. The mixing is largely affected by the near-field presence of vortices. As per our remark, mixing efficiency is greater in geometry having 3° of divergence angle in the upper wall than the 1.5° divergence angle. The mixing efficiency of geometries with and without any divergence angle is given in Fig. 9. Further, the recirculation happening in the cavity and the shock formation leads to turbulence into the flow field; which shall promote diffusion and hence efficient mixing as a result.

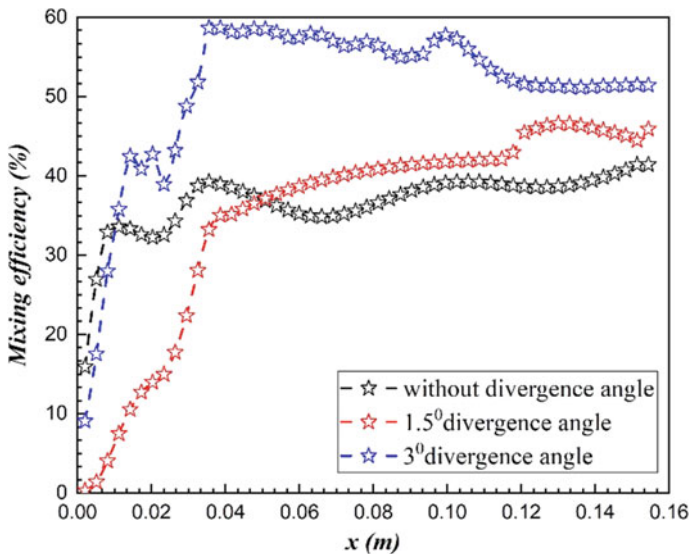


Fig. 9 Mixing efficiency graph for divergence angle a 1.5° and b 3° at $M = 2.5$

4 Conclusions

In this study, computations were performed to investigate the effect of inclusion of divergence angle in the trapezoidal shaped cavity injector in a generic scramjet combustor. Two-dimensional CFD approach is used with SST turbulence model to simulate the flow inside the cavity. The following conclusions have been drawn from the performed investigation based on the comparison of two different geometries that were considered for this research. Parameters used to compare the two different geometries observations include Mach number contours, mass fraction contours and mixing efficiency graph.

From Mach number contour, it is evident that the bow shocks get established at $M = 2.5$, thus further observations and comparisons are made at $M = 2.5$. It has been observed that there are less flow separations and less shockwaves are sustained in the geometry with 1.5° divergence angle when compared to the geometry with 3° divergence angle.

In the mass fraction contour, it has been observed that there were low flow turbulence and profound combustion was taking place the geometry with 3° divergence angle when compared to the geometry with 1.5° divergence angle.

From the mixing efficiency graphs, it has been observed that the mixing is taking place more prominently in the geometry with 3° divergence angle when compared to geometry with 1.5° divergence angle. Thus, when the divergence angle of wall cavity increases, the mixing efficiency is improved.

References

1. Huang W, Jin L, Yan L, Tan JG (2014) Influence of jet-to-crossflow pressure ratio on nonreacting and reacting processes in a scramjet combustor with backward-facing steps. *Int J Hydrogen Energy* 39(36):21242–21250
2. Shen W, Huang Y, Liu Z, You Y (2021) Mixing and transient combustion processes of scramjet combustor with transverse injector and hypermixer. *Case Studies Thermal Eng* 26:101104
3. Gruber MR, Baurle RA, Mathur T, Hsu KY (2001) Fundamental studies of cavity-based flameholder concepts for supersonic combustors. *J Propul Power* 17(1):146–153
4. Lu W, Zhansen Q, Liangjie G (2015) Numerical study of the combustion field in dual-cavity scramjet combustor. *Procedia Eng* 99:313–319
5. Ali M, Ahmed K, Kumar R, Alvi F (2011) Flowfield characteristics of oblique shocks generated using microjet arrays. In: 49th AIAA Aerospace Sciences Meeting including the New Horizons Forum and Aerospace Exposition, p 485
6. Choubey G, Pandey KM (2016) Effect of variation of angle of attack on the performance of two-strut scramjet combustor. *Int J Hydrogen Energy* 41(26):11455–11470
7. Choubey G, Devarajan Y, Huang W, Mehar K, Tiwari M, Pandey KM (2019) Recent advances in cavity-based scramjet engine—a brief review. *Int J Hydrogen Energy* 44(26):13895–13909
8. Choubey G, Pandey KM (2018) Effect of different wall injection schemes on the flow-field of hydrogen fuelled strut-based scramjet combustor. *Acta Astronaut* 145:93–104
9. Mahto NK, Choubey G, Suneetha L, Pandey KM (2016) Effect of variation of length-to-depth ratio and Mach number on the performance of a typical double cavity scramjet combustor. *Acta Astronaut* 128:540–550

10. Choubey G, Pandey KM (2018) Effect of variation of inlet boundary conditions on the combustion flow-field of a typical double cavity scramjet combustor. *Int J Hydrogen Energy* 43(16):8139–8151
11. Li Z, Moradi R, Marashi SM, Babazadeh H, Choubey G (2020) Influence of backward-facing step on the mixing efficiency of multi microjets at supersonic flow. *Acta Astronaut* 175:37–44
12. Choubey G, Pandey KM, Maji A, Deshmukhya T, Debbarma A (2017) Computational investigation of multi-strut injection of hydrogen in a scramjet combustor. *Materials Today: Proceedings*. 4(2):2608–2614
13. Choubey G, Yadav PM, Devarajan Y, Huang W (2021) Numerical investigation on mixing improvement mechanism of transverse injection based scramjet combustor. *Acta Astronaut* 188:426–437
14. Choubey G, Yuvarajan D, Huang W, Yan L, Babazadeh H, Pandey KM (2020) Hydrogen fuel in scramjet engines—a brief review. *Int J Hydrogen Energy* 45(33):16799–16815
15. Du ZB, Shen CB, Huang W, Yan L, Liang JH, Choubey G (2021) Parametric study on mixing augmentation mechanism induced by cantilevered ramp injectors in a shock-induced combustion ramjet engine. *Aerosp Sci Technol* 108:106413
16. Choubey G, Gaud P, Fatah AM, Devarajan Y (2022) Numerical investigation on geometric sensitivity and flame stabilisation mechanism in H₂ fueled two-strut based scramjet combustor. *Fuel* 312:122847
17. Seiner JM, Dash SM, Kenzakowski DC (2001) Historical survey on enhanced mixing in scramjet engines. *J Propul Power* 17(6):1273–1286
18. Roos T, Pudsey A, Bricalli M, Ogawa H (2020) Numerical investigation of upstream cavity enhanced fuel mixing in scramjet combustors. *Acta Astronaut* 169:50–65
19. Moradi R, Mahyari A, Gerdroodbary MB, Abdollahi A, Amini Y (2018) Shape effect of cavity flameholder on mixing zone of hydrogen jet at supersonic flow. *Int J Hydrogen Energy* 43(33):16364–16372
20. Menter FR (1994) Two-equation eddy-viscosity turbulence models for engineering Applications. *AIAA J* 32(8):1598–1605

A Review on the Selection of Materials and Heat Transfer Properties in Scramjet Engines



Namrata Bordoloi , Krishna Murari Pandey , and Gautam Choubey 

Abstract The scramjet engines are considered as one of the important developments of the hypersonic industry. The engines only operate at supersonic velocities; the supersonic combustion process is so fast that the time available for efficient combustion is very less. The heat produce inside the combustor is very high, so selection of materials is one of the crucial parameters in obtaining efficient combustion. The jet propulsion devices demand the use of special materials that have the capacity to withstand the high temperature environment. So, the selection of appropriate materials is one of the primary requirements for designing the scramjet combustor. The paper reviews the different material properties and the applications on the combustor to enhance the performance, durability, and reliability. The paper uses a subjective approach to review the different material properties. The paper also attempts to cover the heat transfer phenomenon inside the combustor as the temperature and pressure generated in the combustor is quite high. Furthermore, the paper finally overviews the properties of the composite materials for the scramjet combustor with the motive to find the appropriate materials that can used further by the researchers in future.

Keywords Composite · Combustor · Heat transfer · Materials · Propulsion · Scramjet

1 Introduction

The hypersonic industry is exploring options to fly at hypersonic speed since the development of multi-staged rockets. However, rocket propulsion has limited scope in hypersonic travel which led hypersonic research a curious topic among the

N. Bordoloi (✉) · K. M. Pandey
National Institute of Technology Silchar, Silchar 788010, Assam, India
e-mail: namrator@hotmail.com

K. M. Pandey
e-mail: kmpandey2001@yahoo.com

G. Choubey
Institute of Infrastructure Technology Research and Management (IITRAM), Ahmedabad, India

researchers. The development of air breathing jet engines such as turbojet engines, turbofan engine, Ramjet engine, and scramjet engine has paved the way in developing lightweighted vehicles to fly at high velocities [1]. All the jet engines stated here work on the same principle. The supersonic combustor ramjet engines also known as scramjet engines have grabbed the attention of the researchers as it does not have any moving parts unlike other jet engines. These engines use the atmospheric oxygen and do not carry an oxidizer to undergo the combustion process at high velocities [2]. However, the engines cannot start of its own it required a carrier vehicle, which is one of the prime disadvantages of the engine. The process of combustion occurs at supersonic speeds, and very less time is available for efficient fuel burning which decreases the performance of the engine. In order to overcome this problem, researchers have introduced different fuel injection techniques such as fuel injection through single strut injection [3], multi-strut injection [4], cavity injection [5–7], and wall injection with the motive to enhance the performance of the system. Till date, scramjet engines testing has survived the short duration and has proved feasible. However, for longer flight duration for Mach number greater than 5 has its unique challenges in the structure of the system as it experiences extreme thermal loads [8–10]. Furthermore, flights operating higher than Mach 5 demands an exhaustive selection of materials to survive the extreme thermal loads and temperatures at such speeds. It is necessary that the selection of the materials has to be done in such a way that during the combustion process, the thermal energy gets distributed in such a way that the temperature does not exceed the material limits. Additionally, for long-flight scramjet engines, the use regenerative cooling with endothermic hydrocarbon fuels is able to solve the challenge of thermal protection.

The paper reviews the advancement in the selection of the materials and the different techniques to tackle the heat transfer challenges in the scramjet engines with the motive to improve the efficiency of the overall engines.

2 Materials and Heat Transfer Properties Required in the Scramjet Engines

The scramjet engines operated at supersonic speeds and demand appropriate selection of materials which primarily should be low in cost and lightweighted [2]. In order to select the appropriate materials, some of the properties such as specific strength, corrosivity, heat resistivity, strength over density, low thermal expansion, and resistance to embrittlement at low temperature should be take into consideration. One such materials is titanium which has high specific strength, resistance to heat and corrosion, light in weight, etc. [11]. Generally, its usage is seen in fan and compressor as it can withstand lower temperatures (600 °C). Another material is carbon fiber-reinforced plastic (CFRP) which also quits fit the criteria. The use of aluminum alloys is also seen in the literature. These alloys good castability and cost-efficient [12]. The use of superalloys is seen in the make of combustion

chambers due to its good mechanical properties and corrosion-resistance properties. The composite materials provide 20% more strength-to-weight ratio as compared to materials. Different types of composites such as composite matrix composites (CMC), metal matrix composites (MMCs), polymer matrix composites (PMC), and carbon matrix composites are widely used to serve the purpose of withstanding the extreme environment [13]. These composites exhibit high tensile strength, toughness, lightweight, high temperature resistance, etc.; one of the important features of composites is that it can withstand high temperature to around 1500 °C, which is quite beneficial for the scramjet engines [14]. The use of composites in the make of scramjet engines can be perfect candidate among the other materials.

3 Literature Review

The scramjet engines operate at high velocities which have paved the way to design lightweighted space vehicles. Unlike any other rocket engines, the scramjet engines use the atmospheric oxygen to undergo the process of combustion. The engines start its operation at high velocities, due to which the outer body experiences vigorous friction with the atmosphere resulting in aerodynamic heating. On the other hand, the combustion process inside the combustor occurs at high velocities resulting in temperature rise as high as 3000 K. Moreover, due to such high temperature on the inside, and intense friction on the outside requires a stable cooling system, and selection of appropriate materials is necessary to meet the working conditions. The sections below discuss the usage of different materials and different cooling techniques that are already present in the literature in order to provide an overview on the current advances in materials and cooling techniques in the scramjet engines.

3.1 *Material Selection in Scramjet Engines*

The selection and development of materials is very crucial for scramjet engines. The materials for the scramjet engines are expected to have low density and high stiffness and strength and many others. The researchers around the globe are making continuous efforts in the development and selection of materials that can withstand the extreme conditions due to high velocity combustion process occurring inside the combustor. The section reviews the studies on material usage in the already present in the literature with the motive to select the appropriate materials for the scramjet engines.

Seelant [15] and Bauchez et al. [16] studied the different cooling mechanisms and lightweight advanced materials for high-speed flight projects for different materials requirements (CMC, metallic). The aim of the study was to understand the capacity of these materials to withstand the high temperature and generated heat flux at high flight Mach 3 speed.

Draper et al. [17] used TiAl alloy as stiffness structure at the inlet, nozzle, and compressor section with the motive to reduce the weight of the hypersonic propulsion system in the scramjet engines.

Sabarigirinathan et al. [18] manufactured and tested a ramjet engine and performed an analysis on temperature using different fuels. Costa et al. [19] experimentally investigated the Brazilian 14-X hypersonic vehicle. The model exhibited the use of long stainless steel waverider model technology with the motive to provide lift and combustion efficiently in the scramjet engine.

Zander [20] studied the uses of composite materials and regenerative cooling on a proposed scramjet model to understand the heat transfer in the walls and the changes in the combustor due to the generation of extreme temperatures in the combustor. Humphrey [21] fabricated the inlet of ramjet engines with low-carbon mild steel to investigate the effect of the pressure distribution on the inlet. It may be concluded that on using low carbon mild steel at the inlet, the inlet accommodated high pressures than other materials.

Sharma and Mahajan [22] and Zheng et al. [23] fabricated a ramjet nozzle using carbon fiber-reinforced silicon carbide (C/Sic) composite with ceramic materials as lining. The aim of this modification was to reduce the erosion causing by the gases coming out of the nozzle. The exhausted gases are high in temperature, velocity, pressure that eroded the structure and leading to structural failure.

Alvaro F. S. Pivetta [24] numerically analyzes the structure using FEM for 14-XS air breathing engine. In order to withstand the effects of high velocities, the structure used auxiliary devices such as ribs, stringers, and costing materials for thermal protection. Beyer et al. [13] investigated the advanced fuel-cooled structures by introducing fuel-cooled ceramic structures incorporated in the dual-mode ramjet engines with strut integrated design.

Choubey et al. [25], Thong [26], and Nishit and Ulmek [27] reviewed the uses, advantages, applications, and different types of composites. It also highlights the safe properties, strength, and stiffness which are necessary in the materials for scramjet engines.

Ma et al. [28] studied the use of CFRP, MMC, CMC, resin matrix composites in the aircraft engines, rocket motors, scramjet engines. Baroumes et al. [29] studied the usage of CMC in the scramjet engines.

From the discussion above, it has become evident that the ramjet engines easily show structural failure as it gets eroded due to the formation of exhaust gases. The use of composite materials with ceramic materials lining may reduce the erosion of the structure. Also, it can be identified that for the accommodation of high pressure at the inlet of the ramjet the uses low carbon mild steel can be used. In case of scramjet engines, the materials should have the properties such as lightweightness and high tolerance to cylindrical loads. The use of different composites such as CMC, MMC, and metal alloys in the make of the structure of scramjet engines can be proved beneficial. Additionally, Ti AL or any titanium alloys can be uses in the make of inlet, nozzle, and combustor section due to its lightweight property.

3.2 Heat Transfer in Scramjet Engines

The scramjet engines experience high friction from outside and high temperature due to combustion in the inside, so it is very necessary to find appropriate cooling techniques. Research around the globe is making continuous effort to find the optimum cooling technique for long flight duration. The following are some of the studies that discuss the different cooling techniques which will enhance the heat transfer mechanisms.

Zhang et al. [30] studied the thermal behavior on a 3D model of scramjet engines cooling channels for different aspect ratios. The study primarily focuses on the non-cracking zone of the cooling channels. The different aspect ratios are $\lambda = 1, 2, 4,$ and 8 were selection to carry out the simulations. The results obtained from the simulations indicate that heat transfer deterioration was seen due to the low mass flow rate of fuel. It is seen that increasing the aspect ratio significantly reduces the rate of heat transfer deterioration in scramjets. However, the high aspect ratio was not seen beneficial for lowering the wall temperature. Additionally, it was estimated that by increasing the operating pressure can improve the heat transfer rate for an appropriate aspect ratio.

Liang et al. [31] investigate the effects on heat transfer deterioration (HTD) of scramjet engines when it moves at hypersonic speeds. The study focuses on the heat transfer deterioration of n-decane for different flight acceleration. On analysis, two types of HTD, namely type 1 and type 2, were found. The HTD type 1 resulted in thermal boundary layer formation located at the initial section of the tube. The HTD type 2 resulted due to the reduction of turbulent diffusion causing M-shaped velocity profile. On varying the different flight acceleration, it was found that the type 2 HTD was proved stronger than type 1 HTD.

Jin et al. [32] investigate the usage of JP-10 slurry fuel containing nanoparticles of aluminum in a scramjet engine to understand the effects on the heat transfer characteristics. It was observed that the combustion of the slurry fuel containing aluminum nanoparticles in the combustor caused deposition on the inner walls of the engine. From the study of the surface deposition and heat transfer characteristics, it can be observed that convective heat transfer was dominant near the walls of the combustor. The average convective heat transfer coefficient for the slurry fuel was 28.74% higher than the pure fuel. Also, the wall heat flux was 31.85% higher for the slurry fuel than the pure fuel. Thus, it was concluded from the study that slurry fuel containing high wall friction coefficient results in high convective heat transfer coefficient. Additionally, the introduction of the rough surface on the walls changes the heat transfer characteristics resulting in enhancement of the convective heat transfer of the scramjet engine.

In order to improve the fuel air mixing in the combustor of the scramjet engine, Llobet et al. [33] showed the use of generated vortices with the motive to improve the efficiency of the scramjet engine. Llobet et al. used RANS numerical model of the T4 Stalker Tube under Mach 8 flow conditions to under vortex interaction in scramjet engine and compared with the experimental results. For the generation of

the vortices, canonical geometry consisting of flat plate plus a fin with compression angle was used. The comparative study of both experimental and simulation results shows a new approach in the heat transfer characteristics downstream. The heat transfer analysis in the wake region showed good agreement of the simulation results with the experimental results. The simulated results show the formation of counter-rotating vortex which results in low heat flux near the reattachment region. Thus, the vortex generation in the scramjet combustor with the help of injectors provides a new way for the heat transfer analysis in scramjet engines.

Chen et al. [34] attempt to find cause behind abnormal heat transfer for scramjet engines under regenerative cooling methods with supercritical n-decane usage computationally. To achieve the stated objective, different mass flow rates and heat fluxes are considered. The process of abnormal heat transfer is explained with the help of thermal diffusivity, velocity, and vortex evolution. From the evaluation of the simulation results, it was estimated that the temperature was rising with the increase in mass flow rate and heat flux. This abnormality in the heat transfer was observed to the generation of large buoyancy force inside the tube. This was the main reason for the temperature difference at the inlet. Additionally, the generation of small vortices causes heat transfer difference between fluid layers.

Sun et al. [35] developed a 3D model to study the heat transfer deterioration (HTD) in cooling channel of the scramjet engine with endothermic n-decane fuel. The simulations were processed with K-epsilon turbulence modeling to analyze the thermal stratification process in the channels. The simulation results indicate the density and viscosity variables play an important role in HTD phenomenon. It was estimated from the results that the low heat transfer coefficient and high wall temperature regions were found near the boundary. The HTD was found critical near the thermal boundary layer. Zhang et al. [36] developed a thermal protection system to meet the cooling requirements of hydrogen scramjet engines. The protection system consists of active and passive thermal protection system for safe operation under high velocities. The computationally study is progressed by using 1D-coupled heat transfer model for different Mach numbers and equivalent ratios. The study showed that the use of combined active and passive thermal protection system in scramjet engine increases the range of flight velocity with proper selection of materials. The over rise of temperature in the combustor can be avoided with the present system. Thus, the implementation of the combined passive and active thermal protection system is beneficial to avoid overheating in scramjet engines.

Zhang et al. [37] developed a 3D model of the coolant flow to study the thermal behavior inside the cooling channels for regenerative cooling channels in scramjet engines with the motive to identify the appropriate design parameters. To achieve the stated objective, different variables such as aspect ratios, flow area, and fin thickness were considered for the analysis. The simulation results the wall temperature can be reduced by implementing small flow area which in turn causes increase in pressure drop in the cooling channels. The regenerative cooling system in the scramjet engines causes the wall temperature to decrease for aspect ratio ranging from 1 to 8. However, the wall temperature rises with increase in aspect ratio. Thus, the optimal channel aspect ratio should be larger for smaller flow area to reduce the wall temperature.

Additionally, smaller fin thickness decreases the thermal diffusion coefficient which finally helps in wall temperature reduction and increase in pressure drop.

Song et al. [38] conducted an experiment for transpiration cooling using optical heating method in order to achieve a heat flux of 237 W/cm^2 . To investigate the transpiration effectiveness, Inconel tubes are used in the experiments. The analysis shows that transpiration cooling mechanism was able to remove large amount of heat from the engine walls which is beneficial for the scramjet engines.

The above literature discusses the different active cooling technologies used in scramjet engines, namely regenerative cooling, film cooling, transpiration cooling, and their combinations. From the literature, it can be concluded that regenerative cooling technology is a coolant-based forced convection heat transfer in the channels whereas film cooling is achieved by injecting the coolant through an inclined angle. Film cooling provides thermal protection to the walls. Another cooling technology is also discussed is the transpiration cooling which has been seen to have high efficiency as compared to the other two.

4 Conclusions

The ramjets and scramjet engines operate at supersonic speeds, and it is necessary that the selection of the materials and heat transfer cooling technologies should be selected consciously to eliminate structural failure. The paper focuses on reviewing the desirable materials and heat transfer properties which the objective to achieve stable working conditions.

Conclusions drawn on selection material properties from review work:

- To eliminate the erosion of the structure of ramjet engines, the use of composite materials with a lining of ceramic materials is suggested to reduce the erosion due to exhaust gases.
- Low-carbon mild steel materials can be used in inlet of the ramjet engines, as it accommodate high pressures.
- In the scramjet engines, the materials should be lightweighted and acceptable to high tolerance cylindrical loads.
- The use of composites such as CMS, MMC, titanium alloys in the combustor, nozzle, and inlet is suggested.
- The use of titanium is seen in many aircraft engine due to its mechanical properties. However, the titanium alloys have the ability to withstand the temperature up to 2000°C which is superior to use in scramjet engines than titanium.

Conclusions drawn related to heat transfer techniques in scramjet engines from reviewed work:

- Active cooling technology plays an important role for scramjet engines in achieving stable conditions.

- Regenerative cooling, film cooling, and transpiration cooling are the active cooling technologies that are used in scramjet engines.
- Some studies related to the use of endothermic hydrocarbon fuels are seen in regenerative cooling. The heat transfer characteristics under supercritical pressures are studied for active regenerative cooling.
- The studies also show the use of supersonic film cooling by varying flow area, temperature, pressure. Many numerical simulation studies with 3D modeling also discussed.
- Under different flow conditions, the heat and flow characteristics of transpiration cooling are also reviewed. The formation of shock waves creates blockage resulting in rise in temperature in the scramjet engines.

Acknowledgements The authors acknowledge the Computational Laboratory of Mechanical Engineering, Department of National Institute of Technology, Silchar and TEQIP-III for manifesting their support in completion the present work.

References

1. Efsic EJ (2002) Supersonic combustion ramjet propulsion engines
2. Fry RS (2008) A century of ramjet propulsion technology evolution. *J Propul Power* 20(1):27–58. <https://doi.org/10.2514/1.9178>
3. Soni RK, De A (2017) Investigation of strut-ramp injector in a Scramjet combustor: Effect of strut geometry, fuel and jet diameter on mixing characteristics. *J Mech Sci Technol* 31(3):1169–1179. <https://doi.org/10.1007/s12206-017-0215-0>
4. Pandey KM, Choubey G (2016) Computational simulation on the performance of Scramjet combustor using Multi-strut circular shaped injector. In: 52nd AIAA/SAE/ASEE Joint Propulsion Conference, 1–9. <https://doi.org/10.2514/6.2016-5097>
5. Wang H, Wang Z, Sun M, Qin N (2014) Experimental and numerical investigation of cavity-based supersonic flow and combustion. Proceedings of the Institution of Mechanical Engineers, Part G: Journal of Aerospace Engineering 228(5):781–798. <https://doi.org/10.1177/0954410013480300>
6. Gruber MR, Donbar JM, Carter CD, Hsu K-Y (2008) Mixing and combustion studies using cavity-based flameholders in a supersonic flow. *J Propul Power* 20(5):769–778. <https://doi.org/10.2514/1.5360>
7. Suneetha L, Randive P, Pandey KM (2019) Numerical investigation on mixing behavior of fuels in reacting and non-reacting flow condition of a cavity-strut based scramjet combustor. *Int J Hydrogen Energy* 44(31):16718–16734. <https://doi.org/10.1016/j.ijhydene.2019.04.262>
8. Liu Q, Baccarella D, Landsberg W, Veeraragavan A, Lee T (2019) Cavity flameholding in an optical axisymmetric scramjet in Mach 4.5 flows. Proceedings of the Combustion Institute 37(3):3733–3740. <https://doi.org/10.1016/j.proci.2018.08.037>
9. Mitani T, Kouchi T (2005) Flame structures and combustion efficiency computed for a Mach 6 scramjet engine. *Combust Flame* 142(3):187–196. <https://doi.org/10.1016/j.combustflame.2004.10.004>
10. Denman ZJ, Wheatley V, Smart MK, Veeraragavan A (2016) Fuel injection and mixing in a Mach 8 hydrocarbon-fuelled scramjet, 3–6
11. Masashi TMK (2020) Making lighter aircraft engines with titanium aluminide blades IHI Corporation 2020. Accessed: Oct. 31, 2021

12. Sjöberg G (2008) Aircraft engine structure materials. Volvo Aero Corporation (2008)
13. Beyer S, Schmidt-Wimmer S, Quring K, Wilhelmi C, Steinhilber M (2012) Technology status of fuel cooled ceramic matrix composites for dual-mode ramjet (DMR) and liquid rocket engine (LRE) applications. <https://doi.org/10.2514/6.2012-5877>
14. Tenney DR, Lisagor WB, Dixon SC (1989) Materials and structures for hypersonic vehicles. *J Aircr* 26(11):953–970. <https://doi.org/10.2514/3.45868>
15. Steelant J (2008) ATLLAS: aero-thermal loaded material investigations for high-speed vehicles. In: 15th AIAA International Space Planes and Hypersonic Systems and Technologies Conference. <https://doi.org/10.2514/6.2008-2582>
16. Bouchez M, et al (2014) Combustor and material integration for high speed aircraft in the European research Program ATLLAS2. <https://doi.org/10.2514/6.2014-2950>
17. Draper SL, Krause D, Lerch B, Locci IE, Doehnert B, Nigam R, Das G, Sickles P, Tabernig B, Reger N, Rissbacher K (2007) Development and evaluation of TiAl sheet structures for hypersonic applications. *Mater Sci Eng, A* 464(1–2):330–342. <https://doi.org/10.1016/j.msea.2007.02.020>
18. Sabarigirinathan RK, Kumar RS, UdhayaKumar M, Viswanath T, Sai Prasanna Kumar SJV (2016) Design fabrication and performance analysis of Subsubsonic Ramjet engines. *IRJET* 3(4):533–539. Accessed: Oct 31, 2021 [Online]. Available: <https://www.irjet.net/>
19. da Costa FJ, de Paula Toro PG, Rolim TC, Ponchio Camillo G, da Cunha Follador R, Minucci MAS (2012) Design of the Brazilian 14-X hypersonic aerospace vehicle”, 14th Brazilian congress of Thermal Sciences and Engineering
20. Zander F, Morgan R, Zander F, Morgan RG (2007) Transient heat analysis of a carbon composite scramjet combustion chamber laser diagnostics of hyper-velocity flows view project binary scaling laws for hypersonic flows view project transient heat analysis of a carbon composite scramjet Combustion chamber
21. Humphrey CC (2013) Design and fabrication of a ramjet inlet
22. Sharma, Mahajan A (2017) Prevention of erosion by introduction of ceramic matrix materials for ramjet nozzle. *Int J Aerospace Mech Eng* 4(3)
23. Zheng R et al (2014) Development of full scale ramjet nozzle with C/SiC ceramic matrix composite. *Ceram Trans* 248:681–694. <https://doi.org/10.1002/9781118932995.ch78>
24. da Costa FJ, Gilberto P, Toro P, Camillo GP (2013) Brazilian 14-X hypersonic waverider unpowered scramjet aerospace vehicle structural analysis at Mach number 7. In: 22nd International Congress of Mechanical Engineering (COBEM 2013)
25. Choubey G, Suneetha L, Pandey KM (2018) Composite materials used in Scramjet-A Review. *Materials Today: Proceedings* 5:1321–1326
26. Thong WC (2007) High temperature materials for hypersonic flight high temperature materials for hypersonic flight vehicles
27. Nishit T, Ulmek N (2018) Advanced composite materials used in scramjet engine
28. Ma J, Shen L, He Y (2018) Application of composite materials in engine. *Materials Science: Advanced Composite Materials*
29. Baroumes L, Bouillon E, Christin F (2004) An improved long life duration ceramic matrix composite material for jet aircraft engine application. In: 24th International Congress of the Aeronautical Sciences
30. Zhang S, Qin J, Xie K, Feng Y, Bao W (2016) Thermal behavior inside scramjet cooling channels at different channel aspect ratios. *J Prop Power* 32(1):57–70. <https://doi.org/10.2514/1.B35563>
31. Liang J, Liu Z, Pan Y (2016) Flight acceleration effect on heat transfer deterioration of actively cooled scramjet engines. *J Thermophys Heat Transfer* 30(2):279–287. <https://doi.org/10.2514/1.T4704>
32. Jin Y, Dou S, Wang X, Yang Q, Xu X, Pan L (2021) Effect of nano-sized aluminum additive on wall heat transfer characteristics of the liquid-fueled scramjet engine. *Appl Thermal Eng* 197. <https://doi.org/10.1016/j.applthermaleng.2021.117387>
33. Llobet JR, Basore KD, Gollan RJ, Jahn IH (2020) Experimental and numerical heat transfer from vortex-injection interaction in scramjet flow-fields. *Aeronaut J* 124(1280):1545–1567. <https://doi.org/10.1017/aer.2020.39>

34. Chen Y, Li Y, Sunden B, Xie G (2020) The abnormal heat transfer behavior of supercritical n-decane flowing in a horizontal tube under regenerative cooling for scramjet engines. *Appl Thermal Eng* 167. <https://doi.org/10.1016/j.applthermaleng.2019.114637>
35. Sun F, Li Y, Manca O, Xie G (2019) On assessment of heat transfer deterioration of a channel with supercritical n-decane for scramjet engines cooling. *Int J Heat Mass Transf* 135:782–795. <https://doi.org/10.1016/j.ijheatmasstransfer.2019.02.027>
36. Zhang C, Qin J, Yang Q, Zhang S, Bao W (2015) Design and heat transfer characteristics analysis of combined active and passive thermal protection system for hydrogen fueled scramjet. *Int J Hydrogen Energy* 40(1):675–682. <https://doi.org/10.1016/j.ijhydene.2014.11.036>
37. Zhang S, Feng Y, Zhang D, Jiang Y, Qin J, Bao W (2016) Parametric numerical analysis of regenerative cooling in hydrogen fueled scramjet engines. *Int J Hydrogen Energy* 41(25):10942–10960. <https://doi.org/10.1016/j.ijhydene.2016.03.176>
38. Song KD, Choi SH, Scotti SJ (2006) Transpiration cooling experiment for scramjet engine combustion chamber by high heat fluxes. *J Propul Power* 22(1):96–100. <https://doi.org/10.2514/1.11300>

Review on Enhancement of Thermal Capacity in Heat Exchangers with Various Nanofluids



Geeta Kumari, Susheel Kumar, K. M. Pandey, and B. R. Ramesh Babu

Abstract One of the most preferable modern technologies that have been invented to aid in the field of heat transfer purpose is the use of nanofluids in place of conventional fluids. The thermo-physical properties of nanofluids results in enhanced rate of heat transfer and that is why it has drawn the attention of researchers for more than a decade. Heat exchangers are broadly used in many areas of engineering field. There are many types of heat exchanger for example counter-shell and tube heat exchanger, plate type heat exchanger, spiral heat exchanger, etc. But it is cross flow heat exchanger works in a more effective manner with high rate of heat transfer. Efforts have been practiced to improve heat transfer rate in heat exchangers and to reduce transfer time and finally boost the energy utilization efficiency. The efforts generally include some passive and active methods like turbulence creation, exchange surface extension or the using fluids with better thermo-physical characteristics. Now-a-days, one of the most exclusively practiced methods for the increment of heat transfer rate in contrasting varieties of heat exchangers is the use of nanofluids. The objective of this review paper is to sum up the heat transfer improvement potential of nanofluids and the effect of its concentration and diameter on heat transfer enhancement.

Keywords Nanoparticles · Nanofluid · Cross-flow heat exchanger · Heat transfer enhancement · Thermo-physical properties

G. Kumari

Department of Management, Malla Reddy College of Engineering & Technology, Hyderabad, India

S. Kumar · K. M. Pandey (✉)

Mechanical Engineering Department, National Institute of Technology Silchar, Silchar, India
e-mail: kmpandey2001@yahoo.com

B. R. R. Babu

Prathyusha Engineering College, Chennai, India

1 Introduction

Cross flow heat exchangers exhibit a pivotal contribution in the refrigeration, air conditioning and ventilation system that needs heat to be transferred from one means of fluid to another. In cross-flow heat exchangers, working fluids flow at right angles to each other. The ascertainment of a model heat exchanger is on the basis of the kinds of various service conditions. It ought-to withstand various weather conditions that may not be favorable for its working, and also considering parts of fouling in the heat exchanger and various checks on the diameter, length, weight, and tube configuration on account of requirement of size of heat transfer or inventory consideration. Correspondingly, the improvement of overall system performance determined by design development of heat exchangers and its dependableness. To increase heat transfer capacity by increasing the Nusselt Number and effectiveness of heat exchangers, fins having high efficiency have been introduced. The conduction phenomenon in a heat exchanger can be obtained by utilizing the accurate measurement of convective heat transfer correspondence on the basis of least-squares that can only be applied to the flow characteristics and LMTD, i.e., logarithmic mean temperature difference. After that Numerical mode could be used for the execution of a heat exchanger through the use of Simulation (ANSYS-FLUENT), and also using Artificial Neural Network (ANN) as a tool, for modeling, validation and for justifications of results. A nanofluid means those fluids that contain nanometer-sized metal or non- metal particles, called nanoparticles that form a colloidal suspension in a base liquid. Conventional fluids like deionized (DI) water, ethylene glycol (EG), etc. which are used as usual working fluids in various heat transfer applications have innate low thermal conductivity than that of metals as well as metal oxides. Therefore, solid nanoparticles (Np) are added to the conventional fluids to improve their thermal conductivity. The resultant of this suspension is termed as nanofluid. This term was coined by Choi of the Argonne National Laboratory, U.S.A. in the year 1995 [1]. So, nanofluids means nano-sized powders of metal or non-metal having sizes less than 100 nm suspended in a base liquid.

Present day nanotechnology provides new windows to process and fabricate materials with crystal sizes typically below 50 nm [2]. The different types of nps that have been used for improving thermal conductivity are copper oxide, alumina trioxide, titanium dioxide, silver, diamond, etc.

Basically, there are two elemental methods of producing nanofluids; one is the single- step direct evaporation procedure and the other is the two-step method. The one-step method comprises direct evaporation and then condensation of the solid nano-sized particles in the conventional liquid for making the stable nanofluids. In the second method, the nps, obtained by some other methods are dispersed into the conventional liquid [3, 4]. In an evaluation by Wang et al. [5], the two-step procedure is universally used for synthesizing of nanofluids from the available commercially supplied nano powders. In this procedure, at first the nps were produced and after that these were dispersed in the base fluids. Ultrasonic machines are commonly used for dispersing the particles and reducing the agglomeration of solid particles. After their

preparation; various measures are to be taken before their use in experiments of its heat transfer characteristics. Several tests should be done for their characterization and functionalization. Some of the commonly used tests are x-ray diffractometry, FTIR, TEM, TGA, and Raman spectroscopy. Details vary according to the material type.

2 Literature Review

Gao and Geer [1] had performed a fractional characterization of cross flow heat exchangers for determining the ephemeral answer of the mass flow rate and the corresponding temperature of fluid at inlet with stepwise changes. By differing minimum fluid capacity, i.e., C_{min} no significant change in the behavior of fluid temperature at outlet was recorded. For enhancing the efficiency and optimizing the frame of heat exchanger, a total factual course of action of ephemeral analysis's given for the heat exchanger. Fadare and Fatona [2] used MATLAB as tool alongside used Artificial Neural Network technique for mapping and evaluating the performance factors such as heat transfer coefficient, thermal capacity, effectiveness of multi pass, multi tube heat exchangers. The results obtained by the ANN numerical analysis validated the results obtained from the experimental analysis. Their study showed how ANN can be utilized as a modeling technique to get results that are comparable with experiment results. Brabin and Ananth [6] had surveyed investigational setting of split flow heat exchanger. The heat exchanger performance was investigated by the use of Aluminum oxide (Al_2O_3) with the conventional fluid like pure water, or even a matter of fact with ethylene glycol, by forming their mixture. Their thermal properties are determined. The results exhibited that the heat transfer properties were improved for mixture of ethylene glycol and water used as cooling fluid, as compared with using only pure water as cooling fluid. Ravi Kumar et al. [7] surveyed cross-flowing heat exchangers by differing height of fins by employing Numerical Simulation using Computational Fluid Dynamics. It was observed that heat transfer rate reduces with the increase in fins height. Crane and Jackson [8] conducted experiments on heat recuperation. It is the heat that is generally wasted in cross flow heat exchanger at the hot fluid outlet. The heat recuperation was obtained through air cooling with segments of Bi_2Te_3 . More than 40 W/l of power density can be attained from heat exchangers comprising Bi_2Te_3 as thermo-electric material. Moreover, there was a need of evaluating methods to use thermo-electric materials in heat exchangers to provide better heat recuperation. Chad Harris et al. [9] analyzed that the heat transfer in case of a cross flow micro heat exchanger became more extensive when the transfer of heat occurs from fluids (e.g., water-glycol) to gases (e.g., air) for some prevailing fore region pressure drop for every liquid having normal values for conventional scale heat exchangers. Thermal diffusion lengths were found to be decreased in cross flow micro heat exchangers when micro channels were used which in turn increased the heat transfer or volume. When comparisons were made to conventional cross flow heat exchangers, micro heat exchangers exhibit improved result with regard

to heat transfer rates or volume and what not. LIGA, sequence and bonding were being used for manufacturing plastic heat exchanger of cross flow type. Alotaibi et al. [10] in their study of single pass heat exchanger with varying inlet conditions such as ambient temperature, pressure. The heat exchanger tube carries water inside and the air is flowing over the tubes to cool the heat exchanger. Numerical analysis showed that the effectiveness of the heat exchanger can be controlled by adjusting the water flow rate, the inlet air temperature and the inlet water temperature. Tan et al. [11] using artificial neural network predicted the properties of individual fluid stream flowing inside the heat exchanger, their results suggested that performance of compact heat exchanger can be numerically calculated by using neural network model. Panchal [12] analyzed the affects of temperature distribution in case of multi pass heat exchanger, they found that temperature difference between fluids can increase the mixing efficiency of air over the water tubes and also increases the air side velocity thereby increasing the heat transfer efficiency of heat exchanger. Meikandan et al. [13] did numerical studies and developed a model neural network to identify the effects of fouling factor in the cross flow heat exchanger; experimental results verified his numerical results and showed that the increase in mass flow rate in case of fouling increases the heat transfer coefficient in heat exchanger. His model also suggested that numerical analysis gave identical results as compared to the experimental analysis of heat exchangers. Mohammed et al. [14] in their study instead of focusing on design od heat exchangers for better heat transfer characteristics, tried to focus on the properties of nanofluids used, such as type of nanofluid, its physical and chemical and thermal attributes. The used micro channels for the use of nanofluids unlike the traditional water-based system in heat exchanger. And although because of the use of micro channels there was a significant pressure drop associated, the increase in heat transfer coefficient compensates for this pressure drop. Sohani et al. [15] studied indirect evaporative cooling in heat exchangers, they developed GMDH model, which helps in analyzing air properties such as dew point temperature, exit temperature, humidity present in air. Upon investigating in 12 cities all having different weather conditions they classified cities in four major categories. They found that with the increase in humidity or decrease in inlet air temperature leads to decrease in optimized velocity of air, also the optimized WAR decreases with decrease in humidity and temperature of ambient inlet air. On an average of these 12 cities they found that Coefficient of performance is increased by 8.9% and average annual Cooling Capacity increases by 6.9%. Wu et al. [16] used artificial neural network named as GABP model and compared the results obtained with BP model. It was found that performance of cross flow heat exchanger in cooling tower using GABP model was much higher and more accurate as compared with the BP model. GABP model took input parameters of heat exchanger and gave output as dry bulb temperature, heat absorbing capacity etc. It also predicted the mass transfer properties of the heat exchanger used in the cooling tower. Shah et al. [17] using CFD modeling and simulations analyzed bundled cross flow heat exchanger. The bundle type of heat exchanger is aligned at various angles. CFD simulations results in correlations between the different angles and the heat transfer capacity. One important finding that they reported was that the pressure drop also depended on the angle of

arrangement, and pressure drop at 60° was much different than that of 45° . Aasi et al. [18] used three fluid heat exchanger along the cross flow. The purpose of their study was to relate the non-uniformity during flow to the efficiency of heat exchanger. It was found that the effect of non-uniformity in flow is dominant in turbulent region of flow and not so significant in the laminar region. And among all the three fluids there is a combination which drastically affects the capacity or the efficiency of cross flow heat exchanger. Also the non-uniformity in horizontal direction affects more as compared to the longitudinal direction of flow. Jha and Bhaumik [19] demonstrated CFHT type heat exchangers which are compact cross flow helical tube type, using air as cooling mechanism for the heat exchanger. The results showed that Reynolds number increased almost twice because of the reflection phenomenon due to the compact helical shape of the tube. Also dead zones which were earlier observed in straight tubes are now diminished. Since air is used for cooling mechanism there's a significant amount of pressure drop noted in the air side of the heat exchanger. Vargas and Bejan [3] said that for any complex geometrical analysis it should be modeled as something small but comparable. Thus they modeled the fins of heat exchangers that are mounted above aircrafts with the heat exchangers having smooth plates. This geometrical optimization can be used in system such as ship, heavy machinery etc. Kang and Tseng [20] analytically studied the correlation between rates of heat transfer and pressure drop in case of micro heat exchanger. Results showed that for same effectiveness the pressure drop and heat transfer rate is affected by the average temperature of the cold side and hot side of flow in heat exchanger. Also the size of heat exchanger and the type of material used significantly affected these two properties, for example when copper is used for heat exchanger material the thermal conductivity increased to 400 W/mK as opposed to 148 W/mK . Hajabdollah and Seifoori [21] analyzed the undesirable flow patterns that occurs in the optimal design of heat exchangers. They took consideration of six factors that includes heat exchanger effectiveness, fins efficiency, heat transfer coefficient, total annual cost, inlet profiles viz. linear, parabolic and power law model. Results showed the feasible and optimized design of cross flow heat exchanger with a reduction in total cost and increase in heat exchangers effectiveness. Triboix [22] suggested the formula for finding out NTU, i.e., number of transfer units and the effectiveness of cross flow heat exchanger in the case where fluids do not mix with each other in single pass. Dixit and Ghosh [23] analyzed the affects of ambient surroundings on the performance of heat exchangers. In application like cryogenics the effectiveness of heat exchanger seems to have paramount importance therefore how the heat exchanger interacts with surroundings is important. The results showed that when the ambient temperature is higher than both cold and hot fluid, effectiveness of hot fluid depends inversely on heat leaking out and that for the cold fluid is directly proportional to the heat entering inside. The direction of heat flow through exchanger depends on the temperature difference between fluids and ambient conditions, which in turn decides the heat exchanger performance. Cross flow heat exchanger best replicated the counter current flow type heat exchanger when heat conductance ratio is on the lower side. Nuntaphana et al. [24] modeled 23 different types cross flow heat exchanger having spiral arrangements and monitored the effects of tube diameter,

fins length and heights on the thermal capacity of heat exchanger. Results showed that for inline arrangements of heat exchanger with increase in tube diameter the pressure drop across also increases but the net heat transfer coefficient associated with it reduces. Similar results occurred if we increased the length of fins in heat exchanger. However there's one arrangement in which the pressure drop is not significant and also the heat transfer coefficient increases significantly the arrangement was called staggered arrangement of heat exchanger. Heris et al. [25] experimented using square cross section ducts in heat exchangers, although the pressure drop in square cross section type ducts is much less as compared to the circular ducts the square duct also reduces the thermal capacity and heat exchangers effectiveness. In their study they tried to enhance the effectiveness of square duct heat exchanger by using Al₂O₃ nanoparticles suspended in water. By varying the concentrations of nanoparticles they obtained that up to 27.6% of enhancement in heat transfer coefficient can be achieved using 2.5% of concentration of nanoparticles as compared with the pure water as base fluid. Results also showed that there is an decrease in wall temperature and increase in heat exchangers effectiveness if the mass flow rate is increased. Magazoni et al. [26] developed numerical simulation technique for cross flow heat exchangers to evaluate thermal properties related to the heat exchangers. The comparison can be made with various types of heat exchangers having single pass and multiples passes, parallel as well as cross flow heat exchangers. Results showed that errors decreases as the number of transfer units NTU increased. Cabezas-Gomez et al. [27] developed new type of flow arrangement as opposed to the traditional multi pass heat exchanger systems. In this new system, fluid flows in two tube circuits, each tube circuit consists two tube lines. the new system is compared with standard two pass cross flow heat exchanger by varying NTU's, different capacity ratios. And results showed that the new proposed heat exchanger system delivers higher entropy generation, higher efficiency and higher thermal capacity over a wide range of input parameters. The scope of these new systems can be realized in automotive industries and refrigeration systems. Kotcioglu et al. [28] studied the second law of thermodynamics related to entropy generation and its relation with fluid friction and heat transfer in cross flow heat exchangers. It was found the irreversibility in the fluid flow inside the heat exchanger decreases with increase in fluid flow velocity. And by decreasing irreversibility in flow higher heat transfer coefficient can be achieved which in turn increases the effectiveness of the cross flow heat exchanger. For proper mixing of fluid flow to reduce irreversibility they introduced a new kind of mixer called as CDLVG which means convergent divergent longitudinal vortex generator. Ogulata and Doba [29] in their experiment manufactured plate type cross flow heat exchanger mainly because it has the highest waste water heat recovery. The idea here is that they wanted to minimize the entropy generation inside the heat exchanger, which in turns decreases various frictional as well as heat transfer losses, thereby increasing the effectiveness of the heat exchanger. They achieved the desired results by varying various parameters such as optimum path length which means the size and area of the heat exchanger, Other parameters included dimensionless mass velocity flow and temperature difference. Gupta and Das [4] investigated the second law of thermodynamics, in consideration with back mixing flow at the exit fluid of a cross

flow heat exchanger. The results showed promises of utilizing the exergy of exit fluid from heat exchanger, results indicated that while destruction of exergy of the outlet fluid decreases the effectiveness of heat exchanger it also influence the maximum entropy paradox of second law of thermodynamics. San and Jan [30] utilized the concept of second law and incorporated the exergy concept in wet cross flow heat exchanger. By monitoring the performance of this heat exchanger with different atmospheric weather conditions, they found out that the effectiveness of wet cross flow heat exchanger is more in winter condition when surrounding temperature at outlet is lower as compared to the summer conditions. Wen et al. [31] used finite volume expression to develop a correlation between air and liquid flow rate, on heat transfer coefficient for a cooling tower as sink and heat source. They concluded that the effect of air and liquid mass flow rate is very much significant in increasing heat transfer coefficient as compared to the inlet temperature of air and liquid. Sozen et al. [32] used Alumina or fly ash debris nanoparticles suspension in both parallel flow and cross flow heat exchanger, results indicated that there is a 5.8% increase in effectiveness of heat exchanger by using nanofluid suspension as compared to the conventional water-based system in heat exchanger. Their study also gave scope to using metal oxides nanoparticles suspension to be used in heat exchangers to enhance the thermal conductivity and heat transfer coefficient in heat exchangers. Lalot and Palsson [5] developed a method for early detection of fouling in a cross flow heat exchanger without raising any false alarms. By using numerical techniques and creating a neural network of collected data points of both the clean and fouled heat exchanger, through regression and correlation they trained the neural networks to detect fouling as early as possible, thereby increasing the effectiveness of a heat exchanger. Starace et al. [33] found that whole scale computational analysis of heat exchanger is very much costly and leads to over sizing and overestimation, so they developed a Hybrid approach that focuses on iterative approach on determining the heat transfer coefficients on either the hot side or the cold side. And this iteration is found valid for the whole heat exchanger in increasing the effectiveness by focusing on just the parts where there is higher energy flux present. It was found that heat transfer rate is higher on the cold inlet side and cold outlet side, thereby, favoring the cold side. Thus our focus should be on the hot side of the heat exchanger geometry to improve the heat transfer rate. Ranjbarzadeh et al. [34] in their experimental set up used Graphene oxide water-based nanofluid system with varying concentrations. Tests were conducted in subsonic wind tunnels, with varying Reynolds Number. Key results suggested that there is an 21% increase in the friction factor and 51.4% improvement in Nusselt Number, an although there is a pressure drop the overall effect of the nanofluid suspension is that it increases the heat transfer coefficients by 42.2% as compared with pure water-based system. Navarro and Cabezas-Gomez [35] used computational program to evaluate the thermal efficiency of cross flow heat exchangers, this computational technique was further utilized to improve the performance of heat exchangers. Al Nahian et al. [36] analyzed cross flow heat exchanger using various concentrations of nanofluids along with changing the base fluid, they used Cu-water, Al_2O_3 -water to analyze the effects of changing the nanoparticle, and they used Al_2O_3 -ethyl glycol and Al_2O_3 -water to analyze the effects of changing

the base fluid. They altered the concentrations to arrive at various conclusions one of which was, that Cu-water has the highest thermal conductivity, and with the increase in Reynolds number there is an increase in heat transfer coefficient. Singh et al. [37] used Al_2O_3 -ethyl glycol nanofluid system alongside pure water-based system for comparison and to find out the thermal performance. In their study they found that the overall heat transfer coefficient along with thermal conductivity and viscosity is increased when we use nanofluid system instead of pure water base system. Kadhim et al. [38] used Magnesium Oxide (MgO) as nanofluid and Pyrex glass having dimension $(250 \times 500 \times 1200)$ heat exchanger. They concluded that with increase in nanoparticle concentration there is an increase in density, viscosity but although the rate of heat transfer increased there is a decrement in specific heat. Ionescu and Neagu [39] used COMSOL software-based an Finite Element Method technique to evaluate the performance of cross flow micro heat exchanger, they used Al_2O_3 -water-based nanofluid system varying the concentration, and comparing with pure water-based system, they found that using higher concentrations of Al_2O_3 -water nanofluid suspension with greater mass flow rate, there is an increase in heat transfer characteristics as well as rise in pressure drop alongside higher friction factor. Chennu et al. [40] in their analysis used Al_2O_3 -water-based nanofluid system in a compact type cross flow heat exchanger. They found that for a constant temperature and flow rate, almost 13% of increase in heat transfer coefficient, and pressure drop can be obtained just by varying the mass flux.

2.1 Thermal Conductivity

Increasing the level of concentration tends to increase the thermal conductivity of nanofluids as reported by Pak and Cho [41], Xuan and Li [42] Xuan and Roetzel [43], Heris et al. [44]. Various experiments were conducted using the mixture of water and nanoparticles of Copper (Cu), Titanium Dioxide (TiO_2), Copper Oxide (CuO), and Aluminum Oxide (Al_2O_3). Results showed that Aluminum oxide nanoparticles show the maximum heat transfer as greater than 40%. Bhattacharya et al. [45] with the help of modeling simulated the effects of concentration in increasing the thermal conductivity. Lee et al. [46] found that the dispersion medium plays an important role, as these liquids play the role of base fluid; they observed that nanoparticles, when mixed in water, oil, or ethyl glycol, tend to increase the thermal conductivity ratios of the medium and decrease these ratios in the base fluid. The magnitude of solid–solid interactions and volume concentration is taken care of by the mass equilibrium of the suspension; these properties are greatly affected by the value of pH, particulate shape and size, and surface additives. It is being noticed that two main kinds of accumulation or connection happen in nanofluids. The primary connection happens when nanoparticles are joined through the strong point of solid boundary layer interactions, which, as depicted by Prasher et al. [47] is one of the main reasons for the increase in thermal; conductivity. Timofeeva et al. [48], studied silicon carbide (SiC), nanoparticles in two types of dispersion mediums. One is water, and the other

one is ethyl glycol, what they found is that the thermal conductivity ratio is almost 5% higher in ethyl glycol suspension as compared to the water suspension. Lower the thermal resistance of the base fluid in the suspension, the better the thermal conductivity of the nanofluid system. And a water-based nanofluid system gives lower thermal resistance to base fluid as compared to ethyl glycol nanofluid system. Wang [49] investigated the method of finding thermal conductivity of nanofluid suspension systems using transient hot wire system. In the suspension system the nanoparticles experiences various forces such as Van-der Waals forces of attraction, electrostatic forces between ions and dipoles, Brownian motion etc., these forces along with microstructure of nanoparticles affects the thermal conductivity and viscosity of the nanofluid system.

2.2 Viscosity

The measurement of rheological properties of nanofluids was done by Dong and Leyuan [50] and Prasher et al. [47]. It has been seen that with increase in the size of diameter of ethyl glycol or water suspension there has been a significant increase in viscosity. But keeping the volume concentration constant the increase in viscosity is greater in water-based nanofluid suspension as compared to the ethyl glycol suspension Timofeeva et al. [48]. Based on basic equation of Einstein for solid interfaces the increase in viscosity should not depend on the base fluid of suspension and only varies with the volume concentration Vold et al. [51]. Nguyen et al. [52] used Viscometers for measurement of viscosity in nanofluid suspension system.

2.3 Heat Transfer Enhancement

Li and Xuan [53] and Sundar and Sharma [54] investigated the water-based Aluminum oxide nanofluid system, numerical studies with the help of finite volume inside a circular tube is considered along with boundary conditions of steady state and turbulent flow. Results obtained showed the relationship between increase in heat transfer with high Reynolds Number and increased volume concentration.

Shuichi [55] studied the heat transfer inside horizontal circular tube with forced convection having constant and uniform heat flux as boundary conditions, and concluded that because of the nanoparticles dispersed in the suspension increases the heat transfer. Various experimental works considering forced convection heat transfer was done using different nanofluid systems. The most prominent systems were Cu-water, Al_2O_3 -water and TiO_2 -water nanofluid systems. Considering thermal conductivity, Cu-water-based system showed the highest increase in heat transfer. And although the increase in thermal conductivity for Al_2O_3 -water and TiO_2 -water nanofluid systems was comparable, the increase in heat transfer was much greater in Al_2O_3 -water than TiO_2 -water nanofluid system. Ferrouillat [56] and Vijaya Lakshmi

et al. [57] found out that in case of turbulent flow having constant average velocity the heat transfer coefficient of pure water was greater as compared to Al₂O₃-water then TiO₂-water nanofluid systems. Thus, Suresh et al. [58] developed an hybrid nanofluid system to increase the heat transfer coefficient in case of fully laminar flow. Experimental results between pure water and Cu-Al₂O₃ in water nanofluid system having volume concentration equals to 0.1% showed that at Reynolds Number of 1730, the nanofluid system showed an increase of 13.56% in heat transfer coefficient, and also higher friction factor.

Various studies represented the increase in heat transfer coefficient as Dittus-Boelter Eq. (1):

$$Nu = 0.032 \times Re^{0.8} \times Pr^n \quad (1)$$

where, n is 0.4 for heating and 0.3 for cooling.

Pak and Cho et al. [41] showed the increase in heat transfer coefficient was almost upto 45% by increasing the volume concentration up to 1.34% in Al₂O₃-water nanofluid system in case of turbulent fluid flow. They also gave the relation for heat transfer coefficient in terms Reynolds Number and Prandtl Number Eq. (2).

$$Nu = 0.021 \times Re^{0.8} \times Pr^{0.5} \quad (2)$$

Xuan and Li [59] verified earlier work of pak & cho and showed that heat transfer coefficient increases by 40% by using nanofluid systems in convection heat transfer in horizontal tube. They gave the relation as shown in Eq. (3).

$$Nu = 0.4328(1.0 + 11.285\phi^{0.75} + Pe^{0.218})Re^{0.3333}Pr^{0.4} \quad (3)$$

Yang et al. in his experimental study concluded that heat transfer coefficient is affected by all of the followings be it nanoparticle material, its volume concentration or the base fluid in which it is dispersed.

3 Conclusion

In this era of Nano technology and miniaturization using nanofluids for the cooling prospect of various heat exchangers seems a quite interesting as well as challenging idea. For many decades' various methods were developed and incorporated for cooling of cross flow heat exchangers, but for the past few years' researchers are now focusing on using nanofluids suspensions for the purpose, using various numerical techniques and CFD analysis researchers developed various combinations and parameters that helps in increasing heat transfer coefficient of cross flow heat exchangers.

Some general inferences made during various experimental and numerical analyses are:

1. Thermal conductivity is increases by using nanoparticles dispersed in water making a nanofluid suspension.
2. With increase in volume concentration Viscosity also increases.
3. With increase in Reynolds Number Friction factor also increases.
4. With the increase in volume concentration and Reynolds Number, the value of Nusselt number which is heat transfer coefficient also enhances.

Although use of nanofluids seems promising but it comes with various drawbacks, some of which are poor properties of suspensions, disagreement among researchers for results obtained, improper understanding of the theory related to as to why the properties changes when nanoparticles are used. Future studies can include the use of various metallic nan particles having different shapes and size along with different suspensions for the enhancement of heat transfer coefficient. In the field of air conditioning and refrigeration nan fluids can be researched to increase the heat transfer characteristics of evaporators and condensers making them more efficient.

References

1. Gao T, Geer J (2015) Review and analysis of cross flow heat exchanger transient modeling for flow rate and temperature variations. *Trans ASME*041017-10, pp 1–10
2. Fadare DA, Fatona AS (2008) Artificial neural network modeling of heat transfer in a staggered cross-flow tube-type heat exchanger. *Pacific J Sci Tech* 9(November), pp 317–323
3. Vargas JVC, Bejan A (2001) Thermodynamic optimization of finned cross flow heat exchangers for air craft environmental control systems. *Int J Heat Fluid Flow* 22:657–665
4. Gupta A, Das SK (2007) ‘Second law analysis of crossflow heat exchanger in the presence of axial dispersion in one fluid. *Energy* 32:664–672
5. Lalot S, Palsson H (2010) Detection of fouling in a cross-flow heat exchanger using a neural network-based technique. *Int J Thermal Sci* 49:675–679
6. Brabin TA, Ananth S, Analysis of overall heat transfer coefficient and effectiveness in split flow heat exchanger using nano fluids. *J Adv Mech Eng Sci (JAMES)*, 28–40
7. Ravikumar K, Raju N, Saheb M (2017) CFD analysis of a cross-flow heat exchanger with different fin thickness. *Int J Dyn Fluids* 13(2):345– 362
8. Crane DT, Jackson GS (2003) Optimization of cross flow heat exchangers for thermoelectric waste heat recovery. *Energy Conv Manag*, 1–18
9. Harris C, Despa M, Kelly K (2000) Design and fabrication of a cross flow micro heat exchanger. *J Micro Electro Mechanical Syst* 9:502–508
10. Alotaibi S, Sen M, Goodwine B, Yang KT (2003) Controllability of crossflow heat exchangers. *Int J Heat Mass Trans* 47:913–924
11. Tan CK, Ward J, Wilcox SJ, Payne R (2009) Artificial neural network modelling of the thermal performance of a compact heat exchanger. *Appl Thermal Eng* 29(17–18):3609, 1–15
12. Panchal A (2018) Thermal analysis of multi-pass cross flow heat exchanger. 1–111
13. Meikandan M, Sundarraj M, Yogaraj D, Malarmohan K (2018) Experimental and numerical investigation on bare tube cross flow heat exchanger-using COMSOL. *Int. J Ambient Energy*, 2162–8246
14. Mohammed HA, Bhaskaran G, Shuaib NH, Saidur R (2011) Heat transfer and fluid flow characteristics in microchannels heat exchanger using nanofluids: a review. *Renew Sustain Energy Rev* 15:1502–1512

15. Sohani A, Sayyaadi H, Hoseinpoori S (2016) Modeling and multi-objective optimization of an M-cycle cross-flow indirect evaporative cooler using the Group Method of Data Handling type neural network. *Int J Refrigeration*, 1–59
16. Wu J, Zhang G, Zhang Q, Zhou J, Wang Y (2011) Artificial neural network analysis of the performance characteristics of a reversibly used cooling tower under cross flow conditions for heat pump heating system in winter. *Energy Buildings* 43:1–5
17. Kush KNS, Priyank VM, O Yadav DPC (2013) CFD analysis of heat exchanger over a staggered tube bank for different angle arrangement of tube bundles. *Int J Eng Res Tech (IJERT)*, 1–5
18. Aasi HK, Mishra M (2020) Influence of flow non-uniformity on the dynamic behavior of three-fluid cross-flow compact heat exchanger. *Int J Thermal Sci* 149:106177
19. Jha VK and Bhaumik SK (2020) Enhanced cooling in compact helical tube cross-flow heat exchanger through higher area density and flow tortuosity. *Int J Heat Mass Transf*, 1–14
20. Kang S-W, Tseng S-C (2007) Analysis of effectiveness and pressure drop in micro cross-flow heat exchanger. *Appl Therm Eng* 27:877–885
21. Hajabdollahi H, Seifoori S (2016) Effect of flow Maldistribution on the optimal design of a cross flow heat exchanger. *Int J Thermal Sciences* 109:242–252
22. Triboix A (2009) Exact and approximate formulas for cross flow heat exchangers with unmixed fluids. *Int Commun Heat Mass Transfer* 36:121–124
23. Dixit T, Ghosh I (2013) Two-stream cross flow heat exchangers in thermal communication with the surroundings – A generalized analysis. *Int J Heat Mass Transf* 66:1–9
24. Nuntaphana A, Kiatsiriroatb T, Wang CC (2005) Air side performance at low Reynolds number of cross-flow heat exchanger using crimped spiral fins. *Int Commun Heat Mass Transfer* 32:151–165
25. Zeinali Heris S, Nassan TH, Noie SH, Sardarabadiand H, Sardarabadi M (2013) Laminar convective heat transfer of Al_2O_3 /water nanofluid through square cross-sectional duct. *Int J Heat Fluid Flow* 44:375–382
26. Magazoni FC, Cabezas-Gomez L, Alvarino PF, Saiz-Jabardo JS (2018) Closed form relationships of temperature effectiveness of cross-flow heat exchangers. *Thermal Sci Eng Prog*, pp 1–34
27. Cabezas-Gomez L, Navarro HA, de Godoy SM, Campo A, Saiz-Jabardo JS (2009) Thermal characterization of a cross-flow heat exchanger with a new flow arrangement. *Int J Thermal Sci* 48:2165–2170
28. Kotcioglu I, Caliskan S, Cansiz A, Baskaya S (2010) Second law analysis and heat transfer in a cross-flow heat exchanger with a new winglet type vortex generator. *Energy*, pp 3686–3695
29. Ogulata RT, Doba F (1997) Experiments and entropy generation minimization analysis of a cross-flow heat exchanger. *Int J Heat Mass Transf*, pp 373–381
30. San J-Y, Jan C-L (2000) Second-law analysis of a wet crossflow heat exchange. *Energy*, pp 939–955
31. Wen X, Liang C, Zhang X (2012) Experimental study on heat transfer coefficient between air and liquid in the cross-flow heat-source tower. *Build Environ* 57:205–213
32. Sozen A, Variyenli HI, Ozdemir MB, Guru M, Aytac I (2015) Heat transfer enhancement using alumina and fly ash nanofluids in parallel and cross-flow concentric tube heat exchangers. *J Energy Ins*, 1–11
33. Starace G, Fiorentino M, Longo MP, Carluccio E (2016) A hybrid method for the cross flow compact heat exchangers design. *Appl Thermal Eng*, 1–25
34. Ranjbarzadeh R, Meghdadi Isfahani AH, Afrand M, Karimipour A, Hojaj M (2017) An experimental study on heat transfer and pressure drop of water/graphene oxide nanofluid in a copper tube under air cross-flow: applicable as a heat exchanger. *Appl Thermal Eng* 125:69–79
35. Navarro HA, Cabezas-Gomez L (2005) A new approach for thermal performance calculation of cross-flow heat exchangers. *Int J Heat Mass Transf* 48:pp 3880–3888
36. AlNahian J, Pandit PP, Mamun MAH (2019) Numerical study of a crossflow heat exchanger to investigate thermal performance using nanofluids. In: *AIP Conference Proceedings* 2121, 070020

37. Singh A, Gangacharyulu D, Sharma S, Study of heat transfer of aluminum oxide in water and ethylene glycol based nano fluid in a single pass multi tube cross flow heat exchanger. *IJERT* 5(8). ISSN: 2278-0181
38. Kadhim ZK, Kassim MS, Abdul Hassan AY, Effect of (Mgo) Nanofluid on heat transfer characteristics for integral finned tube heat exchanger. *Int J Mechanical Eng Tech (IJMET)* 7(2)
39. Ionescu V, Neagu AA (2018) Numerical simulation of Al₂O₃ – water nano fluid effects on the performance of a cross flow micro heat exchanger. *Mater Sci Eng* 400:042032
40. Chennu R, Rao R, Veeredhi (2019) Measurement of heat transfer coefficient and pressure drops in a compact heat exchanger with lance and offset fins for water based Al₂O₃ nano-fluids. *Heat Mass Transf*, 250
41. Pak BC, Cho YI (1998) Hydrodynamic and heat transfer study of dispersed fluids with submicron metallic oxide particles. *Experimental Heat Transf* 11:151–170
42. Xuan Y, Li Q (2000) Heat transfer enhancement of nanofluids. *Int J Heat Fluid Flow* 21:58–64
43. Xuan Y, Roetzel W (2000) Conceptions for heat transfer correlation of nanofluids. *Int J Heat Mass Transf* 43:3701–3707
44. Heris SZ, Etemad G, Esfahany MN (2006) Experimental investigation of oxide nanofluids laminar flow convection heat transfer. *Int Commun Heat Mass Transfer* 33:529–535
45. Bhattacharya P, Saha SK, Yadav A, Phelan PE, Prasher RS (2004) Brownian dynamics simulation to determine the effect thermal conductivity of nanofluids. *J Appl Phys* 95:6492–6494
46. Lee S, Choi SUS, Li SA, Eastman JA (1999) Measuring thermal conductivity of fluids containing oxide nanoparticles. *J Heat Transfer* 121(2):280–289
47. Prasher R, Song D, Wang J, Phelan P (2006) Measurements of nanofluid viscosity and its implications for thermal applications. *Appl Phys Lett* 89(13):133108
48. Timofeeva EV, Yu W, France DM, Singh D, Roubort J L (2010) Base fluid and temperature effects on the heat transfer characteristics of SiC in EG/H₂O and H₂O nanofluids. *J Appl Phys*, 109.
49. Wang Z (2009) Thermal wave in thermal properties measurements and flow diagnostics: with applications of nanofluids thermal conductivity and wall shear stress measurements. PhD thesis, Oregon State University
50. Dong L, Leyuan Y (2010). Single-phase thermal transport of nanofluids in a minichannel. Department of Mechanical Engineering University of Houston Houston, TX 77004-4006 USA
51. Vold IMN, Kristiansen KA, Christensen BE (2006) A study of the chain stiffness and extension of alginates, in vitro epimerized alginates, and periodate oxidized alginates using size-exclusion chromatography combined with light scattering and viscosity detectors. *Biomacromol* 7(7):2136–2146
52. Nguyen C, Desgranges F, Galanis N, Roy G, Mare T, Boucher S, Angue M (2008) Viscosity data for Al₂O₃water nanofluid-hysteresis: is heat transfer enhancement using nanofluids reliable? *Int J Therm Sci* 47(2):103–111
53. Li Q, Xuan Y (2002) Convective heat transfer and flow characteristics of Cu-water nanofluid. *Sci China Series E: Tech Sci* 45(4):408–416
54. Syam Sundar L, Sharma KV (2011) Laminar convective heat transfer and friction factor of Al₂O₃ nanofluid in circular tube fitted with twisted tape inserts. *Int J Auto Mech Eng* 3:265–278
55. Shuichi T (2012) Turbulent heat transfer behavior of nanofluid in a circular tube heater under constant heat flux. *Adv Mech Eng*, article ID 917612, 7p
56. Ferrooullat S (2011) Hydraulic and heat transfer study of SiO₂/water nanofluids in horizontal tubes with imposed wall temperature boundary conditions. *Int J Heat Fluid Flow* 32:424–439
57. Vijaya Lakshmi B, Subrahmanyam T, Dharma Rao V, Sharma KV (2012) Turbulent film condensation of pure vapors flowing normal to a horizontal condenser tube- constant heat flux at the tube wall. *Int J Auto Mech Eng* 4:455–470
58. Suresh S, Venkitaraj KP, Selvakumar P, Chandrasekar M (2012) Effect of Al₂O₃–Cu/water hybrid nanofluid in heat transfer. *Exp Thermal Fluid Sci* 38:54–60
59. Xuan Y, Li Q (2002) Investigation convective heat transfer and flow features of nanofluids. *J Heat Transfer* 125:151–155

A Review on Paraffin Phase Change Material-Based Thermal Management of Li-Ion Battery



Durgesh Kumar Mishra, Sumit Bhowmik, and Krishna Murari Pandey

Abstract At high discharge rate and abusive environment, huge amount of heat is generated inside battery system that can reduce the cycle life or damage the battery. Therefore, thermal management of Li-ion battery system is essential to eliminate heat generated inside the battery that leads to performance enrichment and eliminate thermal runaway. There have been different technologies implemented for battery thermal management which includes active cooling (forced air cooling, water cooling and thermoelectric cooler), passive cooling (phase change material (PCM) cooling, natural air cooling and heat pipe) and coupled cooling (Air + PCM cooling, water + PCM cooling, etc.) system. Among all the system, PCM integrated battery has gained huge attention just because of low cost, calm to operate and easy availability of PCM. In the present review article, a thermal management of Li-ion battery system incorporated with PCM has been studied according to different analysis methods. Paraffin, an organic kind of PCM is utilized in all the paper reviewed due to high heat storage capacity but less thermal conductivity and leakage during phase transformation creates problem. So, composite kind of PCM has been developed after mixing properties enhancing material in a suitable proportion with paraffin. Properties enhancing material must have good thermal conductivity and encapsulated in nature that can improve thermal conductivity and hold liquid PCM to eliminate leakage. Experimental, numerical and analytical investigations have been carried out to design battery with passive cooling system. From all these investigations, it was trying to find out the thermo-mechanical behavior of composite PCM and their performance during thermal management.

Keywords Phase change material · Battery thermal management · Paraffin · Composite · Thermal runaway

D. K. Mishra · S. Bhowmik · K. M. Pandey (✉)
Mechanical Engineering Department, National Institute of Technology, Silchar, India
e-mail: kmpandey2001@yahoo.com

© The Author(s), under exclusive license to Springer Nature Singapore Pte Ltd. 2023
V. K. Singh et al. (eds.), *Advances in Thermal Sciences*, Lecture Notes
in Mechanical Engineering, https://doi.org/10.1007/978-981-19-6470-1_13

149

1 Introduction

Li-ion battery is playing a crucial role in the field of energy management, when fossil fuels are suffering from scarcity and environmental issues. Owing to the high energy density, high cell voltage and long cycle life, Li-ion batteries are playing a crucial role in the field of electronic devices and electric vehicles as power source. At the same time, Li-ion battery is also anguishing with some inherent issues, in which one of the main issues is temperature rise during charging and discharging process. Because, the rise of temperature inside battery pack affects the performance, cycle life of the battery and thermal safety. That's why thermal management of Li-ion batteries plays a significant role [1–4]. There are basically three kinds of thermal management system for Li-ion battery shown in Fig. 1. Active cooling system is a traditional thermal management technology such as air cooler, water cooler and thermoelectric cooler. But there are some huddles in active cooling system which is low heat transfer rate, complexity of equipment and high initial and maintenance cost. That's why it is necessary to develop a new kind of thermal management system which contains rapid heat dissipation and keep the battery system in optimal temperature range. Phase change materials (PCMs) are used as passive thermal management played a very crucial role. This kind of thermal management system stands out from active (traditional) system because of its lightness, compactness and high efficiency. PCMs are works in a cyclic manner that can absorb or release a large amount of latent heat at the time of phase transformation [5–9]. A major advantage of the PCM thermal management system is that the heat generated during discharge is stored as latent heat. In this way, PCM is used to transfer that heat to the cell module during relaxation and keeps it at a temperature above the surrounding temperature for a long time and will increase the overall energy efficiency of the battery system. This can be a significant advantage in electric vehicle applications under cold conditions, when the battery operates intermittently. The PCM will help to keep the battery temperature higher and, therefore, enable the battery to operate with higher effective capacity. Another example is space application, where Li-ion batteries are used in satellites. As the satellite is orbiting the earth, it goes through a sudden temperature change when it moves from the light side to the dark side of the earth. The sudden drop in temperature affects the performance of the battery. The heat stored in the battery pack using a PCM can be used to decrease the effect of this sudden temperature change [10–13].

There are different categorization of PCM which can be divide as organic, inorganic and eutectic. In the current work, paraffin is used as PCM which is an organic kind of PCM contains some beautiful quality such as easy availability and high heat storage capacity. Paraffin is a saturated hydrocarbon with the general chemical formula C_nH_{2n+2} . The commercial grade paraffin is a combination of hydrocarbon, and it is produce through the distillation of crude oil. The number of carbon atom increases melting temperature and heat storage capacity also increases. It was seen from various literature that pure paraffin and commercial paraffin contains better thermal stability and stable properties after 1000–2000 cycles [14–18]. There are many research programs have been carried out on the thermal characterization of

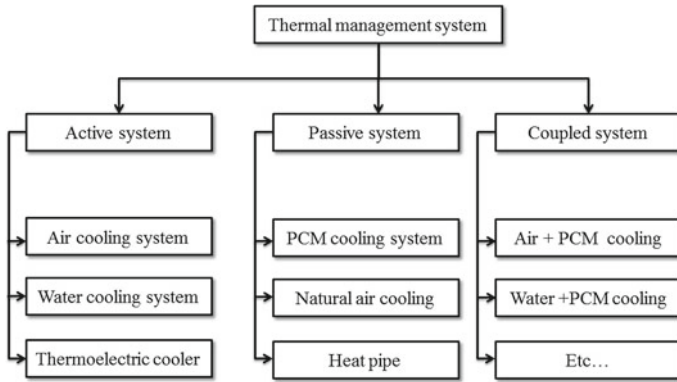


Fig. 1 Different kind of thermal management system for Li-ion battery

paraffin at the time of melting and solidification. The research found that paraffin possesses some good quality such as high heat storage capacity but at the same time, low thermal conductivity and leakage during phase change creates problem. So, fabrication of composite PCM after mixing of high conductivity material in the form of filler and fiber and incorporation of encapsulating material with the paraffin, which can reduce the problem at the same time it affects the heat storage capacity. The properties enhancing material used by the various researcher to improve desired property is micro graphite powder, graphite sheets, expanded graphite (EG), high density polyethylene (HDPE), carbon fiber (CF), multi-wall carbon nanotubes (MWCNTs), silicon carbide (SiC), low density polyethylene LDPE, silica fume and graphene [19–23].

The main body of this paper is categorized according to analysis methods followed by the various authors, which is not explained earlier. On that way it is divided in experimental, numerical, analytical, analytical and numerical and experimental and numerical subsections. The discussion is focused on development of passive thermal management system of battery incorporated with PCMs. It has been also seen that at what temperature which kind of PCM is suitable for battery module. The various thermal properties are also discussed and compared. It is expected that current work is beneficial for the researcher who is working on battery system.

2 Analysis Methods

2.1 Experimental Method

The experimental methods are taken as the most scientific methods among all the methods. An experiment is a study of cause and effect of all variable at a time but, in other methods, there is manipulation of one variable all other trying to keep constant.

There are various advantages of experimental methods, such as precise control of variables, can be replicated and give quantitative data which can be analyzed statically. For designing purpose of battery, the various authors analyzed and discussed.

Jiang et al. [24] analyzed thermo-physical properties of paraffin and EG composite PCM for thermal management in Li-ion batteries. Different mass fractions of EG in the composite were investigated for the performance of batteries. Mass fraction of the EG was varied from 9 to 30% and seen that there is dramatically decrease in leakage as well as increase the thermal conductivity of the PCM which control the temperature rise inside the battery. Authors proposed that the mass fraction of EG between 16 and 20% is most suitable composition due to shape stability and efficient performance. Experimentally and numerically, it was observed that composite PCM improves the thermal management at the place of air cooling and pure PCM. Ling et al. [25] studied 20-cell Li-ion battery pack working at 5 and -10°C incorporated with a high thermal conductive composite and a low thermal conductive composite PCM. The composition used during present work was 60% RT44HC with low thermal conductive silica fume and high thermal conductive EG. Results revealed that in the case of less conductive composite, there is an uneven temperature distribution in the battery pack which led to high voltage difference and loss of capacity. High conductive material is especially beneficial to maintain uniform temperature when ambient temperature dropped from 5 to -10°C . Therefore authors suggested that the composite based on EG shows better performance for the battery pack at low temperature. Wang et al. [26] performed an experimental examination for thermal management of Li-ion battery using passive method. Paraffin and EG were utilized for the preparation of composite and enveloped into aluminum box. Temperature measurement takes place at different discharge rates at different ambient temperatures. After investigation results show that with presence of composite PCM the average temperature of the battery pack reduced and uniformity of temperature occur. Author also revealed that after complete melting of PCM thermal control performance starts deteriorate, that's why dosage estimation of PCM is key problem during this application. Wang et al. [27] experimentally investigated the heat storage capacity of pure PCM and composite PCM at various heat flux. They also studied the effect of cooling system in the battery pack through composite PCM. Experimental results revealed that with the incorporation of aluminum foam one can accelerate the melting process and the distribution of temperature is more uniform compare to pure paraffin. It was seen that paraffin/aluminum foam has a suitable cooling effect which can limit the temperature rise during discharge. He et al. [28] fabricated a new kind of composite PCM with the combination of paraffin/EG/CF in order to increase the thermal conductivity for the utilization of BTM. EG/CF works as heat transfer enhancing material which delivers better cooling and maintains uniform temperature within battery pack. Experimental results show that the maximum temperature and change in temperature is retaining stable in successive cycles. Duan and Naterer [29] investigated heat transfer within battery modules used in electric vehicles. An experimental set up is used to perform the analysis of thermal management inside battery modules with PCM. Two different kind of PCM designed for the current analysis: first one is simply PCM surrounded around the heater and other one PCM filled in jacket and wrapped over the heater. In

the both cases, it was seen that the heater is maintained at desire temperature range. In the current paper, the variable ambient temperature and heating rate were also described. Zou et al. [30] studied experimentally the heat transfer characteristics of light weight power battery used for eco-friendly electric vehicles. A novel kind of composite PCM with high thermal conductivity and leakage proof was fabricated. During the fabrication, paraffin was mixed with different percentage of carbon tube, grapheme and EG. It was also observed that if paraffin integrates with copper foam then also the composite will give the same enhanced heat transfer. Analysis was performed for two set of batteries, one contains four numbers and another contains sixteen numbers of batteries. Results revealed that the temperature will be uniform if region is contracted; it means thermal uniformity of four batteries is more compare to sixteen batteries. Zou et al. [31] experimentally studied the thermal performance of Li-ion battery combined with three different kind of composite PCM. Various combination used during present study were paraffin/MWCNT, paraffin/graphene and paraffin/MWCNT/graphene. All the combinations were studied not only for thermal conductivity improvement but also for restrain the rapid temperature rise of liquid composite PCM. Results indicated that composite paraffin/MWCNT/graphene give the better heat transfer effect comparison to other. At last, the composite shows the excellent potential for thermal management in Li-ion power battery. Li et al. [32] studied a sandwich structure combined with paraffin and copper foam for the passive thermal management of high powered Li-ion battery. The efficiency of the system was evaluated experimentally and compared with air cooling system and pure PCM cooling system at different discharge rate. Results indicated that the air cooling system could not fulfill the safety requirement where as pure PCM reduced the temperature dramatically and maintain the temperature within allowable limit. On the other hand, it was seen that composite PCM improved the thermal conductivity and uniformity of the temperature. Pan and Lai [33] investigated composite kind of PCM embedded with battery module for thermal management. In the current study, author performed a comparative analysis on natural cooling, pure paraffin cooling, copper fiber/paraffin cooling and copper foam/paraffin cooling at different discharge rate. Result revealed that copper fiber/paraffin was most effective from all other. Alrashdan et al. [34] studied thermo-mechanical behavior of composite paraffin/EG PCM for Li-ion battery pack. Different kinds of test were performed to analyze the suitable condition for Li-ion battery like thermal conductivity, bursting and tensile-compression test. The results indicated that at low temperature as the paraffin percentage was increasing will increase all required properties. At the same time, the reverse behavior has achieved if the operating temperature was high. Yuan et al. [35] developed a novel kind of composite PCM contain low electric conductivity and high thermal conductivity used for thermal management of battery. A new kind of SiC/EG skeleton material was introduced with PCM to achieve required property. It was seen that with the increase value of SiC the thermal conductivity increased but volume resistivity first increases, then started to decrease. Authors suggested that when SiC was 15%, then highest volume resistivity achieved at the same time thermal conductivity was also a good value. This composition provides more superior cooling performance then others at high discharge rate. Zhang et al.

[36] designed a paraffin/kaolin/EG ternary composite PCM to use in electric vehicle power battery cell thermal management. Various composition of the material were used and analyzed. The results shows that 10% of EG and 10% of kaolin have given the excellent properties. It was seen that after 60 °C and 30 min there was not any leakage found at the same time thermal conductivity achieved was 6 W/m-K. With the incorporation of this composite with battery, it was observed that at 4C discharge also the temperature was controlled less than 45 °C. Finally, authors suggested that the superior temperature control with the help of this novel composite PCM. Lv et al. [37] suggested a new kind of anti-leakage and anti-volume composite PCM. The composite was made up with paraffin/EG/nanosilica/LDPE. Nanosilica contains pores between the ranges of 30–100 nm, which was absorbing liquid paraffin intensively, i.e., cause of leakage prevention. This porous silica trapped into the expanded part of EG and mixed with LDPE gave the volume stability. The enhanced property composite PCM acquires good cooling efficiency and durability, which is suitable for Li-ion battery module. Lv et al. [38] found some of the drawbacks such as leakage, poor mechanical properties and less heat transfer capability. To overcome these drawbacks, a novel composition of materials was suggested. LDPE, EG and paraffin combined with low fins in a definite proportion to achieve suitable properties which is utilized for battery thermal management. LDPE and EG structure is only prevent the leakage but also enhanced the mechanical strength. Authors performed comparison between LDPE/EG/paraffin and EG/paraffin and found that and found that LDPE/EG/paraffin gives the better cooling effect and mechanical properties. Coupling of low fins with the composite gives the excellent temperature control at high discharge rate also. Arora et al. [39] studied the thermal management with the different orientation of cell and incorporation of PCM. It was seen that vertically inverted cells position facilitates minimum thermal variations inside the PCM matrix. The developed system was able to maintain tight control of the battery cell temperature in abusive condition. Results revealed that the management of temperature irregularities is easier in this inverted cell as compare to traditional cell. In addition by connecting thermoelectric devices on a side of battery, this converts waste heat of PCM in electric power. Wang et al. [40] analyzed that recently the Li-ion batteries is exploding and catching fire, so it is required to manage the temperature inside the battery. In this regards, authors suggested passive type of cooling system which contains composite kind of PCM. Here, the experimentation has been done on three combination of PCM, first one was pure paraffin, in second case 80% of paraffin and 20% of EG and third one was the combinations of 50% paraffin, 47% epoxy and 3% EG. Results revealed that second type of PCM works more efficiently at high discharge rate. It was also seen that after 30 cycles of charge–discharge the module temperature for third case was 59.79 °C but in second case, it increases to 64.79 °C, which indicated that epoxy works as a plasticizer can prevent leakage.

2.2 Numerical Method

Numerical analysis is essential in many areas of modern engineering problems. It is the area of mathematics and computer science that creates, analyzes and implements algorithms for obtaining numerical solutions to problems involving continuous variables. The software used for battery thermal system by the various researchers were ANSYS fluent, PDEase2D, COMSOL 2D, SALMONE7.4 and SYRTHES.4.

Javani et al. [41] analyzed PCM-based thermal management system for Li-ion battery pack used in electric vehicles. The PCM select for the current study was n-octadecane which is filled into foam layer which separate the cells. Suitable foam and PCM was decided through experimentation of various available foam and PCM. Analysis of thermal behavior was done on the four cell sub module on different discharge rate in the absence of PCM and also with the incorporation of PCM. Results revealed that 8 °C decrement of maximum temperature, which is a great achievement by researcher. Kizilel et al. [42] studied that how to prevent thermal runaway of battery cell due to catastrophic failure. For this study, authors used PCM-based passive thermal cooling system and compare it with the active cooling system. Here, it has been seen that one can achieve uniform temperature under normal and abusive condition if the passive TMS is used. Results also show that as compare to active cooling system, PCM-based cooling system is much simpler and economic design. Huo et al. [43] investigated numerically the BTM with the integration of PCM to control the temperature. The Boltzmann model is applied to solve this problem, where paraffin is mixed in the porous media. Quartet structure generation set method is used to generate the porous media to solve the current problem. The main attention of the author was on the variation of porosity and Rayleigh number on the heat transfer process. Results show that if one decrease the porosity, then melting rate will increase. Authors show thanks to high heat conductivity framework for making faster heat transfer rate and controlling the temperature properly. Javani et al. [44] searched that there are two main essential parameters that should be minimized for the efficient working of battery in electrical vehicle, first one is minimized the peak temperature and second is prevention of temperature gradients. The significant goal of this study is to eliminate active cooling system because it requires extra energy. So, here a passive, i.e., PCM-based cooling system is used for the analysis. Four different thickness layers were used, and comparative analysis has been performed on temperature distribution through numerical study. Results indicate that as the thickness of the PCM increases the maximum temperature reduce. The PCM with thickness 3 mm, 6 mm, 9 mm and 12 mm decreases the temperature by 2.8 K, 2.9 K, 3.0 K and 3.0 K, respectively. Hallaj and Selman [45] used PDEase2D finite element software to simulate the thermal behavior of PCM incorporated battery system. It was seen from the simulation result that, at different discharge rate, the integrated battery module contains more thermal uniformity then non-integrated module. Researcher also observed that heat generated at the time of discharge is stored in PCM, which is utilized at the charging cycle. At the time, when battery is in relax mode or temperature go down below melting temperature of PCM, then

stored heat started to reject in module. This is beneficial at the time when vehicle went suddenly in cold condition or when in space system battery temperature drops significantly. Khateeb et al. [46] studied the use of PCM in Li-ion battery for electric scooter. The use of PCM is very advantageous which provides light weight, compact size and energy efficient system compare to active cooling system like fan, blower and pump for thermal management. A PCM with melting temperature 41–44 °C mixed with aluminum foam and fin attached with battery module were simulated for the present work. Simulation was performed in the condition of summer as well as winter at the same time effect of air conditioning was also studied. The simulation results revealed that PCM is the highly efficient agent for thermal management in Li-ion battery used in electric scooter. Huo and Rao [47] worked for low temperature case because at lower temperature power and energy densities decreases that's why heat preservation is required to maintain the battery surroundings at working temperature. Authors tried to construct a lattice Boltzmann model to solve the battery thermal management at low temperature problem and have seen the effects of environmental temperature, latent heat and thermal conductivity. Results indicated that the natural convection of the PCM tried to decrease temperature and increase non-uniformity of temperature. A heavy latent heat can reduce non-uniformity effect but low environmental temperature and high thermal conductivity increase the heat dissipation. So, authors suggested that increasing the latent heat is best way to work at low temperature. Wu et al. [48] investigated the optimum mass fraction of EG in the composite PCM and found that 15–20% EG fraction is efficient for battery thermal management. Authors wanted to improve more suitable composite and tried to develop pyrolytic graphite sheets enhanced composite. It was seen that convective heat transfer coefficient is 50 W/m²k in pyrolytic graphite sheets which is very less compare to PCM module which is 200 W/m²k. Mortazavi et al. [49] studied a combined atomistic-continuum multiscale modeling of the graphene and hexagonal boron-nitride mixed with paraffin for thermal management of rechargeable batteries. A comparable study was performed within no PCM, pure paraffin, graphene/paraffin and hexagonal boron-nitride/paraffin. Among all the cases, authors suggested that graphene network with paraffin is an optimal solution for the thermal management. Qu et al. [50] developed a two-dimensional transient model of square Li-ion battery for passive thermal management. A solid-liquid phase change of paraffin into copper foam was characterized by thermo-electrochemical model of battery. The model was composed of charge conservation, species conservation and energy conservation equations. The behavior of foam-PCM composite on convective heat transfer was investigated. Results indicated that at the allowable discharge range 1C and 3C the surface temperature of the battery reduced dramatically with the use of foam-paraffin composite. Yan et al. [51] developed a composite board contains three parts, which is an insulation panel, a heat conducting shell and PCM. Thermal performance of composite board used for battery was investigated in normal operating as well as in abusive condition. Results showed that utilization of composite board can improve the heat dissipation capacity and uniformity of temperature. It was suggested that with the increase of latent heat of PCM can drastically enhance the thermal performance of composite board. That's why a PCM with latent heat 1125 kJ/kg and

phase transition temperature 303.15 K and 323.15 K were recommended for battery thermal management. Somasundaram et al. [52] developed a 2D transient mathematical model considering conservation of energy, species and charges together for spiral wound cylindrical Li-ion battery and solve it numerically. Authors performed numerical analysis for the passive thermal management with and without PCM at various charge rates. Thermal and electrochemical behavior has been discussed on the design of different layer heat generation and spiral layer structure. In addition the passive thermal management at 5C, discharge rate shows lower overall temperature.

3 Conclusion

The current paper reviews the existing research findings for thermal management of Li-ion battery that obtained from various analysis methods. During the working cycle, battery generates heat which reduces the efficiency, cause of thermal runaway and batteries explosion. So, it is required to manage the temperature inside the battery. Temperature variation and temperature range that influences the battery system performance is two major parameters. The battery thermal energy management is very significant to enhance the battery performance. Conventional battery thermal energy management, like air and liquid cooling make the complete system too massive, compound and costly in terms of fans, blower, pumps, etc. PCMs thermal management is a better selection at high discharge rate, high operating temperature and abusive condition. Then again thermal conductivity of PCM is not up to the mark. So, a composite kind of PCM is introduced after mixing with property enhancing material. The examination is carried out on the several significant parameters such as phase change storage energy unit, thermal conductivity of composite PCM, geometric parameter, ambient temperature, the rate of charge and discharge on the thermal management of Li-ion battery. Then again the optimization mass of properties enhancing material in composite PCM. The effect of different control parameter, for example initial temperature, thermal resistance, ambient temperature and melting temperature have been seen on the performance of temperature management. It revealed that after complete melting of PCM thermal control performance starts deteriorate, that's why dosage estimation of PCM is key problem during this application. The benefit of air cooling system is that if the PCM has been melted completely at that time also temperature can still maintained in a safe limit.

References

1. Giuliano MR, Advani SG, Prasad AK (2011) Thermal analysis and management of lithium-titanate batteries. *J Power Sources* 196(15):6517–6524
2. Zhang X (2011) Thermal analysis of a cylindrical lithium-ion battery. *Electrochim Acta* 56(3):1246–1255

3. Yang K, An J, Chen S (2010) Thermal behavior analysis of nickel/metal hydride battery during overcharging. *Sci China Chem* 53(5):1177–1182
4. Shi J, Wu F, Chen S, Zhang C (2006) Thermal analysis of rapid charging nickel/metal hydride batteries. *J Power Sources* 157(1):592–599
5. Mishra DK, Bhowmik S, Pandey KM (2020) Polyethylene glycol based form stable composite phase change material: a review. *J Phys: Conf Series*, 012025. IOP Publishing
6. Nagano K, Mochida T, Takeda S, Domański R, Rebow M (2003) Thermal characteristics of manganese (II) nitrate hexahydrate as a phase change material for cooling systems. *Appl Therm Eng* 23(2):229–241
7. Mishra DK, Bhowmik S, Pandey KM (2021) Analysis on development of beeswax as phase change material for thermal energy storage. In: *Advances in Production and Industrial Engineering*. Springer, Singapore, pp 379–388
8. Mishra DK, Bhowmik S, Pandey KM (2022) Analysis of heat transfer rate for different annulus shape properties-enhanced Beeswax-based phase change material for thermal energy storage. *Math Probl Eng* 2022:1–21
9. Mishra DK, Bhowmik S, Pandey KM (2022) Development and assessment of Beeswax/expanded graphite composite phase change material for thermal energy storage. *Arabian J Sci Eng*, 1–20
10. Rao Z, Wang S (2011) A review of power battery thermal energy management. *Renew Sustain Energy Rev* 15(9):4554–4571
11. Xia G, Cao L, Bi G (2017) A review on battery thermal management in electric vehicle application. *J Power Sources* 367:90–105
12. Ling Z, Zhang Z, Shi G, Fang X, Wang L, Gao X, Fang Y, Xu T, Wang S, Liu X (2014) Review on thermal management systems using phase change materials for electronic components, Li-ion batteries and photovoltaic modules. *Renew Sustain Energy Rev* 31:427–438
13. Manoj KP, Mysamy K, Saravanakumar PT (2020) Experimental investigations on thermal properties of nano-SiO₂/paraffin phase change material (PCM) for solar thermal energy storage applications. *Energy Sources, Part A: Recov, Utilization, Environ Effects* 42(19):2420–2433
14. Zhao CY, Tao YB, Yu YS (2020) Molecular dynamics simulation of nanoparticle effect on melting enthalpy of paraffin phase change material. *Int J Heat Mass Transf* 150:119382
15. Akgun M, Aydın O, Kaygusuz K (2007) Experimental study on melting/solidification characteristics of a paraffin as PCM. *Energy Convers Manage* 48:669–678
16. Akgun M, Aydın O, Kaygusuz K (2008) Thermal energy storage performance of paraffin in a novel tube-in-shell system. *Appl Therm Eng* 28:405–413
17. Sun X, Liu L, Mo Y, Li J, Li C (2020) Enhanced thermal energy storage of a paraffin-based phase change material (PCM) using nano carbons. *Appl Therm Eng* 181:115992
18. De SR, Ambrogi V, Carfagna C, Ambrosio L, Nicolais L (2006) Effect of microencapsulated phase change materials on the thermo-mechanical properties of poly(methyl-methacrylate) based biomaterials. *J Mater Sci—Mater Med* 17:1219–1226
19. Sharma A, Tyagi VV, Chen CR, Buddhi D (2009) Review on thermal energy storage with phase change materials and applications. *Renew Sustain Energy Rev* 13(2):318–345
20. Liu M, Saman W, Bruno F (2012) Review on storage materials and thermal performance enhancement techniques for high temperature phase change thermal storage systems. *Renew Sustain Energy Rev* 16(4):2118–2132
21. Agyenim F, Hewitt N, Eames P, Smyth M (2010) A review of materials, heat transfer and phase change problem formulation for latent heat thermal energy storage systems (LHTESS). *Renew Sustain Energy Rev* 14(2):615–628
22. Ibrahim NI, Al FA, Rahman S, Yilbas BS, Sahin AZ (2017) Heat transfer enhancement of phase change materials for thermal energy storage applications: a critical review. *Renew Sustain Energy Rev* 74:26–50
23. Safari A, Saidur R, Sulaiman FA, Xu Y, Dong J (2017) A review on super cooling of phase change materials in thermal energy storage systems. *Renew Sustain Energy Rev* 70:905–919
24. Jiang G, Huang J, Fu Y, Cao M, Liu M (2016) Thermal optimization of composite phase change material/expanded graphite for Li-ion battery thermal management. *Appl Therm Eng* 108:1119–1125

25. Ling Z, Wen X, Zhang Z, Fang X, Gao X (2018) Thermal management performance of phase change materials with different thermal conductivities for Li-ion battery packs operated at low temperatures. *Energy* 144:977–983
26. Wang W, Zhang X, Xin C, Rao Z (2018) An experimental study on thermal management of lithium ion battery packs using an improved passive method. *Appl Therm Eng* 134:163–170
27. Wang Z, Zhang Z, Jia L, Yang L (2015) Paraffin and paraffin/aluminum foam composite phase change material heat storage experimental study based on thermal management of Li-ion battery. *Appl Therm Eng* 78:428–436
28. He J, Yang X, Zhang G (2019) A phase change material with enhanced thermal conductivity and secondary heat dissipation capability by introducing a binary thermal conductive skeleton for battery thermal management. *Appl Therm Eng* 148:984–991
29. Duan X, Naterer GF (2010) Heat transfer in phase change materials for thermal management of electric vehicle battery modules. *Int J Heat Mass Transf* 53(23–24):5176–5182
30. Zou D, Liu X, He R, Zhu S, Bao J, Guo J, Hu Z, Wang B (2019) Preparation of a novel composite phase change material (PCM) and its locally enhanced heat transfer for power battery module. *Energy Convers Manage* 180:1196–1202
31. Zou D, Ma X, Liu X, Zheng P, Hu Y (2018) Thermal performance enhancement of composite phase change materials (PCM) using graphene and carbon nanotubes as additives for the potential application in lithium-ion power battery. *Int J Heat Mass Transf* 120:33–41
32. Li WQ, Qu ZG, He YL, Tao YB (2014) Experimental study of a passive thermal management system for high-powered lithium ion batteries using porous metal foam saturated with phase change materials. *J Power Sources* 255:9–15
33. Pan M, Lai W (2017) Cutting copper fiber/paraffin composite phase change material discharging experimental study based on heat dissipation capability of Li-ion battery. *Renew Energy* 114:408–422
34. Alrashdan A, Mayyas AT, Al-Hallaj S (2010) Thermo-mechanical behaviors of the expanded graphite-phase change material matrix used for thermal management of Li-ion battery packs. *J Mater Process Technol* 210(1):174–179
35. Yuan W, Yang X, Zhang G, Li X (2018) A thermal conductive composite phase change material with enhanced volume resistivity by introducing silicon carbide for battery thermal management. *Appl Therm Eng* 144:551–557
36. Zhang X, Liu C, Rao Z (2018) Experimental investigation on thermal management performance of electric vehicle power battery using composite phase change material. *J Clean Prod* 201:916–924
37. Lv Y, Situ W, Yang X, Zhang G, Wang Z (2018) A novel nanosilica-enhanced phase change material with anti-leakage and anti-volume-changes properties for battery thermal management. *Energy Convers Manage* 163:250–259
38. Lv Y, Yang X, Li X, Zhang G, Wang Z, Yang C (2016) Experimental study on a novel battery thermal management technology based on low density polyethylene-enhanced composite phase change materials coupled with low fins. *Appl Energy* 178:376–382
39. Arora S, Kapoor A, Shen W (2018) A novel thermal management system for improving discharge/charge performance of Li-ion battery packs under abuse. *J Power Sources* 378:759–775
40. Wang Z, Li X, Zhang G, Lv Y, Wang C, He F, Yang C, Yang C (2017) Thermal management investigation for lithium-ion battery module with different phase change materials. *RSC Adv* 7(68):42909–42918
41. Javani N, Dincer I, Naterer GF, Rohrauer GL (2014) Modeling of passive thermal management for electric vehicle battery packs with PCM between cells. *Appl Therm Eng* 73(1):307–316
42. Kizilel R, Sabbah R, Selman JR, Al-Hallaj S (2009) An alternative cooling system to enhance the safety of Li-ion battery packs. *J Power Sources* 194(2):1105–1112
43. Huo Y, Guo Y, Rao Z (2019) Investigation on the thermal performance of phase change material/porous medium-based battery thermal management in pore scale. *Int J Energy Res* 43(2):767–778

44. Javani N, Dincer I, Naterer GF, Yilbas BS (2014) Heat transfer and thermal management with PCMs in a Li-ion battery cell for electric vehicles. *Int J Heat Mass Transf* 72:690–703
45. Al-Hallaj S, Selman JR (2000) A novel thermal management system for electric vehicle batteries using phase-change material. *J Electrochem Soc* 147(9):3231–3236
46. Khateeb SA, Farid MM, Selman JR, Al-Hallaj S (2004) Design and simulation of a lithium-ion battery with a phase change material thermal management system for an electric scooter. *J Power Sources* 128(2):292–307
47. Huo Y, Rao Z (2017) Investigation of phase change material based battery thermal management at cold temperature using lattice Boltzmann method. *Energy Convers Manage* 133:204–215
48. Wu W, Wu W, Wang S (2017) Thermal optimization of composite PCM based large-format lithium-ion battery modules under extreme operating conditions. *Energy Convers Manage* 153:22–33
49. Mortazavi B, Yang H, Mohebbi F, Cuniberti G, Rabczuk T (2017) Graphene or h-BN paraffin composite structures for the thermal management of Li-ion batteries: a multiscale investigation. *Appl Energy* 202:323–334
50. Qu ZG, Li WQ, Tao WQ (2014) Numerical model of the passive thermal management system for high-power lithium ion battery by using porous metal foam saturated with phase change material. *Int J Hydrogen Energy* 39(8):3904–3913
51. Yan J, Wang Q, Li K, Sun J (2016) Numerical study on the thermal performance of a composite board in battery thermal management system. *Appl Therm Eng* 106:131–140
52. Somasundaram K, Birgersson E, Mujumdar AS (2012) Thermal–electrochemical model for passive thermal management of a spiral-wound lithium-ion battery. *J Power Sources* 203:84–96

A Comprehensive Study of an Ejector System and Its Applications: A Review



Abhishek Kulkarni, Surendra Kumar Yadav, and Arvind Kumar

Abstract The review aims to give a writing overview of the examination endeavors achieved in the case of an ejector geometry framework. An ejector is a device used to increase the delivery rate of a fluid. They are used in the refrigeration cycle and the rocket engines as well. It is difficult to understand the flow characteristics of the fluids and the thermodynamic properties of the streams. They can be understood using some computational techniques and tests. The mathematical models for the flow of the fluids inside the ejector are least observed since it is difficult to investigate a fast-moving stream of the fluids inside the ejector. Ejectors have many applications, where heat transfer takes place at a higher rate and helps create the vacuum. This review paper examines the construction and working, applications, and new advances related to the ejectors. Furthermore, it is observed that there is a special need to investigate various aspects of the ejector.

Keywords Ejector · Working fluids · Geometry optimization · Mathematical modeling · Applications

1 Introduction

A supersonic ejector is used for a broad range of applications in the industries as a compressor. These include desalination, refrigeration, steam turbine, paper making machine, wood drying equipment, etc. The analysis of the flow of the fuels through the section of the ejector is quite complicated when we consider the high-speed flow the motive fuel and its mixing with the secondary fuel or the ambient fluid when we consider the effects of compressibility at higher Mach numbers. Hence, the ejector is basically a flow device that does not have any moving part [1]. The ejectors were first used in the vacuum braking systems of the railway trains, which date back to the eighteenth century. The ejector was driven by the waste steam from the steam engine, which was used to maintain vacuum partially in the braking cylinders fitted

A. Kulkarni · S. K. Yadav (✉) · A. Kumar
Department of Mechanical Engineering, K. R. Mangalam University, Gurugram,
Haryana 122001, India
e-mail: surendra.yadav@krmangalam.edu.in

© The Author(s), under exclusive license to Springer Nature Singapore Pte Ltd. 2023
V. K. Singh et al. (eds.), *Advances in Thermal Sciences*, Lecture Notes
in Mechanical Engineering, https://doi.org/10.1007/978-981-19-6470-1_14

161

to the cartridges. The ejector has always had the potential to be used in various areas of application because of its ability to use the extra gas as a driving fluid and its simple design. Therefore, the ejectors are extensively found and their uses are seen in various applications in the industries. But, due to not being fully understood and the fact that a slight change in the geometry of the ejector and the working parameters will result in the difference in the performance characteristics, new designs of the ejectors are used which are based on the existing design [2]. The ejectors are used in the industries in numerous ways, i.e., to create a vacuum at different levels by using them in stages, and they can be used as transfer pumps as well as mixing pumps. The important reason that the ejectors are preferred over regular pumps is that they have a very simple and sturdy design. In addition to that they hold the capacity to handle extensive volumes of gases in a relatively limited amount of size of equipment. The ejectors also require less maintenance as the operation is simple. The ejector works upon the principle of compressing and transporting a pressurized fluid from the suction point to the exhaust point. The pressure of an actuating fluid or the primary fluid is brought to the level of that of the secondary fluid. During this expansion, the velocity of the primary fluid is increased by accelerating it by the influence of the nozzle shape as the velocity with which it enters is a negligibly small orifice. Due to the increased velocity of the primary fluid, a region of low pressure is induced in the suction chamber, which helps mix the fuels. As the mixing takes place, the primary fuel decelerates, and the velocity of the secondary fuel increases. This mixture is introduced into the diffuser and is decelerated rapidly because of the neck of the ejector. Here, it is compressed to the exit pressure [3]. The function of subparts of the ejector (refer to Fig. 1) is described below.

- Primary fluid chest: This is a connecting chamber that is used to introduce the pre-eminent high-pressure fluid into the nozzle section of the ejector.
- Suction chamber: It is also called the secondary inlet through which the secondary fluid is taken in because of the pressure difference created by the expansion of the primary fluid. In the cases, where a compact design and cost-cutting are

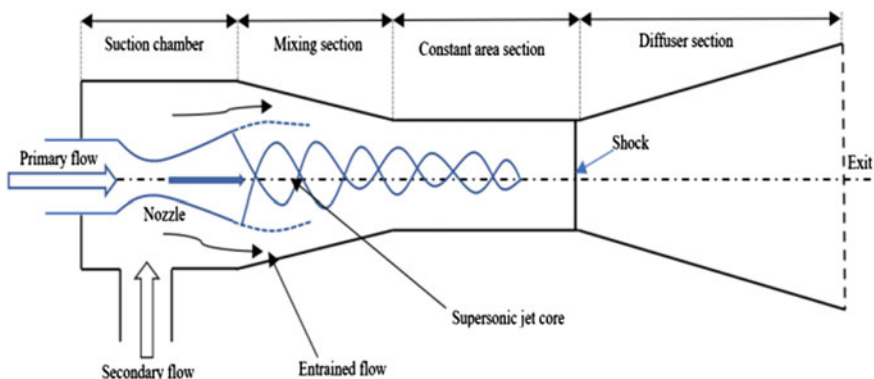


Fig. 1 Ejector system [13]

required, the suction chamber is eliminated. For this purpose, a nozzle and a diffuser connection are incorporated in the vessel or the ejector body that needs to be evacuated. It is so designed that the inlet velocity of the fluid should be lowered, and hence, it will ensure the minimum level of swirl in the other parts.

- **Nozzle:** This main component of the ejector assembly converts the high-pressure primary fluid into a high-velocity stream directed toward the diffuser. Because of the nozzle, the exit velocity and the total flow inside the ejector are controlled. Other dimensions are governed by the guidelines provided by the ESDU, which suggest the appropriate radii for the convergent and divergent sections. Also, the nozzle tip is sharply designed to help the mixing of the two streams.
- **Diffuser inlet:** The inlet section of the diffuser is designed in such a way that it should be able to withstand the high-velocity fluids being converted into high pressure. In this section, the mixing of the motive fluids takes place and is compressed. The best results depend upon the length of the chamber, which enables the mixing of the two streams.
- **Throat:** It is a converging section with a reduced diameter between the diffuser inlet and outlet where the velocity of the fluids is brought down to subsonic. It is at this section where the compression takes place.
- **Diffuser outlet:** The diffuser outlet is the ejector's diverging section, which completes the conversion process of velocity into pressure. Since the velocity of the mixture of fluids is subsonic, the diffuser outlet further reduces the velocity of the fluid to a reasonable level to convert the velocity into the pressure energy completely [4].

2 Compressible Fluid Dynamics (CFD) Analysis

In an ejector refrigeration framework, the ejector works as a blower yet without utilizing any movable parts. The authors prepared a CFD model using an ERS test rig using R134a [5]. The ideal mathematical boundaries and uneven surface of the nozzle were acquired using CFD examinations. The study results showed that the throat and the nozzle should be located closer to each other when designing the ejector since the entrainment portion of the ejector is dependent upon the length of these two parts. Steam ejectors were examined mathematically using various nozzle geometries and CFD strategies. The exhibition of the steam ejectors with five unique nozzle shapes, specifically, square, conelike, curved, rectangular, and cross-formed nozzles, has been thought about under similar conditions [6]. The ratio increment can be accomplished by effective blending because of the connections between the streamwise and the spanwise vortex. Streamwise vortex results in disfiguring and breaking the spanwise vortex because of its strength. Crashes of these vortices in the blending channel at an early stage would increase the mechanical energy and lessen the pressure in the region for the auxiliary stream to go through, which results in a notable reduction of the entertainment ratio and backpressure. This situation must be avoided while designing the nozzles [7]. The two significant boundaries used to

portray the ejector execution are ratio and backpressure. The CFD has proven to be an effective tool for stream field investigation and ejector execution expectations for a long time. Various CFD examinations have been completed to contemplate the impact of ejector calculation on its execution, for example, nozzle exit position, the region proportion of nozzle throat to steady region segment, and the length of consistent region segment [8]. Guillaume et al. [9] worked on the productivity of a fly siphon by utilizing a curved nozzle, yet the nozzle is a combining one, and the wind streams inside the fly siphon at low speed without concerning the compressibility. Chang and Chen [10] tentatively explored a steam-stream refrigeration system utilizing petal and cone-shaped nozzles. Their exploratory outcomes show the COP of the framework with a petal nozzle is superior to that with a funnel-shaped nozzle when worked at bigger region proportions. Narabayashi et al. [11] did exploratory and CFD investigations of stream in single and multi-opening nozzle fly siphons. The productivity of the five-nozzle fly siphon was low because of a low mass-stream proportion fly siphon due to a channel stream obstruction between the nozzle fingers and throat. Recently, a two-stage supersonic ejector system was proposed and analyzed numerically. It was suggested that the two-stage ejector system is more efficient and has better suction power than single-stage ejectors [12, 13].

3 Nozzle Geometry

It can be observed through the computer simulation that the computational fluid dynamics techniques help in the prediction of the performance of the ejector without the use of an actual model and explain some of the facts that limit the performance or working of an ejector. Hence, we can use CFD to analyze the supersonic ejector and the flow process that occur within it. Computational techniques can be advantageous over analytical and experimental techniques since we can obtain results for the flow process of the fluid flowing streams inside the ejector, which is the main study objective while testing an ejector. Since the flow of the primary fluid should be supersonic for the stable operation of the ejector, the flow of the fuel inside the ejector is confined, and the mixing process is complex due to the initial supersonic fluid and subsonic later fluid. The CFD analysis will visualize the flow and provide the mass flow results without affecting the flow process.

The developments in computer technology and hardware and the advancements in software have changed the course of the design of the automobile, airplanes, and ships. Using the commercialized software packages, the design and analysis of the processes have not only saved time and cost but have also allowed the study of systems for controlled experiments, which are difficult to perform. A comparative analysis of CRMC and the conventional nozzle was investigated analytically and numerically. It was found that the flow behavior of fluid inside the CRMC nozzle geometry is in better condition as compared with conventional nozzle [14]. Khan et al. [15] performed a numeric study to optimize micro jets' potency by controlling the initial pressure in a suddenly expanded 2D planar channel. The author carried out the analysis in this

research to design a supersonic C-D nozzle, considering the compressible flow of the perfect gas. The authors here observed the pressure and velocity inside the duct by analyzing different counters and plots. The nozzle is designed so that the total flow is kept constant and due to which the speed of the fluid flowing through it will increase when the section is narrowed. The primary or the motive fluid is isentropic, and during the subsonic flow, the gas is compressible. As the cross-section area decreases at the throat, the state of choked flow is reached, and a sonic velocity of the gas is achieved. As the gas moves further into the increased cross-section, the fluid will start to expand, and the flow will become supersonic. Varga et al. [16] discussed this principle, illustrating that the nozzle controls the characteristics of the fluid flowing through it. The authors analyzed a De-Laval nozzle and explained its concepts and the working of this nozzle. The theoretical analysis was done at different nozzle sections, and the changes in the characteristic flow framework were studied using CFD. A simulation for the shockwave was also prepared using the CFD, and a significant increase in the velocity as well as the temperature and pressure reduction was observed. Dongping Zeng et al. [17] studied a novel drug delivery method known as a needle-free injection (NFI), which involves using a high-speed stream of fluid to deliver a drug into the skin. NFIs are an old strategy that has great potential to become an important drug delivery method. Although they have shown obvious advantages over standard needle injection, they have not gained widespread acceptance due to their unpleasantness. As the diameter of the nozzle gets bigger, the injected depth gets larger, which could cause more bleeding. This causes the wound to widen, which could cause more serious injuries.

The theoretical model has first been proposed to understand the influence of numerous factors on the controllability of spring-powered jet injection. The model proposed various controllability factors for the injection. A study conducted by Chen and Zhou [18] revealed that the maximum pressure that a jet can exert upon the skin is known as stagnation pressure. A similar method was used by Taberner et al. [19] for controlling a prototype jet injector. A custom-made, high stroke linear electromagnetic-force motor was used to control the flow of a drug through a jet injection device. Through this procedure, the researchers were able to improve the efficiency of the drug's injection. The goal was to improve the model by identifying the factors that affect the penetration capability of an injection, but this was not yet possible due to the lack of friction and hydraulic loss in the system. The concept of particle growth and nucleation during the partial expansion of dilute supercritical solutions is presented.

4 Mixing Geometry

This paper portrays an exploratory investigation of a steam-ejector cooler utilizing an ejector with an essential nozzle that could be moved pivotally inside the blending chamber area [20]. The results for the coefficient of execution and cooling limit created by changing the operating conditions of the nozzle were considered. The test

apparatus and technique are depicted, and results are introduced, which unmistakably show the advantage of utilizing a particularly essential nozzle. Smith-Kent et al. [21] stated that the ordinary strong rocket engines have an appropriate fuel grain size and the diameter of the throat of the nozzle for the push. Pintle nozzles have been proposed as a method for giving variable and programmable push inside specific cut-off points. Subsequently, a pintle nozzle can provide a strong rocket engine. This paper audits the one-dimensional investigation to incorporate the conditions expected to be the best for an ejector working in a refrigeration cycle [22]. The considered arrangement gives a more prominent pressure proportion while utilizing a similar measure of essential mass flow. The outcomes obtained show that utilizing the third stage, the ideal gas model used could lose actual significance [23]. The current paper fostered a thermodynamic displaying strategy for ejectors utilized in discharge refrigeration framework [24]. For a fixed-geometry ejector, the cooling limit was observed to be restricted by the condenser pressure. The cooling limit could be improved with a higher set evaporator temperature. Furthermore, with lower condenser pressures, a bigger cooling limit could be accomplished with even lower evaporator pressures [25]. It is hypothesized that the secondary fumes arrive at sonic speed and are successfully choked at some cross-part of the ejector. Standard estimations of spout stream empower the limit of the ejector to be found, and thusly a forecast of steam nozzle cooler execution occurs [26]. In this review, an ejector model was created for the assessment of fume ejector execution. In this model, real gas conditions are thought of. The scope of its applications is not limited to dry fume ejectors as on account of the 1D technique. The proposed model thinks about the energy transfer between the two streams (essential and optional) during their connection in the mixing chamber, until the auxiliary stream is introduced [27]. The CFD investigation was performed for the supersonic stream in the consistent strain blending ejector. The CFD result was approved with test information. From this approval, it can be presumed that CFD reproduction has a decent similarity with test results [28]. This review utilized CFD methods to explore the stream construction and execution of an ejector utilized in a MED framework. The impacts of different forces on the ejector execution were examined. The CFD results were observed to be in good concurrence with the exploratory outcomes [29].

The ideal upsides of two significant ejector geometry boundaries in this work: essential spout exit position and meeting point of blending segment, were examined by CFD procedure. The CFD model was first and foremost adjusted with genuine exploratory information. Afterward, the model design was utilized to create as numerous as 95 distinct ejector calculations and 210 unique geometries. The impacts of the two calculation boundaries on the ejector execution were separately investigated [30]. The thermo-blower in MED-TVC plants ought to be intended for higher release strain. Blending proficiency of a common thermo-blower has a direct effect after entraining pace of low-pressure steam [31]. The observations were made on how the ideal region ratios and COP esteems changed with the differing temperature. The ideal region proportion increases with generator temperature diminish with condenser temperature and are significantly less influenced by the variety in evaporator temperature [32]. It was checked that the CFD is an effective way to

foresee the entrainment proportion and essential back pressure of the ejector. The arranged ejector exhibitions from the trial and the computations show the exactness of the model. The benefits of CFD over other regular strategies were proposed. The review showed that the built CFD model may not address the examination ejector impeccably. Subsequently, a few enhancements for the model arrangement and the computation space are required [33]. In this research, the definition predicts a variety of various stream boundaries viz., Mach number, static tension, of the CRMC ejector. The scientific results have good concurrence with re-enactment and trial results demonstrating the viability of the model. Further, the advantage of utilizing the present scientific model contrasted with the isentropic model has likewise been introduced [34].

5 Diffuser Geometry

In this work, the calculation advancement of the ejector in the SOFC framework was mathematically explored using CFD. Ideal upsides of the four significant calculation boundaries like nozzle divergent part length, nozzle exit position, mixing chamber length, and diffuser length were studied for a wide scope of activity conditions [35]. In this study, the CFD model was first and foremost approved with the real trial results. The authors used different parameters for the adjustable ejector in the multi-evaporator refrigeration system [36]. A small-capacity heat pump was studied with the best ejector geometry experimentally and numerically. Various ejector lengths and diameters for the mixer section and different angles for the diffuser were considered. After the proper investigation, it was observed that the length and the angles had a huge impact [37]. The effect of different length of diffuser section was also analyzed on the performance of the ejector and suggested that the optimum length of the diffuser section plays a significant role in the enhancement of ejector performance [38].

6 Mathematical Modeling of Ejector

Zhu et al. [39] studied another displaying strategy for ejectors with high entrainment proportion, lower pressing factor increase, and overheated working fluid in anodic distribution [40]. A commonplace SOFC framework incorporates an energy component stack and fringe parts. They include a heat exchanger, fuel processor, blender, and a reformer [41]. The framework is built with no moving parts and minimum support by utilizing high pressing factor fuel gas as an essential liquid to suck the anodic depletes [39]. The energy spent on the fuel compression is almost 7% of that of the total power [42]. An outrageous consideration ought to be taken in the ejector plan and operation for ideal framework execution. A precise fuel ejector model and

the assessment of on-plan and off-plan exhibitions are fundamental [25]. The practices of an ejector identified with entrainment limit, steam to carbon proportion, and outlet temperature are unequivocally impacted by the calculations and functional states of the ejector [43]. In any case, the greater part of the current models is created based on 1D procedures for cooling and refrigeration applications. These displaying techniques will cause enormous blunders to demonstrate fuel ejectors in SOFC frameworks because of the distinctions in calculations, working liquids properties, and working conditions. Eames et al. [44] depicted improvements in refrigeration cycle execution. The design of ejectors for pressure energy recuperation requires an itemized examination of the inward ejector, working attributes, and geometry. To this point, a trial and mathematical analysis of an ejector refrigeration framework are led to decide the impact of the main ejector measurements, primary working conditions on ejector working qualities, and cycle execution. Results show that an increment in the essential measurement prompts the twofold improvement of the general ejector productivity [45]. Natthawut Ruangtrakoon [46] conducted a mathematical study of the essential nozzle on the ejector execution in an R141b ejector refrigeration. Essential nozzle region proportion is fluctuated to notice its impact on the ejector execution. Six essential nozzles are examined tentatively, and four of them are planned with various throat distances. It was discovered that utilizing a greater nozzle throat worked with lower generator temperature. The goal was that the ejector will be functional at its best execution. Eilers et al. [47] introduced streamlined push vectoring results from logical and test examinations on a limited scope aerospike engine. The push vectoring framework utilizes four auxiliary infusion ports situated at around half of the nozzle length. The subsequent low-pressure base-region diminishes by large push levels. 2D strategy for qualities was utilized to measure the framework and permitted estimation of the ideal nozzle shapes. Mathematical model of supersonic ejector using 1D gas dynamic theory for real fluid by incorporating real gas equation of state (Redlich-Kwong equation) proposed [48] and analyzed numerically.

7 Ejector Applications

Eilers et al. [49] in this paper give a writing audit on ejectors, their parts, and their applications in refrigeration systems. Various examinations are gathered and discussed in a few subjects. They include the foundation and hypothesis of ejector and stream refrigeration cycle, execution attributes, refrigerant, and optimization of stream cooler. Besides, uses of an ejector in various sorts of refrigeration systems are portrayed. Some part of the energy delivered in the ignition is lost to the environmental factors as waste. This waste heat can be used in certain kinds of refrigeration systems [50, 51]. It is trusted that this paper will be valuable for any newbie in this field of refrigeration advances. The core of the ejector refrigeration framework was designed by Sir Charles Parsons around 1901 to eliminate air from a steam motor's condenser. In 1910, an ejector was utilized by Maurice Leblanc in the first steam jet

refrigeration system [52]. This system experienced a rush of prominence during the mid-1930s for air molding massive structures [53]. Steam jet refrigeration frameworks were later replaced by frameworks utilizing mechanical blowers. Since then, improvement and refinement of the steam refrigeration framework have been nearly at a stop as most endeavors have been focused on further developing fume pressure refrigeration frameworks [54–57].

8 Summary and Future Scope

A comprehensive review of the fundamental background of ejectors and the working conditions they operate on is presented. Many researchers aimed to present their findings on the factors that vary the operation of the ejector and its application. It was concluded that the working of the ejector depends upon the various boundary conditions that many authors varied to study the changes in the flow field. This was carried out to improve the working of the ejector. It was observed that the ejector has many applications, and one of them is in refrigeration or cooling systems. Since each vehicle nowadays comprises an air conditioning system, they can be used in stages to improve efficiency. As of now, we can presume that the complete understanding of the ejectors is not achieved. New presumptions on blending and streaming qualities were constantly settled and applied to the numerical model and virtual experience examination. Even though these reenacted results were professed to turn out to be more precise than others, not very many of them were tentatively checked and endorsed. But we can say that the mathematical investigations could help us understand the ejectors, and it very well may be presumed that there is yet a need to continue the research around here.

References

1. Su L (2015) CFD simulation and shape optimization of supersonic ejectors for refrigeration and desalination applications
2. Hart JH (2002) Supersonic ejector simulation and optimisation. Doctoral dissertation, University of Sheffield
3. Gurulingam S (2014) Investigations on enhancement of entrainment ratio in jet ejector using forced draught. Doctoral dissertation, Department of mechanical engineering, Pondicherry engineering college
4. Olaru I (2020) A fluid flow analysis of a jet ejector system used in industrial applications. *J Eng Stud Res* 26(3):143–147
5. Wang L, Yan J, Wang C, Li X (2017) Numerical study on optimization of ejector primary nozzle geometries. *Int J Refrig* 76:219–229
6. Hu J, Shi J, Liang Y, Yang Z, Chen J (2014) Numerical and experimental investigation on nozzle parameters for R410A ejector air conditioning system. *Int J Refrig* 40:338–346
7. Besagni G, Mereu R, Inzoli F (2016) Ejector refrigeration: a comprehensive review. *Renew Sustain Energy Rev* 53:373–407

8. Ringstad KE, Allouche Y, Gullo P, Ervik Å, Banasiak K, Hafner A (2020) A detailed review on CO₂ two-phase ejector flow modelling. *Thermal Sci Eng Progress*, 100647
9. Guillaume DW, Judge TA (1999) Improving the efficiency of a jet pump using an elliptical nozzle. *Rev Sci Instrum* 70(12):4727–4729
10. Chang YJ, Chen YM (2000) Enhancement of a steam-jet refrigerator using a novel application of the petal nozzle. *Exp Thermal Fluid Sci* 22(3–4):203–211
11. Narabayashi T, Yamazaki Y, Kobayashi H, Shakouchi T (2006) Flow analysis for single and multi-nozzle jet pump. *JSME Ser. B.* 49(4):933e939
12. Kumar A, Kumar V, Subbarao PMV, Yadav SK, Singhal G (2021) Numerical assessment on the performance of variable area single-and two-stage ejectors: A comparative study. In: *Proceedings of the Institution of Mechanical Engineers, Part E: Journal of Process Mechanical Engineering*, 09544089211033129
13. Yadav SK, Pandey KM, Kumar V, Gupta R (2021) Computational analysis of a supersonic two-stage ejector. *Materials Today: Proceedings* 38:2700–2705
14. Yadav SK, Kumar V, Pandey KM, Gupta R (2021) Development of the constant rate of momentum change (CRMC) variable area nozzle. *Materials Today: Proceedings* 38:2325–2331
15. Khan SA, Aabid A, Baig MAA (2018) CFD analysis of CD nozzle and effect of nozzle pressure ratio on pressure and velocity for suddenly expanded flows. *Int J Mech Produc Eng Res Develop* 8(3):1147–1158
16. Varga S, Oliveira AC, Ma X, Omer SA, Zhang W, Riffat SB (2011) Comparison of CFD and experimental performance results of a variable area ratio steam ejector. *International Journal of Low-Carbon Technologies* 6(2):119–124
17. Zeng D, Kang Y, Xie L, Xia X, Wang Z, Liu W (2018) A mathematical model and experimental verification of optimal nozzle diameter in needle-free injection. *J Pharm Sci* 107(4):1086–1094
18. Chen K, Zhou H (2011) An experimental study and model validation of pressure in liquid needle-free injection. *Int J Phys Sci.* 6:1552–1562
19. Taberner AJ, Ball NB, Hogan NC, Hunter IW (2006) A portable needle-free jet injector based on a custom high power-density voice-coil actuator. *Conf Proc IEEE Eng Med Biol Soc* 1:5001–5004
20. Li Y, Deng J, Ma L (2019) Experimental study on the primary flow expansion characteristics in transcritical CO₂ two-phase ejectors with different primary nozzle diverging angles. *Energy* 186:115839
21. Smith-Kent R, Loh HT, Chwalowski P (1995) Analytical contouring of pintle nozzle exit cone using computational fluid dynamics. In: *31st Joint Propulsion Conference and Exhibit*, p 2877
22. Khoury F, Heyman M, Resnick W (1967) Performance characteristics of self-entrainment ejectors. *Ind Eng Chem Process Des Dev* 6(3):331–340
23. Grazzini G, Mariani A (1998) A simple program to design a multi-stage jet-pump for refrigeration cycles. *Energy Convers Manage* 39(16–18):1827–1834
24. Ma Z, Bao H, Roskilly AP (2017) Thermodynamic modelling and parameter determination of ejector for ejection refrigeration systems. *Int J Refrigeration* 75:117–128
25. Eames IW, Aphornratana S, Haider H (1995) A theoretical and experimental study of a small-scale steam jet refrigerator. *Int J Refrig* 18(6):378–386
26. Munday JT, Bagster DF (1977) A new ejector theory applied to steam jet refrigeration. *Ind Eng Chem Process Des Dev* 16(4):442–449
27. Cardemil JM, Colle S (2012) A general model for evaluation of vapor ejectors performance for application in refrigeration. *Energy Convers Manage* 64:79–86
28. Utomo T, Ji M, Kim P, Jeong H, Chung H (2008) CFD analysis on the influence of converging duct angle on the steam ejector performance. *Eng Opt*, 2–8
29. Ji M, Utomo T, Woo J, Lee Y, Jeong H, Chung H (2010) CFD investigation on the flow structure inside thermo vapor compressor. *Energy* 35(6):2694–2702
30. Zhu Y, Cai W, Wen C, Li Y (2009) Numerical investigation of geom-etry parameters for design of high-performance ejectors. *Appl Therm Eng* 29(5–6):898–905
31. Kouhikamali R, Sharifi N (2012) Experience of modification of thermo compressors in multiple effects desalination plants in Assaluyeh in IRAN. *Appl Therm Eng* 40:174–180

32. Yapıcı R, Ersoy HK (2005) Performance characteristics of the ejector refrigeration system based on the constant area ejector flow model. *Energy Convers Manage* 46(18–19):3117–3135
33. Sriveerakul T, Aphornratana S, Chunnanond K (2007) Performance prediction of steam ejector using computational fluid dynamics: Part 1. Validation of the CFD results. *Int J Thermal Sci* 46(8):812–822
34. Kumar V, Singhal G, Subbarao PMV (2013) Study of supersonic flow in a constant rate of momentum change (CRMC) ejector with frictional effects. *Appl Thermal Eng* 60(1–2):61–71
35. Zhu Y, Jiang P (2011) Geometry optimization study of ejector in anode recirculation solid oxygen fuel cell system. In: 2011 6th IEEE Conference on Industrial Electronics and Applications, pp. 51–55. IEEE
36. Lin C, Cai W, Li Y, Yan J, Hu Y, Giridharan K (2013) Numerical investigation of geometry parameters for pressure recovery of an adjustable ejector in multi-evaporator refrigeration system. *Appl Therm Eng* 61(2):649–656
37. Banasiak K, Hafner A, Andresen T (2012) Experimental and numerical investigation of the influence of the two-phase ejector geometry on the performance of the R744 heat pump. *Int J Refrig* 35(6):1617–1625
38. Yadav SK, Pandey KM, Gupta R, Kumar V (2021) Numerical study for the influences of nozzle exit position, mixing, and diffuser section lengths on performance of CRMC ejector. *J Braz Soc Mech Sci Eng* 43(11):1–14
39. Zhu Y, Cai W, Wen C, Li Y (2007) Fuel ejector design and simulation model for anodic recirculation SOFC system. *J Power Sources* 173(1):437–449
40. Benjamin TG, Camera EH, Marianowski LG (1995) Handbook of fuel cell performance. Institute of Gas Technology
41. Dicks AL (1996) Hydrogen generation from natural gas for the fuel cell systems of tomorrow. *J Power Sources* 61(1–2):113–124
42. Peters R, Riensche E, Cremer P (2000) Pre-reforming of natural gas in solid oxide fuel-cell systems. *J Power Sources* 86(1–2):432–441
43. Huang BJ, Chang JM, Wang CP, Petrenko VA (1999) A 1-D analysis of ejector performance. *Int J Refrig* 22(5):354–364
44. Haghparast P, Sorin MV, Nesreddine H (2018) The impact of internal ejector working characteristics and geometry on the performance of a refrigeration cycle. *Energy* 162:728–743
45. Croquer S, Poncet S, Aidoun Z (2016) Turbulence modeling of a single-phase R134a supersonic ejector. Part 2: Local flow structure and exergy analysis. *Int J Refrig* 61:153–165
46. Ruangtrakoon N, Thongtip T, Aphornratana S, Sriveerakul T (2013) CFD simulation on the effect of primary nozzle geometries for a steam ejector in refrigeration cycle. *Int J Therm Sci* 63:133–145
47. Eilers S, Matthew W, Whitmore S (2010) Analytical and experimental evaluation of aerodynamic thrust vectoring on an aerospike nozzle. In: 46th AIAA/ASME/SAE/ASEE Joint Propulsion Conference & Exhibit, p 6964
48. Mohammadi S, Farhadi F (2013) Experimental analysis of a Ranque-Hilsch vortex tube for optimizing nozzle numbers and diameter. *Appl Therm Eng* 61(2):500–506
49. Chunnanond K, Aphornratana S (2004) Ejectors: applications in refrigeration technology. *Renew Sustain Energy Rev* 8(2):129–155
50. Hilsch R (1947) The use of the expansion of gases in a centrifugal field as cooling process. *Rev Sci Instrum* 18(2):108–113
51. Deisstter RG, Perlmutter M (1960) Analysis of the flow and energy separation in a turbulent vortex. *Int. J. Heat Mass transfer*. 1:173–191
52. Ahlborn BK, Groves S (1997) Secondary flow in a vortex tube. *Fluid Dyn Res* 21:73–86
53. Ahlborn BFK, Gorden JM (2000) The vortex tube as a classic thermodynamic refrigeration cycle. *J Appl Phys* 88(6):3645–3653
54. Guan T, Zhang JZ, Shan Y, Hang J (2017) Conjugate HT on leading edge of a conical wall subjected to external cold flow and internal hot jet impingement from chevron nozzle—Part 1: Experimental analysis. *Int J Heat Mass Transf* 106:329–338

55. Katoch M, Kumar K, Dahiya V (2021) Dust accumulation and reduction in electrical performance of solar PV panels. *Materials Today: Proceedings*
56. Yadav SK, Pandey KM, Gupta R (2021) Analytical and Numerical study on the performance of supersonic ejector at different operating conditions and working fluids. *J Appl Fluid Mech* 14(6):1705–1716
57. Yadav SK, Pandey KM, Gupta R (2021) Recent advances on principles of working of ejectors: a review. *Materials Today: Proceedings* 45:6298–6305

Computational Analysis on the Flow Behavior and Performance Evaluation of Single and Double Offset Butterfly Valves



Kushal Saxena , Nivedita Bhadauria , and Vivek Kumar Patel 

Abstract Valves are the key components for the safety of the professionals working on the machineries involved in the functioning of any industry. There are various sectors in which machinery like pump, turbines, and boilers are working in which flow and pressure regulations are the parameters to be controlled for their efficient and safe performance. Butterfly valves are one of the tools which implement the flow regulating mechanism to manage the flow of certain incompressible and compressible fluids. Butterfly valves are a light weight, low cost, and easily operateable. It is a quarter turn valve, includes a disk that rotates by right angle (90°) to regulate the flow of fluids. The foremost purpose of this study is to analyze the flow behavior of a butterfly valve. CFD analysis using ANSYS Fluent has been carried out in this work to compute various performance parameters responsible for characterization of a butterfly valve. In this present study, simulation of a 2.9 m butterfly valve has been carried out at 0.1 m single offset and 0.1 m double offset for discharge of $21.2 \text{ m}^3/\text{s}$. Based on the various literature surveys, eight different valve opening positions 20° , 30° , 40° , 50° , 60° , 70° , 80° , and 90° were selected. CFD analysis provided better interpretations for flow behavior and performance parameters. The study concluded that flow coefficient had a major dependency on opening angle than offset. In comparison to 0.1 m single offset, the double offset have a better characteristic.

Keywords Butterfly valves · Computational fluid dynamics · Torque · Pressure drop · Opening angles

K. Saxena (✉)

Department of Mechanical Engineering, Rajkiya Engineering College Mainpuri, Mainpuri, Uttar Pradesh, India

e-mail: kushal.saxena@recremainpuri.in

N. Bhadauria

Air India Engineering Services Limited, Kolkata, West Bengal, India

V. K. Patel

Department of Applied Mechanics, Motilal Nehru National Institute of Technology Prayagraj, Prayagraj, Uttar Pradesh, India

e-mail: vivek@mnnit.ac.in

1 Introduction

Today, as fossil fuels are depleting and very high hikes in their prices, the researchers are shifting toward cheaper, renewable, and less polluting resources. Valves serve a very important role in well-functioning of the key components of any power industry. For heavy machineries, valves serve as the most important safety equipment. Butterfly valves serve as the easy installation and the low cost valve to regulate the flow control operations. Technically, butterfly valve is a rotary equipment to control the flow of any fluid in a system. It mainly consists of a disk, to rotate up to 90°. Due to this feature, it gains popularity as a quarter turn valve. It operates to regulate the flow in a linear or bidirectional manner. Butterfly valves offer a large number of advantages such as lightweight, compact size, easy to operate and install. They are highly applicable to HVAC, high temperature applications, petroleum industries, wastewater treatment, and fire protection systems. A butterfly valve comprises of valve body, disk, seat, and stem. A butterfly valve is considered to be a member of quarter turn valve's family. The disk is the most important part responsible for its working to regulate the flow passage area. As the valve is said to be closed, the disk has to be turned through some actuator may be a manual lever or some gear mechanism which will restrict the flow. The disk has to be again rotated by a 90° turn to allow the opening of the valve which will allow the flow to begin. Rahmeyer et al. [1] contributed with his efforts to analyze the performance of butterfly valve. Flow coefficient is considered to be a major parameter to contribute in the performance of a butterfly valve. The research produces two different standards ISA S39.2 and ISA S75.02 to compute the flow coefficient during laboratory testing. Ogawa Kazuhiko et al. [2] experimentally investigated the hydrodynamic characteristics and torque coefficient of a butterfly valve. The work concluded that the modified torque equations considering the effects of pipe walls provided accurate hydrodynamic characteristics for study of actual butterfly valves. Lin Fangbiao et al. [3] performed an experimental investigation using a coin-shaped disk located perpendicular to the flow and validated the results with computational fluid dynamics (CFD). Several performance parameters including drag, lift, moment, and discharge coefficients were quantified at different angles. The work concluded that CFD analysis provided reasonable results that were validated with the experimental data obtained from the tests performed on the coin-shaped disk. Song Guan Xue et al. [4] investigated the hydrodynamic flow characteristics of a butterfly valve with the help of numerical method of analysis using CFX. Flow patterns were visualized to quantify the different coefficients. CFX provided pressure contours, velocity contours, and streamlines to study the flow behavior, and the graph depicted accuracy between the experimental and simulated results for around 20° opening angles. Henderson et al. [5] through a numerical study emphasized on the torque being acted on a safety valve employed in a hydropower generation system. CFD assisted in prediction of torque coefficient, and its results were in well accordance with the experimental results. Prema et al. [6] optimized the design of a butterfly valve using CFD by figuring out the effects of certain flow parameters including pressure difference and flow coefficient for different designs

of valves. The computed values of the parameters depicted a significant increase for optimized design compared to the baseline design. Jun et al. [7] applied topology optimization techniques to design the structure of double eccentric butterfly valve. ANSYS CFX simulations were carried out to validate the results of optimization techniques. Bhosale et al. [8] analyzed the stresses induced in a butterfly valve disk using finite element method. At the specified pressure of 1.3 MPa, 47.174 N/mm² stress was induced which was much below the yield stress of the material that concluded that the safety of the valve. Elbakhshawangy et al. [9] numerically investigated the attributes for an incompressible, viscid, and turbulence flow through a 20 cm valve diameter butterfly valve. The numerical results concluded that there was a large dependency of the flow characteristics on the opening angles for the valve. Xun et al. [10] in the numerical investigation made an observation that there is a direct proportional dependency of surface roughness on the flow parameters such as pressure drop in an eccentric butterfly valve. Rajesh [11] et al. analyzed the self-regulated flow device used for the cooling mechanism of electronic modules in data center. Kan and Chen [12] numerically studied the flow behavior for a link rod-operated butterfly valve designed for high enthalpy steam. The results of the study served a great purpose in the designing of the link rod butterfly valves. The survey of the literature focused on the optimization in design of the butterfly valves as serves as an essential component responsible for the safely working of various engineering devices, and CFD analysis provided accuracy in results on being validated with the experimental works. The present work employed CFD to analyze the performance parameters of an offset butterfly valve.

2 Methodology and Validation

2.1 Governing Equations

Following equations are used in the numerical calculation of various flow parameters and flow patterns:

Continuity Equation:

$$\frac{\partial u}{\partial x} + \frac{\partial v}{\partial y} + \frac{\partial w}{\partial z} = 0$$

Navier–Stokes Momentum Equation:

$$X \text{ - direction} \rightarrow u \frac{\partial u}{\partial x} + v \frac{\partial u}{\partial y} + w \frac{\partial u}{\partial z} = -\frac{1}{\rho} \frac{\partial u}{\partial x} + \nu (\nabla^2 u)$$

$$\begin{aligned}
 Y \text{ - direction} & \text{---} u \frac{\partial v}{\partial x} + v \frac{\partial v}{\partial y} + w \frac{\partial v}{\partial z} = -\frac{1}{\rho} \frac{\partial v}{\partial x} + \vartheta (\nabla^2 v) \\
 Z \text{ - direction} & \text{---} u \frac{\partial w}{\partial x} + v \frac{\partial w}{\partial y} + w \frac{\partial w}{\partial z} = -\frac{1}{\rho} \frac{\partial w}{\partial x} + \vartheta (\nabla^2 w)
 \end{aligned}$$

Reynolds-averaged Navier–Stokes Equation (RANS):

$$\begin{aligned}
 X \text{ - direction} & \text{---} \operatorname{div}(UU) = -\frac{1}{\rho} \frac{\partial P}{\partial x} \vartheta \operatorname{div}(\operatorname{grad} U) \\
 & \quad + \frac{1}{\rho} \left[\frac{\partial(-\rho \overline{u'^2})}{\partial x} + \frac{\partial(-\rho \overline{u'v'})}{\partial y} + \frac{\partial(-\rho \overline{u'w'})}{\partial z} \right] \\
 Y \text{ - direction} & \text{---} \operatorname{div}(VU) = -\frac{1}{\rho} \frac{\partial P}{\partial y} \vartheta \operatorname{div}(\operatorname{grad} V) \\
 & \quad + \frac{1}{\rho} \left[\frac{\partial(-\rho \overline{u'v'})}{\partial x} + \frac{\partial(-\rho \overline{v'^2})}{\partial y} + \frac{\partial(-\rho \overline{v'w'})}{\partial z} \right] \\
 Z \text{ - direction} & \text{---} \operatorname{div}(WU) = -\frac{1}{\rho} \frac{\partial P}{\partial z} \vartheta \operatorname{div}(\operatorname{grad} W) \\
 & \quad + \frac{1}{\rho} \left[\frac{\partial(-\rho \overline{u'w'})}{\partial x} + \frac{\partial(-\rho \overline{v'w'})}{\partial y} + \frac{\partial(-\rho \overline{w'^2})}{\partial z} \right]
 \end{aligned}$$

Realizable k - ε turbulence model:

$$\text{Transport equation for } k \text{---} \frac{\partial(\rho k u_j)}{\partial x_j} = \frac{\partial}{\partial x_j} \left[\left(\mu + \frac{\mu_t}{\sigma_k} \right) \frac{\partial k}{\partial x_j} \right] + G_k - \rho \varepsilon$$

$$\begin{aligned}
 \text{Transport equation for } \varepsilon & \text{---} \frac{\partial(\rho \varepsilon u_j)}{\partial x_j} = \frac{\partial}{\partial x_j} \left[\left(\mu + \frac{\mu_t}{\sigma_\varepsilon} \right) \frac{\partial \varepsilon}{\partial x_j} \right] \\
 & \quad + \rho C_1 S_\varepsilon - \rho C_2 \frac{\varepsilon^2}{k + \sqrt{v \varepsilon}}
 \end{aligned}$$

Fig. 1 Computational domain of the pipe with butterfly valve

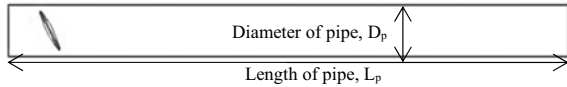


Fig. 2 Validation of present computational study with Henderson et al.

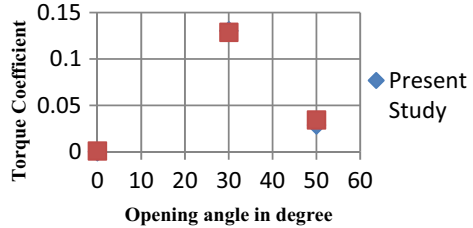


Table 1 Error percentage between present study and Henderson et al.

Degree	Henderson et al	Present study	Error %
0°	0	2.988×10^{-5}	0.003
30°	0.1287	0.1304	1.32
50°	0.0344	0.03126	9.12

2.2 Validation

The geometry of butterfly valve as discussed in the research paper of Henderson et al. [5] has been taken for validation of CFD code. The geometry consists of a symmetric valve of 3.046 m diameter with maximum thickness of 510 mm and minimum thickness of 0 mm in a 3.056 m-diameter and 54 m-long pipe as shown in Fig. 1. The CFD code was tested by comparing the torque coefficient and velocity contour of butterfly valve at three different opening angles, i.e., 0°, 30°, and 50°. An overall average error of 3.5% is obtained which can be justified with difference of geometry and solver used in both cases. Results obtained for validation can be seen in Fig. 2. Table 1 depicts the error percentage between the present computational study, and the Henderson et al. work for the values of torque coefficient.

2.3 Geometry

The present study involves a 3D analysis of a symmetric butterfly valve about its pipe axis. It consists of a pipe of 3.056 m diameter and 54 m long and a valve of 2.9 m diameter with maximum thickness of 510 mm and minimum thickness of 100 mm as shown in Fig. 3. The parametric study was conducted for two offset configuration, i.e., 0.1 m single offset and 0.1 m double offset in x and z direction as shown in Fig. 4a and b, respectively. The flow at inlet is a user-defined profile of fully developed turbulent velocity profile.

Fig. 3 Valve geometry

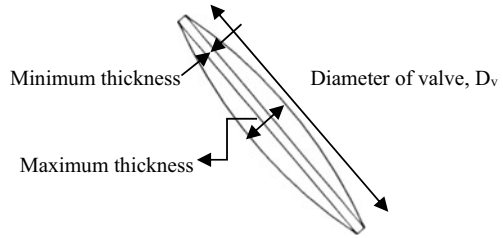
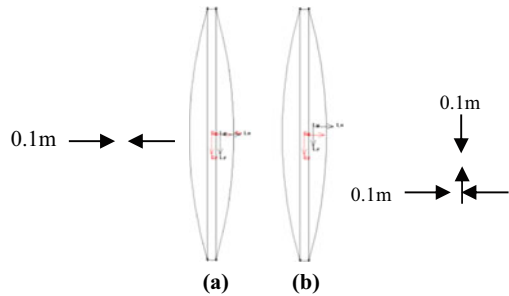


Fig. 4 **a** 0.1 m single offset
b 0.1 m double offset



2.4 Grid Generation and Discretization Scheme

A fine mesh as shown in Fig. 5 was generated across the butterfly valve to get a better flow pattern. A grid independence test was performed with fully open condition of butterfly valve, i.e., at 90° opening angle with a flow rate of $21.2 \text{ m}^3/\text{s}$ by considering pressure drop across the butterfly valve. Grid independency test was performed during the computational work to determine the differences in the results with the change in grid number. The drop in pressure was considered for the grid independency test. The results for the grid size are depicted in Table 2 and Fig. 6. In order to solve pressure–velocity coupling equation, SIMPLE solution scheme is used. A second-order upwind differencing scheme is used for numerical analysis.

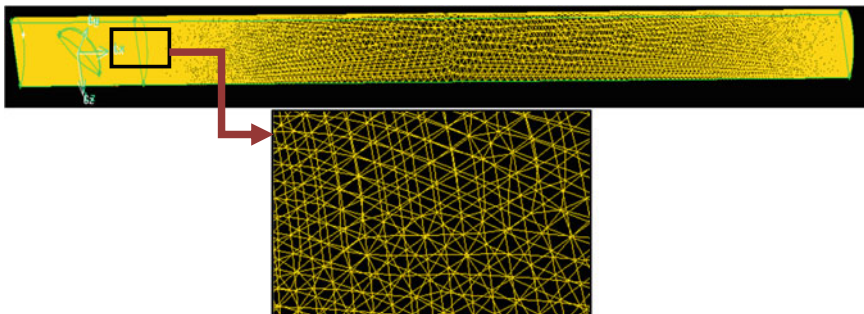


Fig. 5 Grid generation

Table 2 Grid independency test

Grid size	Pressure head
2.5×10^6	134.246
2.9×10^6	130.013
3.1×10^6	130.008

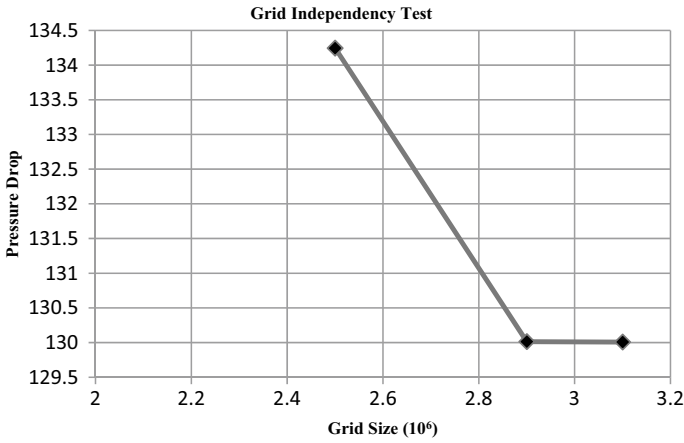


Fig.6 Grid independency test

3 Results and Discussions

Pressure drop, flow coefficient, loss coefficient, and torque coefficient are some of the parameters responsible for the working of butterfly valve. The parametric study conducted for various valve opening angles, i.e., 20° , 30° , 40° , 50° , 60° , 70° , 80° , and 90° , where 0° being fully open condition. The flow conditions and performance parameters calculated are given in Table 3.

Figure 7 compared torque coefficient of both valve configurations. It can be seen that there is a slight difference in C_t value at 20° opening angle but a significant difference at 50° opening angle. It can also be seen that in both configurations, the C_t value first gradually increases and then suddenly decreases to minimum with

Table 3 Flow conditions and performance parameters

Offset value	Performance Parameters	Operating Angle	Flow conditions
0.1 m single	Pressure drop, hydrodynamic torque, torque coefficient, Flow coefficient, loss coefficient	20, 30, 40, 50, 60, 70, 80, and 90	Discharge— $21.2 \text{ m}^3/\text{s}$ Velocity— 2.91 m/s Reynolds no— 8.8×10^6
0.1 m double			

maximum value at 80° opening angle. On comparing results of both configurations between 30° and 80°, opening an overall improvement of 21% is obtained for 0.1 m double offset valve. Figure 8 compared flow coefficient of both valve configurations. There is a significant difference in C_v value at 50° opening angle, but for rest of the positions, there is very small variation between both the configurations. Figure 9 compared loss coefficient of both valve configurations. It can be seen that in both valve configurations, loss coefficient decreases as the opening angle increases and becomes asymptomatic from 60° opening. On overall improvement of 4% is obtained between 20° and 70° opening angle in case of double offset valve as compared to single offset valve.

Figures 10a, 11a, 12a, 13a, 14a, 15a, and 16a represent the static pressure difference of 0.1 m single offset valve, and Figs. 10b, 11b, 12b, 13b, 14b, 15b, and 16b represent the static pressure difference of 0.1 m double offset valve at various opening angles. From the figures, it can be seen that static pressure difference for both configurations is decreasing as the area between pipe surface and valve is increasing. Static pressure difference becomes least for 0.1 m double offset valve from 50° opening angle onward.

Figures 17a, 18a, 19a, 20a, 21a, 22a, 23a, and 24a represent velocity contour of 0.1 m single offset butterfly valve, and Figs. 17b, 18b, 19b, 20b, 21b, 22b, 23b, and 24b represent the velocity contour of 0.1 m double offset butterfly valve. It can be seen from the velocity contour of both the configuration that a very large wake region

Fig. 7 Coefficient of torque versus opening angles

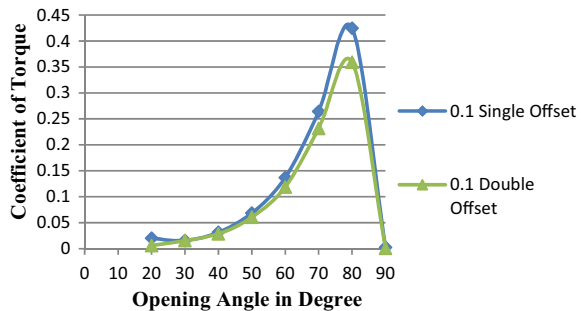


Fig. 8 Flow coefficient versus opening angles

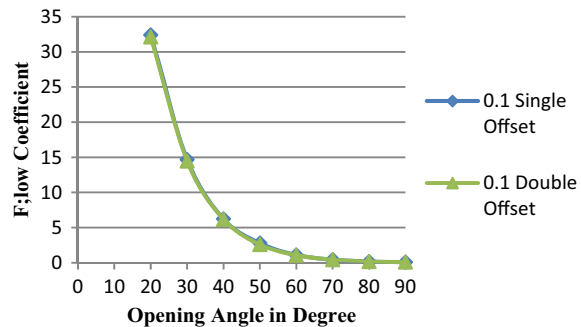


Fig. 9 Loss coefficient versus opening angles

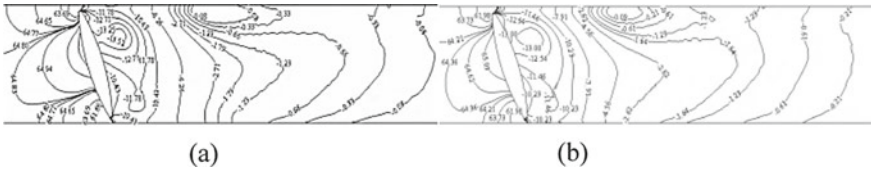
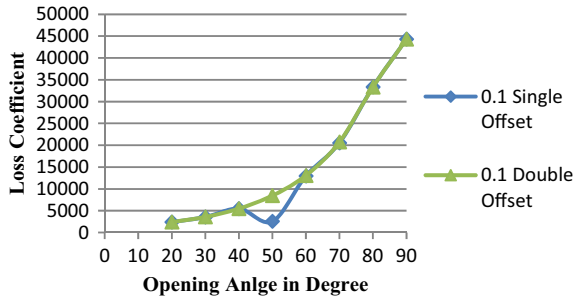


Fig. 10 Pressure variation at 20° opening

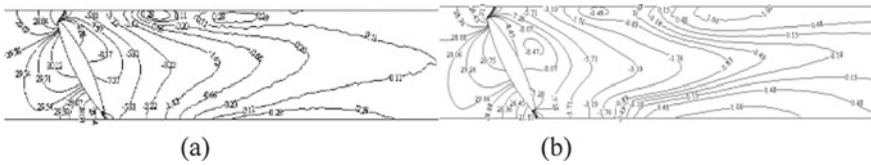


Fig. 11 Pressure variation at 30° opening

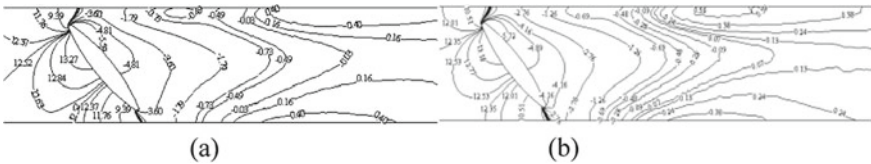


Fig. 12 Pressure variation at 40° opening

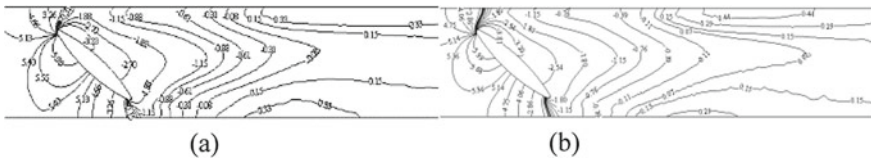


Fig. 13 Pressure variation at 50° opening

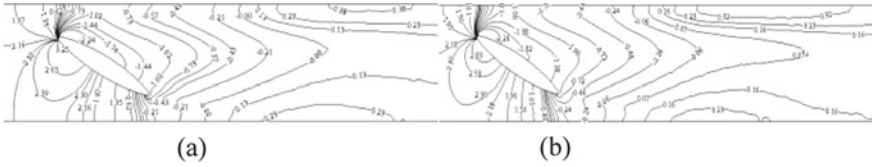


Fig. 14 Pressure variation at 60° opening

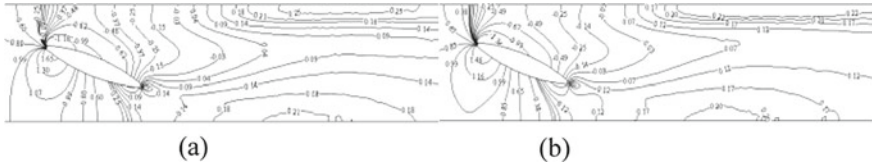


Fig. 15 Pressure variation at 70° opening

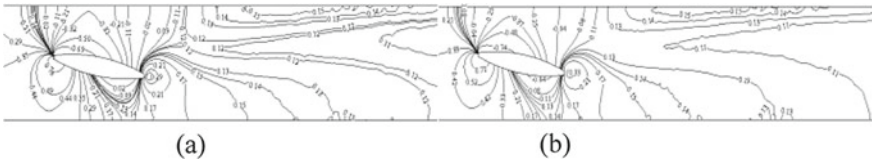


Fig. 16 Pressure variation at 80° opening

is present across the valve body between 20° and 30° opening angles but begins to decrease from 40° opening angle and becomes negligible from 60° opening angle, and flow becomes more attached to the valve disk. At 20° opening angle, vortices of very high intensity are generated at downstream of valve but begins to reduce with increase in opening angle as the area between pipe wall and valve increases. From 70° opening angle onward, a negligible region of vortices appeared only at the rear end of the valve.

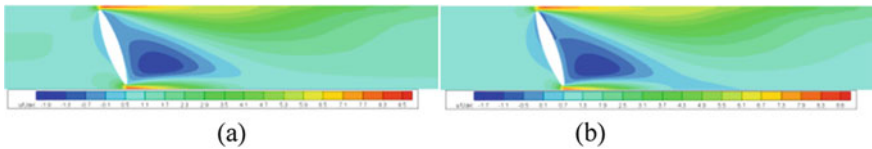


Fig. 17 Velocity contour at 20° opening

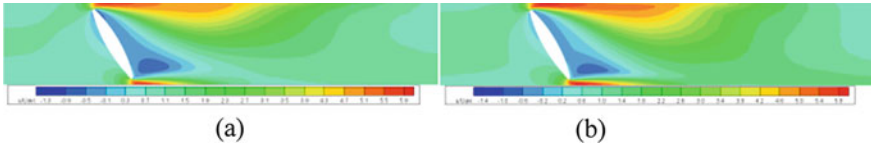


Fig. 18 Velocity contour at 30° opening

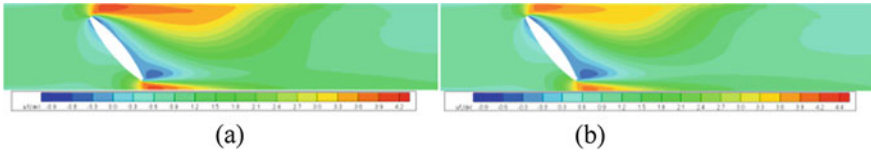


Fig. 19 Velocity contour at 40° opening

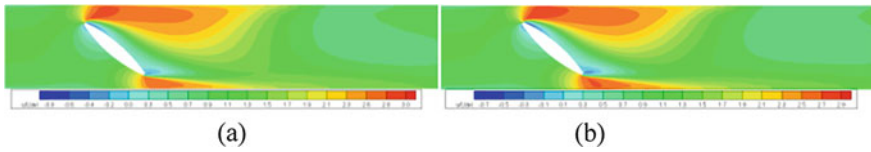


Fig. 20 Velocity contour at 50° opening

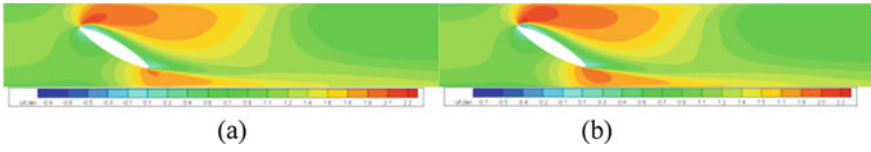


Fig. 21 Velocity contour at 60° opening

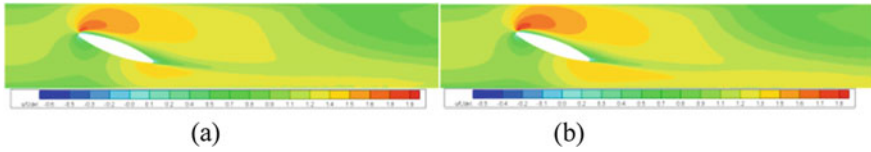


Fig. 22 Velocity contour at 70° opening

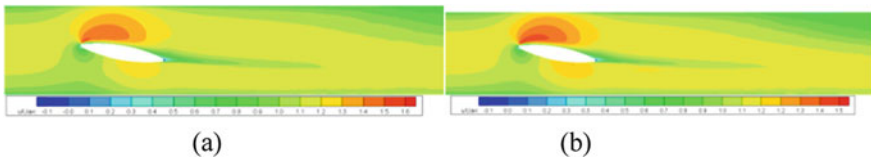


Fig. 23 Velocity contour at 80° opening

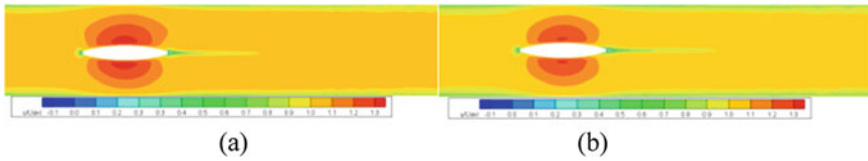


Fig. 24 Velocity contour at 90° opening

4 Conclusions

The present investigation of the flow over an offset butterfly valve is done by numerical method to depict the flow behavior and to compute various performance parameters such as pressure drop, hydrodynamic torque, torque coefficient, flow coefficient, and loss coefficient. Following conclusions can be drawn from the present computational work:

- a. There is a formation of wake region at low opening angles, i.e., between 20° and 40° , which leads to generation of high-intensity vortices or eddies downstream of the valve body. Because of this phenomenon, flow separation can be seen in between these angles. However, wake region practically disappears at higher opening angles.
- b. The torque coefficient and the loss coefficient vary with the change in opening angle as well as with the offset configuration.
- c. The value of loss coefficient obtained for double offset configuration is less as compared to that of single offset configuration for most of the opening angles.
- d. Whereas, a significant change in torque coefficient can be seen between the two valve configurations depicting that 0.1 m double offset valve offers less hydrodynamic torque as compared to that of 0.1 m single offset configuration.
- e. It can be concluded that flow coefficient is independent of the offset value, except at 50° opening angle, but it does change with the opening angle; therefore it is dependent only on degree of opening.
- f. Computational fluid dynamics proved to be a useful tool to predict very complex fluid flow problems, but it has few limitations which are mainly centered in turbulence modeling. It was found that between 20° and 40° opening angles CFD was not able to model the performance parameters.

References

1. Rahmeyer W, ASCE AM, Driskell L (1985) Control valve flow coefficient. *J Trans Eng* 111(4):358–364
2. Ogawa K, Kimura T (1995) Hydrodynamic characteristics of a butterfly valve-prediction of torque characteristics. *ISA Trans* 34:327–333

3. Lin F, Schohl GA (2004) CFD prediction & validation of butterfly valve hydrodynamic forces. ASCE, World Water Congress
4. Song XG, Park YC (2007) Numerical analysis of butterfly valve—prediction of flow coefficient & hydrodynamic torque coefficient. In: Proceedings of WCECS
5. Henderson AD, Sargison JE, Walker GJ, Haynes J (2008) A numerical prediction of the hydrodynamic torque acting on a safety butterfly valve in a hydro-electric power scheme. WSEAS Transactions on Fluid Mechanics, 1790–5087
6. Prema B, Bhojani S, Gopalakrishnan N (2010) Design optimization of butterfly valve using CFD. In: Proceedings of the 37th National & 4th International Conference on Fluid Mechanics and Fluid Power, IIT Madras, Chennai, India
7. Kim J-O, Min S, Heum Baek S, Kang S (2012) Structural design strategy of double—eccentric butterfly valve using topology optimization techniques. World Academy Sci, Eng Tech 66:469–474
8. Bhosale AT, Dhekane AS (2013) Finite element analysis of butterfly valve disc. Int J Eng Res Tech 2(7):2110–2114
9. Elbakhshawangy HF, Abd El-Kawi OS, Sarhan HH (2015) Numerical study of incompressible flow characteristics through butterfly valve. J Multidisciplinary Eng Sci Tech 2(7):1641–1652
10. Sun X, Kim HS, Yang SD, Kim CK, Yoon JY (2017) Numerical investigation of the effect of surface roughness on the flow coefficient of an eccentric butterfly valve. J Mech Sci Technol 31(7):2839–2848
11. Kasukurthy R, Challa PS, Palanikumar RR, Manimaran BR, Agonafer D (2018) Flow analysis and linearization of rectangular butterfly valve flow control device for liquid cooling. IEEE Itherm, 683–687
12. Kan B, Chen L (2020) Numerical analysis of flow field in link rod butterfly valve for high temperature steam. J Brazilian Soc Mech Sci Eng 42(202)

Spiral Wound Gasket in a Typical Liquid Engine Convergent-Divergent Nozzle



Suman Sharma, Chitaranjan Pany, R. Suresh, Sirajudeen Ahamed,
and C. K. Krishnadasan

Abstract Liquid engines with convergent-divergent nozzles are tested for their endurance capability through long duration hot tests. Gas entry at the fore end interface of metallic ring and silica phenolic throat may cause considerable charring, with the likelihood of throat erosion. To prevent this gas entry, a spiral wound gasket is worked out. Its design, thermo-structural analysis and effect on the system are presented in this paper.

Keywords Gasket · Throat · Nozzle · Interface · Liquid engine · Tightness class · Transient · Thermal · Thermo-structural analysis · Coefficient of thermal expansion

Abbreviations

A^*	Cross-sectional area at nozzle throat
A	Local cross-sectional area of flow
a	Leakage exponent
b_0	Basic gasket seating width (mm)
b	Effective gasket contact width (mm)
CTE	Coefficient of thermal expansion
c^*	Characteristic velocity
c_p	Specific heat at constant pressure
D^*	Diameter at nozzle throat

S. Sharma (✉) · C. Pany · R. Suresh · S. Ahamed · C. K. Krishnadasan
VSSC, Trivandrum, India
e-mail: suman_sharma@vssc.gov.in

C. Pany
e-mail: p_chitaranjan@vssc.gov.in

R. Suresh
e-mail: r_suresh@vssc.gov.in

S. Ahamed
e-mail: s_sirajudeen@vssc.gov.in

G	Effective gasket diameter (mm)
G _b	Gasket property to describe assembly loading curve (to achieve minimum tightness)
g	Gravitational acceleration
G _s	Gasket property to describe unloading curve (to achieve minimum tightness after load reduction associated with application of pressure)
h _g	Heat transfer coefficient
ID	Inner diameter
k _i	Thermal conductivity in ith direction
m	Gasket maintenance factor
MEOP	Maximum expected operating pressure
N	Gasket contact width (mm)
P	Design pressure (MPa)
p*	Atmospheric pressure (MPa)
Pr	Prandtl number
p _c	Chamber pressure
PVRC	Pressure Vessel Research Committee
q _c	Heat flux normal to surface
q _v	Heat generated per unit volume
r _c	Throat radius of curvature
RT	Room temperature
ROTT	Room temperature tightness test
SP	Silica phenolic
SWG	Spiral wound gasket
SS	Stainless steel
S _{ya}	Design assembly seating stress (MPa)
S _L	Minimum permitted value of operating gasket stress
S _{m1}	Required gasket operating stress for required joint tightness (MPa)
S _{mo}	Largest of S _{m1} , 2P and S _L (MPa)
TRR	Throat retainer ring
TSR	Throat seating ring
T _c	Tightness class factor
T _p	Dimensionless measure of tightness = ratio of pressure to square root of leak rate in dimensionless form
T _{pmin}	Minimum required tightness (value of T _p to ensure satisfactory leakage performance in operation for specified tightness class); must be greater than 1.1
T _{pmax}	Maximum permitted tightness for design
T _{pa}	Adjusted assembly tightness (value of T _p required to ensure T _{pmin} in operation)
T	Temperature
t	Time
T _w	Bulk fluid temperature
W _{m2}	Minimum load required for gasket seating (N)
y	Gasket seating stress

η	Assembly efficiency
ρ	Density
σ_{cf}	Variable properties correction factor
μ_g	Viscosity of combustion gases

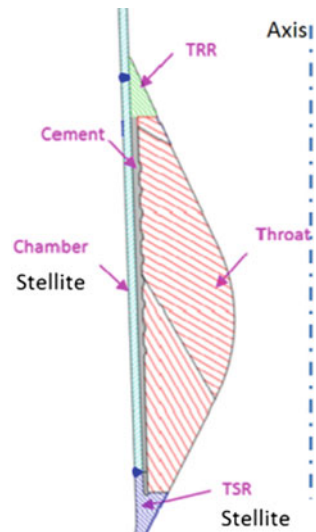
1 Introduction

Graphite, carbon phenolic and SP have been the candidate materials for nozzle inserts. Since liquid engine nozzles are subjected to oxidizing gases, SP makes a promising material for ablative throat requirement. SP throat inserts for liquid stages of launch vehicles have been realized and flown successfully.

A typical nozzle system consists of an ablative throat, TRR, TSR and chamber as shown in Fig. 1. Also, ply orientation for ablative material is chosen to have lowest char depth and optimal backwall temperature. It is seen from various arc jet tests carried out on specimens of varying ply orientation that 90° ply shows highest surface and lowest backwall temperature [1]. Hence, a dual ply ablative throat is configured with higher ply orientation at fore end and lower ply orientation at aft end.

In successfully tested throat inserts (ground tests) earlier, thrust chamber outer surface blackening and throat back wall charring have been observed. Reason could be either hot gas seepage (indicated by temperature measurements) or exothermic decomposition of fuel. Gap is formed at fore end interface of TRR and SP throat during nozzle operation.

Fig. 1 Elements of liquid engine nozzle system (Nominal)



Earlier works have discussed thermo-structural analysis of liquid engine nozzle system without considering gasket at fore end interface [2–5]. In this work, design and thermo-structural analysis with SWG at this interface are studied with the objective of preventing gas entry. Temperature dependent material properties, evaluated through tests, are considered for the study. Effect of SWG on the system is also discussed and compared with the nominal condition, i.e., without gasket.

1.1 *Spiral Wound Gasket (SWG)*

This semi-metallic gasket is manufactured under pressure by spiral winding, using a preformed V-shaped metal (SS) strip and soft flexible graphite filler on the outer periphery of metal winding mandrels. Its construction [6] is shown in Fig. 2.

Salient characteristics of SWG are as follows. Its compressibility can be controlled. It is suitable for low seating stress applications while providing good sealability. It also delivers excellent conformity to flange surface along with providing good chemical resistance. It is suitable for maximum temperature application of 450 °C, i.e., 723 K. This makes it a good candidate sealing agent.

2 Geometrical Configuration

Gasket is accommodated at the interface of TRR and throat as shown in Fig. 3. It is 2.5 mm wide, 4.5 mm in height and positioned in the assembly at the middle of TRR-throat interface. This location is chosen because in nominal (without SWG) condition, axial gap at ID increases while axial gap at OD decreases as duration of nozzle operation increases.

Fig. 2 Gasket construction [6]

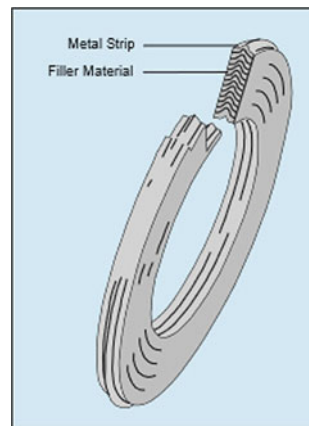
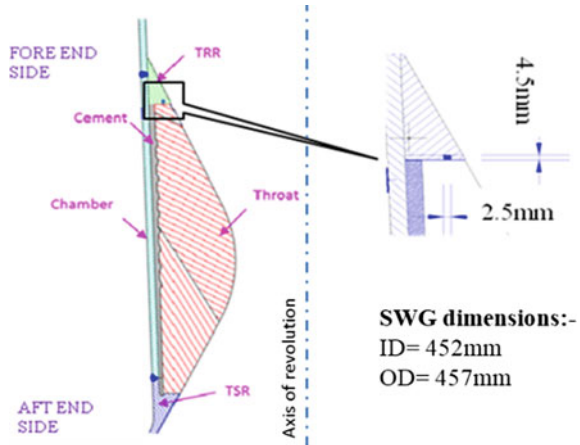


Fig. 3 Configuration of nozzle assembly with SWG at fore end interface



3 Gasket Assembly Load

Evaluation of the assembly load on gasket is carried out as per the ASME standard conventional (Boilers and Pressure Vessel Div-1 s-VIII) [7] and ASME standard tightness based code (PVRC-ROTT Gasket Constants (for all internal pressures) design [8].

3.1 Effective Contact Width of Gasket (B)

Nominal width of the gasket in contact with the flange surface,

$$N = (OD - ID)/2 = 2.5 \text{ mm}$$

As per ASME Boiler and Pressure Vessel code Appendix-2 [7], basic gasket seating width,

$$b_0 = N/2 = 2.5/2 = 1.25 \text{ mm}$$

Therefore, effective gasket contact width, $b = b_0$ if $b_0 < 6.35 \text{ mm}$, i.e., $b = 1.25 \text{ mm}$.

3.2 Effective Gasket Diameter (G)

Since $b_0 \leq 6.35 \text{ mm}$, G equals to mean diameter of the gasket contact face. Therefore,

$$G = (457 + 452)/2 = 454.5 \text{ mm}$$

3.3 Gasket Assembly Stress or Load

Gasket assembly load has been estimated in following sub-sections using conventional and tightness based design. Standard conventional-based design suggests values of “m” and “y” as applied to gaskets [7]. In general, the defined values have been proven successful in actual applications.

PVRC has, through many years of research and development (involving actual gasket tests), conceived a new philosophy that addresses the mechanism of sealing. It recommends minimum levels of gasket assembly stress to fulfill the operational requirements of a user. The new procedure [8] is similar to the existing ASME Section VIII calculation, except it incorporates new gasket constants (to replace the traditional “m” and “y”) that have been determined through an extensive test program. These gasket constants have been discussed below.

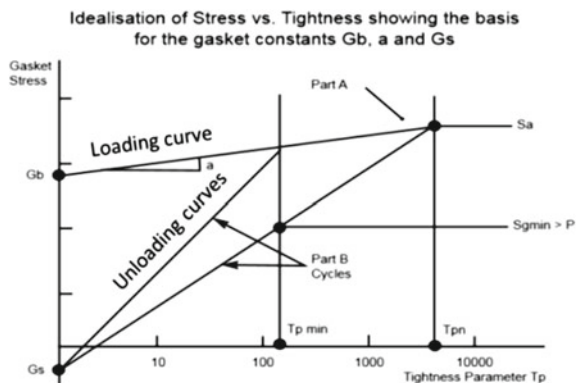
Behavior of gasket for loading (Part A)/unloading (Part B) cycle is shown in Fig. 4. G_b and a represent initial gasket compression characteristics during initial installation. G_s represents unloading characteristics typically associated with the operating behavior of gasket.

3.3.1 As Per the ASME B&PV Code

Gasket factors’ [7]— m and y are three and 68.3 MPa, respectively. Minimum load required for gasket seating,

$$W_{m2} = \pi * G * b * y \tag{1}$$

Fig. 4 Idealization of ROTT behavior of gasket [8]



or $Wm2 = \pi * 454.5 * 1.25 * 68.3 = 123 \text{ kN}$

3.3.2 As Per ASME Standard Tightness Based Code

Minimum tightness required during assembly and operation is estimated considering tightness class-1, on the basis of PVRC-ROTT gasket constants [8] as given in Table 1.

Required Minimum Tightness During Operation

$Tpmin = 18.023 * Tc * P = 18.023 * 0.1 * 6.4 = 11.53$ --- ($Tc = 0.1$ for tightness class-1).

Required Assembly Tightness

$Tpa/Tpmin = 1.5$ or, $Tpa = 1.5 * 11.53 = 17.3$

Minimum Required Stress for Gasket Seating

$$Sya = (Gb/\eta)(Tpa)^a \tag{2}$$

Taking $\eta = 0.75$, $Sya = (16.065/0.75)(17.3)^{0.237} = 42.096 \text{ MPa}$

Hence, load on gasket during assembly $= \pi * G * b * Sya = 75.09 \text{ kN}$ (3)

Load on Gasket During Operation

Minimum required operating stress on gasket, $Smo = \max$ of ($Sm1$, $2P$ and SL)

$$Sm1 = Gs[Tpmin]^k \tag{4}$$

where $k = \log[\eta * Sya/Gs]/\log Tpa = \log[0.75 * 42/0.0908]/\log 17.3 = 2.052$

$Sm1 = Gs[Tpmin]^k = 0.0908[11.53]^{2.052} = 13.73 \text{ MPa}$

Table 1 PVRC-ROTT gasket constants (for all internal pressures) [8]

Constant	Gb	a	Gs	Tpmax	SL
SWG	16.065 MPa	0.237	0.0908 MPa	4268	6.21 MPa

Table 2 Assembly load for different seating widths of gasket

Width (mm)	ID (mm)	OD (mm)	Assembly Load (kN)	
			ASME B and PV conventional	Tightness based
2.5	452	457	123	75
5	445	455	243	149
10	445	465	492	301

$$2P = 2 \times 6.4 = 12.8 \text{ MPa} \quad (5)$$

$$S_L = 6.21 \text{ MPa (from table)} \quad (6)$$

Using (4), (5) and (6), $S_{mo} = \max(13.73, 12.8, 6.21) = 13.73 \text{ MPa}$

$$\text{Load on gasket during operation} = \pi * G * b * S_{mo} = 24.5 \text{ kN} \quad (7)$$

3.4 Evaluation of Preload for Higher Gasket Widths

From above two methods of design, required load for the assembly of proposed SWG is 123 or 75 kN. Evaluation of assembly load for different widths (see Table 2) showed that increased requirement of seating width would need higher assembly load.

4 Structural Analysis

Thermo-structural analysis is carried out for a typical liquid engine nozzle assembly by considering SWG at the proposed location—(a) to check the effect of gasket assembly load on throat assembly and (b) to simulate gasket sealing at MEOP and high temperature conditions. Effect of CTE variation (with temperature) of interfacing elements is also accounted.

4.1 Gasket Configuration and Material Details

Initial gasket width and thickness are taken as 2.5 mm and 4.5 mm, respectively (see Fig. 3). SS316L spiral wound filled with flexible graphite is considered as the gasket

Table 3 Room temperature material properties of SP, cement and stellite

	Compressive modulus (N/mm ²)	Compressive strength (N/mm ²)	Inter laminar shear strength (N/mm ²)	CTE ($\times 10^{-6}$ K)
SP: along the ply	12,940	73.5	19.61	7.9
SP: across the ply	13,072	225		30.8
Cement	24,866	29 (4.4 [^])	–	11.9
Stellite	221,000	353 [^]	–	11.7

[^] Tensile strength

Table 4 Ratio of high temperature and room temperature properties of SP, cement and stellite

	Compressive modulus			Compressive strength	Inter laminar shear strength	
	673 K	873 K	1073 K	873 K	873 K	
SP: along the ply	0.74	0.37	0.34	0.19	0.12	
SP: across the ply	0.44	0.31	0.34	–		
Temperature->	1273 K			1273 K	–	
Cement	0.16			0.3	–	
	Stellite					
Temp, K	500	800	1000	1300	1400	1500
Young’s modulus	0.88	0.77	0.66	0.38	0.26	0.13
Temp, K	477	810	1033	1253	1366	1477
Yield strength	0.8	0.6	0.54	0.28	0.18	0.07

material. For this material, stiffness should be in the range of 190–1306 MPa/mm [8].

Assumed gasket elastic modulus, E is 2.8 GPa and Poisson’s ratio is 0.3. Its CTE is assumed as zero. It is also assumed to be at RT in all conditions of operation for FEA.

Material properties of SP throat, stellite chamber, TRR and TSR estimated by tests are given in Table 3. Temperature dependent material properties of SP, stellite and cement with respect to room temperature properties are given in Tables 4 and 5.

4.2 Finite Element Analysis (FEA)

FEA is carried out with 18° sector model using ANSYS 18.0 [9]. Its mesh idealization is shown in Fig. 5. Loads and boundary conditions are shown in Fig. 6. Details are discussed in the sub-sections.

Table 5 Ratio of high temperature and room temperature CTE of SP, cement and stellite

Temp, K	473	573	673	773	873	1073	1273	1473
SP: Along the ply	-1.17	-1.50	-2.23	-2.71	-2.94	-3.59	-4.85	-3.87
SP: Across the ply	3.45	1.83	0.53	-1.56	-2.40	-2.70	-2.71	-2.35
Cement	0.28	-0.14	-0.12	0.09	0.15	0.18	0.11	-0.38
Temp, K	500	700	900	1000	1300	1500		
Stellite	1.06	1.13	1.20	1.25	1.41	1.50		

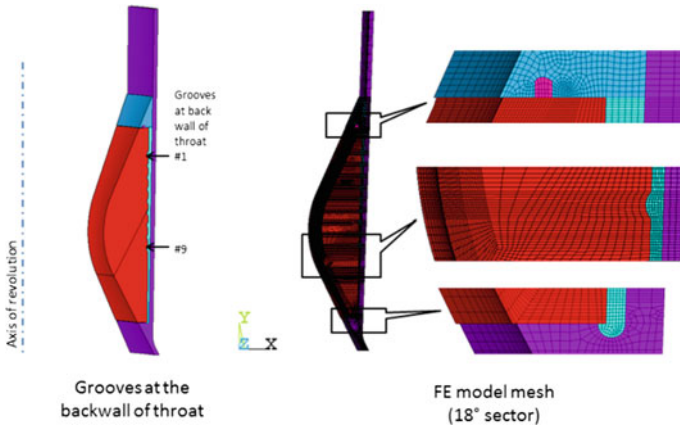


Fig. 5 18° sector FE model

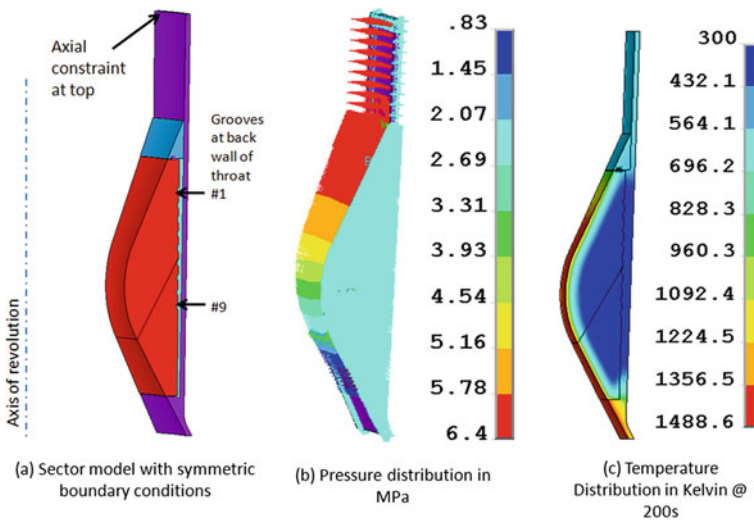


Fig. 6 Loads and boundary conditions (FE model with SWG)

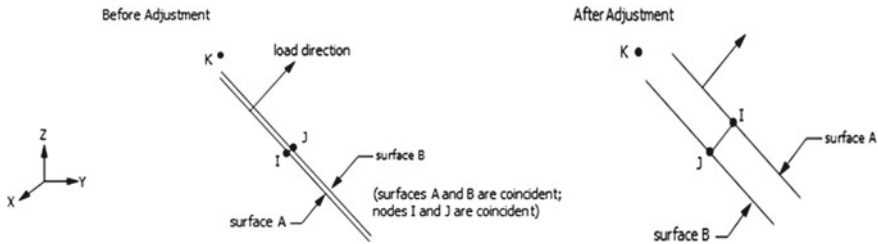


Fig. 7 Preload application in gasket at its mid-height using preload element [9]

4.2.1 FE Model

An 18° sector model was considered for the study. Here, 3D solid, 8-noded structural elements are employed having 3 degrees of freedom, i.e., translations in the orthogonal directions (see Fig. 5).

4.2.2 Boundary Conditions

Axial constraint is provided at top of the chamber as shown in Fig. 6a Couplings are given to simulate weld regions between TRR and chamber. Symmetry boundary conditions are given at the extreme faces of the sector model.

4.2.3 Gasket Preload

Pre-compression of 150 kN is applied on the gasket, with the help of preload elements and section. Preload section is taken at its mid-height. After preload application, nodes become distinct and separated as shown in Fig. 7 in lieu of earlier coincident nodes.

4.2.4 Pressure Load

Pressure distribution along the nozzle axis corresponding to 64 bar is considered as shown in Fig. 6b.

4.2.5 Thermal Load

Transient thermal analysis is carried out using ANSYS 18.0 [9], and temperature profile (see Fig. 6c) is generated for the nozzle assembly. Conductive and convective boundary conditions are considered for this analysis. Conduction occurs within the sub-components and at the interfaces of the assembly. Governing equation for

conduction in two-dimensions [10] is

$$\frac{\partial}{\partial x} \left(k_x \frac{\partial T}{\partial x} \right) + \frac{\partial}{\partial y} \left(k_y \frac{\partial T}{\partial y} \right) + q_v = \rho c_p \left(\frac{\partial T}{\partial t} \right) \quad (8)$$

Convection is considered where the throat, TRR and TSR are exposed to the hot combustion gases. Heat transfer coefficient for convection is estimated using Bartz method [11]. Here, subscript 0 refer to stagnation condition.

$$h_g = \sigma_{cf} \left[\left(\frac{0.026}{D_*^{0.2}} \right) \left(\frac{\mu_g^{0.2} c_p}{Pr^{0.6}} \right)_0 \left(\frac{p_c g}{c^*} \right)^{0.8} \left(\frac{D_*}{r_c} \right)^{0.1} \right] \left(\frac{A_*}{A} \right)^{0.9} \quad (9)$$

Convective heat flux is estimated by Newton's law of cooling.

$$q_c = h_g (T - T_w) \quad (10)$$

Maximum temperature is found to be at the ID of throat reaching up to 1400–1500 K. Temperature distribution corresponding to 200 s is considered for analysis as shown in Fig. 6c. Gasket is assumed to be at RT.

4.3 Load Cases Studied

Structural analysis is carried out for following cases. Case 1 represents the nominal condition without SWG at TRR-throat interface wherein effect of pressure as well as thermal load (200 s) is considered.

While cases 2, 3 and 4 represent nozzle assembly with SWG at TRR-throat interface. In these cases, effect of gasket on the system is checked. (a) Case 2: Effect of gasket preload, i.e., 150kN is studied on the nozzle system. Initial gasket compression of 1–2% is considered. (b) Case 3: Structural analysis of nozzle system with gasket preload and pressure load (see Sect. 4.2.4) is carried out for specified chamber pressure of 64 bar. (c) Case 4: Thermo-structural analysis with gasket preload, pressure load and thermal load at 200 s is carried out.

5 Results and Discussion

There is a net ejection load because of the pressure load at ID of the nozzle system. Pressure load on TRR ID is transferred to throat at its fore end. This load is further transferred to cement by means of nine grooves provided at the back wall of throat. Hence, effect of introduction of gasket on this load transfer mechanism is checked as discussed in sub-sections below. Also, as a result of thermal expansion/contraction

Table 6 Groove load distribution in throat

Cement groove	Axial load (kN)			
	Nominal case	With spiral wound gasket (SWG)		
	<i>Case 1: Pr. (64 bar) + Temp. 200 s</i>	<i>Case 2: Gasket preload (150kN)</i>	<i>Case 3: Case 2 + Pr. (64 bar)</i>	<i>Case 4: Case 3 + Temp. 200 s</i>
1	0	21.4	62	0
2	0	8.2	56	0
3	45	2.5	49	58
4	94	0.0	43	81
5	78	0.0	31	61
6	60	12.4	51	75
7	50	7.9	38	59
8	54	7.0	33	63
9	88	9.2	31	93

at the fore end interface between throat and TRR, gasket preload will vary during nozzle operation. So, its variation has also been checked.

5.1 Effect on Groove Load Distribution

There is a net pressure load acting at throat ID. Also, load from TRR as a result of expansion (throat-TRR butting) and pressure load on TRR ID is transferred to throat. These loads are further passed to cement by means of nine grooves provided at backwall of throat insert as shown in Fig. 6a. It can be seen from Table 6 that groove load distribution is similar for both cases, i.e., nominal (case 1) versus nozzle with SWG case (case 4). It is increased by 21 kN in the latter case. This increased load transfer is distributed from third to ninth grooves. This implies that with the introduction of gasket at the specified interface in the nozzle system, load transfer mechanism through grooves is not disturbed with respect to nominal condition.

5.2 Change in Gasket Preload During Operation

Initial gasket preload provided for seating, i.e., 150 kN (Case 2) decreases by 50% (Case 3) for combined gasket preload and pressure load condition (refer Fig. 8). Subsequently, this reduction is changed to 12.6% (Case 4) w.r.t initial seating condition (Case 2) for combined gasket preload, pressure load and thermal load condition (refer Fig. 8). However, even with this change gasket preload meets the requirement

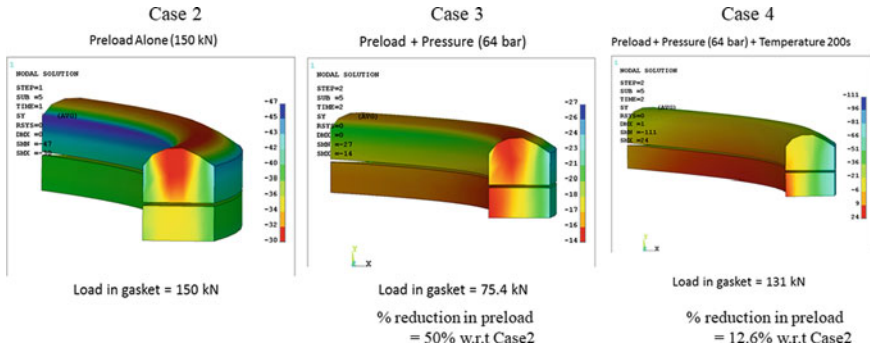


Fig. 8 Change in gasket preload for different load cases (with SWG)

during operation, i.e., 24.5 kN. Hence, it helps in preventing gas entry at TRR-SP throat interface during the entire nozzle operation time.

6 Conclusion

In this paper, design and thermo-structural analysis with SWG (or seal) at TRR-throat interface is studied. Load cases are—(a) gasket seating load or preload, (b) gasket preload with pressure load distribution corresponding to chamber pressure of nozzle system and (c) gasket preload with pressure as well as thermal load at 200 s. Effect of CTE variation (with temperature) of interfacing elements is also accounted.

Study shows that proposed gasket helps to prevent the hot gas entry at the interface of fore end metallic ring and throat insert, along with satisfying its assembly and operating requirements. (a) Load required for seating the gasket is sufficient to maintain the required tightness during operating condition (as per ASME tightness-based code rules). (b) Load distribution among grooves with introduction of gasket in nozzle assembly remains comparable with nominal condition for 200 s condition. Hence, gasket can be incorporated at fore end interface as groove load transfer mechanism remains undisturbed. (c) Initial gasket seating preload changes by 50% for pressure load case. This change is reduced to 12.6% for combined pressure and thermal load condition with respect to initial gasket seating load. Even with this variation, condition of minimum gasket operating load is satisfied. Hence, it helps in preventing gas entry at the intended interface. (d) It is also observed in ASME design calculations that increased requirement of seating width would need higher assembly load. So, limit of assembly load should be checked appropriately if it is to be used in any of the assemblies.

References

1. Phadnis TR, Raveendranath P, Jayachandran T (2020) Effect of ply orientation on the in-depth response of carbon phenolic ablative. *J Thermophys Heat Transf* 34(3)
2. Kumar RR, Vinod G, Renjith S (2005) Thermo-structural analysis of composite structures. In: Elsevier, *Material Science & Engineering A* 412, pp 66–70
3. Tiwari SB, Suresh R, Rao BN (2011) Thermo-structural analysis of a composite contour nozzle. In: *International conference on composites for 21st century and future trends 2011*, IISc Bangalore
4. Sharma S, Pany C, Suresh R (2020) Thermo-structural analysis of liquid engine throat with presence of voids in bonding material between throat and back-up chamber. In: *International conference on advanced thermostructural materials & thermal protection systems 2020*. HTPA-4, Trivandrum
5. Kiran JA, Pany C, Suresh R (2019) Study of standalone ablative divergent nozzle for solid motors. In: *ISAMPE national conference on composites-INCCOM-16*
6. Flexitallic catalogue for spiral wound gasket. <https://flexitallic.com>. Last accessed on 15 Oct 2021.
7. ASME Boiler and Pressure Vessel Code—Section VIII—Division 2 (Rules for construction of pressure vessels) (2010)
8. John H (1998) *Bickford: gaskets and gasketed joints*. Marcel Dekker Inc., New York
9. ANSYS, Inc. Release 18.0.
10. Lewis RW, Nithiarasu P, Seetharamu KN (2004) *Fundamentals of the finite element method for heat and fluid flow*. John Wiley & Sons Ltd, England
11. Bartz DR (1957) A simple equation of rapid estimation of rocket nozzle heat transfer coefficients. *Jet Propul*, pp 49–51

Design and Testing of a Liquid Rocket Engine



G. Dinesh Kumar, KJ Hari Krishnan, S. Gokulakrishnan, M. Lokeshwar, and S. Rogith

Abstract Liquid rocket engines are widely used in the aerospace industry for their good controllability. This project aims to design, fabricate and test a small liquid rocket engine using kerosene and gaseous oxygen. The engine was designed to withstand a chamber pressure of 20 bar. However, the maximum chamber pressure the engine can withstand was not limited to 20 bar, and it was capable of withstanding a chamber pressure of 30 bar during combustion. Cold flow testing of the engine was done for a chamber pressure of 4, 6, 8 and 10 bar. Upon successful completion, the hot flow testing was simultaneously carried out for two cases. Initially, the fuel and oxidizer were fed in such a way that the chamber pressure during combustion was around 9 bar. Later, for the second test, both the fuel and oxidizer feed pressure were raised in order to raise the chamber pressure to 12.5 bar. The test results of all the cases were tabulated and detailly discussed in this paper.

Keywords Liquid rocket engine · Kerosene · Oxygen · Aerospace industry

Nomenclature

A_t	Throat area
A_e	Exit area
A_c	Chamber area
A_{inj}	Injector area
C^*	Characteristic velocity
c_f	Thrust coefficient
d_t	Throat diameter

G. D. Kumar (✉)

Aeronautical Department, Hindustan Institute of Technology and Science, Tamil Nadu, Padur 603103, India

e-mail: gdineshk@hindustanuniv.ac.in

K. H. Krishnan · S. Gokulakrishnan · M. Lokeshwar · S. Rogith

Aerospace Department, Hindustan Institute of Technology and Science, Tamil Nadu, Padur 603103, India

d_e	Exit diameter
d_c	Chamber diameter
d_{inj}	Injector diameter
g	Acceleration due to gravity
I_{sp}	Specific impulse
L_c	Combustion chamber length
\dot{m}_o	Mass flow rate of oxygen
\dot{m}_f	Mass flow rate of fuel
\dot{m}_t	Total mass flow rate
M_c	Mach number at chamber exit
M_e	Mach number at exit
P_c	Chamber pressure
P_e	Exit pressure
R	Gas constant
T_e	Exit temperature
T_c	Chamber temperature
t	Thickness
ρ	Density
V	Volume
V_{exit}	Exit velocity
γ	Adiabatic constant
σ_y	Yield stress

1 Introduction

Liquid rocket engine uses liquid fuel and oxidizer for combustion. The liquid propellant engine is more complex than the solid propellant counterparts; however, they offer several advantages. By controlling the flow of the propellant to the combustion chamber, the engine can be throttled, stopped or restarted. The higher stages of the rocket require more throttling to align the satellite to its correct orbit and orientation. So, the necessity of developing the liquid rocket engine with less cost, and more efficiency is increasing day by day. Here, the fuel and oxidizer will be atomized using an injector. The injector will have very small outlet holes. When the fuel is pumped with high pressure, the fuel gets atomized. The atomized fuel will completely mix with an oxidizer (gaseous oxygen in this case) in the combustion chamber for combustion. The combusted product will be expanded through the nozzle. Since the exhaust flow is supersonic, a convergent-divergent nozzle is preferred.

Marques [1] a small liquid rocket propellant engine was designed, and a prototype was made. It was able to produce a 25 N thrust. This project is aimed to study the stability of the liquid engine with regenerative cooling and external pressurization and check the feasibility of the self-pressurized system. They have observed that the working of the external pressurized system was stable and behaved as they expected

[2]. In the SMART rocket project, the student from TU Dresden has developed a liquid oxygen and ethanol driven 500 N sounding rocket. The rocket has two stages, the first stage is of rocket engine, and the second stage is of parachute system. This rocket motor uses green propellant combination of liquid oxygen (LOX) as oxidizer and ethanol as fuel. They calculated that the engine can give a thrust of 700 N [3]. This paper aims in the development of hydrogen peroxide monopropellant thrusters using catalytic beds. This paper focuses on two different design thrusters with 5 and 25 N, and they used two different catalytic beds with a different configuration. They have tested pure silver gauzes and pellet coated with manganese oxide, to find the optimum one for future industrial development [4]. The liquid rocket engine operates at high pressure, which is above the critical pressure of propellants generally. This paper presents different case studies attempted at PRS to study supercritical combustion. It demonstrates the development of combustion methodology, which is capable of future full-scale thrust chamber simulations. A good result was found in test results data which had the best match to the CFD model. A detailed study for supercritical combustion of liquid oxygen and methane was performed using equilibrium and near-equilibrium steady flame combustion methodology [5]. This paper presents an improvement on the performance of the supersonic nozzle by understanding the geometrical parameters. In this research, supersonic nozzle was analyzed by keeping the same expansion ratio and boundary conditions. The nozzle design was varying convergent section length and angle by keeping the same expansion ratio and boundary conditions. The result of this paper says that the nozzle thrust performance increases during the 28.5° inlet angle would produce maximum thrust force.

2 Design Calculation

Some initial assumptions are made according to the requirement [6, 7, 8]. The chamber pressure was taken as 20 bar. The oxidizer to fuel ratio was taken as 2.5. The contraction ratio was taken as 3. The maximum thrust which the engine is capable to produce under ideal condition was 500 N. The characteristic length of the combustion chamber was taken as 1.27 m for complete combustion to occur. The nozzle convergence and divergence angle after flow analysis in ANSYS was taken as 60° and 15° [9], respectively. With these data, combustion equilibrium analysis (CEA) for kerosene and oxygen gas was carried out, and the results are tabulated below (Table 1).

Table 1 CEA result

Parameters	CEA result
Convergence ratio $\left(\frac{A_c}{A_r}\right)$	3
Inlet Mach number (Mc)	0.203
Divergence ratio $\left(\frac{A_e}{A_r}\right)$	3.9706
Exit Mach number (Me)	2.5
Chamber temperature (Tc)	3520.5 K
Chamber pressure (Pc)	20 Bar
Characteristic velocity (C*)	1764.3 m/s
Isp \times g	2517.3 m/s

2.1 Mass Flow Calculation

$$\dot{m}_t = \frac{F}{I_{sp}} = \frac{500}{2517.6} \quad (1)$$

$$\dot{m}_t = 0.1986 \frac{\text{kg}}{\text{s}}$$

2.2 Throat Diameter Calculation

$$A_t = \frac{\dot{m}_t \times C^*}{P_c} \quad (2)$$

$$A_t = \frac{0.1986 \times 1764.3}{20 \times 10^5} = 1.752 \times 10^{-4} m^2$$

$$d_t = \sqrt{\frac{4A_t}{\pi}} = 0.015m$$

2.3 Exit Diameter Calculation

$$\frac{A_e}{A_r} = 3.9706 \quad A_e = 6.9565 \times 10^{-4} m^2 \quad (1)$$

$$d_e = \sqrt{\frac{4A_e}{\pi}} = 0.03m$$

2.4 Combustion Chamber Diameter Calculation

$$\frac{A_c}{A_t} = 3 \quad A_c = 5.256 \times 10^{-4} m^2$$

$$d_c = \sqrt{\frac{4A_c}{\pi}} = 0.026m \quad (4)$$

2.5 Combustion Chamber Length Calculation

$$L_C = \frac{V_c}{1.1 \times A_c} = 0.385m \quad (2)$$

2.6 Combustion Chamber Thickness Calculation

$$\sigma_y = 207 \text{ Mpa}$$

$$\sigma = \frac{\sigma_y}{\text{FOS}} = \frac{207}{10} = 20.7 \text{ Mpa}$$

$$t_{\min} = \frac{PD}{2\sigma} = \frac{30 \times 10^5 \times 3 \times 10^{-2}}{2 \times 20.7 \times 10^6} = 2.2 \text{ mm}$$

$$t = \text{Fos} \times t_{\min} = 10 \times 2.2 \text{ mm} = 22\text{mm} = 0.022m \quad (6)$$

2.7 Oxygen Injector Design

$$\dot{m}_t = 198.6g/s \quad \dot{m}_o = 141.85g/s \quad \dot{m}_f = 56.75g/s$$

$$\dot{m} = c_d A_{\text{inj}} \sqrt{2\rho \Delta P}$$

$$A_{\text{inj}} = 5 \times 10^{-5} m^2 \quad (7)$$

$$d_{\text{inj}} = \sqrt{\frac{4A_{\text{inj}}}{\pi}} = 0.008m$$

2.8 Fuel Injector Design

$$\begin{aligned} \dot{m} &= A c_d A_{inj} \sqrt{2\rho \Delta P} \\ A_{inj} &= 3.144 \times 10^{-6} m^2 \\ d_{inj} &= \sqrt{\frac{4A_{inj}}{\pi}} = 0.002m \end{aligned} \quad (8)$$

2.9 Final Design Parameters

See (Table 2)

3 Engine Design

With the parameters mentioned in (Table 2), the engine was modeled in CATIA V5 (Figs. 1, 2 and 3).

4 Fabrication

The entire engine was fabricated using mild steel, and the nozzle was made with graphite and mounted on mild steel to withstand high exit temperature (Figs. 4 and 5).

Table 2 Final design parameters

Parameters	Value
Mass flow (\dot{m})	0.1986 kg/s
Diameter of combustion chamber (d_c)	0.026 m
Diameter of nozzle throat (d_t)	0.015 m
Diameter of nozzle exit (d_e)	0.03 m
Chamber length (L_c)	0.385 m
Total thickness (t)	0.022 m
Contraction angle (β)	60°
Divergence angle (α)	15°
Exit diameter of oxygen injector	0.008 m
Exit diameter of fuel injector	0.002 m

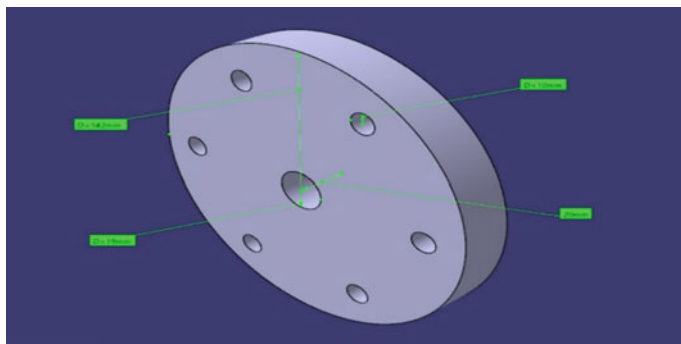


Fig. 1 Flange design

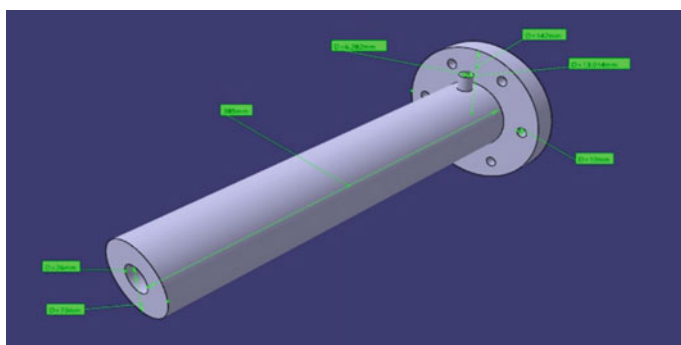


Fig. 2 Combustion chamber design

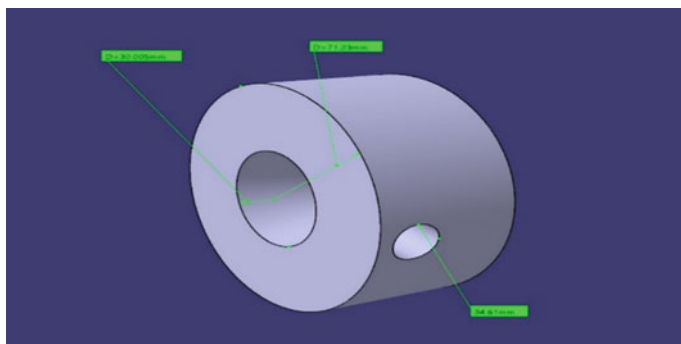


Fig. 3 Nozzle design



Fig. 4 Graphite nozzle

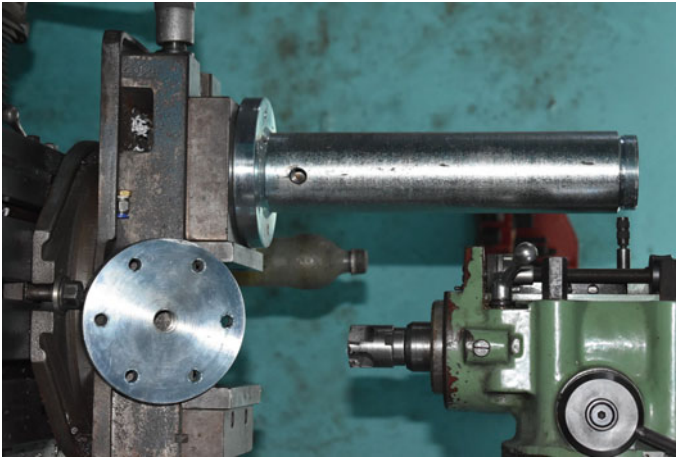


Fig. 5 Combustion chamber made using mild steel

5 Experimental Setup

5.1 Experimental Setup for Cold Flow

The oxygen cylinder was connected to the oxygen settling chamber. The oxygen from the main tank was fed to the oxygen settling chamber until we achieved the desired chamber pressure. The oxygen settling chamber was connected to the oxygen injector through a solenoidal valve. This solenoidal valve allowed us to manually control the oxidizer supply (Figs. 6 and 7).

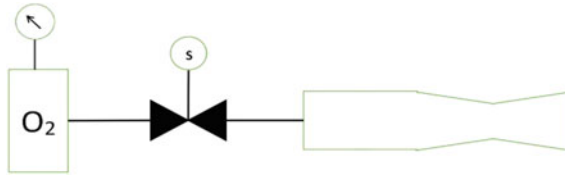


Fig. 6 Schematic of cold flow setup

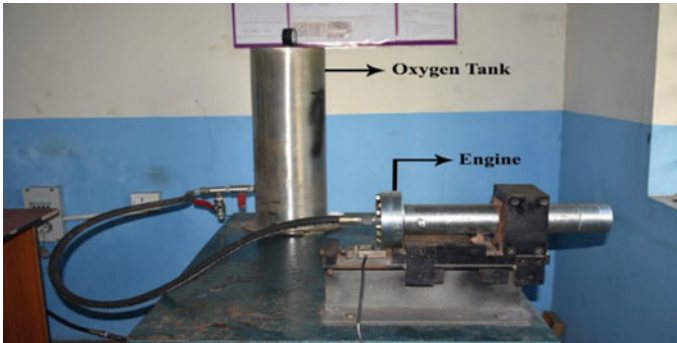


Fig. 7 Cold flow setup

5.2 Experimental Setup for Hot Flow

The oxygen cylinder was connected to the oxygen settling chamber. The oxygen from the main tank was fed to the oxygen settling chamber until we achieved the desired chamber pressure. The oxygen settling chamber was connected to the oxygen injector through a solenoidal valve. This solenoidal valve allowed us to manually control the oxidizer supply. The nitrogen cylinder was connected to tank 2. The nitrogen from the main supply tank was fed to tank 2 by keeping the solenoidal valve connecting tank 2 to tank 1 closed until the desired chamber pressure was achieved. Tank 1 contains kerosene. Tank 1 was connected to the fuel injector through a solenoidal valve. A high power 22,000 V igniter coil is also connected to the chamber to ignite the fuel oxidizer mixture. A load cell along with rail mechanism was used to measure the thrust. This load cell was connected to A12E output display unit (Figs. 8 and 9).

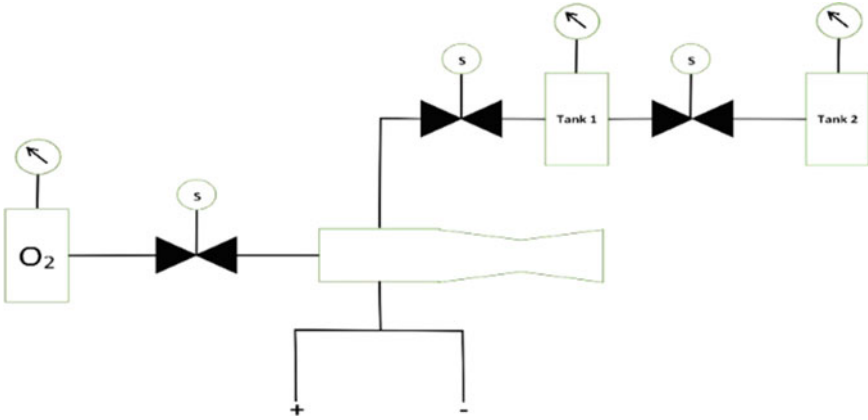


Fig. 8 Schematic of hot flow setup



Fig. 9 Hot flow setup

6 Results and Discussion

6.1 Results for Cold Flow

The testing was carried for four different chamber pressures (4, 6, 8 and 10 bar). The results for all the case are tabulated.

It can be noted from (Table 3) that as the chamber pressure increases the characteristic velocity remains constant since the fluid is unchanged and the temperature is also not varying. The temperature was about 300 K which was the room temperature during testing. The exit velocity decreases due to the increase in the density at the

Table 3 Cold flow result

Contents	$P_c = 4$ bar	$P_c = 6$ bar	$P_c = 8$ bar	$P_c = 10$ bar
Exit pressure (bar)	1.3	2.2	3	3.8
C^* (m/s)	407.7	407.7	407.7	407.7
Max mass flow rate (Kg/s)	0.1734	0.2601	0.3468	0.4335
Exit velocity (m/s)	147	130	127	125.7
Exit Mach number	0.445	0.39	0.386	0.38

exit. However, due to the increase in mass flow rate, there is an increment in the thrust. The specific impulse and the thrust coefficient are decreasing.

6.2 Results for Hot Flow

This testing was carried out for two cases. Initially, the fuel and oxidizer were fed in such a way that the chamber pressure during combustion was around 9 bar. Later, for the second test, both the fuel and oxidizer feed pressure were raised in order to raise the chamber pressure to 12.5 bar. The test results of all the cases are tabulated (Figs. 10, 11, 12 and 13).

From (Table 4), it is clear that, as the oxygen and fuel feed pressure increase, the chamber pressure and exit temperature are increasing rapidly. While performing both the tests, it was observed that test 2 produced more thrust, and also, the fuel was atomized very well as compared to test 1. Hence, the pressure drop on fuel injector is suggested to be at least 3 bar for future tests.

Fig. 10 Hot flow at $P_c = 9.1$ bar





Fig. 11 Hot flow at $P_c = 12.42$ bar

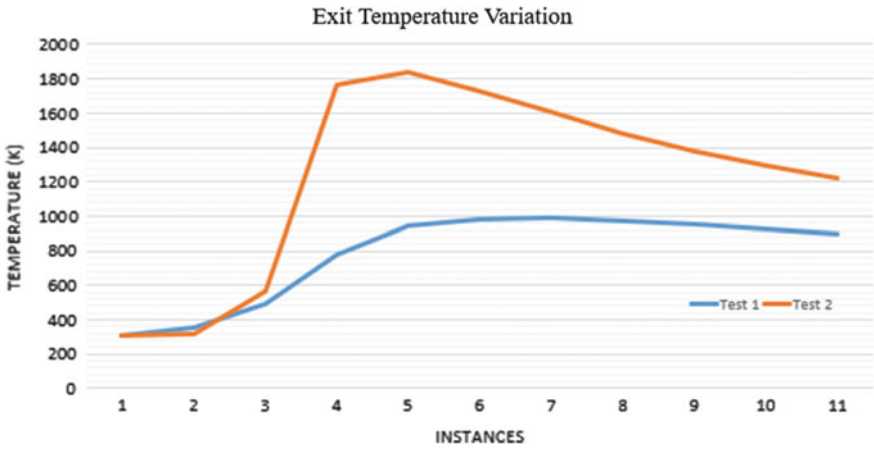


Fig. 12 Temperature variation during static test

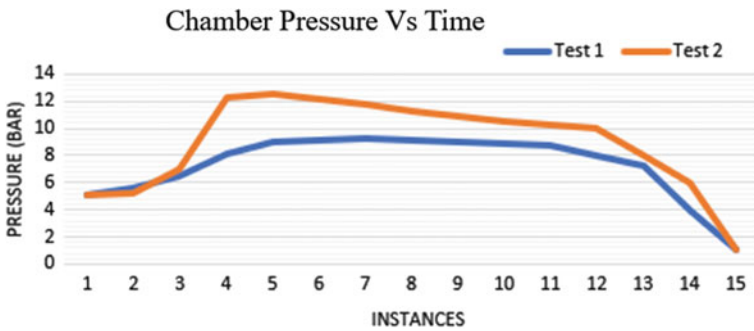


Fig. 13 Chamber pressure variation during static test

Table 4 Hot flow result

Title	Test 1	Test 2
Chamber pressure (bar)	9.1	12.42
Exit temperature (K)	986	1841
C^* (m/s)	809	1106
Exit density (kg/m^3)	0.384	0.206
Exit velocity (m/s)	730.9	1365
Exit Mach number	1.339	1.83
Thrust (N)	145.2	271
Isp (s)	74.5	139.1
C_F	0.9034	1.234

7 Conclusion

This rocket engine produced a Thrust of 271 N and 145.2 N for the chamber pressure of 12.42 bar and 9.1 bar, respectively. The successful static test proves that the calculations done and the assumptions made are correct. This static test can be carried for various oxygen and fuel injecting pressure. However, the pressure drop on fuel injector is suggested to be at least 3 bar, as this pressure is necessary to produce good atomization of the fuel and start the combustion quickly. Since the wall thickness is too high, this engine can be used for multiple tests. The graphite nozzle alone needs to be changed after few tests to maintain the same area ratio, as the combusted gas may corrode the layer of the graphite nozzle after several tests and making it to be unsuitable for the test.

References

1. Marques MPPM (2016) Small liquid propellant rocket engine
2. Bach C, Sieder-Katzmann J, Weig F, Tajmar M (2016) Development of a liquid-propellant student sounding rocket
3. Cervone A, Torre L, d'Agostino L (2017) Development of hydrogen peroxide monopropellant rockets
4. Sharma A, Agarwal D, Pisharady J, Kumar S, Sunil (2018) Preliminary combustion modeling & dynamics study in liquid rocket engines: an overview
5. Chohan I, Samo S, Hussain T, Tunio I, Durani H (2017) Influence of convergent section length and angle on performance of supersonic nozzle
6. Gordon S, McBride BJ (1994) CEA Analysis 1994: NASA RP-1311
7. China Lake, California, Rocket Lab: How to design, build and test small liquid-fuel rocket engines (1971) 9600-1980-4
8. Sutton Gp, Biblarz O (2010) Rocket propulsion elements. 8th edn. Wiley
9. Hamedi-Estakhrsar M, Mahdavy-Moghaddam H, Jahromi M (2018) Investigation of effects of convergence and divergence half-angles on the performance of a nozzle for different operating conditions. J Brazilian Soc Mech Sci Eng

Thermal Management Challenges in Small Satellites



Kamlesh Kumar Baraya

Abstract Small satellites provide many unique advantages. They are economical to launch, provide greater flexibility, and can be developed in a very short span of time. Small satellites provide unique opportunities for university students to gain experience in space technology and carry out research and development to explore the novel technologies at a very low cost and minimal risk. Utilization of small satellites poses some technological challenges also. Thermal management of small satellites is one of the challenges to be addressed by designers of small satellites. Thermal management ensures that temperature of all the components in the satellite remains within required limits during all the mission phases. Less mass, small volume, and high power densities make the thermal management task of small satellites difficult and challenging. In this paper, various thermal management challenges encountered in the development of small satellites are discussed. Technologies to address these challenges are also discussed.

Keywords Small satellites · Thermal management · Temperature

1 Introduction

Satellites of low mass and size are called small satellites. Usually small satellites have mass under 500 kg. Satellites are classified according to their mass. Table 1 shows the classification of small satellite according to their mass. CubeSat are a class of micro or nano satellites. CubeSat are made of multiple units of volume. Each unit has a volume of $10\text{ cm} \times 10\text{ cm} \times 10\text{ cm}$ and mass of around 1 to 1.33 kg. PocketQube is another class of small satellite, which is a size of 5 cm cuboid and mass up to 250 g. An 8U CubeSat has eight units of $10\text{ cm} \times 10\text{ cm} \times 10\text{ cm}$.

Small satellites offer many advantages over large satellites. Launch cost of small satellites is lower. Small satellites can be launched from smaller launch vehicles. Small launch vehicles are cheaper to build and can be built in much less time than big

K. K. Baraya (✉)

Thermal Engineering Division, Space Applications Centre, ISRO, Ahmedabad 380015, India
e-mail: kkumarbaraya@gmail.com

Table 1 Classification of small satellites according to mass [1]

Class name	Mass (Kg)
Mini satellite	100–500
Micro satellite	10–100
Nano satellites	< 10 kg

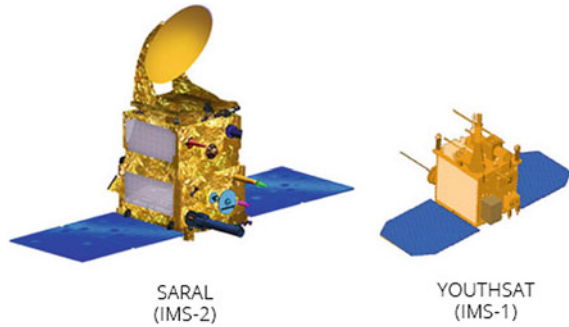
launch vehicles. Small satellites can be launched as co-passengers of large satellites. They can be launched in multiple numbers. Sometimes hundreds of small satellites can be launched from a single launch vehicle. Small satellites are more valuable and more capable as government and commercial missions push high tech missions with smaller budgets and shorter schedules. Small satellites can be mass-produced easily when constellation of thousands of satellites is to be built in space.

Small satellites have created a significant disruption in the space industry. Small satellites to be launched in LEO can be produced at a considerably lower cost. Lower cost offers opportunity for high production rate, and consequently, more satellites can be launched per year. Lower cost of small satellites has opened the space market for private companies. Private companies are holding significant market share of small satellites. Large satellites are launched for longer operational life span ranging from 10 to 15 years, and due to high launch and other cost, they are manufactured to the highest quality standards, which further increase the cost of large satellite. Small satellite's operational life expectancy is 2–3 years, and launch cost is lower. Therefore, quality standards for manufacturing small satellites are less stringent which allow using cheaper components in small satellites. Small satellites need not be state of the art so they can be produced faster and efficiently. Commercial off the shelf components can be used to build small satellite. This makes the manufacturing of small satellite cheaper, faster, and efficient.

Small satellites can provide stand-alone platform for imaging and scientific payloads, which can be launched within short duration. ISRO has developed two kinds of buses for different payloads. IMS-1 is a bus for 100 kg class satellites including payload capability of around 30 kg. YOUTHSAT was a small satellite configured on IMS-1 bus. IMS-2 bus is developed for 400 kg class satellite with a payload capability of around 200 kg. IMS-2 is envisaged to be workhorse for different types of remote sensing applications [2]. SARAL satellite is first mission configured on IMS-2 bus. Figure 1 shows YOUTHSAT and SARAL satellites configured on IMS-1 and IMS-2 bus, respectively.

Launching of small satellite carries less financial risk, so they provide very good platform to test any new technology and demonstrate the proof of concept. Small satellites are used by universities and research institute for space science research. Tens of thousands of small satellites will be needed over the next decade. Small satellites are needed for data demand of industries, governments, and people. Earth observation constellations are needed to make advanced data available about our planet earth. Compared to larger satellites, small satellites are increasingly required to handle more data for collecting remote sensing images, data from ground-based sensors, and smart devices. Small satellites will play a critical role in the future of

Fig. 1 Small satellites developed by ISRO [2]



space infrastructure and exploration, as well as provide customers with real-time data to make informed and actionable decisions. Electronic components are being further miniaturized. High data rate communication can generate lot of unwanted heat. Due to all these developments, small satellites are required to dissipate hundreds of watts of heat from a small volume. These developments are making thermal management task of small satellites really difficult. Besides power dissipation from electronic components, thermal management task of small satellite is made more challenging due to constraints of low mass, small size, and limited power supply.

Small satellites launched in low earth orbit (LEO) with altitude of about 400 km are influenced by atmospheric drag. At this altitude, any piece of space debris is influenced by the atmospheric drag and consequently is pulled down toward earth into the dense atmosphere, and it is burned in the atmosphere. Therefore, any piece of space debris remains in space for 2–3 decades only. However, large satellite launched in geostationary earth orbit (GEO) will remain in space for many decades even after end of their useful life. As environment, drag in GEO is negligible compared to LEO. Therefore, LEO orbits are cleaned naturally in few years. While in GEO, space debris go on accumulating with every launch. For testing new technologies or exploring space launching small satellites in LEO is preferable than in GEO. Because space debris generated due to them in LEO is cleaned naturally within few years.

2 Thermal Management Philosophy

The objective of the thermal control system in a small satellite is to provide a comfortable environment for all sub-systems of satellite so that they can provide best performance during the operational life of the satellite. In space, there is no convection. The mechanisms of heat transfer in satellite are conduction and radiation only. Different components of satellites interact thermally through conduction and radiation while satellite elements interact with space environment through radiation mode only. The heat transfer within the satellite and with space environments is managed such that heat balance at each element of satellite results in temperature, which should be

within allowable limits. The satellite receives two types of heat loads 1. Internal and 2. External. The heat dissipated by various sub-systems and their components in the satellite is internal heat load. External heat load is the heat load received from space environment mainly from sun, earth, or other planetary body around which satellite is orbiting. Earth emits infrared radiation due to its own temperature. The average temperature of the earth is considered at about $-20\text{ }^{\circ}\text{C}$. At this temperature, the earth emits about 236 W/m^2 of heat radiation [3]. This is called the earthshine load. Higher the altitude of the satellite, less is the effect of earthshine load on the satellite. In LEO, the earthshine load always affects satellite. In circular orbit earthshine heat flux, falling on the satellite is constant throughout the orbit.

The some fraction of the solar radiation coming toward the earth is reflected back to space. This reflected solar radiation is called albedo radiation. The fraction of solar radiation reflected is called the albedo constant. The average value of albedo constant is taken as 0.3 for calculating external loads on the satellite. Small satellites are normally placed in LEO.

Thermal management ensures effective radiation and conduction path for heat to diffuse to external surfaces, and finally heat is radiated to space from external surfaces. A judicious combination of radiators and insulation on external surface helps to maintain the comfortable temperature within the satellite. Radiators on the external surfaces help to radiate heat generated within satellite to space environment, while insulations on external surfaces of satellite isolate the satellite from extreme cold of space, which is at 4 K and prevents the external heat load in the form of radiation coming from sun or other sources.

3 Thermal Management Techniques for Small Satellites

There are different approaches to carry out the task of thermal management of satellites. All thermal management techniques are categorized into passive thermal control and active thermal control. Passive thermal control elements are those, which do not require any external power for their performance, and they do not have any moving parts [4]. Therefore, passive thermal control elements are highly reliable and provide long operational life. While active thermal control techniques require power to regulate the temperature of any component in the satellite. In small satellites due to limitation of mass, volume, and power, passive thermal control techniques are preferred. Multi-layer insulation (MLI) blankets, optical solar reflector (OSR), thermal control tapes and paints, thermal interstitial materials, heat pipes, and heaters are some of the commonly used thermal control elements.

3.1 Multi-Layer Insulation (MLI) Blankets

MLI blankets are used to provide radiative isolation on surfaces. MLI blankets prevent direct radiative heat load from sun or other sources falling on the surfaces of satellite, and it also prevents thermal radiation from the surfaces to cold space. Thus, MLI prevents heating of surfaces from other heat sources, and it also prevents cooling of surfaces by radiating to cold space. MLI consists of multiple layers of aluminized Mylar separated by Dacron mesh. Multiple layers of aluminized Mylar minimize the radiation heat transfer, and separation of these layers by Dacron mesh reduces the conduction heat transfer between Mylar layers. These layers are covered by thick aluminized Kapton layer for protection.

3.2 Optical Solar Reflector (OSR)

Optical solar reflector (OSR) is a very important thermal control element of satellite thermal management system. It is used on radiator surfaces of satellite. It enhances the infrared emission of radiation, and it reduces the absorption of short wavelength visible radiation from sun and albedo radiation from earth. OSR is made by coating rear surface of quartz with silver to reflect the incoming solar radiation. A protective metallic layer is also coated on rear side. The solar absorptivity of OSR surface varies from 0.08 at beginning of life to 0.21 at the end of life. The emissivity provided by OSR surface is 0.78.

Besides MLI and OSR, various thermal control tapes and paints are used as thermal control elements to modify the radiative properties of surfaces. Black paint and tape provide high IR emittance and high solar absorptance. Aluminum paint and low emittance tape provide low IR emittance and low solar absorptance surface. Coating of white paint on a surface provides high IR emittance and low solar absorptance.

3.3 Thermal Interstitial Materials

Thermal interstitial materials are used to enhance the thermal contact conductance across surfaces in contact. Thermal contact conductance governs the heat flow across two surfaces in contact. Thermal contact conductance depends on many parameters such as pressure on surfaces, roughness, flatness, thermal conductivity, and elasticity of the material under contact. Thermal interstitial material fills the micro irregularities on the surfaces in contact, which aids in enhancing the heat conduction path across surfaces. Thermal grease, metal foils, etc., are commonly used as thermal interstitial material in satellites.

3.4 Heat Pipes

Heat pipe is also a very important thermal control element in satellites. Heat pipe is a two-phase heat transport device working on the principle of evaporation and condensation of a working fluid in a closed system, with fluid flow caused by capillary action developed in its wick [5]. Heat pipe is made of a sealed metallic hollow tube. Inner walls of tube are lined with porous wick structure to provide capillary action. The wick structure has suitable pores to produce sufficient capillary action to recirculate the fluid in the heat pipe. The pores of the wick are saturated with suitable working fluid, and remaining space in heat pipe is occupied by the vapor of the working fluid. When the heat is applied at one end of heat pipe, the fluid evaporates absorbing its latent heat. As pressure builds up at evaporator section due to evaporation the vapor flows down to other end of the heat pipe. The vapor condenses at the other end due to lower temperature releasing the latent heat absorbed during evaporation. The condensed fluid flows back to evaporator end due to capillary action of the wick maintaining the cycle of evaporation and condensation in the heat pipe. Ammonia-based heat pipes are used in satellites for better performance within operating temperature ranges. Heat pipe can provide very high effective thermal conductivity compared to ordinary metals. One can easily get the thermal conductivity of a heat pipe more than 10 times that of copper. Use of heat pipe saves mass as well as volume in the satellite. In small satellite, mini heat pipes can be used to transport heat from heat source to the radiator panel.

3.5 Heaters

Heaters are indispensable part of any thermal management system in satellites. If temperature of any element of satellite goes below allowable limit, heaters are used to maintain the temperature above cold limit of that element. Two types of heaters are used in satellites 1. Tape heaters and 2. Foil heaters. Tape heaters are used for curved surfaces like plumb lines, tank, etc. In foil heaters, resistive heating element is laminated between very thin Kapton layers. Foil heaters can be used for temperature ranging from -65° to 150°C . In small satellites, heater power should be optimized properly as availability of power is usually very limited.

4 Thermal Management Challenges

Small satellites offer many advantages, but there are many challenges in designing them. Thermal issue is one of the challenges in designing small satellites. Thermal issues are more critical in micro and nano satellites. Thermal management of satellite ensures that temperature of all the components of the satellite should remain within

allowable temperature limits during all phase of mission. Proper thermal management ensures that satellite functions to provide required performance for the expected life of the satellite. Most electronic components operate at their optimum performance at room temperature, i.e., around 0 to 40 °C. Thermal management of satellite must ensure temperature of electronics within such required temperature limits. Temperature beyond the required limits adversely affects the operational life and performance of components. Low mass, small volume, and high power densities make the task of thermal management of small satellites very challenging. Some of the challenges in thermal management of small satellites are discussed hereafter.

4.1 Low Mass

Low mass of small satellites poses a very critical thermal challenge [7]. Low mass implies low over all heat capacity of the satellite. As small satellites are normally placed in LEO. In LEO, the sun illuminates the satellite for some portion of the orbit, and remaining portion is in the shadow of earth. The shadow period of the orbit is called eclipse. As the altitude of orbit decreases, the fraction of the orbit period under eclipse increases. Variation of eclipse period with altitude at different sun aspect angle (SAA) is shown in Fig. 2. Due to low thermal mass of small satellites, temperature of the satellite changes very fast as the external load changes on the satellite. During eclipse period, satellite cools vary fast due to low thermal mass. Due to small orbital period of LEO, the satellite has to face large number of thermal cycling. Thermal cycling shortens the life of the satellite components. Varying heat load on the satellite makes the thermal management task difficult. Appropriate thermal management is required to maintain the temperature of components within allowable limits under varying heat loads.

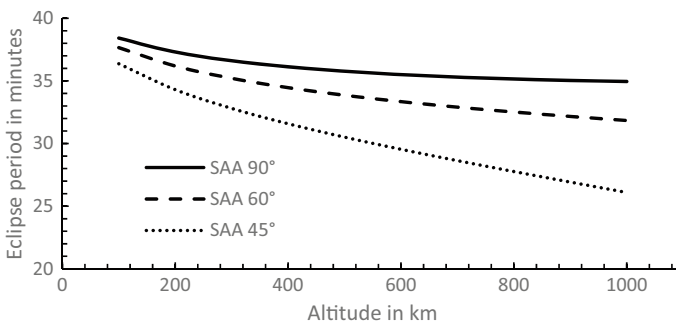


Fig. 2 Variation of eclipse period with altitude at different sun aspect angle (SAA)

4.2 *Small Volume*

Small volume also poses challenges for thermal management. In small satellites, ratio of external area to internal volume is higher than the large satellites. Therefore, satellite will be more affected by external space environment. All the components of the payload have to be accommodated in the limited space. Internal heat dissipation per unit volume may be high in small satellites. It causes high heat flux densities, and there is almost no scope to use heat spreader or large heat sinks. Radiative coupling between internal components becomes significant when high heat dissipating components are arranged very closely. In such situation, temperature of components may rise beyond allowable limits. Therefore, small volume or size of small satellites makes thermal management task really challenging.

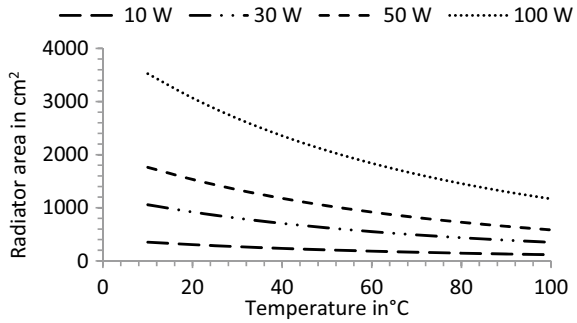
4.3 *Small Surface Area*

Passive thermal management of satellite controls the temperature of satellite by applying MLI, optical solar reflector or thermal paints/tapes on the external or internal surfaces of satellite. To regulate the temperature of the satellite, thermal engineer either isolates the surface from the space environment by covering it by MLI or tries to change the thermal characteristics of the surface by changing infrared emissivity or solar absorptivity of the surfaces. A 1U CubeSat has only 600 cm² external surface area available. As many small satellites do not have separate solar panels, most small satellites have solar panels mounted on the main body/bus of the satellites. Due to large demand of electric power for payload and thermal control heaters, solar cells cover most of the external surface area. Some area is covered by interface with the launch adapter. Therefore, very little surface area is left for thermal engineer to apply thermal control elements.

Small surface area means radiator area to dissipate heat to space is also very scarce. If satellite is dissipating large amount of heat, suitable radiator area is required to dissipate that much heat to control the temperature of all components. In such a situation, thermal engineer is required to be involved from the beginning of design phase of the satellite. Not all faces of the satellite are suitable for radiator area. Some face may be having better view factor to cold sky than other faces. Figure 3 shows the radiator area variation with temperature at different heat load levels assuming no external heat loads. It is seen that radiator area required decreases with increase in temperature of radiator. The layout of the internal components should be planned in such a way that maximum heat should be dissipated to the face, which is having best view factor to the cold sky.

In large satellites, multi-layer insulation (MLI) blankets are widely used to isolate the external surfaces from the extremes of the space environments. Micro and nano satellites have small size external surfaces. On such small surfaces, MLI is not as effective as it is on large surfaces. On small surfaces, the effect of edges of the surface

Fig. 3 Radiator area variation with temperature at different heat loads



on which MLI is applied dominates. MLI is very tightly stuck on the edges of the surfaces while it is fluffy at other places. Due to this, the heat transfer coefficient provided by MLI becomes quite uncertain. In such situation, prediction of orbital temperature is not easy task. Therefore, in micro and nano satellites cases, thermal design of satellite is preferred without the application of MLI. Therefore, MLI should be used with due cautious on small satellites.

4.4 High Power Density

High power density is one of the critical challenges in the thermal management of small satellites. Due to small size of satellite, small PCB cards may be densely packed with heat dissipating components. Many high heat dissipating electronic components being packed into small space further creating a hotter ambient inside the satellite. High power density becomes further challenging as radiator area is generally in scarcity.

Due to limited space in small satellites, PCB cards are stacked together. In such situation if high dissipating card is placed away from satellite chassis, then it becomes difficult to efficiently conduct heat away from PCB cards and temperature of some components on such PCB card may rise beyond allowable limits.

4.5 Limited Power for Heaters

If eclipse period is significantly large, heater is required to regulate the temperature of satellite during eclipse period. Heaters require high capacity battery for longer eclipse periods. In many small satellite solar cells are mounted on the body of the satellite. Many times small satellites do not have provision for separate extended solar panels. In such case, power available for heaters is very limited. It becomes a challenging task to regulate the temperature of all components of the satellite with limited heater power. Availability of power is constrained by the area available

to mount the solar cells on the external surfaces of the satellite. Passive thermal management of the satellite is achieved by cold biasing the satellite, and then, heaters are used to maintain the temperature of the components of the satellite at the level of cold limit. When thermal control requirement of a payload is very stringent than cold, biasing becomes very important, and heater power requirement becomes inevitable. In such scenario, the estimation of temperatures has to be very accurate. Otherwise, thermal engineer may have large margins in heater power requirements, which can further complicate the thermal management task of the satellite.

5 Special Techniques to Address Thermal Control Challenges

Many technological developments have taken place, which can be applied to address the thermal management challenges of small satellites. Few technological developments have reached to a stage where they can be readily applied, while many are still in the developing stage. Some of the potential technologies for small satellites are discussed hereafter.

5.1 Phase Change Material (PCM)

If power dissipation in an electronic component is only for a part of the orbital period then phase change material can be considered to manage the temperature of such components. In imaging satellites, heat dissipation in detectors is only for a fraction of orbital period. In a typical imaging satellite heat dissipation is for imaging period, which is 10 to 15 min while orbital period is around 100 min. If temperature of the detector reaches beyond allowable limits the performance of the detectors is adversely affected. PCM can be used as passive thermal control management to avoid the temperature excursions on the detectors or electronic components. PCM-based thermal control module (TCM) is suitable for thermal management of small satellites, as it does not require additional radiator area. Use of PCM saves heater power also as stored heat in PCM is released to keep the satellite warm during cold phase of satellite. Phase change material is sealed in a metallic enclosure, and sufficient space is left for volumetric expansion during heating. The heat dissipating component to be cooled is fixed on the one of the faces of the sealed enclosure. During heat dissipation period, the heat is transferred conductively to the phase change material. Phase change material absorbs some part of heat as sensible heat and remaining part of heat as latent heat by transforming solid to liquid phase. During non-heat dissipating period, latent heat of PCM is released to surrounding, and it solidifies to its original temperature. Thus, PCM prevents the temperature of heat dissipating components from shooting up beyond allowable limits during operational period.

Performance of the PCM can be significantly improved by adding the fin structure on the internal wall of the container of PCM [8].

5.2 Vapor Chamber with PCB Cards

In small satellites, traditional heat sink or heat spreaders are difficult to use due to constraints of mass and size. Vapor chamber works on the principle of heat pipe. Heat pipe transports heat in a linear dimension, while vapor chamber is able to spread heat in a two-dimensional plane. Vapor chambers are used to spread heat over a larger area. Vapor chambers are passive phase change device producing a relatively small thermal resistance. Vapor chambers have proven to be excellent among the most passive cooling device [9]. Vapor chambers can be made of thickness of about 3 to 5 mm. As vapor chambers require very less space, they are suitable for small satellite applications. Vapor chambers can be used for high heat dissipating components. A vapor chamber can also be built with suitable through holes for passing the leads of heat dissipating component. Heat dissipating components can be placed at discreet locations and in direct contact with the vapor chamber surface. Vapor chamber can create almost isothermal surface. Vapor chamber can handle high heat fluxes in the range of 100 to 200 W/cm². Application of vapor chamber can provide effective thermal conductivity above 5000 W/m/K easily.

5.3 Multi-Functional Structure

Small satellites have limitations of both mass and volume. Separate thermal control elements, e.g., heat pipe, loop heat pipe, and heat sink, not only increase mass and volume but as separate part their interface with satellite chassis causes an added thermal resistance which increases the temperature of components mounted on them. It will be very beneficial in small satellites if thermal control elements are integrated with the structure of the satellite. Thus, the chassis of the satellite can work both as a structural as well as thermal member. Such integration will reduce the overall mass of the satellite with minimum requirement of additional space. Loop heat pipes and heat pipes can be built on the satellite chassis using 3D printing. Satellites structure can also be developed with in-built fluid loops for thermal control using 3D printing. Such multifunctional structures of small satellite can greatly reduce mass and volume requirements.

5.4 Variable Emissivity Radiator

Variable emissivity radiator surfaces have the ability to change the emissivity of the surface depending on the temperature. Vanadium di oxide-based radiator surfaces have shown temperature-dependent emissivity properties [10]. When the temperature of the surface increases, emissivity of the surface also increases which enables the surface to dissipate larger heat loads into cold space, thus preventing the temperature of components inside satellite from rising beyond allowable limits. Similarly, when the temperature of the radiator surface decreases, the emissivity of the surface also decreases which reduces the heat radiating into the cold space from the surface, thus preventing the lowering of the temperature of the components. Thermochromics surfaces can change the radiative properties of the surface depending on the temperature. In small satellites, the heater power is very scarce due to limited capacity of solar power generation. Use of variable emissivity radiator can reduce the requirement of heater power significantly. When the temperature of the components decreases due to decrease in external or internal heat loads, normally heaters are switched on to maintain the temperature of components above cold temperature limits. In case of variable emissivity radiators, instead of switching on the heaters, the emissivity of the surface will change such that less heat is radiated to space and thus obviating the need of heater to maintain the temperature of components. In cold case, thermal heater can consume around 30 to 40% of total power of the satellite. Such radiators are free of any moving parts.

6 Guidelines for Efficient Thermal Management of the Small Satellites

The basic philosophy of thermal management is same irrespective of the size of the satellite. Techniques to solve thermal issues of big satellites are used for small satellites also. Following are some general guidelines for thermal management of small satellites.

- High heat dissipating PCB cards should be mounted closer to interface with the satellite chassis [11].
- Sufficient number of copper layers can be added within the PCB card for in-plane heat transfer.
- High power components can be mounted near the edge of the PCB card.
- Edges of the PCB card and enclosure/chassis should have good contact area for efficient conductive heat transfer.
- High power components can be placed such as to keep the low power density on the PCB card.
- Sufficient number of fasteners should be provided for mounting the board on the enclosure or chassis to provide excellent thermal contact conductance at the board interface to dissipate heat efficiently.

- When heat is to be dissipated, component surfaces should be flush mounted to have large area in contact for conductive transfer of heat.
- If some component or payload is cold biased, it can be isolated using low conductive washers to reduce the requirement of heater power.

7 Conclusions

The thermal management task of small satellites involves many limitations and uncertainties. These limitations and uncertainties make the thermal management of small satellites a challenging task. To realize a practical thermal management solution for small satellites, the thermal engineer should be involved in the design phase from the beginning itself, so that thermal issues are taken into consideration concurrently with the satellite and payload design. Thermal engineer should also keep in mind the general guidelines for efficient thermal management of small satellites. Many new technologies are coming up to solve the thermal management problems in satellites. Thermal engineers should keep themselves updated with latest thermal control techniques to solve the challenges in the thermal management of small satellites.

References

1. Baturkin V (2003) Small satellite thermal control-present-day tendencies. In: Presented at 33rd international conference on environmental systems (ICES), SAE International, Vancouver, B.C. Canada, July 7–10
2. Isro.gov.in/spacecraft/small-satellites. Last accessed 22 Nov 2021
3. Karam R (1998) Satellite thermal control for system engineers. Progress in astronautics and aeronautics. AIAA Virginia vol 181
4. Agrawal BN (1986) Design of geosynchronous spacecraft. Englewood Cliffs, Prentice Hall, NJ
5. Baraya KK (2014) Applications of heat pipes in satellites. An Int J Heat Pipe Sci Technol 5(1–4):555–562, Begell House. <https://doi.org/10.1615/HeatPipeScieTech.v5.i1-4.640>
6. Ku J (1999) Operating characteristics of loop heat pipes. In: Presented at 29th international conference on environmental systems, Denver, Colorado, July12–15
7. Butcher MR (1999) Spacecraft thermal design: particular problems with small satellites. Proc Inst Mech Eng J Aerospace Eng Part G 213. 10.1177%2F095441009921300405
8. Desai AN, Gunjal A, Singh VK (2020) Numerical investigations of fin efficacy for phase change material (PCM) based thermal control module. Int J Heat Mass Transf 147. <https://doi.org/10.1016/j.ijheatmasstransfer.2019.118855>.
9. Bulut M, Kandlikar SG, Sozbir N (2019) A review of vapor chambers. Heat Transfer Eng 40:1551–1573. <https://doi.org/10.1080/01457632.2018.1480868>
10. Hendaoui A, Émond N, Chaker M, Haddad É (2013) Highly tunable-emittance radiator based on semiconductor-metal transition of VO₂ thin films. Appl Phys Lett 102. <https://doi.org/10.1063/1.4792277>
11. Young J, Inlow S, Bender B (2019) Solving thermal control challenges for cubesats: optimizing passive thermal design. In: Presented at IEEE aerospace conference, MT, USA

Piezo-Actuated and Hydraulically Amplified Linear Compressor for Pulse Tube Cryocooler



Faisalkhan R. Pathan, Numan Ahmad, Gagan Agrawal, Naimesh R. Patel, Reena R. Trivedi, and Shaunak R. Joshi

Abstract Linear actuator device for gas compression has significant importance in a cryocooler system. The compressor provides acoustic power to drive the cooling phenomenon in the pulse tube cryocooler. In general, the compressor is designed based on electromagnetic effect. But, such compressors have limiting factors, such as heating due to eddy current, large size, and exhibit electromagnetic interference (EMI), which is undesired for space applications. A novel linear-drive compressor actuated using a piezoelectric actuator is presented in this paper. Piezoelectric actuators have an inherent limitation of extremely small elongation as compared to their length. A hydraulic amplification system along with resonance amplification is proposed. Motion transfer is done using different diameter pistons and housing assembly. This paper includes theoretical formulation and numerical study of the amplification system. An equivalent analytical spring-mass-damper model is formulated to determine resonance frequency. Amplitudes of the piezoelectric actuator elongation and piston displacement are shown. Design is aimed to achieve an operating frequency of 100 Hz.

Keywords Piezoelectric actuator · Linear compressor · Hydraulic amplification · Resonance amplification

1 Introduction

Oscillatory pressure waves are required to drive the pulse tube cryocoolers. Generally, two types of gas compressors, namely rotary and linear, are employed in cryocoolers to generate pressure oscillations. Linearly actuated compressors are considered superior in terms of reliability and ease of balancing compared to rotary compressors.

F. R. Pathan · R. R. Trivedi
Institute of Technology, Nirma University, Ahmedabad, Gujarat, India

N. Ahmad · G. Agrawal (✉) · N. R. Patel · S. R. Joshi
Space Applications Centre, ISRO, Ahmedabad, Gujarat, India
e-mail: a_gagan@sac.isro.gov.in

Voice coil actuators, based on electromagnetic principles, are used as linear actuating devices in linear compressors. Due to their large size for a given force requirement and electromagnetic interference (EMI), electromagnetic actuator-based compressors are considered undesired for space applications. Piezoelectric actuators with motion enhancements can be used as an alternative to cater to these issues for driving miniature pulse tube cryocoolers. Due to the high power-to-volume ratio of piezoelectric actuators and their ability to operate at a wide range of frequencies, these can be considered best for use in miniature-sized compressors.

Piezoelectric actuators provide limited stroke only. Some form of motion amplification mechanism is needed to achieve the desired stroke. Various means of mechanical flexure-based amplification, or hydraulic amplification, can be used to generate motion amplification. Hydraulic amplification systems are preferable for use in miniature-sized compressors due to not comprising the structural stiffness of the amplification mechanism. This paper describes a motion amplification scheme using a hydraulic system along with mechanical resonance.

Various designs and studies on piezo-based hydraulic amplification system, which are used primarily for static motion amplification, have been reported in research papers [1–3]. Steyn et al. [1] presented a hydraulic amplification for micro-electro-mechanical systems (MEMS). Authors have reported an amplification ratio of 48:1 for the intended applications in microscale static motion.

Yoon et al. [2] presented a high stroke piezoelectric actuator that uses a hydraulic amplification system. The displacement amplification mechanism can generate stroke in the range of a few millimeters.

Tang et al. [3] developed a single hydraulic displacement amplifier for piezo-actuated large stroke precision positioning. The amplifier mechanism can achieve an amplification ratio of 34.6:1 with a maximum output displacement of 1.02 mm for the given piezoelectric actuator with 30 μm stroke length.

Some researchers [4–8] have shown the development of piezoelectric actuator-based hydraulic amplification systems for a continuous dynamic operation. Garaway et al. [4] have used a single hydraulic amplification system with flip-flop membranes instead of pistons to produce desired pressure oscillations. The system is suitable for miniature pulse tube cryocoolers at high frequencies up to 500 Hz.

Sobol et al. [5–8] have developed various configurations of piezoelectric linear compressors. A linear compressor driven by a piezoelectric actuator along with a mechanical amplification system in resonance is described in [5]. A double hydraulic amplification system [6] is used in a miniature compressor for continuous flow in multi-stage Joule–Thomson cryocoolers. The compressor employs double hydraulic amplification in the first stage of compression, while the second compression stage uses a single hydraulic amplification.

Further, Sobol et al. [7, 8] have described the use of a piezoelectric actuator with hydraulic amplification configuration in resonance, where the piezoelectric actuator also moves in the housing. The achieved dynamic frequency of the compressor was 103 Hz in comparison to the designed frequency of 115 Hz for the pulse tube cryocooler. The authors have shown that the resonance frequency can be tuned by

changing the mechanical structure with modified stiffness to improve compressor efficiency.

This paper presents a new concept of a piezoelectric actuator-driven displacement amplification system. This system is simple and easy to assemble compared to the complex construction of amplification devices in the available literature. The natural frequency of this system can be tuned accordingly to achieve the required operating frequency of the cryocooler. This design utilizes a hybrid approach of hydraulic amplification along with mechanical resonance. The concept utilizes two stages of hydraulic amplification and an additional spring-mass configuration. The spring-mass system helps to tune the natural frequency to the required operating frequency of the compressor.

The hydraulic amplification mechanism reduces the output force by the same order as the order of displacement amplification. Some minimum force is needed at the output displacement location for the compressor to generate desired pressure oscillations. In this concept, the added spring-mass system works in resonance and thereby increases the output displacement at the gas compression chamber without compromising the output force requirement.

A theoretical analysis of the compressor design has been carried out using MATLAB for numerical simulations. The amplification ratio, hydraulic volume, spring stiffness, and dummy mass are tuned to achieve the operating frequency with required displacement at the gas compression chamber.

2 Compressor Concept

Figure 1 depicts the schematic configuration of compressor concept. One end of a piezoelectric actuator is rigidly attached to the compressor housing. The other end of the piezoelectric actuator is connected to piston-1, which pushes the larger area (A_1) of hydraulic fluid. The smaller area (A_2) piston-2 then produces first-stage amplified displacement. The piston-2 is rigidly connected to a larger area (A_1) piston, which again pushes the hydraulic fluid of the second hydraulic amplification system. Consequently, the second amplification hydraulic fluid produces amplified displacement at piston-3. Both amplification systems use same area ratios, hence the same amplification ratio (A). The total amplification at piston-3 is A^2 times piston-1 displacement.

Piston-4 generates pressure oscillation in compression volume. A lightly damped spring connects piston-3 with piston-4. A dummy mass is rigidly attached to piston-4. This dummy mass and spring combination is used to tune the resonant frequency of the compressor at the driving frequency.

The pistons are attached to the housing with the use of membrane flexures. The membrane flexures prevent leakage and mixing of the hydraulic fluid and compression fluid. Since metallic membranes experience high stresses when subjected to large deformation, they are unsuitable for high-frequency dynamic applications. Further

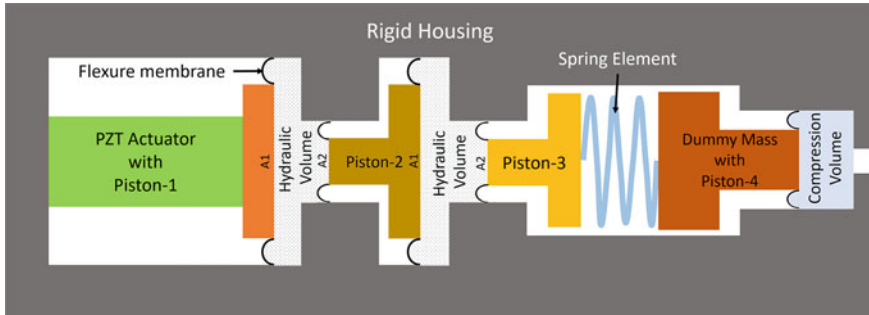


Fig. 1 Schematic of compressor configuration

study is being carried out to assess the use elastomeric materials as membranes flexures.

One of the major disadvantages of a hydraulic amplification system is that the force at the output displacement is reduced by the same order of displacement amplification. If only hydraulic amplification is used, the required displacement at the compressor output cannot be achieved without using an actuator with higher force. Therefore, though the displacement is amplified by A^2 times of the piezo displacement, this displacement is not sufficient to create the required pressure oscillation. It means the input force from the piezoelectric actuator needs to be increased, but it cannot go beyond the maximum force of the piezoelectric actuator. Thereby, only, the hydraulic amplification system (either single or double) cannot produce sufficient stroke and force to generate the required pressure oscillations. Hence, one of the viable approaches to increase the output displacement, while maintaining the required output force, is to drive the compressor in resonance. Since only the Piston-4 needs to be operated in resonance, therefore, the piezo stiffness and hydraulic stiffness should be sufficiently large compared to the gas stiffness and spring stiffness.

3 Theoretical Model

The compressor concept is shown in Fig. 1. It is converted to lumped parameter spring-mass-damper system as shown in Fig. 2. This model is fairly simple and linear. Numerical simulations are carried out in MATLAB. The membrane stiffness is not considered in the current analysis. Further, membrane stiffness can be modeled and incorporated into the model, and accordingly, spring and mass parameters can be tuned to obtain the desired frequency.

The lumped parameter model in Fig. 2 is a four degree of freedom (DOF) system. Mass M_{p1} comprises of piezo-actuator mass, piston-1 mass, and hydraulic mass in the bigger diameter volume of hydraulic amplification system. Masses M_{p2} and M_{p3} correspond to piston-2 and piston-3 masses, respectively. M_{p2} and M_{p3} also include

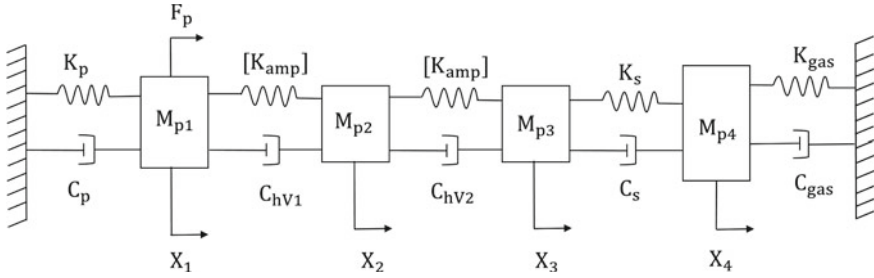


Fig. 2 Lumped parameter spring-mass-damper system of compressor. The hydraulic stiffness of hydraulic amplification is shown as matrix $[K_{amp}]$

corresponding hydraulic masses of the fluid in the amplification system. Mass M_{p4} comprises of compression piston mass along with the dummy mass.

Piezo-actuator stiffness is denoted as K_p . Hydraulic stiffness is denoted as $[K_{amp}]$, which is a 2×2 matrix and simulates the hydraulic amplification [1]. The hydraulic stiffness is expressed in Eq. (1) to Eq. (4).

$$[K_{amp}] = \begin{bmatrix} K_{h1} & -K_c \\ -K_c & K_{h2} \end{bmatrix} \tag{1}$$

where K_{h1} , K_{h2} , and K_c are components of $[K_{amp}]$ matrix defined as below:

$$K_{h1} = \frac{K_w A_1^2}{V_c} \tag{2}$$

$$K_{h2} = \frac{K_w A_2^2}{V_c} \tag{3}$$

$$K_c = \frac{K_w A_1 A_2}{V_c} \tag{4}$$

where A_1 is the area of bigger diameter of hydraulic volume, A_2 is the area of smaller diameter of hydraulic volume. V_c is the total volume of the hydraulic chamber, and K_w is the bulk modulus of the hydraulic fluid. Water is assumed as incompressible hydraulic fluid for calculations.

The hydraulic amplifier system force displacement relations are derived using a three spring coupler analogy of hydraulic amplifier [1], as shown in Fig. 3. This analogy models the effect of displacement X_2 on force F_1 , and accordingly the effect of displacement X_1 on force F_2 (Ref. Eq. (5)).

Using Eq. (1) and three spring coupler analogy, the force and displacement relations can be written as following:

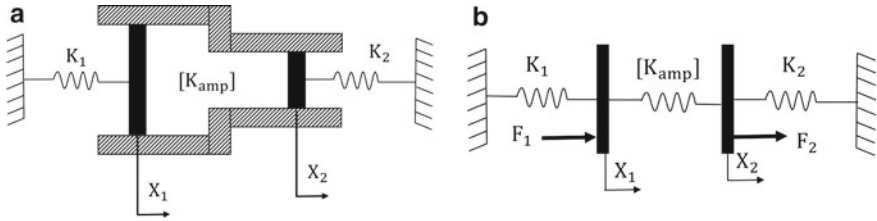


Fig. 3 Three spring coupler analogy of ideal hydraulic amplification system

$$\begin{Bmatrix} F_1 \\ F_2 \end{Bmatrix} = \begin{bmatrix} \frac{K_w A_1^2}{V_c} + K_1 & -\frac{K_w A_1 A_2}{V_c} \\ -\frac{K_w A_1 A_2}{V_c} & \frac{K_w A_2^2}{V_c} + K_2 \end{bmatrix} \begin{Bmatrix} X_1 \\ X_2 \end{Bmatrix} \tag{5}$$

The amplification ratio A is defined as below.

$$A = \frac{A_1}{A_2} \tag{6}$$

In this compressor configuration, same amplification ratio is used for both amplification stages. Therefore, the overall amplification ratio at piston-3 is A^2 .

The spring stiffness is denoted by K_s , and gas stiffness is denoted by K_{gas} . Gas stiffness is theoretically calculated from Eq. (6).

$$K_{gas} = \frac{\gamma P_0 A_g^2}{V_g} \tag{7}$$

γ is the adiabatic gas constant; P_0 is mean pressure of compression volume; A_g is the area of compressor piston, and V_g is the mean volume of the gas compression chamber. The spring stiffness K_s and mass M_{p4} are design parameters, which are used for adjusting the driving frequency of the compressor. The spring K_s should be lightly damped, e.g., wave springs. Helium is considered as operating gas for the calculations.

It is to be noted that, three spring coupler analogy (Eq. 5) is used only to evaluate spring forces for the hydraulic amplifier. The hydraulic volume V_c represents the total volume of both large and small diameters. And since energy losses occur mainly due to the flow between the both, a single value for damping coefficient, instead of a 2×2 matrix, is sufficient to model the energy dissipation in the hydraulic volumes.

C_p is the damping coefficient of piezo actuator. C_{hV1} and C_{hV2} are the damping coefficients of first and second stage of hydraulic volumes; these values represent the hydraulic losses occurred during hydraulic fluid motion. C_{gas} and C_s are the damping coefficient of compression gas and spring, respectively.

The equations of motion are derived using force balancing on the masses and are given in following Eqs. (8–11).

$$M_{p1} \ddot{X}_1 + (C_p + C_{hV1}) \dot{X}_1 - C_{hV1} \dot{X}_2 + (K_p + K_{h1}) X_1 - K_c X_2 = F_p \tag{8}$$

$$M_{p2} \ddot{X}_2 - C_{hV1} \dot{X}_1 + (C_{hV1} + C_{hV2}) \dot{X}_2 - C_{hV2} \dot{X}_3 - K_c X_1 + (K_{h1} + K_{h2}) X_2 - K_c X_3 = 0 \tag{9}$$

$$M_{p3} \ddot{X}_3 - C_{hV2} \dot{X}_2 + (C_{hV2} + C_s) \dot{X}_3 - C_s \dot{X}_4 - K_c X_2 + (K_{h2} + K_s) X_3 - K_s X_4 = 0 \tag{10}$$

$$M_{p4} \ddot{X}_4 - C_s \dot{X}_3 + (C_s + C_{gas}) \dot{X}_4 - K_s X_3 + (K_s + K_{gas}) X_4 = 0 \tag{11}$$

The equations of motion are written in matrix form as following.

$$[M] \left\{ \ddot{X} \right\} + [C] \left\{ \dot{X} \right\} + [K] \{X\} = \{F\} \tag{12}$$

where

$$[M] = \begin{bmatrix} M_{p1} & 0 & 0 & 0 \\ 0 & M_{p2} & 0 & 0 \\ 0 & 0 & M_{p3} & 0 \\ 0 & 0 & 0 & M_{p4} \end{bmatrix}$$

$$[K]^* = \begin{bmatrix} K_p + K_{h1} & -K_c & 0 & 0 & 0 \\ -K_c & K_{h2} + K_{h1} & -K_c & 0 & 0 \\ 0 & -K_c & K_{h2} + K_s & -K_s & 0 \\ 0 & 0 & -K_c & -K_s & K_s + K_{gas} \end{bmatrix}$$

*The 2×2 matrices highlighted with dotted square are the $[K_{amp}]$ matrices (ref. Eqs. (1) and (5))

$$[C] = \begin{bmatrix} C_p + C_{hV1} & -C_{hV1} & 0 & 0 \\ -C_{hV1} & C_{hV1} + C_{hV2} & -C_{hV2} & 0 \\ 0 & -C_{hV2} & C_{hV2} + C_s & -C_s \\ 0 & 0 & -C_s & C_s + C_{gas} \end{bmatrix}$$

$$\{F\} = \begin{Bmatrix} F_p \\ 0 \\ 0 \\ 0 \end{Bmatrix} \text{ and } \{X\} = \begin{Bmatrix} X_1 \\ X_2 \\ X_3 \\ X_4 \end{Bmatrix}.$$

X_1, X_2, X_3 , and X_4 are displacements of piston-1, piston-2, piston-3, and piston-4, respectively. The piezo force is denoted by $F_p = F_0 \sin(\omega t)$, where ω is the forcing frequency in rad/sec.

4 Results and Discussions

The equations of motion (Eq. 12) are solved using MATLAB. The compressor for pulse tube cryocooler is designed for the required parameters of 0.15 cc one-sided (0 to peak) swept volume, 100 Hz operating frequency, 30 bar operating pressure, and 1.3 bar pressure ratio. The piezoelectric actuator, to be used, can generate force of 1600 N and maximum limited stroke of $\pm 15 \mu\text{m}$. Iterative simulations are carried out to determine the optimum values of compressor parameters, like hydraulic amplification ratio (A), piston diameter (PD), spring stiffness (Ks), and tuning mass (M_{p4}).

Initially, geometrical parameters hydraulic amplification ratio (A) and piston diameter (PD) were finalized. Iterations were carried out to find the effect of amplification ratio (A) on the natural frequency, piezo displacement (X_1), piston-2 & 3 (X_2 & X_3), and gas displacement (X_4). Here, elongation of piezoelectric actuator is referred to as piezo displacement (X_1).

The piezo force is given as frequency sweep from 0 to 200 Hz, and the responses at all four piston displacements are estimated. The plots shown in Fig. 2 are with respect to single-stage amplification (A); the corresponding total hydraulic amplification is A^2 .

As described in Eq. (7), the gas stiffness (K_{gas}) is a function of Piston-4 diameter (PD). As PD is increased, gas stiffness will also increase. It leads to a requirement of lesser stroke length at piston-4. Piston-4 diameter is varied from 10 to 14 mm with increments of 1 mm. These variations in piston-4 diameter are shown as PD-10 to PD-14 in the figures below. Corresponding stroke length requirements for PD-10 to PD-14 are 0.95 mm, 0.79 mm, 0.66 mm, 0.56 mm, and 0.49 mm, respectively. The calculated stroke length is “0 to peak” amplitude of required displacement needed to generate the pressure oscillations in the gas compression chamber.

It can be observed from Fig. 4a that the higher the gas stiffness (or Piston-4 dia.), the larger is the maximum piezo displacement. The piezo displacements for PD-13 and PD-14 are near to limiting value of $\pm 15 \mu\text{m}$. Hence, PD-13 and PD-14 are ruled out for compressor design parameters. PD-10 and PD-11 are also eliminated because respective length requirement is higher than the Piston-4 displacement as shown in Fig. 4b. It is also noted that Piston-4 displacement for PD-12 does not vary significantly between amplification ratio of 5:1 and 6:1. Amplification ratio 6:1 is selected as final parameter for compressor design, and PD-12 is considered to be final diameter of Piston-4.

The effect of amplification ratio on natural frequency of the system is shown in Fig. 5. It can be seen that the natural frequency decreases with an increase in amplification ratio. Although the achieved frequency with amplification ratio 6:1

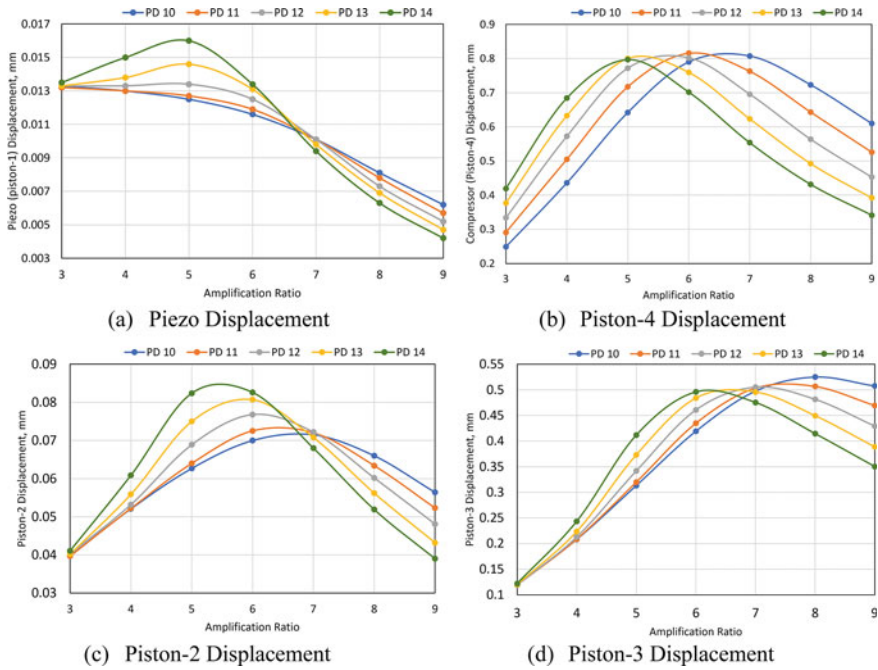
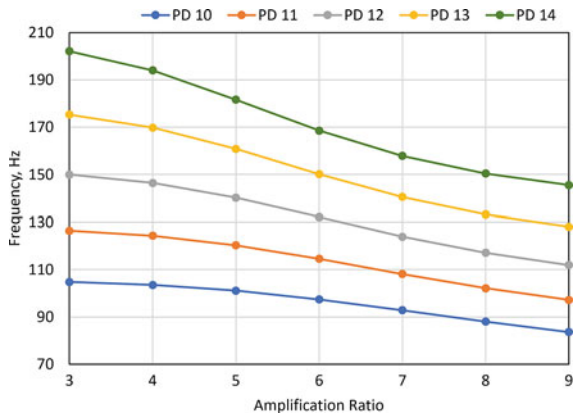


Fig. 4 Effect of amplification ratio (A) on the piezo, piston-2, piston-3, and piston-4 displacements

and piston diameter 12 mm is 130 Hz, the other remaining compressor parameters are tuned further to achieve required frequency and explained later in this paper.

Subsequently, the effect of spring stiffness on piezo displacement and Piston-4 displacement is shown in Fig. 6. The spring stiffness, K_s , is varied in terms of gas stiffness, which is denoted as Ks-factor. Spring stiffness is Ks-factor times the gas

Fig. 5 Natural frequency versus amplification ratio



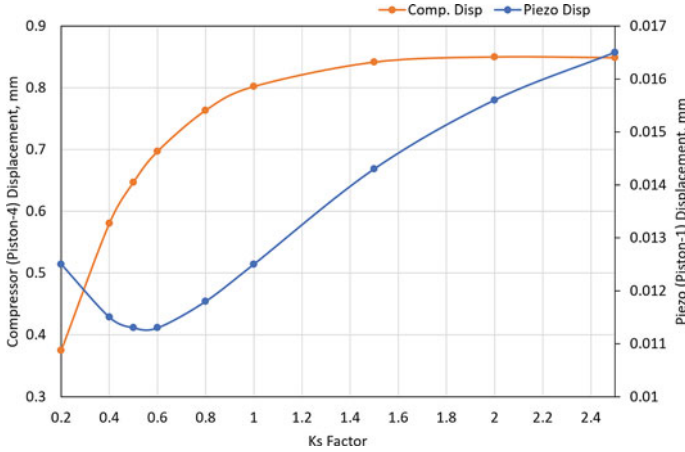


Fig. 6 Variation of piezo displacement and Piston-4 displacement with respect to change in spring stiffness (K_s)

stiffness K_{gas} . This is done in order to know appropriate spring stiffness in conjunction with gas stiffness. It can be observed from Fig. 6 that the compressor displacement almost saturates for K_s -factor values more than 1, while piezo displacement is minimum at K_s -factor of 0.5. Piezo displacement reaches limiting value of $15 \mu\text{m}$ at K_s -factor of 1.8. Therefore, it is inferred that in order to have optimized Piston-4 displacement; K_s -factor should neither be less than 1 nor greater than 1.8. Finally, K_s -factor of 1 is selected for maximum displacement at Piston-4 with minimum piezo displacement.

As the gas piston diameter (piston-4) is selected to be 12 mm, the calculated gas stiffness, K_{gas} , is 68 kN/m. The selected piezoelectric actuator can provide dynamic force of 1600 N with stiffness, K_p 120×10^6 N/m, and peak to peak stroke length of 30 μm . The A_1 area of large piston of hydraulic amplification corresponds to diameter of 75 mm, and accordingly, the smaller area, A_2 , corresponds to diameter of 30.6 mm. The length of fluid volume is 2 mm and 4 mm for bigger piston and smaller piston, respectively. The calculated hydraulic stiffness is $K_{h1} = 3.5 \times 10^9$ N/m, $K_{h2} = 9.7 \times 10^7$ N/m, and $K_c = 5.8 \times 10^8$ N/m. Spring stiffness, K_s , is selected same as gas stiffness since K_s -factor is finalized to be 1.0.

Mass parameters are estimated as: $M_{p1} = 0.09$ kg, $M_{p2} = 0.032$ kg, $M_{p3} = 0.023$ kg, and $M_{p4} = 0.266$ kg. The M_{p4} mass also includes dummy mass, which is tuned to obtain natural frequency of 100 Hz. The damping coefficients are generally obtained from the experimentation. In this paper, the spring damping C_s is assumed to be 2% of critical damping. Since the spring to be selected should be lightly damped, it is a fair assumption.

C_p and C_{gas} are considered 1000 N-s/m and 20 N-s/m which are similar to the experimental values as reported in literature [8]. A parametric analysis is also carried out to determine the effectiveness of C_p and C_{gas} various parameters of compressor. It

is found that the maximum change in piezo displacement and Piston-4 displacement is not more than 2% as C_p is varied by 4 times (1000–4000 N-s/m). Based on analysis, C_p is found to be very less effective on piezo and Piston-4 displacement.

The Piston-4 displacement is primarily affected by spring damping coefficient, C_s and C_{gas} . If C_{gas} is increased from 20 N-s/m to 50 N-s/m, Piston-4 amplitude reduces to 0.4 mm from 0.8 mm. Finally, C_{gas} is taken 20 N-s/m as reference value from literature [8]. However, actual damping coefficient can be estimated from experimentation.

The hydraulic damping coefficients, C_{hV1} and C_{hV2} , depend on the dynamic viscosity of the hydraulic fluid and the geometry of the chamber. These can be assumed to be negligible; however, it is finalized after estimating the effect of hydraulic damping, C_h (is considered same for both C_{hV1} and C_{hV2}), on Piston-4 displacement. The piston-4 displacement reduces by 20% with increase in hydraulic damping coefficient, C_h , from 10 to 50 N-s/m. The initial value of C_h is taken arbitrarily; in actual condition, it will be much less than the finalized value of 50 N-s/m.

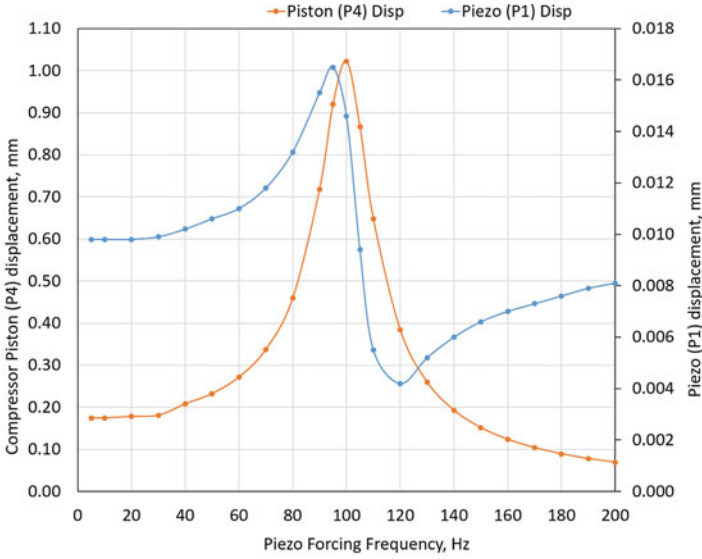
The equations of motion (Eq. 12) are solved for piezo force in sine sweep from 0 to 200 Hz. The simulated piston displacement at different frequencies is depicted in Fig. 7. The behavior of all plots clearly shows that only piston-4 is in resonance at 100 Hz of piezo actuation, and the displacement of other pistons has falling trend at the same frequency. Displacement curve for piston-1, piston-2, and piston-3 shows the similar trend and the difference in displacement value at 100 Hz corresponds to the hydraulic amplification only. The displacements of piston-1, piston-2, piston-3, and piston-4 are 0.0145 mm, 0.0895 mm, 0.5367 mm, and 1.022 mm, respectively, when the piezo actuator is actuated at 100 Hz.

5 Conclusions

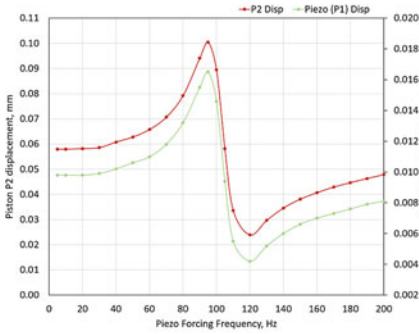
A new concept of piezoelectric actuator-driven linear compressor for pulse tube cryocooler is designed theoretically, which uses added spring-mass system to tune the operating frequency of the compressor. The system employs double hydraulic amplification in conjunction with mechanical resonance.

A lumped parameter spring-mass system model is constructed for simulations in MATLAB. It is shown that for different diameters of compressor piston, the amplification ratios can be optimized. Spring stiffness can further be optimized to achieve maximum piston displacement while maintaining the piezo elongation within the limiting range.

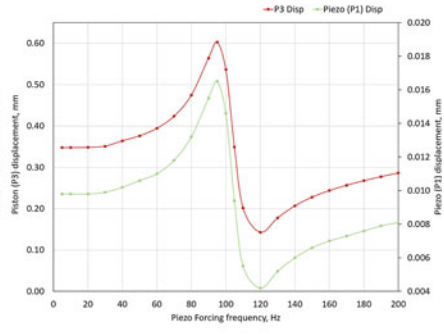
Numerical simulations with optimized parameters show that the design is able to achieve the maximum stroke length requirement of the compressor. This concept offers significant advantage in terms of flexibility to design and optimize the linear compressor for the required driving frequency and stroke volume of pulse tube cryocooler.



(a) Piston-4 displacement along with piston-1



(b) Piston-2 displacement along with piston-1



(c) Piston-3 displacement along with piston-1

Fig. 7 Piston displacement with respect to piezo forcing in frequency sweep

Acknowledgements Authors are grateful to committee members of Technology Development Program-SAC and Director, SAC, ISRO for their encouragement and support in carrying out the research and development activity.

References

1. Steyn JL (2002) Hydraulic amplification for actuation in microelectromechanical systems. Master of Science Thesis, Massachusetts Institute of Technology
2. Yoon H, Washington G (2006) A millimeter-stroke piezoelectric hybrid actuator using hydraulic displacement amplification mechanism. IEEE ISIE 2006, (July 9–12, 2006)
3. Tang H, Li Y, Xiao X (2013) Development and assessment of a novel hydraulic displacement amplifier for piezo-actuated large stroke precision positioning. In: 2013 IEEE international conference on robotics and automation (ICRA), (May 6–10, 2013)
4. Garaway I, Grossman G (2008) Piezo-hydraulic actuation for driving high frequency miniature split-stirling pulse tube cryocoolers. In: AIP conference proceedings 985, pp 622
5. Sobol S, Grossman G (2009) Investigation of cryogenic cooling systems activated by piezoelectric elements. International Cryocooler Conference, Inc., Boulder, CO
6. Sobol S, Tzabar N, Grossman G (2014) Miniature piezoelectric compressor for joule thomson cryocoolers. In: 25th international cryogenic engineering conference and the international cryogenic materials conference in 2014, ICEC 25-ICMC
7. Sobol S, Grossman G (2015) Linear resonance compressor for stirling-type cryocoolers activated by piezoelectric stack-type elements. In: IOP conference series: materials science and engineering 101, pp 012093
8. Sobol S, Grossman G (2012) Development of a linear compressor for stirling-type cryocoolers activated by piezoelectric elements in resonance. In: International cryocooler conference, Inc. Boulder, CO

Transient Thermal Modeling of Thermoelectric Coolers



Akshat Patel , S. S. Sisodia, Vivek Kumar Singh, Prasanta Das, Rakesh Bhavsar, and V. J. Lakhera

Abstract Thermoelectric coolers (TECs) are solid state devices which consume electrical energy to transfer heat from its cold side to its hot side while maintaining the temperature difference across the two sides. They find extensive application in the field of thermal management and cooling of several electronic systems. One such system is that of optical or microwave detectors employed in spacecrafts and satellites. Such detectors operate intermittently and generate high power densities during their operation. TECs can be integrated into existing thermal control setup to ensure that the optimum operating temperature of detector is controlled so that the accuracy and efficacy of the system is maintained. However, integration of TEC into a given thermal control setup is a tedious task because the information regarding the properties of various materials and intricate geometry of the TEC are not available. The present study aims to develop a methodology to model the transient behavior of TEC without its internal geometry such that it can be readily integrated into the existing thermal control setup. The methodology consists of extracting the various parameters and thermal properties of TEC from its datasheet and modeling the TEC within the environment of a commercially available software. The model is validated against the transient experimental results under pulsed operation available in open literature.

Keywords Thermoelectric cooler · Thermal management · Transient behavior

1 Introduction

Thermoelectric coolers (TEC) are also known as Peltier coolers as they work on the principle of Peltier effect which is the inverse phenomena of Seebeck effect. A

A. Patel · V. J. Lakhera
Department of Mechanical Engineering, Institute of Technology, Nirma University,
Ahmedabad 382481, India

S. S. Sisodia · V. K. Singh (✉) · P. Das · R. Bhavsar
Space Applications Centre, ISRO, Ahmedabad 380015, India
e-mail: singhvivek84@gmail.com

thermoelectric element consists of two differently doped elements (p and n type) made from the same metal, and their junctions are connected using metallic strips. When external current is supplied to such an element, the element experiences the Peltier effect, and it begins absorbing heat at one junction and transfers it and emits it at the other junction [1].

An actual TEC consists of several such pairs of thermoelectric elements all of which are connected in series electrically and in parallel connection thermally. The elements are connected between two large ceramic plates which accept and reject heat at cold and hot side, respectively. TECs are simple in operation, occupy very less space and can handle large ranges of heat load under varying conditions. Thus, they find applications in various fields such as electronic cooling systems and laser cooling [2–4], avionic and spacecraft thermal management [1, 5] and photovoltaic systems [6, 7]. The performance of a TEC depends largely on the properties of semiconductors such as Seebeck coefficient, electrical resistivity and thermal conductivity. Apart from these properties, the total number of couples and area–length ratio of the thermoelectric element also influence TEC’s performance.

The ideal steady state energy equation for an ideal thermocouple element is solved and referred in the paper [8] by Mani et al. The energy equation governing the performance of a thermoelectric element is as described in Eq. (1):

$$Q_C = 2N\alpha IT_C - \frac{1}{2}I^2\left(\frac{2N\rho}{G}\right) + (2NkG)\Delta T \quad (1)$$

Here, α , ρ and k are the Seebeck coefficient, electrical resistivity and thermal conductivity of thermoelectric material, respectively, N is the number of thermoelectric couples, and G is geometric factor which is the ratio of cross-sectional area to the length of thermoelectric element. However, these properties are rarely available for a given TEC. Without the knowledge of these parameters and details regarding the intricate internal geometry of the TEC, analytical evaluation of TEC’s performance under a given set of operating conditions becomes challenging, and thus, their integration into an existing thermal control setup also becomes challenging.

These properties can be extracted using the limiting values of the module such as maximum cold side load, Q_{\max} , maximum temperature difference, ΔT_{\max} , maximum current, I_{\max} , and maximum voltage, V_{\max} , which are available in the datasheet of the TEC by equations mentioned in reference [9] (refer Sect. 2 for equations).

However, solution to this system of equations cannot be obtained directly as it contains five unknowns but only three equations. Several numerical studies on the transient performance of TEC are available in open literature which usually involves simulating the full geometry of TEC [10–13]. However, as such studies involve modeling of the entire geometry, they are difficult to integrate into existing thermal control setup as computational cost and complexity increases. Such modeling methodology is more suitable to study the effects of internal geometry on the performance of TEC. To the best of author’s knowledge, there is no research available on modeling of TEC without its internal geometry in the open literature to reduce the overall complexity and to facilitate the integration of such coolers into already

existing systems. Thus, present study aims to devise a parameter extraction strategy and to form a simpler modeling technique to simulate the transient behavior of TEC within a commercially available simulation software.

2 Modeling Methodology

The present study aims to simulate the transient behavior of a given TEC within a commercially available software. The software considered for present study is NX 12.0 whose space thermal systems module is used. The module has a built-in simulation object named ‘Peltier cooler’ which solves Eq. (1) to solve for the temperature difference across the hot and cold side of the module. Hence, a new modeling approach is presented in this study wherein the steady state behavior of TEC is simulated using the simulation object, while the transient behavior is captured using effective thermal properties. Further the approach only consists of the ceramic plates with the original dimensions within the computational domain, thus reducing the computational complexity and cost considerably.

In order to capture the steady state behavior, the ‘Peltier cooler’ object requires the value of α , ρ , k , N and G . In order to extract these properties, a new set of parameters known as module parameters are introduced by simplifying the Eq. (1) as below:

$$Q_C = \alpha_m I T_C - \frac{1}{2} I^2 \rho_m + k_m \Delta T \quad (2)$$

where α_m , ρ_m and k_m are the module parameters which can expressed in terms of datasheet values using Eqs. (3)–(5) as below:

$$\alpha_m = \frac{V_{\max}}{T_h} = 2N\alpha \quad (3)$$

$$\rho_m = \frac{V_{\max}(T_h - \Delta T_{\max})}{I_{\max} T_h} = \frac{2N\rho}{G} \quad (4)$$

$$k_m = \frac{V_{\max} I_{\max} (T_h - \Delta T_{\max})}{2T_h \Delta T_{\max}} = 2NkG \quad (5)$$

Using above equations, module parameters can be independently obtained using the datasheet values. Now, module parameters are also the coefficients of the Eq. (2), and once their values are calculated from datasheet values, the solution of equation for a particular set of operating and boundary condition becomes invariant to the actual values of thermoelectric properties of the semiconductor. Hence, to obtain the value of α , ρ and k , any arbitrary value of N and G can be assumed, and corresponding values of α , ρ and k can be obtained using Eqs. (3)–(5). Any arbitrary values of N and G can be assumed as they will eventually preserve the values of module parameters and thus result in the same solution to Eq. (2).

As mentioned previously, the computational domain consists of only the ceramic plates in their original dimensions, effective specific heat and thermal conductivity is used to capture the thermal mass of the entire system and temperature drop across ceramic plates and metallic connectors. This is done using below equations:

$$(C_P)_{\text{eff}} = \frac{\rho_{\text{Cr}}(C_P)_{\text{Cr}}V_{\text{Cr}} + \rho_{\text{Al}}(C_P)_{\text{Al}}V_{\text{Al}} + \rho_{\text{TE}}(C_P)_{\text{TE}}V_{\text{TE}}}{\rho_{\text{Cr}}V_{\text{Cr}}} \quad (6)$$

$$k_{\text{eff}} = \frac{L_{\text{Cr}}}{A_{\text{Cr}}} \left\{ \frac{L_{\text{Cr}}}{k_{\text{Cr}}A_{\text{Cr}}} + \frac{L_{\text{Al}}}{k_{\text{Al}}A_{\text{Al}}} \right\}^{-1} \quad (7)$$

The temperature drop across thermoelectric couples is handled directly by the simulation object and is hence omitted from Eq. (7). Thus, the ceramic plates are transformed into combined mass plates such that their volume and density is the same as that of the original ceramic plates, but their specific heat and thermal conductivity is such that the thermal inertia and temperature drop across combined mass is the same as in the case of actual TEC. Using this methodology, the transient behavior of TEC is modeled and validated against a reference case in next section.

3 Numerical Model

3.1 Reference case

The reference case taken to validate the numerical results is the study on transient cooling characteristics by Ming et al. The study experimentally investigates the transient behavior of the TEC UT15-200-F2-4040-TA-W6 manufactured by Laird Thermal Systems. The hot side of the TEC is exposed to air and dissipates heat through convection. Air flow is induced over the hot side ceramic plate, and the flow rate is measured using a flowmeter as shown in the schematic. The incoming air is cooled to 21.5 °C using a Julabo F32-EH refrigerating and heating circulator, while the outgoing air rejects the heat using a radiator. Temperature of the cold side is measured through several Omega T-type thermocouples (TT-T-36-SLE). The current input to the TEC module is either in the form of single pulse or multiple pulse.

3.2 Extraction of Thermoelectric Properties

Now, the datasheet of the given TEC contains the following information as tabulated in the Table 1.

Now, the thickness of entire module is reported to be 3.3 mm [15], while the thickness of ceramic plates and connectors is 0.97 and 0.47 mm. Hence, the length

Table 1 Datasheet values of TEC UT15-200-F2-4040-TA-W6 [15]

Quantity	Value
Hot side temperature	27 °C
Maximum cold side heat load	193.4 W
Maximum temperature difference	68.9 °C
Maximum current	15.2 A
Maximum voltage	21.5 V

Table 2 Values of different parameters at N = 200 and G = 4.66 mm

Variable	Value	Variable	Value
α_m	0.07163 V/K	α	$1.7908 \times 10^{-4} \text{ V/K}$
ρ_m	1.0897Ω	ρ	$1.27 \times 10^{-5} \Omega m$
k_m	1.8271 W/K	k	0.9787 W/m.K

of thermoelectric element is 0.42 mm. Further, the geometric factor is evaluated to be 4.66 mm. The number of thermoelectric couples is also reported to be 200. If this data is unavailable, they can be assumed arbitrarily as the steady state response is mathematically invariant to the values of semiconductor properties as far as the values of module properties are preserved as mentioned earlier. Now, using the datasheet values, the module parameters are calculated as below (Table 2).

Hence, the relevant thermoelectric properties of the semiconductor material used to manufacture the TEC are known, and the steady state response of the TEC under a given set of operating and boundary conditions can be predicted by using these properties in Eq. (1).

3.3 Calculation of Effective Thermal Properties

The effective thermal properties of the TEC module in order to capture the transient response can be calculated using Eqs. (6) and (7) as mentioned previously. However, they require the values of volume of ceramic plates, aluminium connectors and thermoelectric elements.

Figure 1 shows the internal geometry of a practical TEC along with detailed schematic of a single thermocouple and idealized geometry considered for simulation. Values of H_0 , H_1 , L_e , H_e and W are known and are tabulated in Table 3 Various dimensions of TEC. The length of aluminum connector strips is missing, and thus, their length is assumed to be twice the length of thermoelectric elements. This assumption will yield a reasonably accurate solution as the distance between two thermoelectric legs is very small. Table 4 tabulates the dimensions of ceramic plates, connectors and thermoelectric couples to calculate the effective thermal properties.

The dimensions mentioned in Table 4 are for a single quantity of the part, while the volume mentioned is the total volume occupied by total quantity of the part.

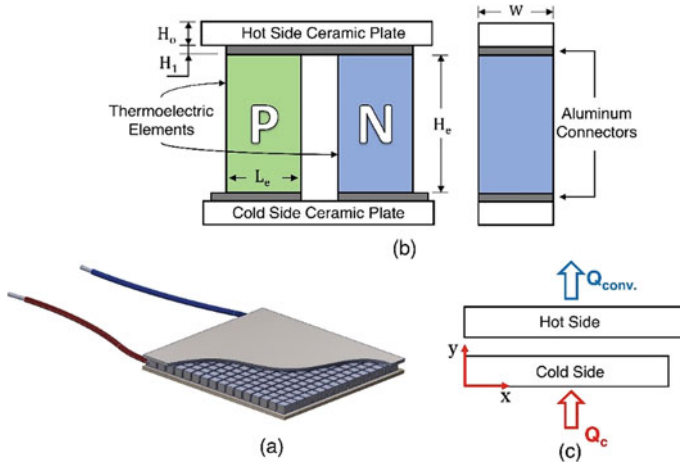


Fig. 1 a TEC with its internal geometry exposed b schematic diagram of a single thermoelectric couple c TEC with only ceramic plates

Table 3 Various dimensions of TEC

Dimension	Value (mm)	Dimension	Value (mm)
H_0	0.97 [14]	H_e	0.42
H_1	0.47 [14]	W	1.4 [14]
L_c	1.4 [14]	–	–

Table 4 Properties of TEC components [10–14]

Part	Quantity	$L \times B \times W$ (mm)	Volume (mm ³)	Density (kg/m ³)	C_p (J/kg. K)	k (W/m. K)
Ceramic plates	2	$40 \times 40 \times 0.97$	3104	3800	850	35
Aluminum connectors	800	$1.4 \times 1.4 \times 0.47$	736.96	2700	795	130
Thermoelectric legs	400	$1.4 \times 1.4 \times 0.42$	329.28	10,922	175	–

Further, the semiconductor material is assumed to be Bi_2Te_3 which is one of the most common materials used for the thermoelectric. This assumption is valid particularly for thermoelectric materials as they have very similar densities and specific heat values [10–12]. Thus, the effective specific heat and thermal conductivity are evaluated to be 1038 J/kg.K and 28 W/m.K, respectively.

3.4 Simulation Setup

The simulation environment used for present study is the space systems thermal module of NX 12.0 where in simulation object called ‘Peltier cooler’ is available. Another reason to consider NX 12.0 for present study is that it is primary tool for thermal analysis of various spacecraft subsystems and payloads, and hence, validation of the transient behavior within such an environment is of primary concern. The ‘Peltier cooler’ simulation object solves the steady state analytical equation for TEC as expressed by Eq. (1) and requires the TEC properties, i.e., α , ρ , k , N and G in order to solve the equation. The simulation object also asks the user to define the hot and cold region wherein the hot and cold side faces within the 3D geometry are to be selected. Apart from these inputs, the voltage or current given to the TEC module is also required to be mentioned [16]. For the present study, current as a function of time is given as the input.

The geometry created to model the TEC is shown in Fig. 1c. The inner faces of the hot and cold side are given as inputs to the simulation object, while the boundary conditions are given to the outer faces. Further, the size of plates modeled are the same as the size of ceramic plates mentioned in TEC’s datasheet. The density and volume of these plates are the same as that of ceramic, while its specific heat and thermal conductivity are equal to effective thermal properties calculated in the previous section.

3.5 Initial and Boundary Conditions

The entire domain is initialized from a temperature of 25 °C, while the input current to the ‘Peltier cooler’ object is 8A. The outer face of hot side is given a convection boundary condition with a heat transfer coefficient of 2100 W/m²K and free stream temperature of 21.5°C [14]. The outer face of cold side is given a heat load of Q_c which varies depending on type of experiment, i.e., single pulse or multiple pulse.

3.6 Mesh Size and Time Step Independence Study

In order to ensure that the numerical solution is independent of the time step and mesh size, the transient response of the TEC module is analyzed under single pulse operation. The steady state current of 8A is instantaneously increased to 12A at $t = 60$ s and is then kept constant till $t = 120$ s after which it instantaneously switches back to steady state value of 8A.

Mesh size of 0.1, 0.5, 1 and 5 mm is considered for the present study, and their effect on the cold side temperature of TEC is shown in Fig. 2. It is observed that the cold side temperature profile coincides perfectly for mesh sizes of 0.5 and 0.1 mm.

Thus, a mesh size of 0.5 mm is considered for the present study as the result becomes independent of the mesh size beyond this size. Temporal-discretization scheme used for present study is first-order fully implicit scheme. The time steps studied for present study are 5, 2, 1, 0.5 and 0.1 s. The error in temperature is within 2% as time step is reduced to 0.1 from 0.5 s. Thus, a time step of 0.1 s is considered for the present study as it yields considerably accurate results and is also sufficiently small such that considerable data points are obtained for comparison (Fig. 3).

Fig. 2 Variation of cold side temperature in response to a single pulse (8-12-8 A) at various mesh sizes

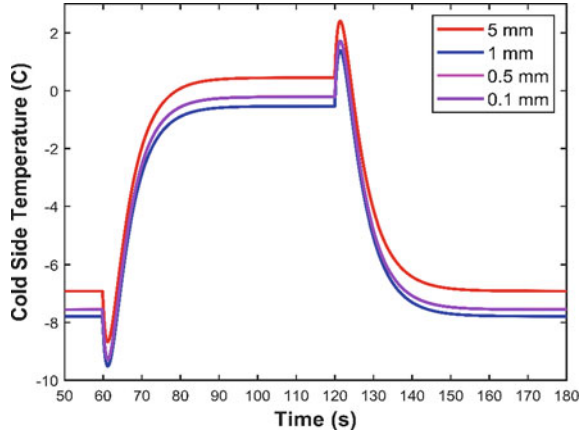
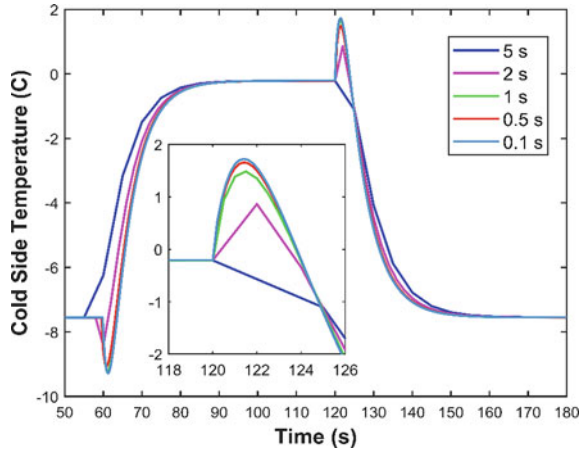


Fig. 3 Variation of cold side temperature in response to a single pulse (8-12-8A) at various time steps



4 Results

4.1 Single Pulse Mode

In single pulse mode, the TEC is given only a single current pulse for a particular duration. The steady state current is instantaneously increased to different current levels of 9A, 10A, 11A and 12A, and the current is maintained at these levels for a pulse duration of 60 s after which the current is again instantaneously reduced to the steady state current level of 8A. The heat load at cold side is kept constant at 10 W.

The comparison between experimental and numerical results in terms of cold side temperature is shown in Fig. 4 along with the different current pulse given as the input to TEC module in 'Peltier cooler' object. It is observed that a steady state error of 0.43 K exists between experimental and numerical results before the pulse. This can be attributed to the experimental errors in the setup and the temperature drops at various thermal interfaces.

The numerical prediction of transient profile of cold side temperature agrees well with the experimental profile with the error being minimum at smallest pulse. This error gradually increases from 0.43% (0.07 °C) at 8-9-8A current pulse to 5.1% (0.43 °C) as 8-12-8A current pulse. However, the peak temperature as predicted by the present model varies within 1% of the experimental values for all current pulses. Hence, the present model is able to predict the transient response of TEC to a single pulse with considerable accuracy, and the observed error can be attributed to various factors such as the perfect convection boundary condition used in numerical solution, contact resistance at various interfaces and other experimental errors.

4.2 Multiple Current Pulse Mode

In multiple current pulse mode, several current pulses are given as input to the 'Peltier cooler' object wherein the steady state value and peak current level are kept constant at 8A and 12A, respectively. Further, the current instantaneously transitions to peak level and dwells for 2 s after which it instantaneously transitions back to steady state value where it dwells for 3 s. Thus, the period of a single pulse is 5 s in which 2 s is the pulse duration. Such current pulses begin to operate from $t = 60$ s, and a total of 7 such current pulses are given. Figure 5 shows the comparison between experimental and numerical results under multiple current pulses at different cold side heat loads of 0, 10 and 20 W. The variation of current with time is represented on the right vertical axis and is highlighted in gray color.

Here also, certain level of steady state error prior to the initiation of current pulses exists, and this error becomes negligible as the cold side heat load is increased from 0 to 20 W. The transient response to multiple pulses predicted by the numerical model has a good agreement with the experimental values. The present model is able to predict the response of TEC to sudden and rapid current fluctuations with good

Fig. 4 Comparison of variation of cold side temperature in response to single current pulse (top) and different current pulses for a pulse duration of 60 s (bottom)

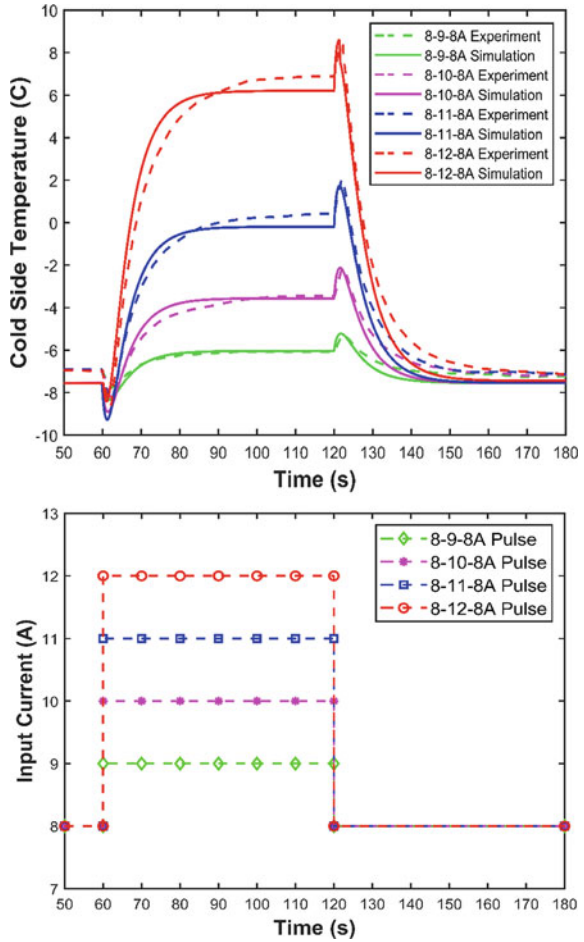
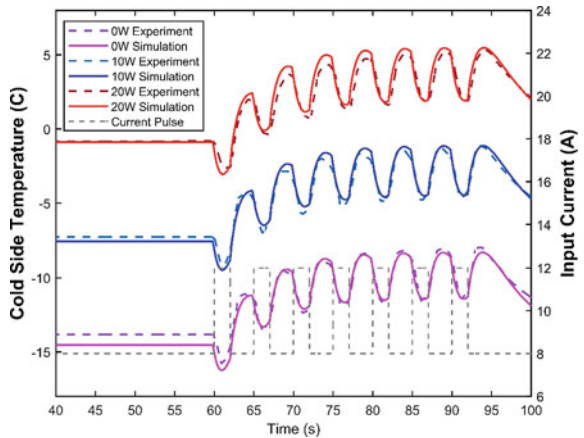


Fig. 5 Comparison of variation of cold side temperature in response to multiple current pulse at different cold side heat loads with along with variation of current with time (highlighted in gray)



accuracy. Further the error in the numerical prediction of the maximum temperature of different peaks when compared to the experimental values is less than 2% with the maximum error of 1.7% in third peak corresponding to the cold side heat load of 20 W.

5 Conclusions

The present study proposes a new modeling methodology to predict the transient response of thermoelectric coolers. The methodology proposes to calculate the instantaneous temperature difference between cold and hot side of TEC by solving the steady state ideal equation, while the transient evolution of hot and cold side is captured using effective thermal properties. The methodology is implemented within a commercially available simulation environment NX 12.0 which is the leading analysis software for various space subsystems and payloads. The TEC is modeled only by its hot and cold side ceramic plates without any internal geometry which reduces the overall computational complexity and cost by several folds.

The methodology exploits the simulation object features of NX 12.0, wherein a built-in object named 'Peltier cooler' automatically solves the steady state equation. The inputs required to this object are the thermoelectric properties of the semiconductor material used to manufacture the TEC. These properties are not readily available and are indirectly extracted using module parameters and by exploiting the fact that solution to steady state equation is invariant to the individual properties if the values of module parameters are kept constant. The effective specific heat is evaluated as the average value of the individual parts such that the thermal inertia of the ceramic plates used to model TEC is equal to the thermal inertia of the entire module. Similarly, the total temperature drop across connectors and ceramic plate is also captured using effective thermal conductivity.

The numerical model and methodology are then validated against the numerical results of a study which involves experimental evaluation of transient response of a commercial TEC to different types of current pulses. The study considered single current pulse of long duration and multiple current pulses for short durations. The results predicted using the present numerical model in both cases have a good agreement with the experimental values, and the model is able to predict the response of TEC to sudden and rapid fluctuations in current with good accuracy. The error between numerical and experimental results is within the acceptable range. These errors can be attributed to the contact resistance at various interfaces, the assumption of perfect boundary condition used in the simulation and the errors in the experimental setup and various instruments.

References

1. Gilmore DG (2002) Spacecraft thermal control handbook volume i: fundamental technologies. 2nd edn. American Institute of Aeronautics and Astronautics, Inc, Virginia
2. Zhu L, Tan H, Yu J (2013) Analysis on optimal heat exchanger size of thermoelectric cooler for electronic cooling applications. *Energy Convers Manage* 76:685–690
3. Zhang W, Shen L, Yang Y, Chen H (2015) Thermal management for a micro semiconductor lased based on thermoelectric cooling. *Appl Therm Eng* 90:664–673
4. Shen L, Chen H, Xiao F, Yang Y, Wang S (2014) The step change cooling performance of miniature thermoelectric module for pulse laser. *Energy Convers Manage* 80:39–45
5. Caroff T, Sarno C, Hodot R, Brignone M, Simon J (2015) New optimization strategy of thermoelectric coolers applied to automotive and avionic applications. *Materials Today: Proc* 2(2):751–760
6. Yin E, Li Q (2021) Device performance matching and optimization of photovoltaic-thermoelectric hybrid system. *Energy Convers Manage* 12
7. Lorenzi B, Mariani P, Reale A, Carlo A, Chen G, Narducci D (2021) Practical development of efficient thermoelectric-photovoltaic hybrid system based on wide-gap solar cells. *Appl Energy* 300
8. Mani PI (2016) Design, modelling and simulation of a thermoelectric cooling system, MSE thesis, Western Michigan University, USA
9. Chen M, Snyder G (2013) Analytical and numerical parameter extraction for compact modelling of thermoelectric coolers. *Int J Heat Mass Transf* 60:689–699
10. Cheng C, Huang S, Cheng T (2010) A three-dimensional theoretical model for predicting transient thermal behavior of thermoelectric coolers. *Int J Heat Mass Transf* 53(9):2001–2011
11. Cheng C, Huang S (2012) Development of a non-uniform current model for predicting transient thermal behavior of thermoelectric coolers. *Appl Energy* 100:326–335
12. Gao Y, Ling S, Dong X (2019) Numerical analysis for transient supercooling effect of pulse current shapes on a two-stage thermoelectric cooler. *Appl Therm Eng* 163:114416
13. Wang S, Liu H, Gao Y, Shen Y, Yang Y, Wang X, Lee D (2021) Transient supercooling performance of thermoelectric coolers with a continuous double current pulse. *J Taiwan Inst Chem Eng* 120:127–135
14. Ma M, Yu J (2016) Experimental study on transient cooling characteristics of a realistic thermoelectric module under a current pulse operation. *Energy Convers Manage* 126:210–216
15. Laird Thermal systems, TEC UT15-200-F2-4040-TA-W6 datasheet. <https://www.lairdthermal.com/products/thermoelectric-cooler-modules/peltier-ultratec-series/UT15-200-F2-4040-TA-W6/pdf/>. Last accessed 20 Oct 2021
16. Siemens NX (2013) NX thermal solver TMG reference manual, 9.0, 2013. Last accessed 22 Oct 2021

Feasibility Study on the Development of PGS-Based Flexible Radiator for Deep Space Applications



N. Ashraf Khan, S. S. Sisodia, V. K. Singh, Prasanta Das, R. R. Bhavsar, and A. Elayaperumal

Abstract In today's scenario, there is a need for compact design of spacecraft that comprises high-power density electronic packages. Due to high heat dissipation, a large radiator is required. Which is difficult to accommodate due to the compactness of spacecraft. Therefore, the need of a flexible foldable radiator arises. Reversible flexible radiator (RFR) is the concept, which is the preferred solution to problems like accommodation of large radiator. RFR discussed in this paper is a passive thermal device, which can be deployed (opened) or stowed (closed) corresponding to the high and low heat loads, respectively. This enables the RFR to function both as a radiator (for excess internal heat dissipation to sink) and as a heat retainer (for retaining equipment heat during cold conditions) alternatively whenever required. This will also drastically reduce the survival heater power requirement to maintain satellite components at required optimal temperature range during cold conditions. The RFR is made up of a sandwich of flexible high thermal diffusivity Pyrolytic graphite sheets (PGS), which primarily function as a heat spreader. The autonomous deployment and stowing of the RFR is achieved by using a rotary shape memory alloy (SMA) actuator which is thermally coupled with the thermally controlled equipment using thermal straps for more accurate response in deployment and stowed condition. This research primarily focuses on the development of a CAD model of reversible flexible radiator, numerical analysis of the CAD model, validation of numerical results with theoretical predictions and with the results obtained the significance of RFR over conventional radiator is established.

Keywords Reversible flexible radiator · Thermally controlled equipment · Pyrolytic graphite sheet · Shape memory alloy actuator · Thermal straps

N. A. Khan · A. Elayaperumal

Department of Mechanical Engineering, College of Engineering Guindy, Anna University, Chennai 600025, India

S. S. Sisodia (✉) · V. K. Singh · P. Das · R. R. Bhavsar

Thermal Engineering Division, Space Applications Centre, ISRO, Ahmedabad 380015, India
e-mail: sssisodia@sac.isro.gov.in

1 Introduction

Modern spacecraft electronics are associated with high heat generation and space constraints to ensure good thermal performance in versatile operating conditions as in Fig. 1a, b. So various types of devices like morphing radiators [1–3], thermal louvers [4, 5], thermochromic coatings [6], electrochromic coatings [7] and deployable radiators [5] are used. This research work is focused on combining the advantages of a thermal louver and a deployable radiator into a single device, and this concept is called reversible flexible radiator (RFR). RFR fin gets deployed when the equipment temperature is higher (cooling) and gets stowed in case of a cold external environment (preventing heat loss) thereby drastically reducing survival heater power. It is evident by a case study done on a reversible thermal panel (RTP) fin used for Venus explorer [9]. The principle of RFR is clearly explained in [12]. The potential of pyrolytic graphite sheet (PGS) to function as a thermal control material in spacecraft was earlier described by Nagano et.al in 2001 [19]. Later in 2015, a more flexible and high thermal conductive graphite sheet made by Kaneka Corporation, Japan was demonstrated to serve the purpose [20] and was proven to have even more superior thermomechanical properties. This sheet was used in the development of a re-deployable radiator [16]. Passive deployment of RFR fin is effected by using either shape memory alloy (SMA) actuators [8–17] or bimetallic strip actuators [18].

Deployable radiators have already been used by National Aeronautics and Space Administration (NASA) and the Japanese Aerospace Exploration Agency (JAXA) [8–17] for their deep space missions. Now Indian Space Research Organization (ISRO) is committed to develop the reversible flexible radiator (RFR) technology for deep space applications. In this paper, the construction, detailed design methods, CAD modeling of 50 W RFR, numerical analysis of RFR CAD model and the significance of RFR over conventional radiator is established.

2 Construction and Design

The RFR fin is made up of a sandwich of pyrolytic graphite sheets (Kaneka, SMC-GSS-B), and these sheets are held together by using transfer adhesive tape (3M966), refer Fig. 2c, d. The foldable portion (along the rotation axis) of the RFR fin is left without applying adhesive tape to obtain more flexibility while deploying and stowing of the RFR deployable fin. The radiative surface of the RFR fin is coated with Silver–Teflon for its good radiative heat transfer performance. The surface of RFR exposed during stowed configuration is coated with multi-layer insulation (MLI). During extreme cold conditions, thermostat controlled survival heaters are used as shown in Fig. 2a, c. The part of the spacecraft where the RFR gets attached is the baseplate. In our work to minimize, the thermal resistance the RFR fin is attached to the thermal double plate of the spacecraft. A CFRP frame is used for structural integrity of RFR. The heat equilibrium equation for RFR fin in steady state condition

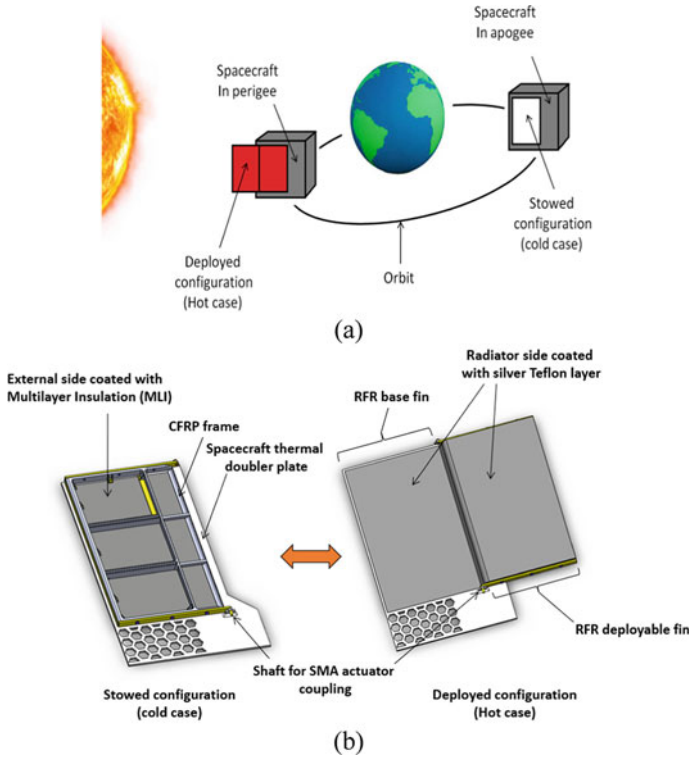


Fig. 1 **a** Conceptual representation of reversible foldable radiator (RFR) in operation under various space conditions; **b** schematic representation of RFR

is given by

$$Q_i + Q_{ext} = \sigma \times \epsilon_r \times F_{rs} \times A_r \times (T_r^4 - T_s^4) \tag{1}$$

Q_i —input heat load, Q_{ext} —absorbed external heat load, respectively, σ —Stefan Boltzmann constant, ϵ_r —emissivity of radiating surface, F_{rs} —view factor, A_r —radiator area, T_r —temperature of the radiator, T_s —sink temperature.

$$Q_{ext} = Q_{Direct\ solar} + Q_{Planetary\ albedo} + Q_{Planetary\ IR} \tag{2}$$

For a typical spacecraft operating in geostationary orbit, all other loads other than direct solar load can be neglected and the external heat load is given by

$$Q_{ext} = \alpha_r \times q_s \times A_r \tag{3}$$

$$q_s = S \times \sin \beta_s \tag{4}$$

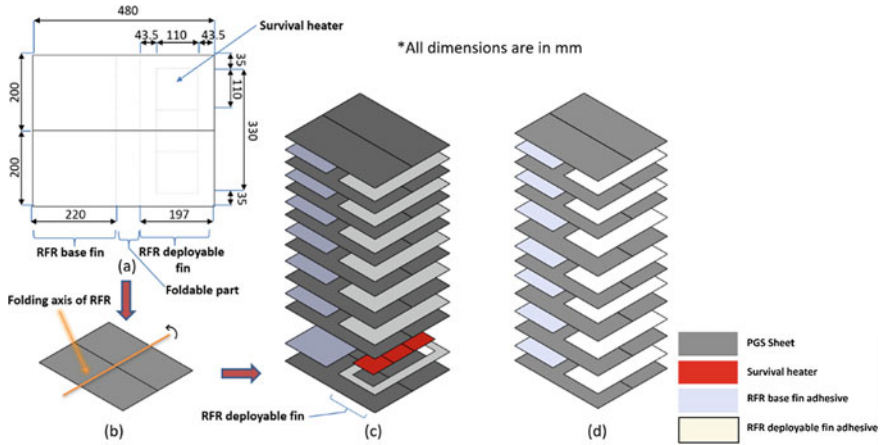


Fig. 2 **a** Dimensions of RFR CAD model; **b** isometric view of RFR fin; **c** exploded view of RFR fin with survival heater (actual model) and **d** exploded view of RFR fin without survival heater (for numerical analysis purpose)

α_r —solar absorptivity of radiator, q_s —incident solar heat flux, S —solar heat flux, β_s —angle between the solar flux and the incident area exposed to the solar flux.

From the Eq. (1), the area of the RFR fin can be determined. The efficiency of RFR fin when deployed is given by

$$\eta = \frac{Q_r}{A_r \times \epsilon_r \times \sigma \times (T_h^4 - T_s^4) + A_{MLI} \times \epsilon_{eff} \times \sigma \times (T_h^4 - T_s^4)} \quad (5)$$

Q_r —heat transfer by radiator, A_{MLI} —area of MLI surface, ϵ_{eff} —effective emissivity, T_h —temperature of the equipment.

The out-plane thermal conductivity of PGS (Kaneka) is 5 W/mK, and the out-plane thermal conductivity value for adhesive material is given as 2 W/mK. The equivalent thermal conductivity of entire RFR fin in out-plane direction is given by

$$k_{RFR(t)} = \frac{(k_{PGS(t)} \times t_{PGS} \times n_{PGS} + k_{ad(t)} \times t_{ad} \times n_{ad})}{(t_{ad} \times n_{ad} + t_{PGS} \times n_{PGS})} \quad (6)$$

$$n_{ad} = n_{PGS} - 1 \quad (7)$$

where $k_{PGS(t)}$ and $k_{ad(t)}$ are the out-plane (in thickness direction) thermal conductivities of PGS and adhesive sheets, respectively, t_{PGS} and t_{ad} are the thickness of PGS

and adhesive sheets, respectively, n_{PGS} and n_{ad} are the number of layers of PGS and adhesive sheets, respectively.

Construction and design of Shape Memory Alloy (SMA) actuator

A bias force type of SMA actuator used here contains an SMA strip (NiTi alloy) and a bias torsional spring (ASTM 304 steel). The SMA is sandwiched between the fixed jig and rotating jig as shown in Fig. 3. The torsion spring (bias spring) and its arm are inserted in the hole specifically made in the jig and this holds the spring. The left end of the jig is fixed, and the right end is the actuation end and is free to rotate about the polar axis. The RFR fin deployment angle is controlled by the SMA actuator, which is in thermal contact with the heat source by using a thermal strap [15] and the SMA is well protected with insulation cover from ambient space. Torque balance equations for the bias SMA actuator are given below.

$$\left[\begin{array}{l} \text{Torque required for} \\ \text{twisting the} \\ \text{martensitic phase} \\ \text{SMA at the beginning} \\ \text{of stowing} \end{array} \right] - \left[\begin{array}{l} \text{Torque exerted} \\ \text{by the torsion} \\ \text{spring for} \\ \text{stowing} \end{array} \right] + \left[\begin{array}{l} \text{Resistance} \\ \text{torque} \\ \text{required for} \\ \text{stowing the} \\ \text{RFR fin} \end{array} \right] < 0 \tag{8}$$

$$\left[\begin{array}{l} \text{Torque exerted by} \\ \text{SMA strip} \\ \text{in austenite phase} \\ \text{at deployment} \end{array} \right] - \left[\begin{array}{l} \text{Torque for} \\ \text{twisting} \\ \text{the bias} \\ \text{spring} \end{array} \right] + \left[\begin{array}{l} \text{Resistance torque} \\ \text{required for} \\ \text{stowing the RFR fin} \end{array} \right] > 0 \tag{9}$$

Equation (8) is for stowing and here the torsion spring bears the driving torque. Similarly, Eq. (9) is for deployment and here the SMA strip bears the driving torque (Tables 1 and 2).

3 CAD Modeling and Numerical Analysis of RFR Fin

The dimensional details of the parts modeled in CAD are given in Table 3 and dimensions of RFR CAD model are shown in Fig. 2a. These individual parts are assembled as shown in Fig. 2c, d. To compare, the RFR with conventional aluminum static radiator over thermal performance. Al radiator of dimension 400 × 480 × 0.5 mm is modeled along with a numerical model of RFR that intended to study the heat dissipation performance under extreme hot conditions. The RFR model as shown in Fig. 2d is used for numerical analysis, and the survival heaters are neglected in our analysis. The appropriate material is assigned. The thermal conductance value between each connection used is 1000 W/m² °C (Transfer Adhesive). Program controlled mesh

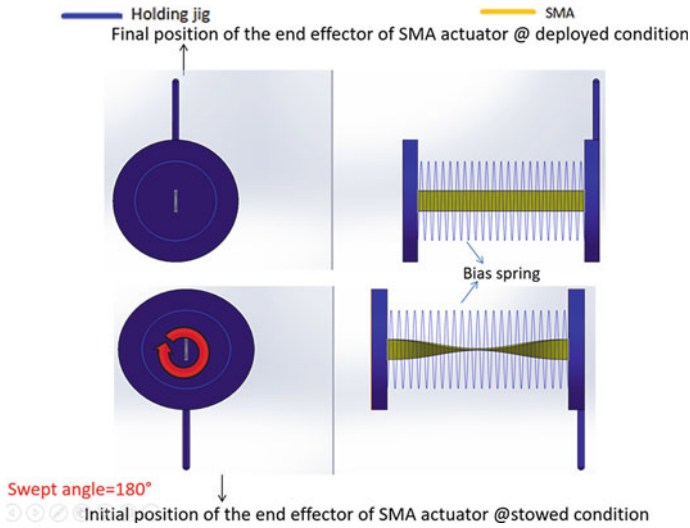


Fig. 3 Schematic representation of a typical twisting strip SMA—bias spring type rotary actuator

Table 1 Specifications of SMA actuator to be used

Parameters	Values
SMA thickness, mm	1
SMA width, mm	10
SMA length, mm	80
SMA material	NiTi
Austenite start temperature, °C	− 15
Austenite finish temperature, °C	5
Martensite start temperature, °C	− 12
Martensite finish temperature, °C	− 38.5
Shear modulus for SMA in martensite phase, kN/mm ²	8.83
Shear modulus for SMA in austenite phase, kN/mm ²	19.6
Resistance torque during stowing of RFR fin, Nmm	12.6
Resistance torque during stowing of RFR fin, Nmm	− 12.6
Swept angle for deployment, degrees	180
Bias spring material	ASTM 304
Diameter of wire, mm	2
Mean diameter of spring, mm	39
Number of turns	23
Initial angle, degrees	270

Table 2 Design parameters required for RFR fin design

Parameters	Value	Governing factors deciding parameters
Sink temperature, °C	- 269	Mission requirements
External heat input (solar + planetary albedo + planetary IR)	Solar = 1322 W (GEO orbit) Solar = 1414 W (LEO orbit)	Mission requirements
Radiative or conductive heat exchange with other structures	By assumption no radiative heat exchange occurs with other radiator structures	Mission requirements
Acceptable temperature range of the thermally controlled equipment, °C	- 20 to + 60	Features of equipment
Footprint area of the equipment, mm ²	110 × 110	Features of equipment
Location of the equipment	Along the mid of the fixed RFR fin edge	Features of equipment
Total radiator area, m ²	0.19	Thermal control parameters
Thickness of the RFR fin, mm	0.5	Thermal control parameters
Dimensions of the RFR fin when deployed, mm	400 × 480	Thermal control parameters

is given with total number of nodes as 33,501 and total number of mesh elements as 4224. Steady state thermal boundary conditions are specified for heat flow. For RFR contacting surface with the CFRP base plate and the boundary conditions for radiative heat transfer are defined on the other surface of the RFR fin as shown in Fig. 4 and the aluminum sheet static radiator is also analyzed in the same way. Input parameters for numerical analysis are given in Table 4.

Numerical analysis result

Usage of PGS sheets minimizes the overall temperature of the radiator and maintains the radiator in uniform temperature. The comparison of steady state thermal analysis results of both conventional aluminum radiator and the reversible flexible radiator (RFR) shows that the temperature distribution of the RFR is more uniform than the conventional Al radiator. Having more uniform temperature over the Al radiator reduces the size of the radiator for given heat input. RFR has another advantage of

Table 3 Specifications of RFR fin components designed

Components	Dimensions, mm	Quantity
PGS sheet	200 × 480 × 0.040	16
RFR base fin adhesive	220 × 400 × 0.025	8
RFR deployable fin adhesive	197 × 400 × 0.025	8
Survival heater	110 × 110 × 0.025	3

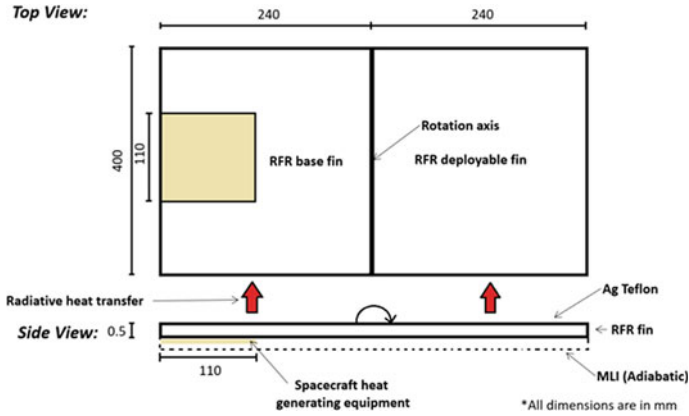


Fig. 4 Schematic model of RFR fin

Table 4 Input parameters for numerical analysis

Parameters	Values
In-plane thermal conductivity of PGS, W/mK	1199
Out-plane thermal conductivity of PGS, W/mK	5
Out-plane thermal conductivity of adhesive material, W/mK	2
Equivalent out-plane thermal conductivity of RFR fin, W/mK	4
Thermal conductance between the contacting layers, W/m ² °C	1000
Magnitude of heat load, W	50
Initial temperature, °C	20
Emissivity of radiative surface	0.77
Ambient temperature, °C	- 269

having less mass. If RFR is clubbed with the passive thermal actuator for its deployment and stowing. Heater power requirement reduces drastically. All mentioned benefits make it a suitable candidate for today’s high heat dissipation problems. The corresponding thermal analysis is given in Fig. 5a, b. A detailed comparison of the aluminum-based static radiator and RFR fin is made in Table 5.

4 Conclusion

A detailed design of 50 W reversible flexible radiator was discussed here. Theoretical preliminary calculations which were made are in close accordance with the numerical analysis results. Comparison between aluminum panel radiator and RFR clearly

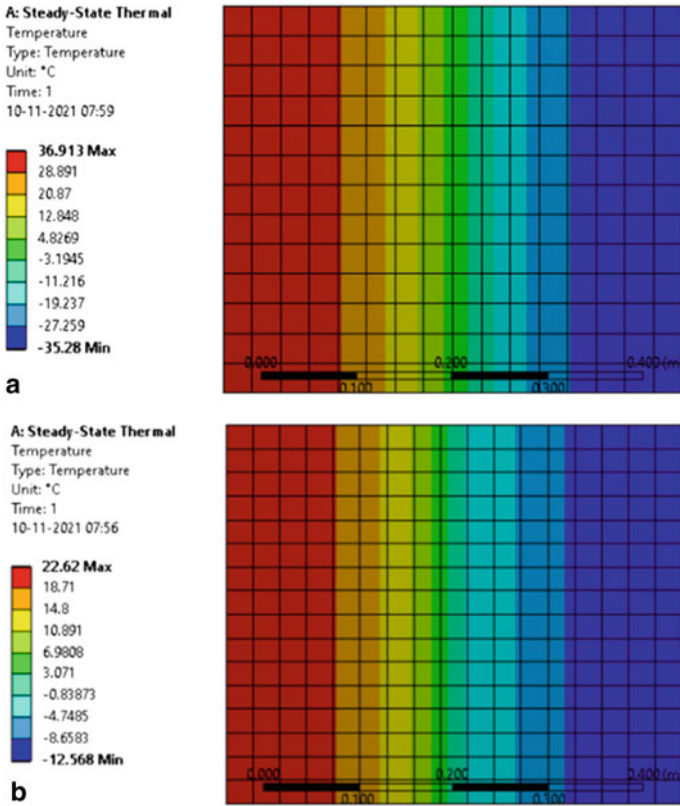


Fig. 5 **a** Steady state thermal analysis result for aluminum sheet (400 × 480 × 0.5), all dimensions are in mm, **b** Steady state thermal analysis result for RFR fin

shows the increased heat spreading capability with less heat transfer area (radiator), less weight and low operating temperature in the latter one. The highly flexible nature of PGS radiator makes it an excellent candidate for passive deployable radiators, and it is highly desirable for deep space applications. Future work to be done are as follows,

- Modeling and simulation of SMA actuator.
- Developing a RFR prototype.
- Experimental testing and validation of the RFR prototype in a space simulated environment in vacuum chamber.

Table 5 Comparison between the aluminum-based radiator and the PGS-based foldable radiator

Parameter	Aluminum-based radiator	RFR fin radiator	Inference
Mass, gm	258	214	RFR is lighter
Flexibility	Not flexible	Flexible with bending radius of 2–5 mm	RFR can be easily used as a flexible “paper like” deployable fin
Maximum temperature, °C	36.9	22.62	RFR fin has low operating temperature
Temperature Gradient, °C	72	35	RFR has uniform temperature distribution
Deployment attachments	Complicated folding attachments for maintaining continuous cross section of radiator from the base to deployable panel are required. It introduces considerable thermal resistance	No specific folding attachments are needed as the sheet itself is a foldable one and no thermal resistance due to folding	RFR is a simple and effective deployable thermal device than aluminum-based deployable device
Versatility in application	Restricted for larger spacecrafts	Can be used in light CubeSat’s to large spacecrafts	RFR has a wide application

References

1. Walgren P et al (2017) Development and testing of a shape memory alloydriven composite morphing radiator. Shape Mem Superelasticity
2. Christoper L et al (2017) Experimental characterization of a composite morphing radiator prototype in a relevant thermal environment. American Institute of Aeronautics and Astronautics
3. Bertagne C, Chong J, Wescott M, McQuien J, Whitcomb J, Hartl D, Cognata T, Sheth R, Erickson L, Benafan O (2017) Overview of technology development of shape memory alloy morphing radiators for crewed space exploration vehicles In: International conference on environmental systems, vol 128, pp 16–20. Charleston, South Carolina
4. Domingo M, Ramirez JJ (2003) Mechanical design and test of rosetta platform louvres. In: Proceedings of the 10th European space mechanisms and tribology symposium. ESA Publications Division, San Sebastian, Spain, pp 289–292
5. Gilmore DG (2002) Spacecraft thermal control handbook, 2nd edn. The Aerospace Press, El Segundo, California
6. Morsy AM et al (2020) Experimental demonstration of dynamic thermal regulation using vanadium dioxide thin films. Sci Rep
7. Kluge O et al (2018) Electrochromics for thermal control on spacecraft. In: Proceedings of the 3rd world congress on momentum, heat and mass transfer. Budapest, Hungary, pp ICHTD 103
8. Nagano H et al (2003) Development of a flexible thermal control device with high-thermal-conductivity graphite sheets. In: 33rd international conference on environmental systems, ICES 2003, SAE International, Vancouver, BC, Canada, pp 2003–01–2471

9. Nagano H et al (2011) Development of a lightweight deployable/stowable radiator for interplanetary exploration. *Appl Therm Eng* 31:3322–3331
10. Nagano H et al (2005) A reversible thermal panel for spacecraft thermal control (evaluation of effectiveness and reliability of new autonomous thermal control device). *Heat Transfer Asian Res* 34(5)
11. Nagano H et al (2006) Simple deployable radiator with autonomous thermal control function. *J Thermophys Heat Transfer* 20(4)
12. Nagano H et al (2006) Study on a reversible thermal panel for spacecraft (detailed design based on parametric studies and experimental verification). *Heat Transfer Asian Res* 35(7)
13. Nagano H et al (2007) Fabrication and testing of a passive re-deployable radiator for autonomous thermal control. *American Institute of Physics* 880(19)
14. Nagano H et al (2009) Experimental investigation of a passive deployable/stowable radiator. *J Spacecraft Rockets* 46(1)
15. Miyata K, Nagano H (2018) Research and development on the flexible thermal management device for expanding the feasibility of space probes. A collection of papers on the study of self control. *Trans Soc Instrum Control Eng* 54(5):508–517
16. Akizuki Y et al (2019) Development and testing of the re-deployable radiator for deep space explorer. *Appl Therm Eng* 165
17. Bacciotti A et al (2021) On the use of shape memory alloys for deployable passive heat radiators in space satellites. In: *IOP conference series: materials science and engineering*, The 49th AIAS conference (AIAS 2020), vol 1038
18. Cannon JR, Iverson BD, Song W, Mulford RB Passively actuated, triangular radiator fin array. <https://par.nsf.gov/servlets/purl/10229718>
19. Ono S et al (2015) Thermophysical properties of high-thermal-conductivity graphite sheet and application to deployable/stowable radiator. *J Thermophys Heat Transfer* 29(2):99–110
20. Kugler SL (2008) Aluminum encapsulated APG high conductivity thermal doubler. *American institute of aeronautics and astronautics*

Analysis of Parameters Affecting Effectiveness of Industrial Cooling Towers



Jitendra Hemwani, Raj Kumar Satankar, Yatna Bhagat,
and Y. P. Deshmukh

Abstract Many manufacturing plants generate a large amount of waste heat due to several chemical reactions and manufacturing operations. Industrial cooling towers are commonly employed to remove the waste heat generated there and hence help the manufacturing plants to run efficiently, economically and effectively. Since the cooling towers needs to operate with optimum parameters as per the requirement of the process, this paper presents the study and experimentation results on the performance characteristics of low approach and range, Induced Draft Cooling Towers (IDCT) used in beverages industry. Following the first law of thermodynamics thermal effectiveness of IDCT has examined for effect of approach, range, along with ambient and operating parameters including wet bulb temperature (WBT), dry bulb temperature (DBT) of inlet air and water temperature at inlet and exit. The data for this study have been measured at Varun Beverages Limited, Sanguem, Goa, India, and graphical modeling has been done using MATLAB software. The thermal effectiveness has maximum value of 73.44 at specific values of parameters considered here, and some variations from the theoretical results have also been reported. The experimentation and results of this paper can be used to design and operation of industrial cooling towers in food and beverage industries.

Keywords Effectiveness · Cooling tower · Wet bulb temperature · Air inlet temperature

J. Hemwani (✉) · Y. P. Deshmukh
G H Raisoni University, Amravati, Maharashtra, India
e-mail: jitendrahemwani@gmail.com

R. K. Satankar
Poornima College of Engineering, Jaipur, Rajasthan, India

Y. Bhagat
Government Polytechnic College, Betul, Madhya Pradesh, India

Abbreviations

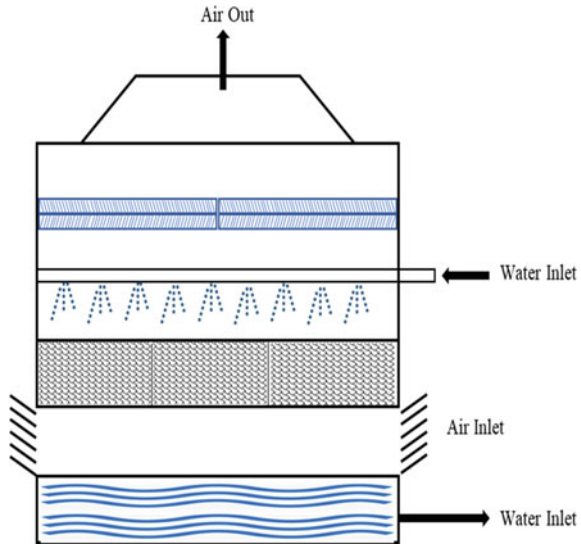
A_{ct}	Approach of the cooling tower
C_{pw}	Specific heat of water
E	Effectiveness of the cooling tower
$E_{act}, E_{rct}, E_{wbi}, E_{tai}, E_{twi}, E_{tvo}$	MATLAB variables for effectiveness (specific suffix is used with E to make effectiveness for specific parameter)
G	Mass of air flow
h_{ai}, h_{ao}	Enthalpy of air at inlet and exit, respectively
h_{wi}, h_{wo}	Enthalpy of water at inlet and exit, respectively
L_i, L_o	Mass of water flow at inlet and exit (basin), respectively
R_{ct}	Range of the cooling tower
T_{ai}	Air inlet temperature
T_{wbi}	Wet bulb temperate of air inlet
T_{iw}, T_{ow}	Water at inlet and exit (basin) temperature, respectively
x_{ai}, x_{ao}	Absolute humidity of air at inlet and exit, respectively

1 Introduction

Industrial cooling tower is used to control operating temperature requirement in power plants and various process industries like chemical, metallurgical and HVAC used in food and ice manufacturing plants [1, 2]. The attractive features including large heat load handling, expensive installation, maintenance and operating cost, better reliability and water conservation made cooling tower more popular in comparison with alternative methods of waste heat rejection [2, 3]. In cooling towers, temperature of the water is reduced by rejecting heat to the interface, and subsequently this heat is taken away by the air, enabling the water to be reused in industrial operations. Figure 1 depicts a schematic representation of an induced draft type counter flow cooling tower, in which air flows upward and water flows downward, creating a significant interface [3, 4]. This causes heat and mass transfer that occurs in two ways: (1) the evaporation of a small amount of water into the air due to a vapor pressure differential causes mass transfer and (2) exchange of heat between ambient air and water causes heat transfer process.

Various researchers worked on the improvement of the effective working of the cooling tower. The main criteria remain to improve the heat energy interaction between the water and air. It is for the first time in 1925 Merkel has developed mathematical modeling for the complex phenomenon of energy transfer between the

Fig. 1 Heat balance in cooling tower



fluids [3–5]. Later including in some recent studies various authors have widely used Markel’s theory to study and analysis of different types of cooling towers [6–9]. Zubair et al. [10], in his investigation, found evaporation was main mode of heat transfer in counter flow type of cooling towers. Novianarenti et al. [4] conducted the experimental study for variants filling of the IDCT to obtain performance characteristics. They used different types of shapes of filler material and found that the wave form filler rejects 4.92 kW of heat in the IDCT, gives the best results as performance then the other used as straight and zigzag filler. They also concluded that the increase in the velocity of air also increases the performance of IDCT. Fanasenko et al. [11] recommended the use of polymer filler for the CT because it decreases the resistance to flow of air it will give higher effectiveness. This recommendation is given after optimizing the structure for heat transfers and mass transfer in the CT. Ghazani et al. [12] presented a comprehensive approach toward cooling tower design and compared a laboratory scale counter flow wet cooling tower using the first and the second laws of thermodynamics literature survey shows that since the cooling towers operates in all the seasons and at different load, the variation in the environmental conditions may cause significant effect on the thermal performance of the system.

The above discussion suggests that the performance of cooling tower is an important concern for both researcher and industry persons. Therefore, it is important for cooling tower designer and system operator to consider ambient operating parameters to maintain the thermal performance at optimum level. Since the effectiveness is most significant parameter to measure the performance of a cooling tower, therefore its direct relation between ambient and operating parameters must be known. Thus, objective of this paper is to present the experimentation-based results of effect of performance parameters on the effectiveness. This paper will help to give direction to the industries to use the IDCT at its optimum performance level, so that it can help in



Fig. 2 Induced draft counter flow wet type cooling at VBL, Sanguem, Goa, India

horizontal deployment of induced draft type cooling towers especially towers having low operating range and low approach where the waste heat recovery is difficult and only possibility is to reject it efficiently and effectively in the atmosphere.

2 Experimental Methodology

2.1 Field Visit and Data Collection

The experimental study and observations for this paper are made at Varun Beverages Limited, Sanguem, Goa, India, which is a fully automated bottling plant. The experimentation was conducted on FRP-induced draft counter flow wet type cooling as shown in Fig. 2. This cooling tower has a capacity of 200TR, and here, it is used for cooling the condenser water of the refrigeration system. The other specifications of cooling towers are mentioned in Table 1.

2.2 Cooling Tower Performance Model

As per Bureau of Energy Efficiency (BEE) India, cooling capacity, range, approach and effectiveness play an important role in the performance of cooling towers. Further in the design of the cooling tower, heat balance between water and air should be satisfied as per Eq. 1.

$$\text{Heat entering in to the CT} = \text{Heat out of the CT}$$

Table 1 Specifications of cooling tower

Component/Parameter	Specification
Model shape	Rectangular
Max heat rejection rate	700 kJ/sec
Wetted surface area	2746 m ²
Air flow	1360 m ³ /min
Water flow rate	2000 L per minute
Water inlet temperature	25–40 °C
Wet bulb temperature (Max)	15–28 °C
Drift loss %	0.02%
Evaporation loss	0.70%
Tower operation	Continuous
Pumping head	3.5 m
Length × Width × Height	3.0 × 3.5 × 3.0 m
Number of fans	1 (Diameter, 1.8 m)
Number of motors	1 (10HP, 960RPM)
Number of water inlet	2 (4")
Number of water outlet	2 (5")
Casing, basin and fan material	FRP
Eliminator and fill material	PVC

(Water + Air) Heat in = (Water + Air) Heat out

$$[L_i \times C_{pw} \times T_{wi}] + G \times h_{ai} = [L_o \times C_{pw} \times T_{wo}] + G \times h_{ao} \tag{1}$$

The total heat rejected by water is function of temperature of water at inlet and exit, while the heat absorbed by air is dependent on enthalpy of the air at inlet. This is further a function of temperature of inlet air and WBT as per Eq. 3.

$$\Delta Q = h_{wi} - h_{wo} = f(T_{wi}, T_{wo}) \tag{2}$$

$$= h_{ai} - h_{ao} = f(T_{wbi}, T_{ai}) \tag{3}$$

In the present case, to measure temperature of air inlet (T_{ai}), temperature of air exit (T_{ao}) and temperature of water at exit (T_{wo}), digital thermometer instant read (Weber make) has been used. Wet bulb temperature (T_{wbi}) and dry bulb temperature of air are measured with the help of sling Psychrometer (GABY instruments make). The values of T_{ai} and T_{ao} recorded with help of digital thermometer were verified using sling Psychrometer. Temperature of water at inlet (T_{wi}) was taken through the digital resistance temperature detector (RTD, Lascar electronics make) fitted in panel (Fig. 3).



Fig. 3 Reading of operating parameters of cooling tower

Further, range, approach and effectiveness have been calculated as per the following formula:

Cooling tower range is difference between the temperature of water entering to the cooling tower and leaving the cooling tower. Using range value, it can be estimated how efficiently the cooling tower is working.

$$\text{Range, } R_{ct} = T_{wi} - T_{wo} \tag{4}$$

Approach of the cooling tower is simply calculated as a difference of temperature of the cold water entering and the wet bulb temperature of air. A small value of approach is considered good from the design and operation point of view. However, a smaller approach value may need additional pumps and fans which increases installation and operating cost.

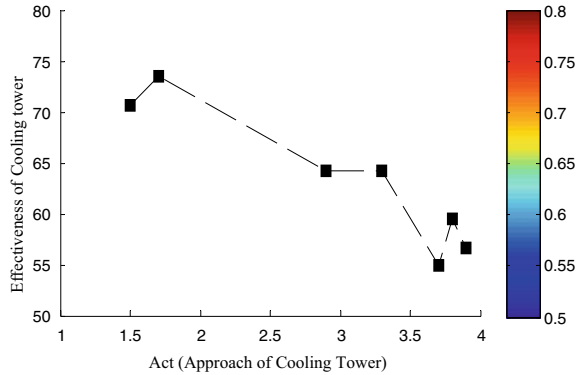
$$\text{Approach, } A_{ct} = T_{wo} - T_{wbi} \tag{5}$$

Percentage effectiveness (efficiency) of cooling tower is calculated as a ratio of range to sum of range and approach (ideal range).

$$\text{Effectiveness} = \frac{R_{ct}}{R_{ct} + A_{ct}} \times 100 = \frac{T_{wi} - T_{wo}}{T_{wo} - T_{wbi}} \times 100 \tag{6}$$

Based on the observations, range, approach, WBT and DBT of inlet air and temperature of water at inlet and exit are considered as independent variables, while effectiveness was considered as a dependent variable. Then, the data were analyzed in MATLAB, and various statistical inferences have made based on the results and plots.

Fig. 4 Effect of approach on effectiveness



3 Results and Discussion

3.1 Effect of Approach and Range on Effectiveness

The graph of effectiveness of cooling tower varies linearly for the values of approach as shown in Fig. 4. It illustrates that the effectiveness of the cooling tower is inversely proportional to the approach of the cooling tower. The statistical analysis of data observed shows that effectiveness ranges from 54.87 to 73.44 for an approach value ranging from 1.5 to 3.9. These results are in line with the previous studies, where the cooling tower reported to attained maximum effectiveness at approximate approach value of 1.5 [13, 14].

Further, the experimental results of effect of range on effectiveness when plotted indicate a nonlinear variation as shown in Fig. 5. Zigzag pattern in graphical model suggests that the effectiveness of CT is the function of not only range but also depends on some other factors. Theoretically, heat load and circulating water flow directly affect the range of the cooling tower. A higher range attended indicates that all the parts of the tower are in proper function and working effectively to reduce the temperature of the water. This also confirms the theoretical studies and discussion in Bureau of Energy Efficiency [14].

3.2 Effect of Operating Parameters on Effectiveness

WBT and DBT of INLET AIR

Theoretically at zero heat load temperature of water at the exit of cooling tower should be equal to the WBT of the inlet air; however, during operation cooling towers always have some load for process heat which is to be rejected in the environment. Therefore, in practice this condition can never be fulfilled, and further, the relationship of WBT and effectiveness is different from the theoretical relation. Hence, the value

Fig. 5 Effect of range on effectiveness

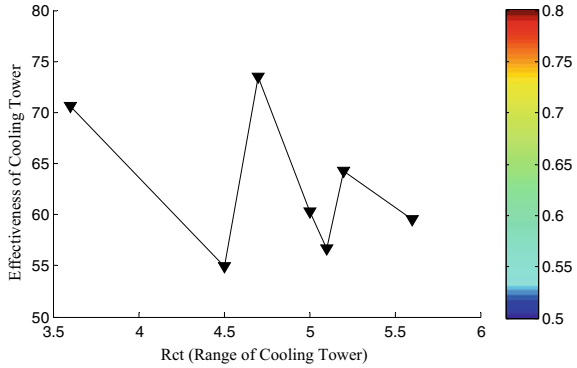
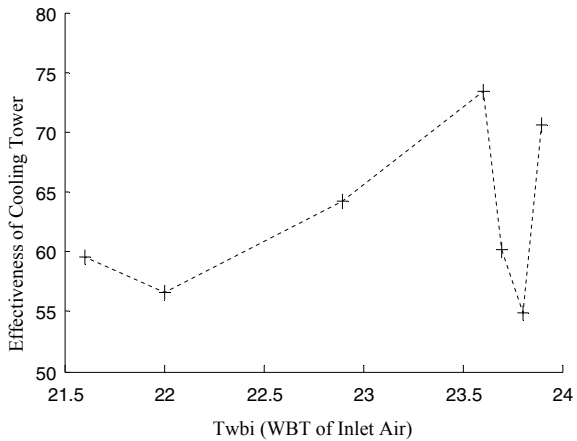


Fig. 6 Effect of WBT on effectiveness



of effectiveness at WBT 23.7, 23.8 and 23.9 °C is somewhat differing from the values in linear graph in Fig. 6.

The Graph Fig. 7 illustrates that effectiveness of cooling tower is a polynomial model of more than one degree because with increases in the DBT of inlet air, effectiveness increases first then decreases. The decrease may be due to the change in the atmospheric variations of the velocity and WBT of the air. Variation in DBT of air inlet itself is not fixed in a day. This variation depends upon the place, location and the surroundings of industrial cooling tower. As per Table 2, the effectiveness of cooling tower is reported maximum as 73.44 minimum as 54.87 at inlet temperature 34.8 and 28 °C, respectively.

Temperature of Water at Inlet and Exit

The effect of temperature of water at inlet on the effectiveness of cooling tower is shown in Fig. 8a, which clearly indicates that effectiveness is inversely proportional to the temperature and varies nonlinearly. The decrease in the effectiveness at the same inlet temperature (at 31 °C) in various observations may be because of change

Fig. 7 Effect of DBT on effectiveness

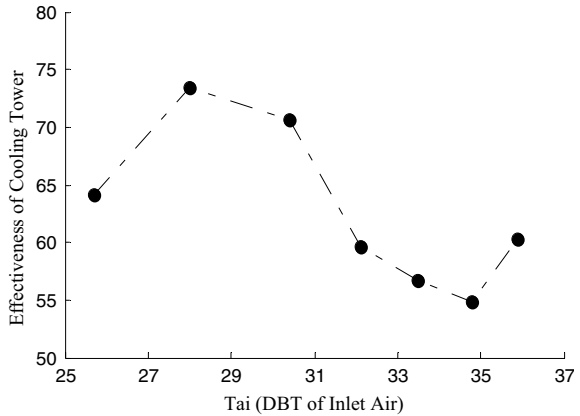


Table 2 Effectiveness data statistics for WBT and DBT of air

Statistical parameter	WBT	DBT	Effectiveness
Min	21.6	25.7	54.87
Max	23.9	35.9	73.44
Mean	23.07	31.49	62.8
Median	23.6	32.1	60.24
Mode	21.6	25.7	54.87
SD	0.934	3.69	6.992
Data range	2.3	10.2	18.57

in some other factors affecting the effectiveness. The water inlet temperature itself depends on the industrial process from which water is absorbing the heat, and this heat is rejected to air in the cooling tower.

The results representing various statistical parameters relating effectiveness with temperature of water at inlet and exit are tabulated in Table 3. The water inlet temperature is ranging from 29 to 32 °C, having mean as 30.86 with standard deviation as 1.069, and effectiveness of CT ranges from 54.87 to 73.44. Minimum value of effectiveness is found as 54.87 at 32 °C, and the maximum value 73.44 occurs at 30 °C.

Water temperature at exit is dependent on the heat exchange between water and air in the cooling tower. This temperature should be minimum as possible so that it can absorb the maximum heat from industrial process. Graphical representation in Fig. 8b shows that temperature of water at exit has nonlinear relation with the effectiveness of cooling tower and with increases in the value of temperature the effectiveness of CT decreases. Maximum effectiveness 73.44 is at temperature of 25.3 °C, and minimum effectiveness 54.87 is at temperature of 27.5 °C.

Fig. 8 **a** Effect of temperature of water at inlet on effectiveness. **b** Effect of temperature of water at exit

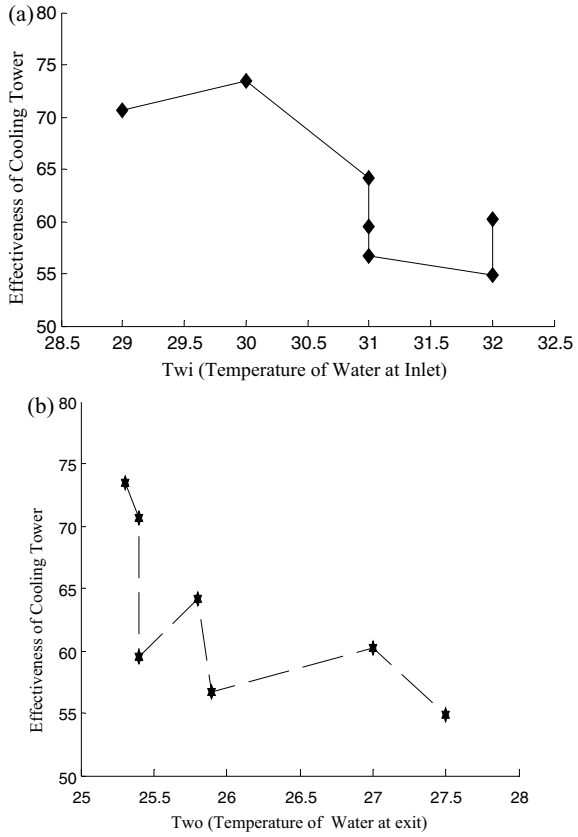


Table 3 Effectiveness data statistics for temperature of water at inlet and exit

Statistical parameter	Water inlet	Water exit	Effectiveness
Min	29	25.3	54.87
Max	32	27.5	73.44
Mean	30.86	26.04	62.8
Median	31	25.8	60.24
Mode	31	25.4	54.87
SD	1.069	0.8658	6.992
Data Range	3	2.2	18.57

4 Conclusion

This paper presents the results of study and observations at V.B.L. (Pepsi Bottling plant) Sanguem, Dist. South Goa, India. The observations are recorded and calculated in the specific range of operating parameters at which IDCT actually operates.

From the analytical study of observations using MATLAB, the following important conclusions can be made.

1. The effectiveness of IDCT is inversely proportional to approach, while it has zigzag variations with respect to range. The effectiveness has maximum value as 73.44 at approach and range value of 4.7 and 1.7, respectively.
2. The effect of WBT of air inlet on the effectiveness may be considered linear, and value of effectiveness increases with increase in the value of WBT.
3. Temperature of water at inlet and exit and DBT of air inlet has nonlinear relationship with effectiveness of cooling tower. The maximum effectiveness occurs at water inlet temperature as 30 °C, water exit temperature as 25.3 °C and air inlet temperature as 28 °C.

In addition to the factors discussed above, the effectiveness may be dependent on some other parameters which have been assumed constant in the present case. In actual practice one of factor may vary therefore variations in measured parameters and their theoretical values have been observed. This gives further scope of study regarding optimizing effectiveness of cooling tower. It is to be noted that the observations in this study are recorded in summer season and on a specific type of cooling tower. The results may be different for other seasons, geographical positions and type of cooling tower. The effectiveness of the IDCT used in this specific application is ranging between 54.87 and 73.44. This suggests that there is scope of increasing effectiveness of CT by operating the CT on specific parameters, and these data will help the designers to give better design the CT to save the operating cost.

References

1. Lemouari M, Boumaza M (2010) Experimental investigation of the performance characteristics of a counter flow wet cooling tower. *Int J Therm Sci* 49(10):2049–2056
2. Naik BK, Muthukumar P (2017) A novel approach for performance assessment of mechanical draft wet cooling towers. *Appl Therm Eng* 121:14–26
3. Li X, Gurgenci H, Guan Z, Sun Y (2018) Experimental study of cold inflow effect on a small natural draft dry cooling tower. *Appl Therm Eng* 128:762–771
4. Novianarenti E, Setyono G, Safitra AG (2019) Experimental study of the performance characteristic an induced draft cooling tower with variates fillings. In: *IOP Conference Series: Materials Science and Engineering*, vol 462, no. 1, p 012027. IOP Publishing
5. Merkel F (1925) Evaporative cooling. *Z. Verein Deutsch Ingen (VDI)* 70:123–128
6. Rajasekar S, Aparna D, Minakshi A, Meyyappan N (2019) Dynamic simulation of heat transfer through cooling tower using MATLAB Simulink. *Am Int J Res Sci Technol Eng Math*, p 116
7. Asvapoositkul W, Kuansathan M (2014) Comparative evaluation of hybrid (dry/wet) cooling tower performance. *Appl Therm Eng* 71(1):83–93
8. Mishra B, Srivastava A, Yadav L (2020) Performance analysis of cooling tower using desiccant. *Heat Mass Transf* 56(4):1153–1169
9. Qi X, Liu Z (2008) Further investigation on the performance of a shower cooling tower. *Energy Convers Manage* 49(4):570–577
10. Zubair SM, Khan JR, Yaqub M (2003) Performance characteristics of counter flow wet cooling towers. *Energy Convers Manage* 44(13):2073–2091

11. Afanasenko VG, Kulakov PA, Galimova YL, Sidorkin DI (2020) Modeling of heat and mass transfer processes in cooling towers and structure optimizing of polymer filler. In: ICMTMTE, IOP publishing, Material science and engineering, 709:044017
12. Ghazani MA, Hashem-ol-Hosseini A, Emami MD (2017) A comprehensive analysis of a laboratory scale counter flow wet cooling tower using the first and the second laws of thermodynamics. *Appl Therm Eng* 125:1389–1401
13. Hensley JC 'Cooling tower fundamentals', SPX cooling technologies, Inc., Overland Park, Kansas, USA; Second Edition pp 22
14. Manual of "Bureau of energy efficiency", Chapter 7: Cooling Towers, pp 140–143

Effect of Magnetic Field on Refrigeration Devices for Improving Its Performance and Refrigerant Properties



Aditya K. Alagatu, Shivam A. Katkar, Rahul A. Dakare, Shantanu M. Darlinge, Sarthak C. Lautawar, Santosh B. Jaju, and Ashish S. Raut

Abstract Refrigeration can be defined as the process of extracting heat from a given space and transferring the same to the other space. Domestic and commercial refrigerator uses vapor compression refrigeration system for cooling the food products. Plenty of research is still going on to improve the system performance and subsequently the system efficiency. The ultimate objective of this project is to increase system performance of domestic refrigerators by focusing on the working of the evaporator which is filled with liquid refrigerant. In our experiment, we have used magnet (magnetic field) at the exit of condenser also known as discharge line of refrigerator. We have used R134a as a refrigerant, and after implementation, we have compared the results with and without applying magnets. As per the experimental results obtained by utilization of magnetic field (Magnets pairs) on the refrigerant discharge line from condenser enhanced the coefficient of performance of the experimental setup by refrigerant viscosity reduction, enhancing the mass flow rate of refrigerant, eventually increment in cooling capacity while lower down the power of compressor.

Keywords Magnetic field · Magnetocaloric effect · COP

1 Introduction

Vapor compression refrigeration cycle is most widely used refrigeration system due to its wide range of applications. There are many researchers who have worked to increase the performance of this system by application of magnetic fields. Since the

A. K. Alagatu (✉) · S. A. Katkar · R. A. Dakare · S. M. Darlinge · S. C. Lautawar · S. B. Jaju · A. S. Raut

Mechanical Engineering Department, G H Raison College of Engineering, Nagpur 440016, India
e-mail: alagatu_aditya.me@ghrce.raisoni.net

S. B. Jaju
e-mail: santosh.jaju@raisoni.net

A. S. Raut
e-mail: ashish.raut@raisoni.net

magnetocaloric phenomenon explored, research in magnetic refrigeration has initiated. Iron thermal effect invented by Warburg in 1881 by placing in varying magnetic field. For magnetic refrigeration (cooling method), the magnetocaloric effect is used. A force which attracts and repels another magnet along with attracts ferromagnetic materials, like iron. Variable magnetic field is generated in space around the magnet at all points. By utilization of magnetic field on discharge line (after condenser) of vapor compression, refrigeration system enhances performance by reducing the viscosity of the refrigerant. This enhanced mass flow rate of refrigerant, and therefore, the cooling/refrigeration capacity enhanced even though by the reducing the compressor power; ultimately, it improves the refrigeration system's coefficient of performance. In this paper, work on magnetic refrigeration system is discussed; magnets pairs are applied on discharge line of domestic refrigerator which working on R134a refrigerants, and its performance is compared with without magnetic field refrigeration system.

2 Literature Review

Mani and Selladurai [1] studied the comparison of influence of a magnetic field on substituting refrigerant such as hydrofluorocarbon and chlorofluorocarbon, by mixture of isobutene, propane. The test was conducted with and without magnets and compared to dichlorodifluoromethane and tetrafluoroethane; the mixture of propane, isobutene shows the improved results as the refrigerating capacity increases by 19.5–50.1% and 28.6–87.2% respectively. Sami and Aucoin [2] experimented by applying magnetic field of almost 1200 Gauss at outlet of condenser of refrigeration cycle and used difluoromethane and pentafluoroethane, trifluoroethane, pentafluoroethane as a mixture for the refrigerant. Ram et al. [3] made a thorough investigation of the magnetocaloric characteristics of many materials, which is an important part of magnetic refrigeration technology. He works with a wide range of magnetocaloric materials in his study, including glass ceramics, spinel ferrites, ferromagnetic perovskites, and oxide-based composites. Magnets have the potential to be used in magneto refrigeration technology, according to comparative research of magnetocaloric characteristics. Sidheshware et al. [4] did experiment on the vapor compression refrigeration system by application of magnetic energy at the outlet of condenser (liquid refrigerant line) in addition to this used various refrigerants during testing, which enhance total performance of vapor compression refrigeration system.

3 Experimental Setup

Figure 1 shows conceptual diagram, and Fig. 2 shows actual vapor compression refrigeration system test rig with magnets; with this experimental setup, investigation was done for enhancing effectiveness of R134a refrigerant. The investigational setup

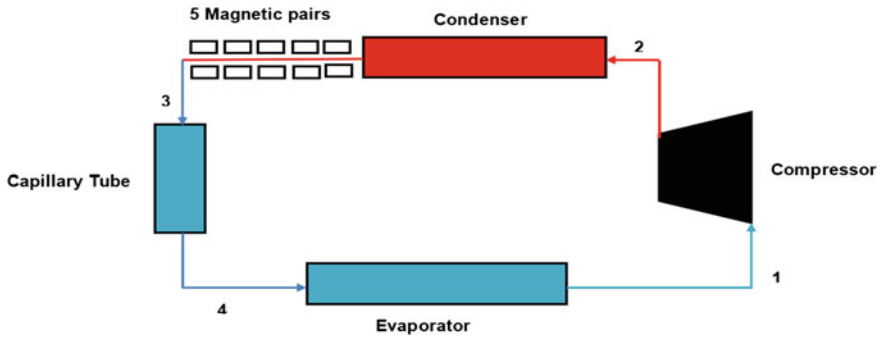


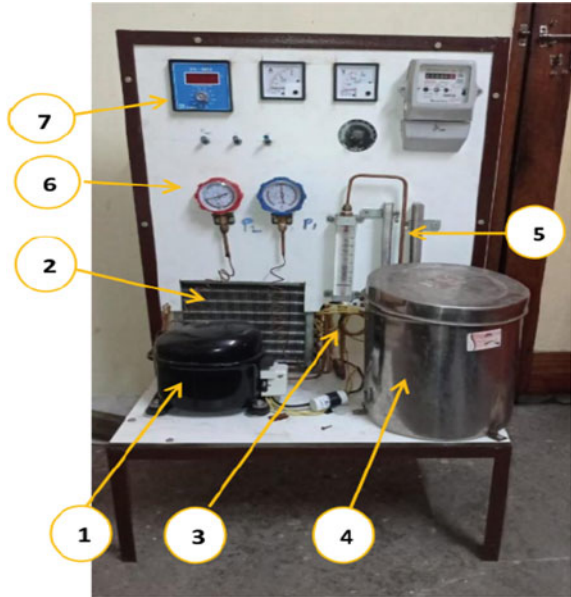
Fig. 1 Conceptual diagram of VCR system with magnets

involves of all basic components of vapor compression refrigeration system such as evaporator, condenser, compressor, and capillary tube in addition to this, the magnets pair (permeant magnets) on copper tubing after condenser (liquid refrigerant line). As the basic working of vapor compression refrigeration system from evaporator refrigerant come out in vapor phase and move in compressor, where its pressure increased, after that it passed through condenser, where heat transfer takes place and its phase change from vapor to liquid. The refrigerant is subsequently pumped into the evaporator through the expansion valve. The readings taken by varying the magnets pair from 1 to 4 near about 3000 Gauss on liquid line (condenser outlet). Suction and discharge pressure measured by pressure gauges. The reference temperature of water on the evaporator side is kept constant throughout the experiment 30 °C, and the reading of thermocouple T1 to T4 is collected at 10 min intervals. The amount of magnet pairs used in liquid line was increased by 1 pair to 4 pairs to determine the influence upon power of compressor and systems COP.

In Fig. 2, following components are shown.

1. Hermetically sealed compressor
2. Condenser (Air cooled)
3. Expansion valve (Capillary tube)
4. Evaporator (Bare tube)
5. Magnets (N-35-Neodymium)
6. Presser gauge
7. Temperature indicator
8. Refrigerant use in system: R134a (Tetrfluroethane)
 - a. R134a properties:
 - i. Chemical Name: CH₂FCF₃.
 - ii. Molar mass: 102.03 gm/mole.
 - iii. Density: 0.00425 gm/c.m³.gas.

Fig. 2 VCRS experimental setup with magnets



4 Result and Discussion

Figure 3 shows the comparison of COP with time in minutes along with magnets pair; it shows that as magnets pair increases along with time, the COP of the vapor compression refrigeration systems is also increases. Comparison of coefficient of performance (COP) versus magnets pairs is presented in Fig. 4. It is observed that the magnetic field affects the coefficient of performance of the system. As per the results obtained during experimentation shows that the COP increased by 2.48% for 1 magnet pair, by 2 magnet pair 10.43%, by 3 magnets pairs 30.96%, and 33.11% for 4 magnets pairs. The COP rises as increases the magnets pairs because of compressor power drop-off and improvement in refrigerant effect.

Figures 5 and 6 show that the refrigerating effect is depicted as a function of magnets pair number. As the magnets pairs increase the refrigerant effect rises, up to 4 magnets pairs. Increase in refrigerant specific heat as rate of heat transmission rises. Substantially, more heat absorbs by refrigerants from water results in heat transfer rate enhancement, ultimately increases the refrigerating effect. The refrigeration effect enhanced by 1.82% as comparison with no magnet pair to 1 magnet pair. Similarly, 9.08, 28.82, and 30.47% when 2, 3, and 4 pairs used, respectively (Table 1).

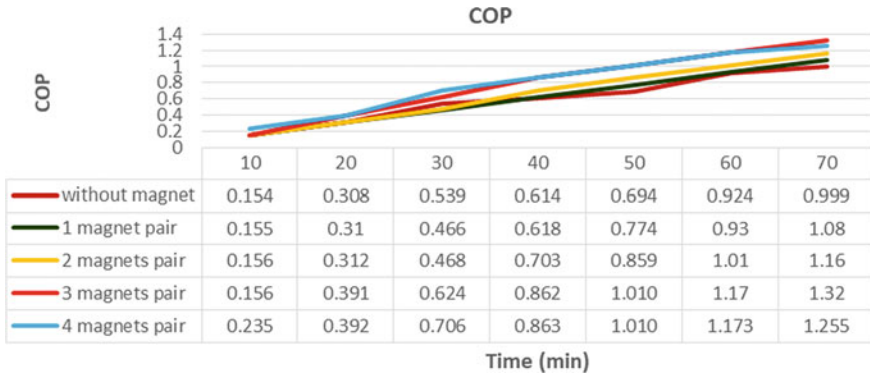


Fig. 3 COP versus time (min)

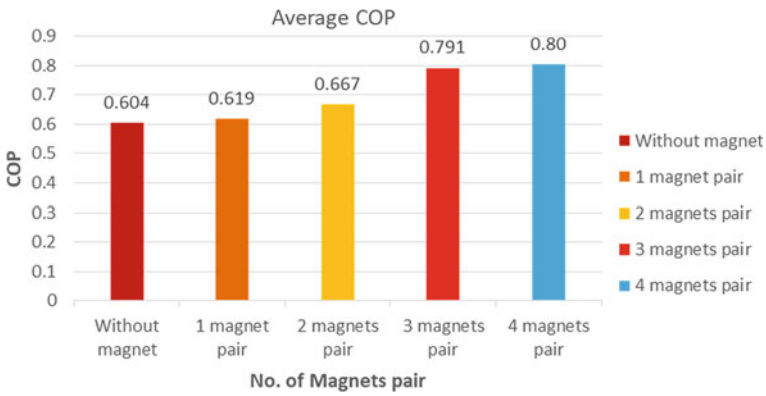


Fig. 4 Coefficient of performances versus no. of magnets pairs

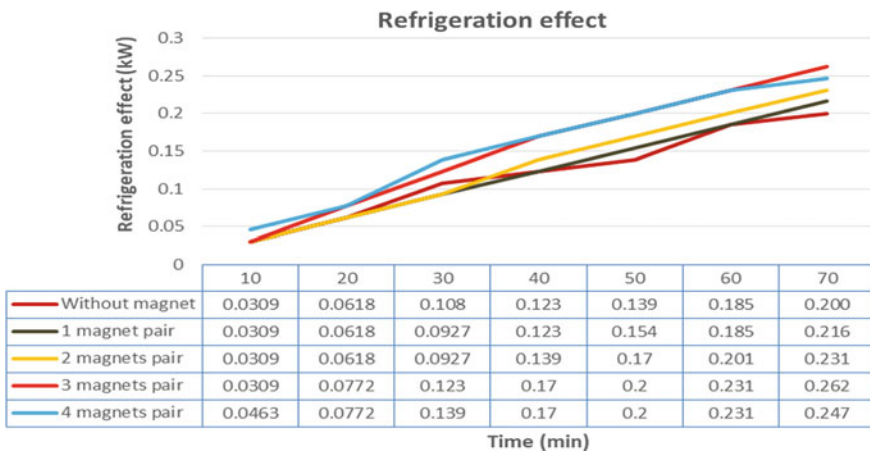


Fig. 5 Refrigeration effect versus time (min)

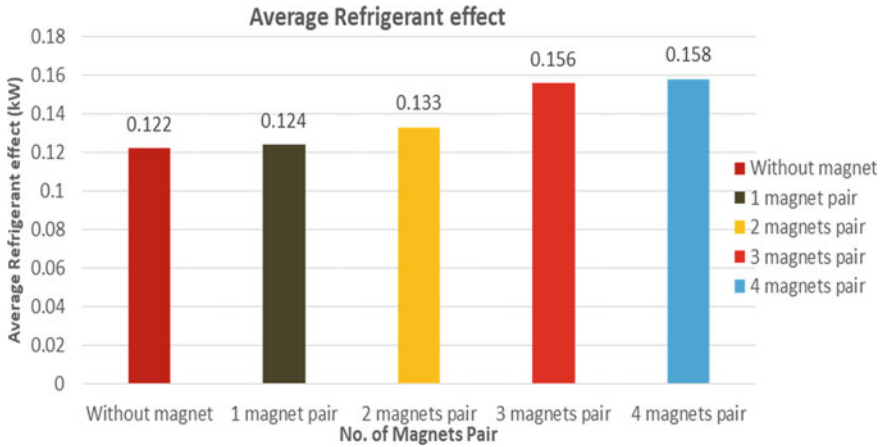


Fig. 6 Refrigeration effect versus no. of magnets pairs

Table 1 Experimental results of VCRS using R134a

Condition	Average time for 10 blinks (sec)	Average refrigeration effect (kw)	Average compressor work (kw)	Average COP
Without magnet pair	56.2	0.122	0.2001	0.604
With 1 magnet pair	56.56	0.124	0.1989	0.619
With 2 magnet pair	56.90	0.133	0.1977	0.667
With 3 magnet pair	57.10	0.156	0.1970	0.791
With 4 magnet pair	57.18	0.158	0.1968	0.804

5 Conclusion

The results of experimentations show by utilizing magnetic pair has a promising effect on R134a vapor compression refrigeration cycle coefficient of performances. As end result of this investigation shows the 33.11% increment in system COP, as the magnets imposed on liquid refrigerant line (outlet of condenser) improved COP of refrigeration systems.

References

1. Mani K, Selladurai V (2008) Energy savings with the effect of magnetic field using R290/600a mixture as substitute for CFC12 and HFC134a. *Therm Sci* 12(3):111–120
2. Sami SM, Aucoin S (2003) Effect of magnetic field on the performance of new refrigerant mixtures. *Int J Energy Res* 27(3):203–214
3. Ram NR, Prakash M, Naresh U, Kumar NS, Sarmash TS, Subbarao T, Kumar RJ, Kumar GR, Naidu KCR (2018) Review on magnetocaloric effect and materials. *J Supercond Novel Magn* 31(7):1971–1979. Springer New York LLC
4. Sidheshware RK, Ganesan S, Bhojwani VK (2020) Experimental analysis of magnetic field effects on compressor energy saving cooling system. In: *E3S web of conferences*, 170, id 01020, pp 1–3. EDP Sciences

Optimization of Significant Parameters for Ramp Film Cooling Using CFD-Integrated RSM Approach



V. G. Krishna Anand 

Abstract The ramp film cooling is a type of film cooling, where the cooling holes are framed behind the right triangular shape protrusion developed on the film cooling surface with the application of thermal resistance coating. This study aims to optimize significant ramp film cooling parameters, viz., ramp angle, the distance between ramp rear edge and film hole starting edge, compound angle, and blowing ratio using CFD-integrated RSM approach. The finite volume-based CFD approach was used to evaluate the response parameter of the experiment design matrix (EDM) framed from the response surface approach. Experimental studies performed with a case identified from EDM of ramp film colling parameters show a good agreement with the computational data. The optimized ramp film cooling parameters identified from this study are ramp angle (α) of 16.98° , the distance between ramp rear edge and film hole starting edge (S) of 0.8 mm, film hole orientation angle (β) of 82.29° , and blowing ratio (M) of 1.99. The optimized ramp film cooling parameters obtained from this study can be useful in the design of ramp film cooling that can deliver improved film cooling performance on gas turbines.

Keywords Ramp film cooling parameters · Computational fluid dynamics · Response surface methodology · Optimization

1 Introduction

Innovative cooling technologies are needed to develop the next-generation gas turbine engines (GTEs). The temperature of gases entering the turbine module of the gas turbine has a direct impact on the output efficiency of GTE. Higher turbine inlet temperature can be achieved through novel cooling methods. Ramp film cooling (RFC) is a modified cooling method for gas turbines where cooling holes are installed behind the right triangle-shaped protrusion developed on film cooling (FC) surface with the application of high resistance coating. Na and Shih [1] performed initial

V. G. K. Anand (✉)

Department of Aeronautical Engineering, MRCET, Hyderabad 500100, India

e-mail: kakrishnaanand@gmail.com

studies on RFC to analyze its performance for FC. They reported that the ramp was very effective to deviate the hot freestream away from the wall surface, and it also helps to reduce the interaction between the coolant and mainstream flows. These effects, in turn, have resulted in the RFC delivering two to three times higher FC performance in comparison with the non-ramp FC model. Halder et al. [2] carried out numerical studies on RFC installed with two-rowed FC holes. The study reported that the α and M as the parameters of significant influence for RFC. Barigozzi et al. [3] conducted experimental studies on the flat surface model installed with ramped configurations. They reported that the ramp-assisted film cooling configuration has delivered effective FC performance on the flat surface model at low M . Chen et al. [4] concluded that the higher ramp angle at higher M has delivered improved RFC performance in comparison with other tested configurations. Yang et al. [5] reported that the combined effects of the ramp with rotating jets have produced improved FC performance on the flat surface model. Also, the effective RFC performance was delivered by the test configuration at higher α and M . Zhou and Hu [6] evaluated the FC performance of sand dune-shaped ramp (SDSR) installed on a flat surface test model. The results of the study show that the performance of SDSR was highly effective in comparison with non-SDSR configuration. The improved effectiveness of the SDSR model was due to its ability to generate anti-opposite rotating vortex structures (ORVSSs), and this effect has caused the coolant to stay close to the bottom wall surface and also has resulted in effective lateral spreading. Lutum and Johnson [7] reported that the length to diameter (L/D) ratio of the FC hole has a major influence on the FC performance of the flat surface model. The L/D ratio of greater than 5 is effective to achieve a higher FC effectiveness on the test surface. Goldstein and Jin [8] performed experimental studies on oriented angle FC holes on the flat surface model and reported that oriented angle FC holes were effective to deliver improved cooling effectiveness on the lateral axis of the test surface. Aga and Abhari [9] concluded that the ORVSS was absent in the case-oriented angle FC hole, and this effect in turn has resulted in higher averaged effectiveness for oriented angle FC hole in comparison with streamwise-oriented FC hole. Zhou et al. [10] showed that the SDSR was effective to deliver better FC performance for real-end wall FC of gas turbine surface at transonic velocities.

Most of the studies reported on literature for RFC were performed with streamwise-oriented FC holes and with variable parameters of, viz., α , S , and M . However, no clear studies were reported on the optimized significant parameters for RFC. Hence, this study is aimed to optimize the range of significant parameters for RFC using the CFD-integrated RSM approach. In addition to parameters reported in the literature for RFC, this study aimed to analyze and optimize the influence of orientation angle FC hole on the performance of RFC.

Table 1 Factors and their levels for RSM

Factors	Ramp angle (α) [°]	Distance between ramp and film hole leading edge (S) [mm]	Film hole orientation angle (β) [°]	Blowing ratio (M)
Levels				
- 1	14	0.8	45	0.4
0	16	2.4	90	1.2
1	18	4.0	135	2.0

2 CFD-Integrated RSM Approach

The variable parameters for RFC widely studied in the literature ([1, 3] and [5]) are α , S, and M. In addition to the investigated parameters (α , S, and M), the present study also investigates the significance of orientation angle of film hole as an additional parameter for the optimization RFC. The range of the chosen RFC factors and their levels of variation are shown in Table 1. The BBD approach is applied to the selected RFC parameters (α , S, M, β), and the experimental design matrix (EDM) is framed for the selected parameters as shown in Table 2. The response parameter (RP) chosen for the framed DM is area-averaged FC (η_{AA}). The CFD method is applied to determine the RP of different cases of DM for RFC. The representation of computational domain (CD) with RFC parameters is shown in Fig. 1.

The cluster-structured grids are employed for the mainstream duct, and unstructured grids are used for the FC hole. The GIS study is performed with three different grids, and the final grid chosen after GIS is 2100000 cells. The boundary condition for the CD is velocity inlet for mainstream (13 m/s) and film hole (varied as per M). The temperature of mainstream and coolant jets is 343 and 303 K, respectively. The regression equation is framed based on the finalized DM, and analysis of variance analysis is performed to identify the significant parameters for RFC.

3 Validation Studies

The computational results are validated through experimental verification. For validation, a case (α —16°, S—0.2D, β —90°, and M—1.2) from design matrix of RSM is experimentally investigated in the film cooling facility. The test plate is fabricated with acrylic material to validate the adiabatic assumption for FC flows. The ramp model and orientation angle of the FC hole are machined through the 5 axis CNC unit. The fabricated ramp test surface is assembled in the test section of the FC facility, and an experimental study is performed with the heated air moving at a velocity of 13 m/s through the test section. The FC air is supplied from the high-pressure compressor. The temperature and pressure measurements on the test surface are

Table 2 Experimental design matrix for RFC parameters

Case No	α (°)	S (mm)	β_r (°)	M
R1	16	2.4	45	2
R2	18	2.4	90	2
R3	18	4	90	1.2
R4	14	2.4	135	1.2
R5	16	4	90	2
R6	14	4	90	1.2
R7	16	4	135	1.2
R8	18	2.4	135	1.2
R9	16	2.4	90	1.2
R10	16	0.8	135	1.2
R11	16	2.4	90	1.2
R12	18	2.4	90	0.4
R13	16	2.4	90	1.2
R14	14	2.4	90	0.4
R15	16	0.8	90	2
R16	14	0.8	90	1.2
R17	16	4	45	1.2
R18	16	2.4	90	1.2
R19	16	2.4	45	0.4
R20	16	0.8	45	1.2
R21	18	2.4	45	1.2
R22	16	4	90	0.4
R23	14	2.4	45	1.2
R24	16	2.4	135	2
R25	16	2.4	90	1.2
R26	16	0.8	90	0.4
R27	16	2.4	135	0.4
R28	14	2.4	90	2
R29	18	0.8	90	1.2

carried out through thermocouple data acquisition and a scan-value pressure scanner. The experimentally obtained temperature values are used for the computation of test plate centerline FCE. The comparison plot for computational and experimental centerline FCE is shown in Fig. 2. The computational data show a close agreement with the experimental test case for RFC.

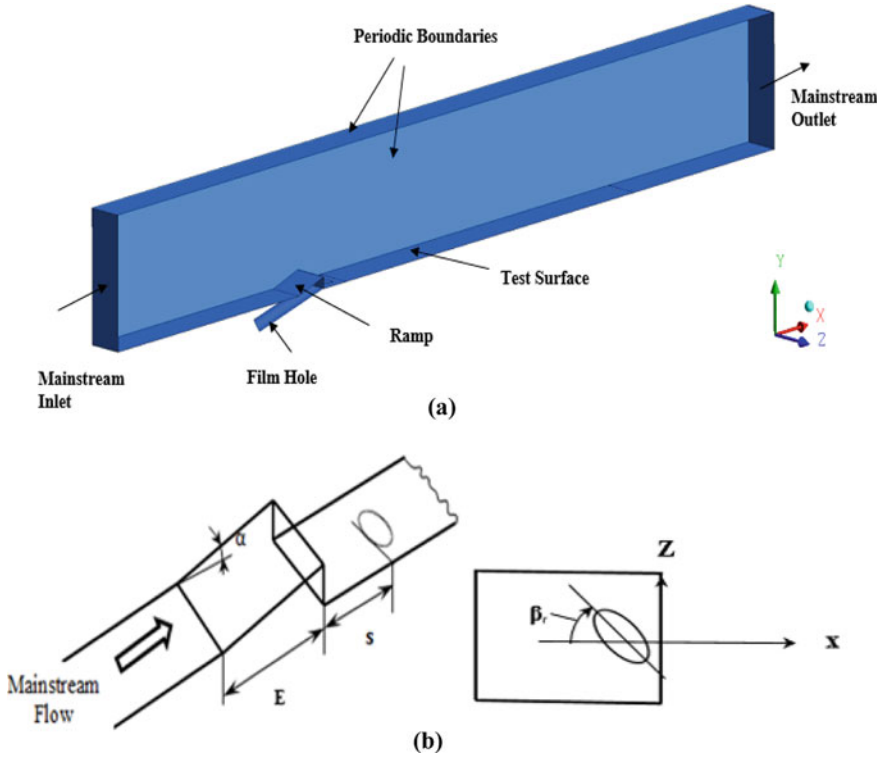
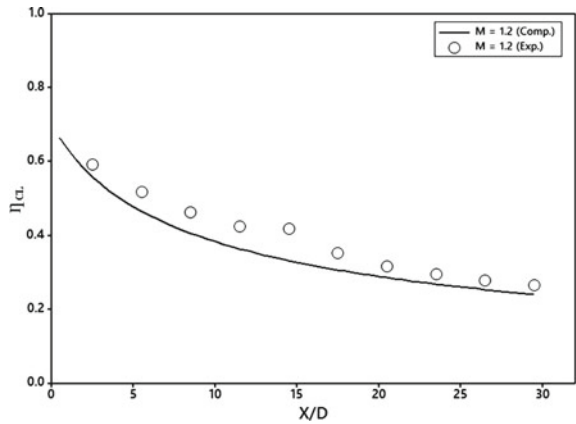


Fig. 1 Details of **a** computational domain **b** ramp film cooling parameters

Fig. 2 Validation comparison of computational and experimental studies of RFC



4 Results and Discussion

The response (Π_{AA}) contour plot generated with two variable parameters (β and M) is shown in Fig. 3. The other two parameters (α and S) of RFC were maintained at the mid-range value. For low M of 0.4, all investigated orientation angles delivered lower Π_{AA} . With the increase in M from 0.4 to 1.2, the Π_{AA} also increases. The M in the range of 1.2–2.0 has delivered the zones of higher Π_{AA} for the film hole orientation angle around 90° .

The response (Π_{AA}) contour plot for the interaction of S and M is shown in Fig. 4. For M of 0.4, an increase in parameter S has delivered almost uniform Π_{AA} . However, with an increase in M (0.4–1.2), the Π_{AA} also increases for the entire range of S (0.8–4 mm). With further increase in M (1.2–2.0), the zones of higher Π_{AA} are observed close to the lower value of S .

The response (Π_{AA}) contour plot for the interaction of β and α is shown in Fig. 5. Herewith increase in β from 45° to 90° , the Π_{AA} also tends to increase until 90° , and after which, the Π_{AA} tends to decrease for an increase in β in range of 90° – 135° . For a film hole orientation angle of 90° , a lower level of α has delivered higher Π_{AA} in comparison with a mid and higher level of α .

The response (Π_{AA}) contour plot for the interaction of S and β is shown in Fig. 6. It is observed from the contour plot that the variation orientation angle has produced a considerable change in Π_{AA} . The mid-level orientation angle of 90° has delivered higher Π_{AA} in comparison with the low- and high-level film hole orientation angle. Also, it is observed that the lower S (0.8 mm) has delivered higher Π_{AA} , and with an increase in S , the Π_{AA} tends to decrease. From the results of response contour plots and variable parameters, it is observed that the variable parameters β and M have a significant impact on Π_{AA} in comparison with α and S . The analysis of variance analysis (ANOVA) performed with the developed regression equation (Eq. 1) also

Fig. 3 Response (Π_{AA}) contour plot for the interaction of β and M

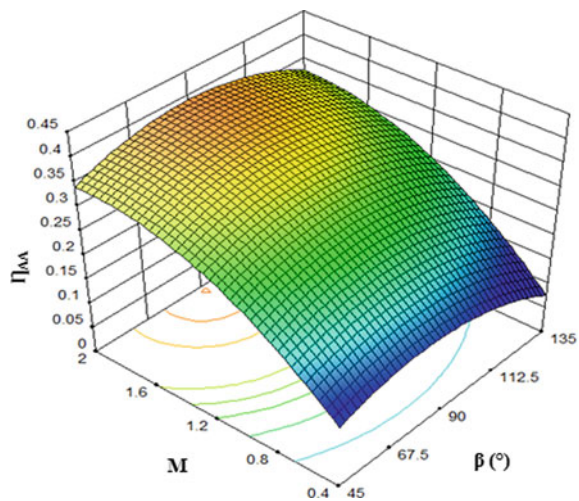


Fig. 4 Response (η_{AA}) contour plot for the interaction of S and M

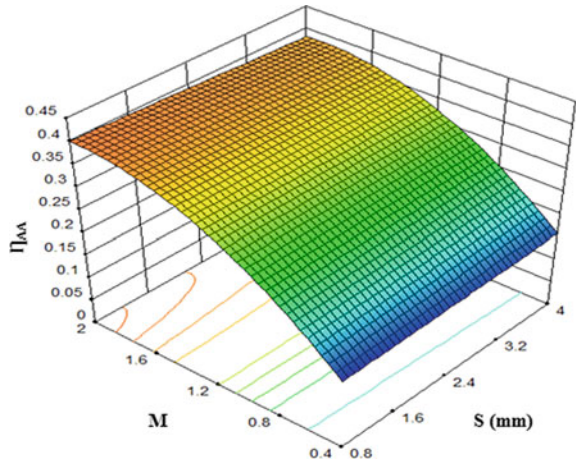
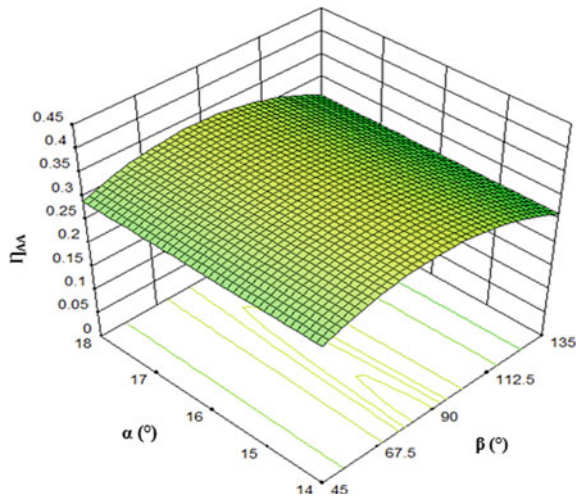


Fig. 5 Response (η_{AA}) contour plot for the interaction of β and α

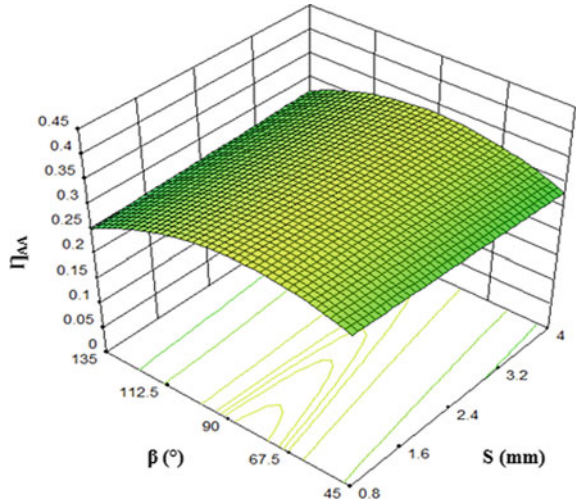


confirms the significant parameters as β and M. The parameters α and S have less influence on η_{AA} .

$$\begin{aligned} \eta_{AA} = & -0.11851 - 0.000458(\alpha) - 0.006927(S) + 0.00393(\beta) + 0.37472(M) \\ & + 0.00015277(S)(\beta) - 0.006250(S)(M) + 0.00022916(\beta)(M) \\ & - 0.000027205(\beta)^2 - 0.097408(M)^2 \end{aligned} \tag{1}$$

The uncertainty between the experimental and RSM data is 4.44%. The optimization studies are performed based on the results regression equation and analysis of

Fig. 6 Response (η_{AA}) contour plot for the interaction of S and β



variance using the DF approach. The optimized RFC parameters are α of 16.98° , S of 0.8 mm, β of 82.29° , and M of 1.99.

5 Conclusion

The significant parameters (α , S, β , and M) of RFC were optimized through CFD-integrated RSM approach. The CFD was used to determine the response parameter of the RSM design matrix. The response (η_{AA}) contour plots were generated to study the interaction effects of variable parameters. The results reveal that the parameters β and M have a significant influence on the response factor of RFC. The analysis of variance analysis also confirms that the parameters β and M are the significant parameters that have a considerable impact on η_{AA} . The optimization studies are performed through the DF approach. The optimized RFC parameters are α of 16.98° , S of 0.8 mm, β of 82.29° , and M of 1.99.

Acknowledgements The author gratefully acknowledges the Department of Science and Technology, Government of India, for the financial support for this research. Also acknowledges the Department of Aeronautical Engineering, Malla Reddy College of Engineering and Technology, Hyderabad for their help and support.

References

1. Na S, Shih TIP (2007) Increasing adiabatic film cooling effectiveness by using an upstream ramp. *ASME J Heat Transfer* 129(4):464–471
2. Halder P, Samad A, Kim JH, Kim KY (2017) Film-cooling characteristics of upstream ramp enhanced turbine blade surface cooling. *Heat Transfer Res* 48(11):969–984
3. Barigozzi G, Franchini G, Perdichizzi A (2007) The effect of an upstream ramp on cylindrical and fan-shaped hole film cooling: Part II – Adiabatic effectiveness results. In: *Proceedings of the ASME turbo expo conference, Montreal, Canada, GT2007–27079*, 4, 115–123
4. Chen SP, Chyu MK, Shih TI-P (2011) Effects of upstream ramp on the performance of film cooling. *Int J Therm Sci* 50:1085–1094
5. Yang W, Pu J, Wang J (2016) The combined effects of an upstream ramp and swirling coolant flow on film cooling characteristics. *J Turbomach* 138:111008-1–111008-10
6. Zhou W, Hu H (2016) Improvements of film cooling effectiveness by using Barchan dune shaped ramps. *Int J Heat Mass Transf* 103:443–456
7. Lutum E, Johnson BV (1999) Influence of the hole length to diameter ratio on film cooling with cylindrical holes. *ASME J Turbomach* 121:209–216
8. Goldstein RJ, Jin P (2001) Film cooling downstream of a row discrete holes with compound angle. *ASME J Turbomach* 123(2):222–230
9. Aga V, Abhari RS (2011) Influence of flow structure on compound angled film cooling effectiveness and heat transfer. *ASME J Turbomach* 133(3):031029
10. Zhou W, Qenawy M, Shao H, Peng D, Wen X, Liu Y (2020) Turbine vane endwall film cooling with barchan-dune shaped ramp in a single-passage transonic wind tunnel. *Int J Heat Mass Transf* 162:1–13

Enhancing Fuel Efficiency of a Two-Wheeler Based on Taguchi and ANOVA Method and Regression Analysis



J. Kevin Joseph, R. Jeyanthinathan, and Lokavarapu Bhaskara Rao

Abstract Fuel is one of the major requirements for everyone in modern life. Fuel is a non-renewable resource. Cost of petrol is sky-scraping in India. Global pollution is also high. To reduce the crisis, auto manufacturers concentrate on the development of the fuel economy of the vehicle. To increase the fuel economy, we reduce the wastage of fuel consumption in any scenario. So, fuel consumption is controlled by different variables. This article mainly focuses on the fuel economy of two-wheeler by optimizing the influenced factors such as load, speed, octane number, and tire pressure. By changing the various levels, the experiment was carried out to calculate fuel mileage by using an average mileage testing bottle. The experimental data have been analyzed by using Taguchi, ANOVA method and regression analysis to provide favorable solution. This paper's, main objective is to find out high influencing factors by applying design of experiments and also suggest the best combination of control factors to give better fuel economy for two-wheelers. From this paper it was found that control variable such as the speed and octane number is the high influencing parameter for fuel consumption. Main effect and interaction effect of control variables were also discussed.

Keywords Mileage · Control factors · Signal to noise ratio · Fuel consumption · ANOVA · Regression analysis

1 Introduction

Transportation is an important requirement in economic growth countries. The people are more interested in buying vehicles. Heavy-duty vehicles bought for business. It helps to transport goods. Light-duty vehicles like two-wheelers and cars bought for

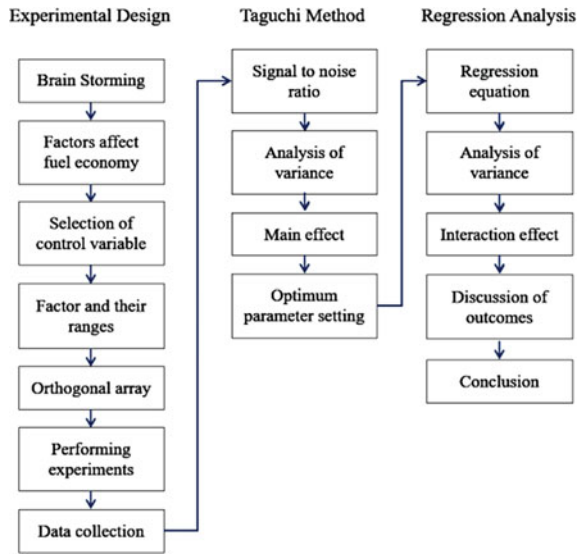
J. Kevin Joseph · R. Jeyanthinathan · L. Bhaskara Rao (✉)
School of Mechanical Engineering, Vellore Institute of Technology, Chennai, Tamil Nadu,
Vandalur-Kelambakkam Road, Chennai 600127, India
e-mail: bhaskarbabu_20@yahoo.com

R. Jeyanthinathan
e-mail: jeyanthinathan2020@vitstudent.ac.in

traveling in shorter and longer distances. The two-wheeled vehicle is a mandatory need for all people. In the modern world, at least two or three motorbikes were bought in every house. And also, every person buys a motorbike for their own purposes. India is the second-largest population country. So compared to other countries, a higher number of two-wheelers are being used in this country. The unwanted usage of fuel causes air pollution to increase and affect the cost of petrol price. This paper's main aim is to focus on the fuel economy of the two-wheeler vehicle by optimizing the influenced factors with various levels. The important tool for optimization is the design of experiments. It helps to analyse factors at various levels of iteration and also interprets the results at various responses [1] Taguchi method is used to determine the leading combination of inputs to produce a greater output. In which experiment it helps to find the best level of control variable and minimize the difference in the noise factors [2]. From the collected data, Taguchi method helps to calculate to s/n ratio and find out major influencing factors. Generate the regression equation for plotting graphs and ANOVA table for data validation. The fuel economy depends on various control factors. The installation of a tire pressure system helps to improve the fuel economy of automobiles. The development of regression equation through the multiple regression analysis to predict fuel economy [3]. From this literature [4], the fuel consumption depends upon engine size, HP, No. of cylinders, weight, length and width of the vehicle. The response factor is taken as mileage. The gas mileage predicted by the T method. The gear 5 or top gear is the most significant parameter for fuel consumption [5].

For a four-wheeled vehicle, speed is the most influencing factor when compared to others. For better fuel economy, the vehicle travels on the optimum combination based on the Taguchi method [6]. The total fuel consumption based on vehicle acceleration, vehicle dynamics, engine idling, engine braking and service braking [7]. The control parameters of the fuel consumption in petrol engines are spark advance, compression ratio, air-fuel mixture, load, and octane number. The octane number is the higher influence parameter in fuel consumption [8]. Percentage of fuel spent in time, the dead weight of the vehicle, average time spent in traffic is the most important parameter for the wastage of the fuel consumption [9]. The Taguchi method was also used to optimize the influencing factor to find out NO_x emission [10]. In Indian roads, uneven surfaces over there, higher clearance and high fluctuating load withstand the vehicle is used. The Indian Road varies from urban and rural areas [11]. The Indian roads may contain smooth roads on national highways, dumps and blocks in village areas, hilly region on north India, desert region in east India and delta region in south India. The people mostly prefer the vehicle with more fuel mileage compared to the speed vehicle. So much research work was done four-wheeler vehicles to find out the optimizing parameter of fuel economy. Most of the middle-class family focuses on buying the two-wheeler vehicle when compared to the cars. In this article, discusses the influencing factor of fuel economy in two-wheeler vehicles. The control factors and levels for the vehicle were identified. The response variable is taken as mileage. Using Taguchi method and regression equation is used to find out the most significant factor.

Fig. 1 Methodology flow chart



2 Methodology

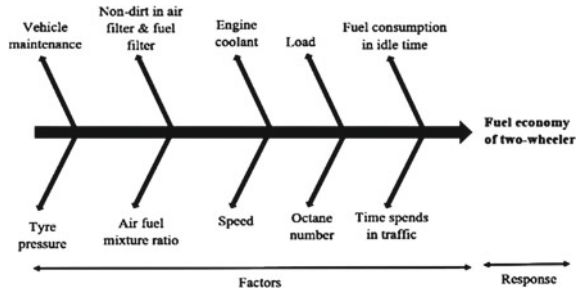
In this paper, a collection of important control factors from the literature reviews. Selection of the control parameters to improve the fuel economy of the vehicle. Appropriate vehicle was selected for the experimental setup. Selection of levels and formation of the orthogonal array should be done. Experiments should be performed at least two times to get the iteration of results. The experiments should be done based on the formation of the array. Signal to noise ratio was found by using Minitab software. Analysis of variance is performed to find out the main effect of the control variable. According to the F-value, the most significant factors are determined. Finally, the optimum combination of input parameters is to find out for better fuel economy of the vehicle. Regression equation is generated and analysis of variance is performed to find out interaction effects between control variables. Surface and contour graphs for the combination of control factors vs mileage are discussed. Figure 1 represents the methodology flow chart.

3 Experimental Design

3.1 Factors that Affect Fuel Economy

For a two-wheeled vehicle, the fuel economy depends upon different factors such as variation of speed, load (passenger occupancy), vehicle frontal design, tire pressure, the octane number of fuels, idle time, engine coolant, maintenance. Always keep a

Fig. 2 The factors depend on the fuel economy



check at the tire air pressure as it influences the fuel economy of the vehicle in a greater way by its ability to withstand the load. Not being as smooth in changing gears causes to affect fuel economy. Taking extra loads also affects the vehicle’s fuel economy. Percentage of fuel spent in idle time in running engines and in lower time signals, engages the gears and pressing clutches which also affect the fuel economy. The vehicle is internally as well as externally unclean as a dirt in the air filter also affects the fuel economy [12]. Figure 2 represents the factors that depend upon the fuel economy. From those factors Octane number, Vehicle Speed at top Gear, Tire pressure, and Load are the most important factors which depend on fuel economy.

3.2 Motorbike Specifications

An experiment was conducted using a Bajaj Platina 100 cc motorbike. Launched in 2006, the Platina is one of the most popular commuter motorbikes in India. Table 1 represents the specification of motorbike.

The 100 cc Bajaj Platina motorbike has won the NDTV profit bike India award in the year 2007 and also in the 100 cc category motorbike of the year award. It was the 8th best-selling motorbikes in India 2021, from April 2020–Jan 2021. In 2021 it is

Table 1 The specification of 100 cc motorbike

Engine class	4 stroke DTS-i single cylinder
Engine displacement	102 cc
Maximum power	7.9 PS @ 7500 rpm
Maximum torque	8.3 Nm @ 5500 rpm
Total no. of cylinders	1
Valve per cylinder	2
Supply of fuel	Fuel injection
Transmission type	Manual transmission
Transmission	4 gears

still one of the best-selling motorbikes in our country for its economic performance and fuel economy.

3.3 Experimental Setup

This experimental test setup includes a two-wheeler motorbike with a single engine cylinder specification and a 500 ml mileage testing bottle as shown in Fig. 3. A mileage or average testing approach is carried out to measure the fuel consumption of the vehicle. The fuel inside the fuel tank is made empty or close to the petrol tank supply. A mileage testing bottle (mile scanner) was left hanging from the handlebar and taped to the fuel tank. One end of the fuel hose pipe is attached to the mileage testing bottle and the other end to the carburetor. The trip meter is set to 0 for every run to get an accurate reading and to minimize systematic error 500 ml average testing bottle is filled with 50 ml for test Run 1. For every run, the motorbike is made to run until there is no fuel left (till the motorbike gets stops running). Note down the distance (km) covered which displays on the trip meter. Mark the result as test Run 1. Likely repeat the procedure for test Run 2. Find out average mileage for two test rides. This procedure is repeated for every iteration.

4 Design of Experiments

In design of experiment, the factors which are being considered are grouped into three ranges or limits, the minimum is given as low the mid-range is given as medium and the maximum range if the factor is given as high. In this paper, speed, octane number, load, and tire pressure are taken as factors. Low-level, mid-level, and high level taken as ranges. All the factors have three ranges except the octane number. The factors and ranges are given in the Table 2. In this paper, the response variable is the fuel



Fig. 3 a and b Mileage testing bottle is being attached on two-wheeler

Table 2 Factors and their ranges

Factor	Range		
	Low level	Mid-level	High level
Speed	40	50	60
Octane number	87	91	–
Load	70 kg	120 kg	160 kg
Tire pressure	(FW = 25 psi & BW = 35 psi)	(FW = 28 psi & BW = 38 psi)	(FW = 30 psi & BW = 40 psi)

economy of the vehicle. There are two test rides are taken for each setting. The mean mileage value for the two test rides is the final mileage of the vehicle. The mileage of the vehicle is equal to the distance traveled per fuel consumption of the vehicle. Table 2 represents the factors and their ranges. At 4th gear, the motorcycle’s speed ranges from 40 to 60 km per hour. All the experiments are conducted at top 4th gear setting. The air pressure in the motorbike’s front tire ranges from 25 to 30 psi, while the air pressure in the rear tire ranges from 35 to 40 psi which are selected for Indian street motorbikes as per manufacturer recommended inflation pressure setting. For test rides, two levels of octane fuel are employed.

$$\text{Mileage of the vehicle} = (\text{Distance traveled per km/fuel used in liter}).$$

4.1 Taguchi L9 Orthogonal Array

By two factorial method the possible combinations for 3 factors with three levels and remaining 1 factor with 2 levels, there will be 54 experiments to perform which is time consuming. This can be avoided by following combinations obtained from Taguchi’s orthogonal array. By design of experiments, total sets of combinations can be reduced to 9 combinations. Table 3 shows the 9 combinations as prescribed by Taguchi. No. of Experiments to perform is given by $F(L-1) + 1 = 4*(3-1) + 1 = 9$ [11].

For the above combination two runs were performed, which is given in Table 4. For run 1 and run 2 is distance (km) traveled per 50 ml.

4.2 S/N Ratio Formulations

S/N ratio formula is given in the Table 5. To maximize fuel economy this paper follows the larger the better response condition. The formula signal to noise = $-10 \log(\sum 1/Y^2)/n$ is used [13].

Based on the analysis of variance for signal to noise ratio Table 6, the factors are ranked. The percentage of Contribution is defined as the ratio of the Sequential

Table 3 Nine combinations settings as prescribed by Taguchi

Iteration	Speed	Load	Tire pressure	Octane no
1	1	1	1	1
2	1	2	2	2
3	1	3	3	2
4	2	1	2	1
5	2	2	3	1
6	2	3	1	2
7	3	1	3	2
8	3	2	1	1
9	3	3	2	1

Sum of squares to the Total Sum. Factor A (speed) records the highest contribution percentage (74.39%), Followed by factor D (octane number) and the third ranked factor is the factor C (type pressure). These three factors have more influence on the response. To control the response, these factors must be kept in optimized value.

A–Speed (m/s), B–Load (N), C–Tire Pressure (N/m²), D–Octane Number.

The response values of each control variable are calculated using the S/N formula = $-10 \log(\sum Y^2/n)$ based on the larger the better response condition. Based on the higher delta magnitude, the ranking is carried out. Table 6 ranks the control factors based on the contribution percentage. The fuel economy depends on the combination of many parameters. The ranks were arranged based on contribution from those four variables. Higher the contribution percentage more significant the variable for the selected control variables and their ranges. From Table 6 speed has 74.39% contribution followed by octane number which is at 12.661% and tire pressure which is at 6.15%. These three are the significant parameter. Table 7 ranks based on the delta value. In both tabulated results, the most significant control variable is A, D, C which takes the first, second and third position, respectively.

Optimum Parameter Settings for Low Fuel Consumption

The general optimized control variable values given in Table 8 are obtained from Fig. 5. Figure 5 mean effect plot was carried out with S/N ratio configuration larger the better. To get the higher or better response condition from the Fig. 5, all the factors selected are to be in higher mileage values. For this analysis, the optimum control factor settings based on the Taguchi method is A1-B1-C2-D2.

From Table 4 experiment, the combination of parameters which gives high mileage result is selected. The optimum control factors are achieved (based on the SN formulae larger the better) are A1 (11.11 m/s), B1 (686.7 N), C2 (262001 N/m²), D2 (91) values. This general optimized combination gives a higher fuel economy of 80 km/lit. From the normal probability plot of Fig. 4 plotted between percent versus residual explains that all data are normally distributed, that is as all the data points are distributed around the straight line. Hence it satisfies the condition. The

Table 4 Nine combinations as prescribed by Taguchi

Speed (km/hr)	Load (kg)	Tire Pressure (psi)	Octane no	Run1	Run 2	Result (mean)	Mileage (Run 1) (km/lit)	Mileage (Run 2) (km/lit)	Mileage Result (km/lit)
40	70	(FW = 25 & BW = 35)	87	3.8	3.7	3.75	76	74	75
40	120	(FW = 28 & BW = 38)	91	4.05	3.95	4.0	81	79	80
40	160	(FW = 30 & BW = 40)	91	3.95	3.8	3.87	79	76	77.4
50	70	(FW = 28 & BW = 38)	87	3.8	3.88	3.84	76	77.6	76.8
50	120	(FW = 30 & BW = 40)	87	3.67	3.76	3.71	73.4	75.2	74.2
50	160	(FW = 25 & BW = 35)	91	3.88	3.7	3.79	77.6	74	75.8
60	70	(FW = 30 & BW = 40)	91	3.75	3.6	3.67	75	72	73.4
60	120	(FW = 25 & BW = 35)	87	3.61	3.5	3.55	72.2	70	71
60	160	(FW = 28 & BW = 38)	87	3.58	3.5	3.54	71.6	70	70.8

Table 5 S/N ratio formulations

Sl. No	S/N ratio response configuration	Formulae
1	The smaller, the better	$S/N = -10 \log(\sum Y^2/n)$
2	The larger, the better	$S/N = -10 \log(\sum 1/Y^2)/n$
3	The nominal, the better	$S/N = -10 \log(\sum Y^2/S^2)$

Table 6 Analysis of variance for S/N ratio

Source	DOF	Seq-SS	Adj-SS	Adj-SS	F-value	Contribution (%)	Significance
Speed (m/s)	2	53.6035	39.3249	19.6625	22.72	74.39	Yes
Load (N)	2	0.4918	3.4225	1.7113	1.98	0.68	No
Tire pressure (N/m ²)	2	4.4342	4.9928	2.4964	2.88	6.15	Yes
Octane number	1	12.6661	12.6661	12.6661	14.63	12.661	Yes
Error	1	0.8656	0.8656	0.8656			
Total	8	72.0612					

Table 7 Response table for signal to noise ratios (larger is better)

Level	Speed (m/s)	Load (N)	Tire pressure (N/m ²)	Octane number
1	37.78	37.51	37.37	37.33
2	37.57	37.50	37.59	37.69
3	37.11	37.46	37.50	—
Delta	0.67	0.05	0.22	0.36
Rank	1	4	3	2

Table 8 Optimum parameter settings for low fuel consumption

Factors		Levels	Mean of S/N ratio	General optimization
Speed (m/s)	A	1	37.7793	A1 (11.11 m/s)
		2	37.596	
		3	37.1133	
Load (N)	B	1	37.5075	B1 (686.7 N)
		2	37.4983	
		3	37.4563	
Tire pressure	C	1	37.3733	C2 (262001 N/m ²)
		2	37.5899	
		3	37.4989	
Octane number	D	1	37.3285	D2 (91)
		2	37.686	

Fig. 4 Residual plot for signal to noise ratio (Taguchi method-larger the better)

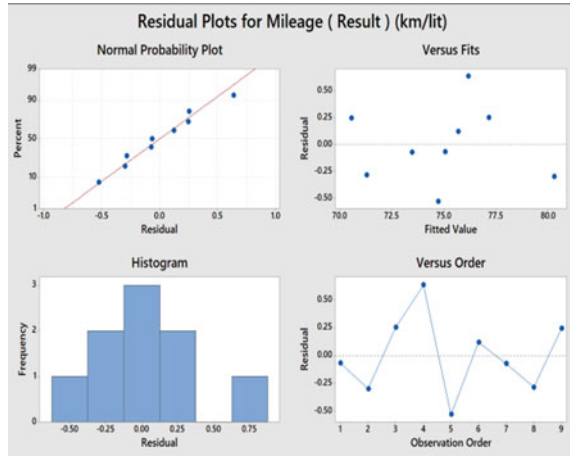
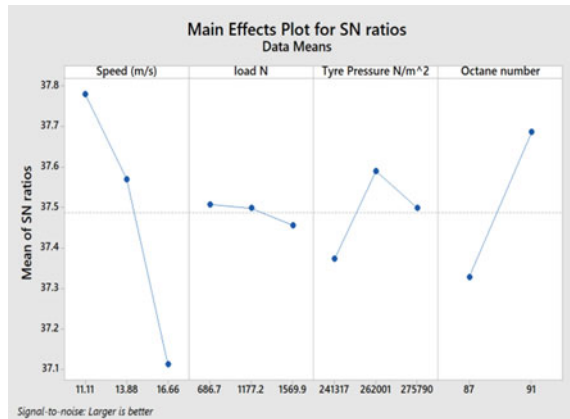


Fig. 5 Main effect plot for signal to noise ratio (Taguchi method-larger the better)



residual versus fitted plot graph of Fig. 4 investigates that the model developed should satisfy the three following conditions, they are even spreading of data, points should be populated nearer to zero and points should be located closer to other points in X-axis. These all three conditions are satisfied from the second graph. Histogram versus residuals graph of Fig. 4 has to follow the following assumptions, it should have even tails across the data and each bar is evenly placed which concludes that data is not either highly skewed or no outliers are included. Even the tail on both sides and each bar is evenly placed is clearly observed from the third graph hence all assumptions are satisfied. Residuals versus order plot graph of Fig. 11 is to interpret that the residuals are independent or dependent with each other. If the data plotted are not following a trend, then the residual points are identified as independent, the fourth graph plotted shows that it follows the trend hence the control variables are not independent.

4.3 Development of Mathematical Model

Generalized Regression Equation

The general formula for regression analysis is given by

$$Y = b_0 + \sum_{i=1}^k b_i x_i + \sum_{i=1}^k b_{ii} x_i^2 + \sum_{i \neq j}^k b_{ij} x_i x_j$$

Here j = total number of control variables = Four

i = number of levels = 3.

i, j = 1, 2, ..., k

k = 3.

One of the advantages of performing regression analysis is that in addition to main effect, interaction effect contribution can also be acquired. Using Minitab software [14] regression analysis is carried out where main factors effects and interaction effects were obtained to find the contributing factor to fuel economy.

Analysis of Variance

The significance is determined based on F-value. From Table 9 the most significant control variable to fuel economy is tire pressure and octane number followed by interaction of tire pressure and octane number. The next significant variable is interaction between speed and tire pressure followed by speed. Load and interaction between load and other parameter is the least significant.

The final regression equation obtained from Minitab can be written as.

Table 9 Analysis of variance

Source	DOF	Adj-SS	Adj-MS	F-value	Significance
Regression	1	70.4404	10.0629	10.07	Yes
Speed (m/s)	1	6.0740	6.0740	6.08	Yes
Load (N)	1	3.6100	3.6100	3.61	No
Tire Pressure (N/m ²)	1	9.8722	9.8722	9.88	Yes
Octane number	1	9.2036	9.2036	9.21	Yes
Speed (m/s) * Load (N)	1	2.9696	2.9696	2.97	No
Speed (m/s) * Tire Pressure (N/m ²)	1	6.5497	6.5497	6.55	Yes
Tire Pressure (N/m ²) * Octane Number	1	7.402	7.4902	7.49	Yes
Error	1	0.9996	0.9996		
Total	8	71.4400			

Mileage (km/lit) = $-1137 + 12.89 \text{ Speed (m/s)} - 0.0410 \text{ Load N} + 0.00439 \text{ Tire pressure (N/m}^2) + 11.51 \text{ Octane number} + 0.00245 \text{ Speed*Load (N)} - 0.000063 \text{ Speed (m/s)} * \text{ Tire pressure (N/m}^2) - 0.000039 \text{ Tire pressure (N/m}^2) * \text{ Octane number}$.

5 Results and Discussion

The regression equation developed earlier was simulated in Minitab software to find out the effect of one factor against fuel economy. For all variation graphs are plotted. The obtained graphs are given. Line graph can also be plotted by taking a dependable control variable and fixing other three control variables at their mean values to find out the effect of dependable variable on fuel economy which is not approached in this article. For better visualization of results surface graph and contour graph are plotted. Since speed is the main factor affecting fuel economy, speed is kept as a dependable variable and with respect to speed another control factor is considered as an independent variable. Figure 6 is a surface plot and Fig. 7 is a contour plot respectively. Both the graphs are plotted for mileage vs the speed and load whereas the octane number and the tire air pressure both are kept fixed at their mean values, i.e., octane number at 88.77 and tire air pressure at 259,702.66 N/m². From Fig. 6 mileage is maximum when control factor such as speed at lower level and load at lower level respectively. The same phenomena are observed from Fig. 7 contour plot where dark green contour region is the region where better mileage will be yielded.

Figure 8 is a surface plot and Fig. 9 is a contour plot respectively. Both the graphs are plotted for mileage vs the speed and tire pressure whereas the octane number and the load both are kept fixed at their mean values, i.e., octane number at 88.77 and load at 1144.6 N. From mileage is maximum when control factors such as speed at lower level and tire pressure at high level, respectively. The same phenomena are observed from Fig. 9 contour plot where dark green contour region is the region where better mileage will be yielded.

Fig. 6 Surface plot of mileage versus load, speed

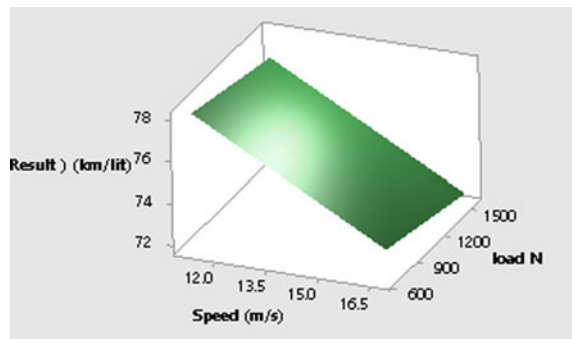


Fig. 7 Contour plot of mileage versus load, speed

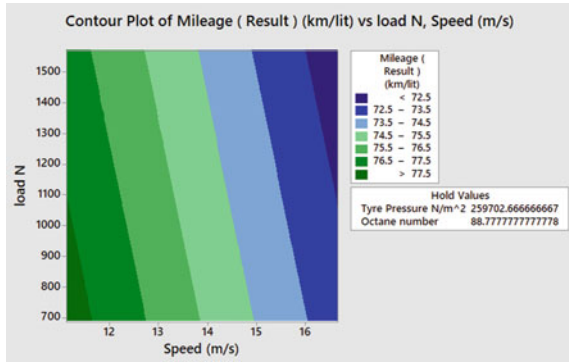


Fig. 8 Surface plot of mileage versus speed, tire pressure

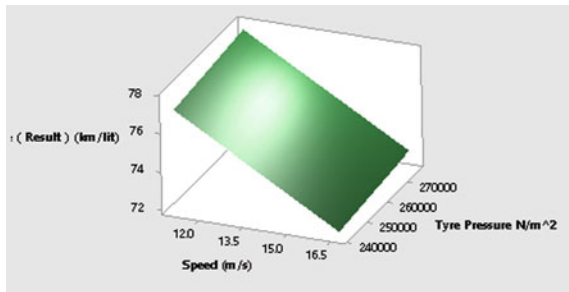


Fig. 9 Contour plot of mileage versus speed, tire pressure

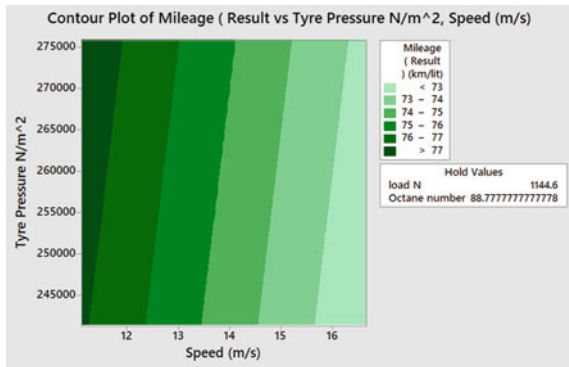


Figure 10 is a surface plot and Fig. 11 is a contour plot respectively. Both the graphs are plotted for mileage vs the speed and octane number where as the tire pressure and the load both are kept fixed at their mean values, i.e., tire pressure at 259,702.66 N/m² and load at 1144.6 N. From mileage is maximum when control factors such as speed at lower level and octane number at high level, respectively. The same phenomena are observed from Fig. 11 contour plot where dark green contour region is the region where better mileage will be yielded.

Fig. 10 Surface plot of mileage versus speed, octane number

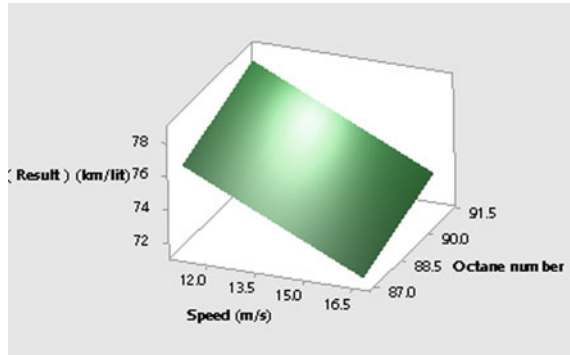


Fig. 11 Contour plot of mileage versus speed, octane number

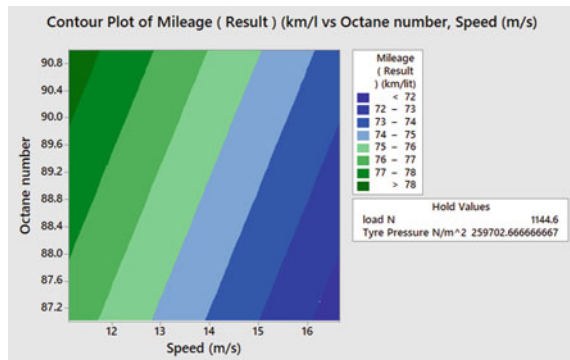


Figure 12 is a surface plot and Fig. 13 is a contour plot respectively. The graph is plotted for mileage vs load and octane number where as the tire pressure and the speed both are kept fixed at their mean values, i.e., tire pressure at 259,702.66 N/m² and speed at 13.88 m/s. From Fig. 12, mileage is maximum when control factors such as load at lower level and octane number at high level, respectively. The same phenomena are observed from Fig. 13 contour plot where dark green contour region is the region where better mileage will be yielded.

Surface and contour plots can also be plotted for control variables such mileage vs octane number, tire pressure and Mileage vs tire pressure, load. The graphs described in this work gives a very good well explanation about main effects and other minute effects between control variables are not shown in the form of graphs. To get a bit more clearer understanding about interaction effect, interaction graphs are also plotted between a combinations of control variables such as speed vs load, speed vs octane number, speed vs tire pressure, octane number vs load, octane number vs tire pressure and tire pressure vs load. For this all-possible combination six interaction effect graphs are plotted which is given. The two figures such as Fig. 14, and Fig. 15 explain about the interaction effect between the combination of two control variables

Fig. 12 Surface plot of mileage versus load, octane number

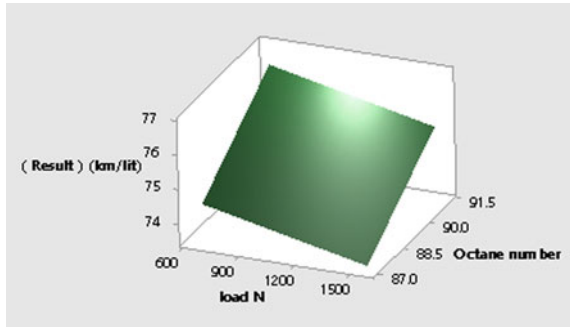


Fig. 13 Contour plot of mileage versus load, octane number

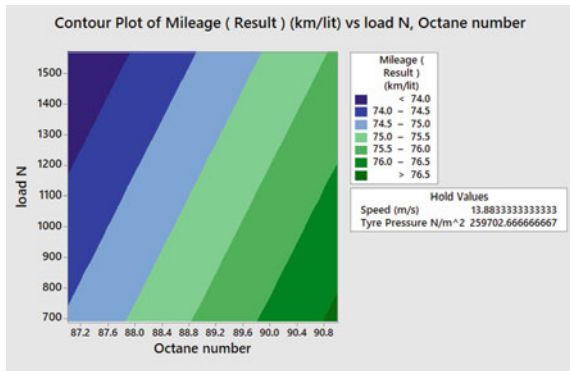
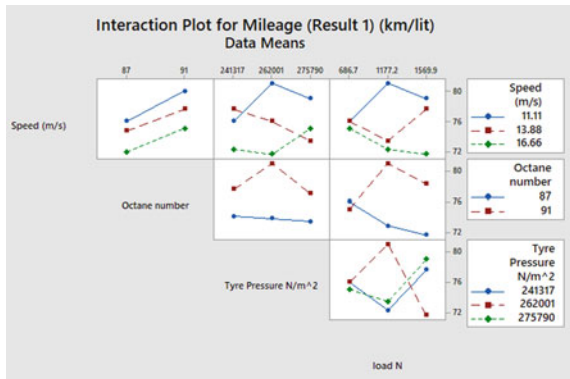


Fig. 14 Iteration 1 mileage interaction plot



for first iteration and second iteration, respectively, and Fig. 16 final result which is the mean of first and second iteration, respectively.

This gives a straightforward answer when the lines are parallel to each other there is no interaction between them. For instance, when you see Fig. 15, interaction plot between speed and octane number where the lines are aligned parallel to each other

Fig. 15 Iteration 2 mileage interaction plot

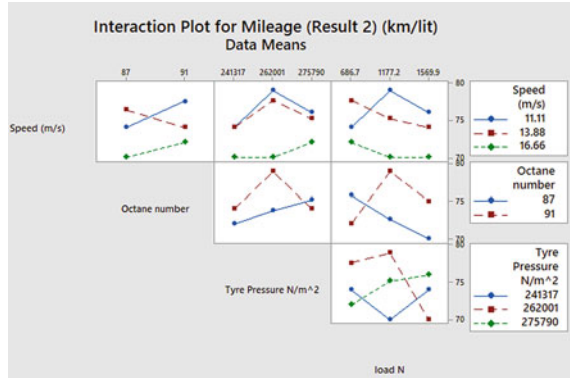
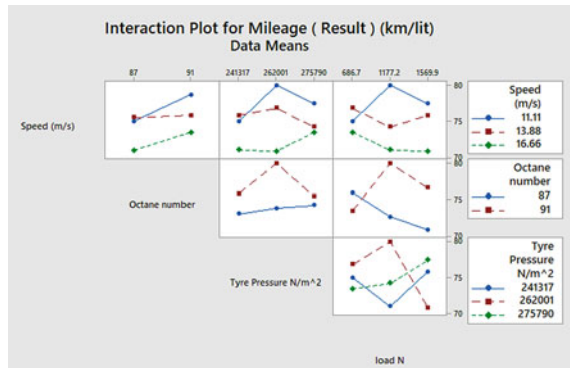


Fig. 16 Mean iteration mileage interaction plot



which means there is no relation or interaction between them at any level. Whenever the lines are intersecting with each other which means there is an interaction between the control variables. More the slope between the lines, the more the interaction between those variables. For instance, consider Fig. 15 interaction plot between speed and octane number, where there is an interaction between speed low level and mid-level line when octane number range gets changed. From these graphs it is very much clearer to visualize where the interaction is happening between these parameters.

6 Conclusion

In this paper, experimental investigation was conducted on Bajaj Platina 100 cc motorbike using Taguchi method, ANOVA table and regression analysis. In this paper, the fuel economy of the vehicle is found out by bottle mileage method. Data used in this article is collected from the experimental results. Taguchi method,

ANOVA table and regression analysis is carried out using the Minitab software tool. Highly influencing control variables affecting fuel economy and optimum combination to cut down fuel consumption is found out from the mean of SN ratio. From this paper, it can be concluded that the fuel economy of a two-wheeler vehicle can be improved when maneuvered under an ideal combination of the influencing control variables. Optimum combination of control variables is A1-B1-C2-D2. From this analysis ideal combination of the control variable for best fuel economy is speed = 11.11 m/s, load = 686.7 N and tire air pressure = 262,001 N/m² and octane number = 91. Regression equation obtained can be used to find one parameter when the other three are known so as to get the best fuel economy within the range.

References

1. Montgomery DC (2017) *Montgomery: design and analysis of experiments*. Wiley
2. Krishnaiah K, Shahabudeen P (2012) *Applied design of experiments and Taguchi methods*. PHI Learning Pvt Ltd
3. Naidu NVR, Rajesh M *Enhancing fuel economy of automobiles through design of experiments*
4. Shah P, Cudney E, Jikar V (2009) Predicting Gas Mileage using the T-Method (No. 2009-01-0986). SAE Technical Paper
5. Goharimanesh M, Akbari A, Tootoonchi AA (2014) More efficiency in fuel consumption using gearbox optimization based on Taguchi method. *J Ind Eng Int* 10(2):1–8
6. Das S, Mukherjee S (2017) Optimization of fuel requirement of a vehicle. *Int J Res Eng Manage* 03(03):1–4
7. Ogorodnov SM, Rogov PS, Maleev SI, Kuznetsov YP, Plotnikov SA (2018) Development of a technique of gear ratios optimization with the aim of simultaneously increasing the vehicle dynamic, fuel efficiency and reducing emissions. In: *IOP conference series: materials science and engineering*, vol 386, no. 1, p 012010
8. Pathak A, Choudhury PK, Dutta RK (2018) Taguchi-grey relational based multi-objective optimization of process parameters on the emission and fuel consumption characteristics of A VCR petrol engine. *Mater Today Proc* 5(2):4702–4710
9. Rajesh B, Rajan J (2019) Optimisation of fuel consumption by Taguchi Method in logistics systems. *Int J Mech Prod Eng Res Dev* 9(2):61–74
10. Sharma A, Ansari NA, Singh Y, Mustefa I, Vivekanandhan C (2018) Optimization of engine parameters using Polanga biodiesel and diesel blends by using Taguchi method. *Mater Today Proc* 5(14):28221–28228
11. Errampalli M, Mallela SS, Chandra S (2020) Calibration of car-following model for Indian traffic conditions. *Transp Res Procedia* 48:829–839
12. Ganesan (2013) *Internal combustion engines*, 4th edn. McGraw Hill, New Delhi
13. Kothari CR (2004) *Research methodology: methods and techniques*. New Age International (P) Limited, New Delhi
14. Alin A (2010) *Minitab*. Wiley Interdisc Rev Comput Stat 2(6):723–727

The Impact of Drying Conditions on Drying Characteristics, Kinetics, and Mass Transfer Parameters of Pumpkin Seeds (*Cucurbita Maxima*)



Priyanka Dhurve and Vinkel Kumar Arora

Abstract The drying characteristics, kinetics, and mass transfer phenomenon of pumpkin seeds were investigated at 40, 50, and 60 °C temperature and 1.5 m/s, air velocity, respectively. The kinetics of the pumpkin seeds drying was predicted with the help of six semi-empirical models. Among all models, the Page model was predicted to be more appropriate for representing the kinetics of drying pumpkin seeds with maximum R^2 (0.9995) and minimum χ^2 (4.81×10^{-5}) and RMSE (0.0069). The D_{eff} , B_i , and h_m of the seeds were found to be improved from 4.33×10^{-10} to 5.4×10^{-10} m²/s, 0.2910 to 0.6095, and 3.321×10^{-8} to 8.656×10^{-8} m/s, respectively, with the increase of temperature. It was also noticed that a less amount of activation energy (17.78 kJ/mol) is needed for moisture diffusion. So, drying at 60 °C air temperature resulted in a high rate of drying and lower drying time, which can be recommended for pumpkin seeds drying.

Keywords Tray drying · Pumpkin seeds · Effective moisture diffusivity · Mass transfer parameters

1 Introduction

Pumpkin is most widely grown vegetable around the globe with worldwide production is 27 million tons in 2019 [1]. The 72–76% of pulp and by-products, i.e., 2.6–16% of peel and 3.2–4.4% of seeds are produced during the processing of pumpkins [2]. Pumpkins seeds are an abundant resource of essential amino acids, proteins, vitamins, minerals, and antioxidants (tocopherols, carotenoid, and phenolic content) [3]. Most countries utilized pumpkin seeds as dried fruits after roasting and salting due to their nutritional values, while countries, pumpkin seeds oil is also used for cooking and pharmacological purpose [4]. Because of high moisture content and water activity, these seeds are extremely liable to microbial spoilage and chemical alteration [5]; therefore, drying of such seeds is important at the early stage of further processing.

P. Dhurve · V. K. Arora (✉)

Department of Food Engineering, National Institute of Food Technology Entrepreneurship and Management, Sonapat, Haryana 131028, India
e-mail: vinkelarora17@gmail.com

Drying is the oldest and most appropriate technique used for preservation and inhibited microbial growth which helps to reduce the deterioration of food materials [6]. Furthermore, it also cuts the transport and storage expenses. The need of dried pumpkin seeds has increased nowadays due to their dietary quality; thus, it stimulated the need for efficient and low-cost drying techniques. Therefore, the assortment of proper drying methods and conditions is a mainly imperative step in food processing. Currently, the utmost used drying method for agricultural material is hot air drying. In this method, the transfer of heat and mass occurs simultaneously in an unsteady state. Hence, the information on heat and mass exchange phenomenon, viz., diffusivity, activation energy, and mass transfer constraints at varied drying conditions are essential to dryer design and for value products [7].

Effect of drying conditions of any drying method is important to supply the best quality of food materials. For optimization and simulation, mathematical modeling is proposed. Subsequently, mathematical modeling is comprehensively utilized for the assurance of the absolute time needed for drying and the improvement of drying kinetics. Several studies of drying kinetics for pumpkin seeds have been done with natural and forced convection solar drying [8], solar and hot air drying [9], fluidized bed drying [10–12], and infrared dryer [13] has been reported previously. However, studies on pumpkin seeds drying that estimated mass transfer parameters are very limited with mathematical modeling of moisture ratio.

The objective of the present work is to investigate the characteristics of pumpkin seeds dried using a tray dryer at different temperature. Also, to determine the mass transfer characteristics such as effective moisture diffusivity, activation energy, and mass transfer parameters at different level of temperature.

2 Materials and Methods

2.1 Raw Materials

The procurement of pumpkins (*Cucurbita maxima*) was done New Delhi market, India. Pumpkin sliced by half to remove seeds and then washed with distilled water. The clean seeds were packed in an LDPE airtight bag at $-10\text{ }^{\circ}\text{C}$ till trials. Fresh seed's initial moisture content (IMC) was determined using AOAC method 934.06 [14].

2.2 Drying Systems and Experimental Procedure

A lab-scale tray drying system was used to study thin layer drying kinetics under different temperature. The tray dryer consists of a circulation fan with a 0.5 hp motor, an electrical heater, and a drying chamber.

Pumpkin seeds having an IMC of 1.33 kg water/kg dry matter were fed to dry in a dryer at air 40, 50, and 60 °C temperatures and 1.5 ms⁻¹ constant air velocity. The dryer was operated for 30 min without load before each experiment. For experiments, seeds were evenly spread on a tray in dryer. The mass of the tray was documented at certain time intermissions, 10 min intermissions in the first 1 h, 15 min intermissions in the next 1 h, and at last, for 20 min, till a persistent mass was accomplished. After drying, the last sample was placed in a desiccator to cool, and then, the final moisture content (FMC) and dry mass were determined. The trials were repeated three times.

2.3 Drying Characteristics

The moisture ratio was evaluated by given Eq. 1:

$$M_R = \frac{M - M_e}{M_i - M_e} \quad (1)$$

where M_R : ratio of water content, M : water content at period t , M_i and M_e : IMC and EMC, respectively. The unit of water content is kg H₂O/kg dry matter.

The drying rate (D_R) stated the quantity of moisture removed from the sample per unit time, and it was estimated by Eq. 2 [15].

$$D_R = \frac{M_{t+dt} - M_t}{dt} \quad (2)$$

where M_{t+dt} : water content at different succession period (kg H₂O/kg dm), t : period (min), d_t : period difference (min).

2.4 Drying Kinetics

The moisture ratio data were calculated and fitted into six semi-empirical models to evaluate the pumpkin seeds drying kinetics. The mathematical models depleted in the current work are depicted in Table 1. The constants of the model were calculated with the help of nonlinear regression analysis. The conditions set to choose best-fit model were maximum R^2 and minimum χ^2 and root mean square error (RMSE). These statistical indicators were determined by the equation given in Jahedi et al. (2018) [16].

Table 1 Semi-empirical models used to predict the pumpkin seeds drying behavior

Models	Equations	References
Page	$M_R = e^{(-kt^n)}$	[17]
Modified page	$M_R = e^{(-kt)^n}$	[18]
Newton	$M_R = e^{(-kt)}$	[19]
Henderson and pabis	$M_R = a \times e^{(-kt)}$	[20]
Two-term	$M_R = a \times e^{(-kt)} + b \times e^{(-k_1t)}$	[21]
Logarithmic	$M_R = a \times e^{(-kt)} + c$	[9]

2.5 Diffusion Coefficient (D_{eff}) and Activation Energy (E_a)

The moisture diffusivity concept is undertaken to correlate drying kinetics and experiment data of agricultural products throughout the falling rate phase. The fact was that moisture diffusion is affected by a moisture concentration gradient. The mechanism of moisture transportation or D_{eff} of materials is explained by Crank’s simplified solution of Fick’s second equation as follows [22]:

$$M_R = \left[\frac{8}{\pi^2} \right] \sum_{n=0}^{\infty} \frac{1}{(2n + 1)^2} \exp \left[\frac{-\pi^2(2n + 1)D_{eff} \cdot t}{4H^2} \right] \tag{3}$$

As the first term ($n = 0$) of Eq. 3 expressed the better immediate solution in the extended drying, which is given as follows:

$$\ln \cdot M_R = \ln \left[\frac{8}{\pi^2} \right] - \left(\frac{\pi^2}{4H^2} D_{eff} \cdot t \right) \tag{4}$$

The plot of natural logarithmic M_R against drying time was used to get the slope to compute moisture diffusivity as follows [15]:

$$\text{Slope} = \frac{D_{eff} \times t}{4H^2} \tag{5}$$

where t : time (min), H : half of the thickness of seed (m).

The relationship between D_{eff} and inverse absolute temperature (1/K) was implicit to be an Arrhenius function to calculate activation energy and represented by Eq. 6 [23]:

$$D_{eff} = D_0 \exp \left(- \frac{E_a}{R(T + 273.15)} \right) \tag{6}$$

The E_a was calculated by slope obtained from plot $\ln (D_{eff})$ against $1/T$.

2.6 Mass Transfer Constraints

The Biot number (B_i) and convective mass transfer coefficient (h_m) are considered parameters of mass transfer, and they were estimated by Eqs. (7–9) [24]. It is stated that the B_i is a dimensionless number that evaluates the relationship between the heat transfer rate of internal convection and external convection [25]. It correspondingly indicates the resistance of water diffusion within a drying material. Biot number is calculated as follows [26].

$$B_i = \frac{24.848}{D_i^{0.375}} \quad (7)$$

Dincer number (D_i) is stated by the influence of airflow on heating and cooling coefficient. D_i is expressed by using Eq. 8:

$$D_i = \frac{v}{kH} \quad (8)$$

And the h_m was governed by the Eq. 9:

$$B_i = \frac{h_m H}{D_{eff}} \quad (9)$$

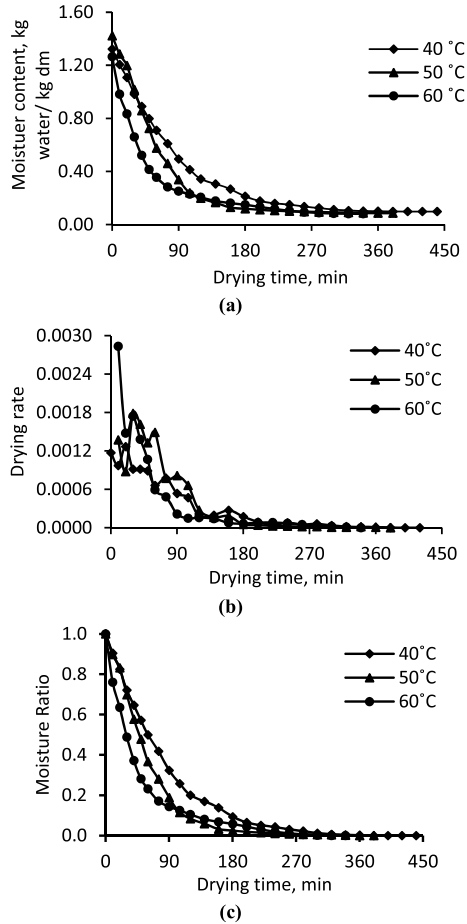
where v : airflow, ms^{-1} ; H : drying material thickness (0.00379 m), m; k : constant of drying was selected from the best-predicted model.

3 Results and Discussion

3.1 Evaluation of Characteristics of Drying

Pumpkin seeds were dehydrated from average IMC, i.e., 1.33 ± 0.079 kg $\text{H}_2\text{O}/\text{kg}$ dm to average FMC, i.e., 0.088 ± 0.0084 kg $\text{H}_2\text{O}/\text{kg}$ dm. The total time taken to complete the drying process was over 7.2, 6.2, and 5.4 h at 40, 50, and 60 °C, respectively. Figure 1a reveals the moisture content of seeds decreases with the progress of drying in all experiments. Continuously decrease in moisture content expressed that the moistures dispersion process overseen by interior mass transfer. The process of drying from start to end is only taken place in the rate of falling phase. It was also seen that a steeper slope at a higher temperature indicates a higher drying rate (Fig. 1b). Higher temperatures exhibit to faster drying time and at the same time high drying rate due to a rise in temperature gradient between air and seeds, which helped to boost moisture evaporation from seeds [10, 27].

Fig. 1 Kinetics of pumpkin seed drying: **a** variations in MC; **b** variation in the D_R , and **c** M_R variation with time



The high drying rate was detected at the commencement of drying due to high IMC in the seed causing the excessive rate of diffusion of water from the seed center to the outer layer and neighboring seed surface [11]. As drying progresses, the moisture evaporation rate from the center to the surface is restricted which diminishes the drying rate significantly which can be expressed by a reduction in moisture ratio (Fig. 1c). In Fig. 1c, moisture ratio curve shows a slight lag in increasing the rate of drying because the seeds' surface temperature was lower than the drying temperature. Hence, the surface moisture gradient elevated steadily as the surface temperature of seeds increased resulting in a rising driving force for mass transfer externally.

These findings were comparable to the previously published reports for other seeds of castor (*Ricinus communis*) [28], watermelon [29, 30], and *Jatropha curcas* L [31].

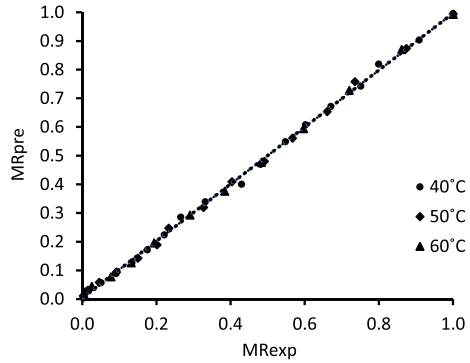
3.2 Mathematical Modeling

From the statistical indicators obtained from experimental data fitted in all models, it was noticed the R^2 of all models varied from 0.95 to 0.99; values of RMSE varied from 0.0069 to 0.0390, and χ^2 ranged from 4.81×10^{-5} to 1.32×10^{-3} . Among all models except the modified page model, all models fit adequately to experimental data. Page model gave comparatively highest R^2 (0.9995) and lowest χ^2 (4.81×10^{-5}) and RMSE (0.0069) values at a temperature of 50 °C which was found quite well to represent the behavior of pumpkin seed drying in tray drying. From Table 2, it was seen that constant of drying (k) increased with the ascent of temperature true to form, showing the impact of drying temperature on water evaporation during drying. Page model empirical constant (n) affects the drying time moderately and helps to give the best result for estimating moisture loss [32]. The experimental data M_R versus predicted M_R were compared for validation and presented in Fig. 2.

Table 2 Statistical indicators and drying coefficients of semi-empirical models at different drying conditions

Models	$T, ^\circ\text{C}$	Constants	R^2	χ^2	RMSE
Newton	40	$k = 0.0111$	0.9849	1.70×10^{-3}	0.0412
	50	$k = 0.0170$	0.9867	1.33×10^{-3}	0.0365
	60	$k = 0.0236$	0.9960	3.23×10^{-4}	0.0180
Logarithmic	40	$k = 0.0116; a = 1.1115; c = -0.0233$	0.9946	6.11×10^{-4}	0.0247
	50	$k = 0.0173; a = 1.0841; c = -0.0142$	0.9923	7.69×10^{-4}	0.0277
	60	$k = 0.0240; a = 1.0128; c = 0.0088$	0.9967	2.65×10^{-4}	0.0163
Modified page	40	$k = 0.0107; n = 1.0000$	0.9861	1.56×10^{-3}	0.0390
	50	$k = 0.017; n = 1.0000$	0.9750	1.32×10^{-3}	0.0363
	60	$k = 0.0236; n = 0.9991$	0.9960	3.23×10^{-4}	0.0184
Page	40	$k = 0.0028; n = 1.3008$	0.9983	1.90×10^{-4}	0.0138
	50	$k = 0.0044; n = 1.3242$	0.9995	4.81×10^{-5}	0.0069
	60	$k = 0.0201; n = 1.0417$	0.9963	3.01×10^{-4}	0.0174
Henderson and pebis	40	$k = 0.0123; a = 1.0985$	0.9932	7.66×10^{-4}	0.0277
	50	$k = 0.0180; a = 1.0752$	0.9915	8.49×10^{-4}	0.0291
	60	$k = 0.0241; a = 1.0177$	0.9963	3.00×10^{-4}	0.0173
Two term	40	$k = 0.0842; a = -0.2587;$	0.9995	5.20×10^{-5}	0.0072
	50	$b = 1.2604; k_1 = 0.0141$	0.9965	3.47×10^{-4}	0.0186
	60	$k = 0.0196; a = 1.1624;$ $b = -0.1624; k_1 = 1.000$ $k = 0.0256; a = 0.9873;$ $b = 0.0371; k_1 = 0.0057$	0.9968	2.55×10^{-4}	0.0160

Fig. 2 Experimental versus predicted moisture ratio plot of pumpkin seed



3.3 Mass Transfer Characteristics

The D_{eff} changed from 4.33×10^{-10} to 5.39×10^{-10} as the temperature escalated from 40 to 60 °C. It was indicated that moisture diffusivity rises with the raise of temperature. The reason might be that diffusion of water molecules from the product creates the intercellular pore inside the product causes the rise of porosity [33]. Comparable results were stated for black pepper by Jayatunga et al. [34], watermelon seeds by Dhurve et al. [29]. The energy needed to activate the drying of pumpkin seeds was obtained to be 17.78 kJ/mol.

A dimensionless Biot number (B_i) signifies the evaporation rate of water during the drying. Generally, drying conditions and type of food product influence the Biot number values. The B_i and h_m values were computed by Eqs. (6–8) were summarized in Table 3. From observation, the decision was made that with the temperature rise, the Bi number increased from 0.2910 to 0.6095. It was reported that if the B_i is below 30, then drying is constrained by diffusion and surface [35]. The value obtained in the current study falls within 30 which signifies the drying of pumpkin seeds restricted by diffusion and surfaced. Comparable results were found for cocoyam, apples, and moringa leaves dehydrated in a convective drying [36] and vacuum dryer [37] as the temperature rise. The values of h_m at various temperatures were varied from 3.321×10^{-8} to 8.656×10^{-8} for pumpkin seed. The results verify that h_m increases with the increase of temperature. The reason for the rise in the rate of mass transfer is the emerge of available thermal energy within food commodities due to the elevation of heat which excites the water molecules [38].

Table 3 Values of mass transfer constraints and activation energy at different drying conditions

Drying Conditions, °C	D_{eff} (m^2s^{-1})	E_a (KJ mol^{-1})	k	B_i	$h_m \times 10^{-8}$ (ms^{-1})
40	4.33×10^{-10}	17.78	0.0028	0.2910	3.321
50	4.80×10^{-10}		0.0044	0.3448	4.301
60	5.39×10^{-10}		0.0201	0.6095	8.656

4 Conclusion

A tray dryer was used to dry pumpkin seeds at three distinct temperatures 40, 50, and 60 °C, and at 1.5 m/s, it is concluded that.

1. The drying time and drying rate were essentially influenced by temperature later demonstrated by an increment in mass exchange coefficient. It was noticed that drying was taken place in the period of falling rate.
2. Among all models, the most precisely fitted model was found to be Page model with R^2 (0.9995) for anticipating pumpkin seeds drying kinetics.
3. The values of D_{eff} , B_i , and h_m were obtained in the range of 4.33×10^{-10} to 5.39×10^{-10} , 0.2910 to 0.6095, and 3.321×10^{-8} to 8.656×10^{-8} , respectively.
4. Lower drying time and fast mass diffusion were observed at a temperature of 60°C; thus, it is very well suggested for future drying, and also, E_a was found to be in the moderate range.
5. However, it is advisable to perform experiments on investigate the effect of high temperature on nutritional profile.

Acknowledgements The authors are thankful to the Department of Food Engineering, NIFTEM for providing facilities during the experiment.

References

1. FAO: FAOSTAT. <https://www.fao.org/faostat/en/#data/QCL/visualize>. Accessed 25 Oct 2021
2. Rico X, Gullón B, Alonso JL, Yáñez R (2020) Recovery of high value-added compounds from pineapple, melon, watermelon and pumpkin processing by-products: an overview. *Food Res Int* 132:1–21. <https://doi.org/10.1016/j.foodres.2020.109086>
3. Cuco RP, Cardozo-Filho L, da Silva C (2019) Simultaneous extraction of seed oil and active compounds from peel of pumpkin (*Cucurbita maxima*) using pressurized carbon dioxide as solvent. *J Supercrit Fluids* 143:8–15. <https://doi.org/10.1016/j.supflu.2018.08.002>
4. Al-Khalifa AS (1996) Physicochemical characteristics, fatty acid composition, and lipoxygenase activity of crude pumpkin and melon seed oils. *J Agric Food Chem* 44:964–966
5. Can A (2007) An analytical method for determining the temperature dependent moisture diffusivities of pumpkin seeds during drying process. *Appl Therm Eng* 27:682–687
6. Kaveh M, Rasooli V, Amiri R (2018) ANFIS and ANNs model for prediction of moisture diffusivity and specific energy consumption potato, garlic and cantaloupe drying under convective hot air dryer. *Inf Process Agric* 5:372–387
7. Chayjan RA, Kaveh M (2014) Physical parameters and kinetic modeling of fix and fluid bed drying of terebinth seeds. *J Food Process Preserv* 38:1307–1320
8. Can A (2000) Drying kinetics of pumpkinseeds. *Int J Energy Res* 24:965–975. [https://doi.org/10.1002/1099-114X\(200009\)24:11%3c965::AID-ER635%3e3.0.CO;2-W](https://doi.org/10.1002/1099-114X(200009)24:11%3c965::AID-ER635%3e3.0.CO;2-W)
9. Sacilik K (2007) Effect of drying methods on thin-layer drying characteristics of hull-less seed pumpkin (*Cucurbita pepo* L.). *J Food Eng* 79:23–30. <https://doi.org/10.1016/j.jfoodeng.2006.01.023>
10. Jittanit W (2011) Kinetics and temperature dependent moisture diffusivities of pumpkin seeds during drying Kasetsart. *J Nat Sci* 45:147–158

11. Uddin Z, Suppakul P, Boonsupthip W (2016) Effect of air temperature and velocity on moisture diffusivity in relation to physical and sensory quality of dried pumpkin seeds. *Dry Technol* 34:1423–1433. <https://doi.org/10.1080/07373937.2015.1119840>
12. Mujaffar S, Ramsumair S (2019) Fluidized bed drying of pumpkin (*Cucurbita* sp.) seeds. *Foods* 8:1–13. <https://doi.org/10.3390/foods8050147>
13. Doymaz I (2016) Experimental study on drying characteristics of pumpkin seeds in an infrared dryer. *Lat Am Appl Res* 46:169–174
14. AOAC (1990) Official methods of analysis of the association of official analytical chemists, 15th edn, Arlington, Virginia, USA. <https://doi.org/10.1371/journal.pone.0013135>
15. Babar OA, Arora VK, Nema PK, Kasara A, Tarafdar A (2021) Effect of PCM assisted flat plate collector solar drying of green chili on retention of bioactive compounds and control of aflatoxins development. *Sol Energy* 229:102–111. <https://doi.org/10.1016/J.SOLENER.2021.07.077>
16. Rad SJ, Kaveh M, Sharabiani VR, Taghinezhad E (2018) Fuzzy logic, artificial neural network and mathematical model for prediction of white mulberry drying kinetics. *Heat Mass Transf* 54:3361–3374. <https://doi.org/10.1007/S00231-018-2377-4>
17. Yarahmadi N, Hojjatoleslami M, Boroujeni LS (2020) Different drying methods of pistacia atlantica seeds: impact on drying kinetics and selected quality properties Negar. *Food Sci Nutr* 8:3225–3233. <https://doi.org/10.1002/fsn3.1582>
18. Guiné RPF, Pinho S, Barroca MJ (2011) Study of the convective drying of pumpkin (*Cucurbita maxima*). *Food Bioprod Process* 89:422–428. <https://doi.org/10.1016/j.fbp.2010.09.001>
19. Roberts JS, Kidd DR, Padilla-Zakour O (2008) Drying kinetics of grape seeds. *J Food Eng* 89:460–465
20. Figiel A (2010) Drying kinetics and quality of beetroots dehydrated by combination of convective and vacuum-microwave methods. *J Food Eng* 98:461–470
21. Chayjan RA, Salari K, Abedi Q, Sabziparvar AA (2013) Modeling moisture diffusivity, activation energy and specific energy consumption of squash seeds in a semi fluidized and fluidized bed drying. *J Food Sci Technol* 50:667–677
22. Crank J (1975) *The mathematics of diffusion*. Clarendon Press, Oxford, UK, London
23. Dhurve P, Tarafdar A, Arora VK (2021) Vibro-fluidized bed drying of pumpkin seeds: assessment of mathematical and artificial neural network models for drying kinetics. *J Food Qual* 2021:1–12. <https://doi.org/10.1155/2021/7739732>
24. Dincer I, Hussain MM (2002) Development of a new Bi–Di correlation for solids drying. *Int J Heat Mass Transf* 45:3065–3069. [https://doi.org/10.1016/S0017-9310\(02\)00031-5](https://doi.org/10.1016/S0017-9310(02)00031-5)
25. Şevik S, Aktaş M, Can E, Arslan E, Doğuş A (2019) Performance analysis of solar and solar-infrared dryer of mint and apple slices using energy-exergy methodology. *Sol Energy* 180:537–549. <https://doi.org/10.1016/j.solener.2019.01.049>
26. Tarafdar A, Jothi N, Kaur BP (2021) Mathematical and artificial neural network modeling for vacuum drying kinetics of *Moringa olifera* leaves followed by determination of energy consumption and mass transfer parameters. *J Appl Res Med Aromat Plants* 24:100306. <https://doi.org/10.1016/J.JARMAP.2021.100306>
27. Malakar S, Alam M, Arora VK (2022) Evacuated tube solar and sun drying of beetroot slices: comparative assessment of thermal performance, drying kinetics, and quality analysis. *Sol Energy* 233:246–258. <https://doi.org/10.1016/J.SOLENER.2022.01.029>
28. Perea-Flores MJ, Garibay-Febles V, Chanona-Perez JJ, Calderon-Dominguez G, Mendez-Mendez JV, Palacios-González E, Gutierrez-Lopez GF (2012) Mathematical modelling of castor oil seeds (*Ricinus communis*) drying kinetics in fluidized bed at high temperatures. *Ind Crops Prod* 38:64–71. <https://doi.org/10.1016/j.indcrop.2012.01.008>
29. Dhurve P, Arora VK, Yadav DK, Malakar S (2022) Drying kinetics, mass transfer parameters, and specific energy consumption analysis of watermelon seeds dried using the convective dryer. *Mater Today Proc*. <https://doi.org/10.1016/J.MATPR.2022.02.008>
30. Doymaz I (2014) Experimental study and mathematical modeling of thin-layer infrared drying of watermelon seeds. *J Food Process Preserv* 38:1377–1384. <https://doi.org/10.1111/jfpp.12217>

31. Keneni YG, Hvosllef-Eide AT, Marchetti JM (2019) Mathematical modelling of the drying kinetics of *Jatropha curcas* L. seeds. *Ind Crop Prod* 132:12–20. <https://doi.org/10.1016/j.indcrop.2019.02.012>
32. Ertekin C, Firat MZ (2017) A comprehensive review of thin-layer drying models used in agricultural products. *Crit Rev Food Sci Nutr* 57:701–717. <https://doi.org/10.1080/10408398.2014.910493>
33. Aprajeeta J, Gopirajah R, Anandharamakrishnan C (2015) Shrinkage and porosity effects on heat and mass transfer during potato drying. *J Food Eng* 144:119–128. <https://doi.org/10.1016/j.jfoodeng.2014.08.004>
34. Jayatunga GK, Amarasinghe BMWPK (2019) drying kinetics, quality and moisture diffusivity of spouted bed dried Sri Lankan black pepper. *J Food Eng* 263:38–45
35. Getahun E, Delele MA, Gabbiye N, Fanta SW, Vanierschot M (2021) Studying the drying characteristics and quality attributes of chili pepper at different maturity stages: experimental and mechanistic model. *Case Stud Therm Eng* 26. <https://doi.org/10.1016/J.CSITE.2021.101052>
36. Ndukwu MC, Dirioha C, Abam FI, Ihediwa VE (2017) Heat and mass transfer parameters in the drying of cocoyam slice. *Case Stud Therm Eng* 9:62–71. <https://doi.org/10.1016/J.CSITE.2016.12.003>
37. Nadi F, Tzempelikos D (2018) Vacuum drying of apples (cv. Golden Delicious): drying characteristics, thermodynamic properties, and mass transfer parameters. *Heat Mass Transf* 54:1853–1866. <https://doi.org/10.1007/S00231-018-2279-5>
38. Darvishi H, Farhudi Z, Behrooz-Khazaei N (2017) Mass transfer parameters and modeling of hot air drying kinetics of dill leaves. *Chem Prod Process Model* 12:1–12. <https://doi.org/10.1515/CPPM-2015-0079>

Study of Aerodynamic Components on the Rear of the Car and the Effects of Varying Design Parameters



Harshit Dawar , Gurparas Singh, and Himanshu

Abstract Aerodynamics plays an important role in motorsport and the automotive industry, has made remarkable advances over the past three decades and is still an outstanding research area today. Every year lap time records are broken in almost every eminent motorsport branch due to advancements, which are mostly down to the aerodynamics of the vehicle. In the present work, the effect of design and specific orientation of aerodynamic components, namely, the rear wing and the diffuser was studied to determine coefficient of drag and lift of the vehicle. The work is divided into two sections, firstly the CAD model of three different rear wing profile was developed using Ansys Fluent Simulation software for the wing profile used in the car without altering diffuser. Thereafter, after careful calibration of the boundary conditions the numerical simulation of the same was carried out. The models were divided into four cases: without rear wing (only car), the model with a full rear wing, a quarter sized rear wing and a wing that is half the size of the rear wing. It was concluded that the full wing creates the most drag, but the lift is more than enough to compensate for that. Surprisingly the drag created in half wing is not as much as the drag created by Quarter wing, which is counter intuitive because in the half wing model, the surface area is double the surface area of the wing in quarter wing.

Keywords Computational fluid dynamics · Aerodynamics · Car · Car wing · Car spoiler · Wing span · Fluent · ANSYS

1 Introductions

The prominence of aerodynamics in the motorsport industry is not unheard of. Ever since Colin Chapman stuck a wing on the back of a formula one car the motorsport world changed forever. We wanted to explore the same. Considering the current formula one climate where the turbulent models are being completely transformed by changing the front and the rear wing, we thought that it is pertinent to carry out

H. Dawar (✉) · G. Singh · Himanshu
University of Petroleum and Energy Studies, Dehradun, Uttarakhand, India
e-mail: harshidawar9@gmail.com

research regarding the effect on turbulence and the drag/lift coefficients of various sizes of the rear wing. We studied the literature already studied by Ghaffar et al. [1] and Mckay [2] and found out that although many research papers have been published regarding the effect of aerodynamics none tests the size of the rear wing, against a standard f-1 sized diffuser. We based our study on the methodology used by Hu et al. [3] where they tested various diffuser angles on a sedan vehicle to get the optimum value and hence compared the results. In this project we studied how different wing parameters affect the downforce and drag and how they can be optimized for maximum downforce without creating much drag at the expense. We test our study using a CFD software (ANSYS) to simulate the conditions and entirely learn the behavior of a wing. Wing span sizes will be varied as: full length wing; half-length wing; three-quarter of the track width; and no wing at all, all the while considering a diffuser working along with it. The project analyses and then compares the different wingspans with the diffuser or without conditions and hence find an optimal solution by performing a CFD analysis.

2 Methodology

A 3-D model was made using the CAD software SolidWorks and CATIA. The dimensions of this model were taken, using the A5 car segment vehicle size class specifications which goes from 4701 to 5000 mm for executive cars. For example, Mercedes Benz E class, BMW 5 series. The vehicle model made here is a sedan. In order to reduce the computation time, the sedan was simplified. The rear-view mirrors, the front grill, the bottom transmission and the shafts from the underbody were omitted. Three different models of wings were designed of quarter width, half width and full width, and a standard diffuser according to the research conducted by Huminic et al. [4] and Hu et al. [3] for all the four models with half wing, full wing, quarter wing and no wing. The models will be therefore tested using Ansys fluent simulation tool [5, 6]. Among the major forces acting on the body due to the air we have two main forces that is the Lift force and the Drag (frictional) force. Where the drag force is the horizontal force opposing the motion of the vehicle and the lift force is the vertical force acts vertically downwards to push the vehicle to the ground mathematically described as:

$$C_D = \frac{D}{\frac{1}{2} \rho V^2 A} \quad (1)$$

$$C_L = \frac{L}{\frac{1}{2} \rho V^2 A} \quad (2)$$

We need to model the flow to solve these equations correctly and obtain this value, and to do the same we have the choice of various turbulence models. Turbulence models: There are basically three different types of turbulence models namely,

1. First order closure model
2. Second order closure model
3. Gradient diffusion assumption second order diffusion model:

The Navier Stoke's 3-D equation is all instantaneous

$$\frac{\partial u_i}{\partial x_i} = 0 \quad (3)$$

$$\frac{\partial u_i}{\partial t} + u_j \frac{\partial u_j}{\partial x_j} = -\frac{1}{\rho} \frac{\partial p}{\partial x_i} + \frac{\partial (2\nu s_{ij})}{\partial x_j} \quad (4)$$

$$\frac{\partial \theta}{\partial t} + u_j \frac{\partial \theta}{\partial x_j} = \frac{1}{\rho C_p} \frac{\partial \left(k \frac{\partial \theta}{\partial x_j} \right)}{\partial x_j} \quad (5)$$

$$\frac{\partial c}{\partial t} + u_j \frac{\partial c}{\partial x_j} = \frac{\partial \left(D \frac{\partial c}{\partial x_j} \right)}{\partial x_j} \quad (6)$$

$$s_{ij} = \frac{1}{2} \left(\frac{\partial u_j}{\partial x_i} + \frac{\partial u_i}{\partial x_j} \right) \quad (7)$$

So, to link all the Reynold's stresses with the mean velocity gradient, we have the Boussinesq-eddy turbulent heat and mass transfer. It is theoretically more accurate and a better method than the other models, and the second order closure model is applied for the momentum and not for the heat and mass flux.

$$\frac{\partial U_i}{\partial x_i} = 0 \quad (8)$$

$$\frac{\partial U_i}{\partial t} + U_j \frac{\partial U_j}{\partial x_j} = -\frac{1}{\rho} \frac{\partial P}{\partial x_i} + \frac{\partial \left(2\nu S_{ij} - \overline{u'_j u'_i} \right)}{\partial x_j} \quad (9)$$

$$\frac{\partial \theta}{\partial t} + U_j \frac{\partial \theta}{\partial x_j} = \frac{1}{\rho C_p} \frac{\partial \left(k \frac{\partial \theta}{\partial x_j} - \overline{u'_j \theta'} \right)}{\partial x_j} \quad (10)$$

$$\frac{\partial C}{\partial t} + U_j \frac{\partial C}{\partial x_j} = \frac{\partial \left(D \frac{\partial C}{\partial x_j} - \overline{u'_j c'} \right)}{\partial x_j} \quad (11)$$

Boussinesq hypothesis:

$$-\overline{\rho u'_j u'_i} = 2\mu_t S_{ij} - \frac{2}{3} \rho k \delta_{ij} \quad (12)$$

where

$$\mu_t = \rho C_\mu \frac{k^2}{\varepsilon} \quad (13)$$

(Turbulent viscosity)

$$S_{ij} = \frac{1}{2} \left(\frac{\partial U_j}{\partial x_i} + \frac{\partial U_i}{\partial x_j} \right) \quad (14)$$

(Mean Strain rate)

$$k = \frac{1}{2} \overline{u'_j u'_i} = \frac{1}{2} (u'^2 + v'^2 + w'^2) \quad (15)$$

(Kinetic energy of turbulent fluctuations)

$$\varepsilon = \nu \overline{\frac{\partial u'_i}{\partial x_j} \frac{\partial u'_i}{\partial x_j}} \quad (16)$$

(Dissipation of turbulent kinetic energy)

k is a measure of energy associated with the turbulent fluctuations.

ε is caused by the work done by the smallest eddies in the flow against the viscous stresses.

2.1 Design of Model and Wing Profile

The vehicle of sedan type [7] was specifically chosen, so that the results could be validated from the official data from the Tesla database, and hence the design is loosely based on a Tesla Model S. The model was simplified by removing the rear wings and the closure of panel gaps over the surface of the entire model. The tires were also simplified to reduce the computational time. The design of the car and the dimensions of the model are as follows:

Height: 1445 mm, Width: 2189 mm, Length: 4970 mm (Fig. 1).

The design of the wing: The wing profile was designed using the software aero foil engineering app. the wing was designed on the basis of the following specifications.

NACA 63,010, Wing span-1.9 m, AR = 6:4, $C_D = 1.0$, $C_L = -7.541$, Chord length = 250 mm (Fig. 2).

2.2 Mesh Details

The Mesh and the boundary conditions were set as follows for the simulation (Figs. 3 and 4).

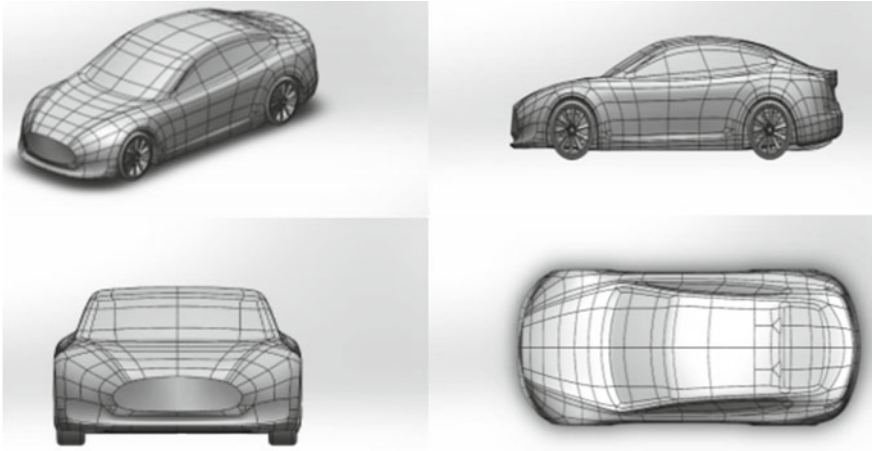


Fig. 1 Images of the car, in clockwise direction from the top left image, front perspective view, left side view, front view, top view

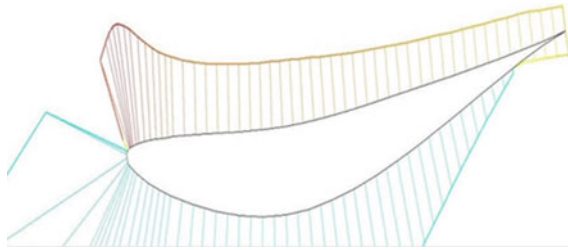


Fig. 2 Pressure gradient distribution over the wing

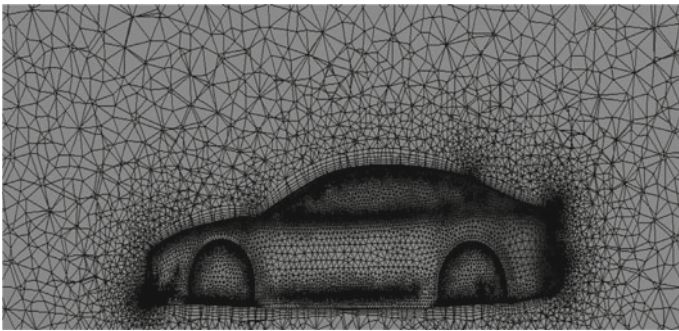
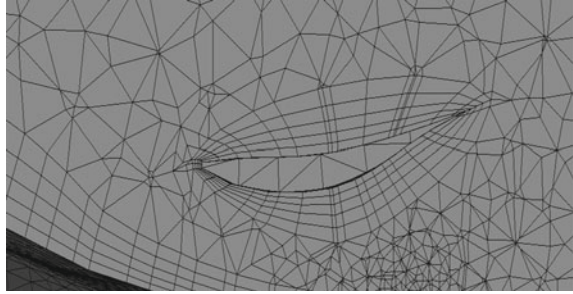


Fig. 3 Mesh details

Fig. 4 Inflation layer around the wing



Mesh details:

Global mesh quality minimum size: 0.5 m
 Maximum size: 1.0 m
 Curvature capture: Enabled
 Curvature normal angle: 18 deg

Inflation layer is used here to capture the boundaries layer separation accurately and to get a much better understanding of the boundary effects of the flow around the body more accurately. Inflation: Based on what is advised for vehicle external aerodynamics with ANSYS FLUENT[®] by Lanfrit [5] guideline, the inflation option has been set as “First Aspect Ratio” instead of “Smooth Transition” (which was the default value).

Use Automatic Inflation
 Program Controlled
 Inflation Option First Aspect Ratio
 First Aspect Ratio = 5
 Maximum Layers = 5
 Growth Rate = 1.2 (20%)

2.3 *Boundary Conditions (Table 1)*

2.4 *Reference Values*

Reference Values are computed from Inlet.

For Calculating the Area, we have used the inbuilt method of fluent called Projected Areas that is available under Reports, in Results. We have kept in mind that the Minimum Feature Size value is kept as minimum as possible, or you can keep the Minimum Feature Size is equal to the size the smallest feature in the direction of area projection.

Table 1 Boundary conditions

Boundary conditions (for all cases and benchmarks)		
Velocity inlet	Velocity	31.298 m/s
	Turbulence specification method	Intensity and viscosity ratio
	Turbulent intensity (%)	1.00
	Turbulent viscosity ratio	10
Pressure outlet	Gauge pressure	0 Pascals
	Turbulence specification method	Intensity and viscosity ratio
	Backflow turbulent intensity (%)	10.00
	Backflow turbulent viscosity ratio	10
Wall zones Wall roughness	Shear condition	No slip
	Wall motion	Stationary wall
	Roughness models	Standard
	Sand-grain roughness	
	Roughness height (m)	0
	Roughness constant	0.5
Fluid property	Fluid type	Air
	Density	1.175 kg/m ³
	Kinematic viscosity	1.8247 × 10 ⁻⁵ kg/m s

3 Results of the Simulation

The results of the simulations have been divided into four different cases based on the four different types of orientations/wing setups of rear wing.

- Case 1: The vehicle without the rear wing.
- Case 2: The vehicle with the full rear wing.
- Case 3: The vehicle with the quarter sized rear wing.
- Case 4: The vehicle with half the size of the rear wing.

3.1 Case 1: Simulation Results of the Vehicle Only

We can see that the velocity cut plot distribution without the wing we see a smaller recirculation area (Figs. 5 and 6).

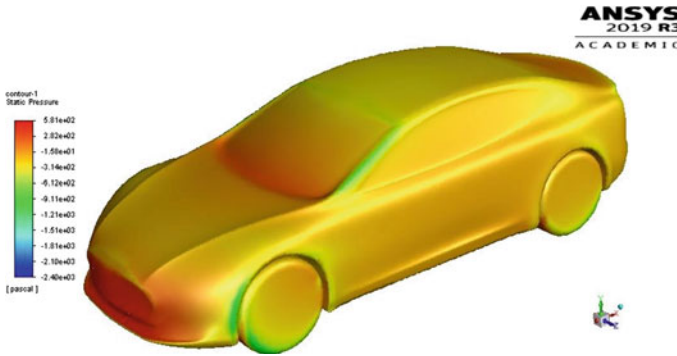


Fig. 5 Pressure distributions contours of Case 1

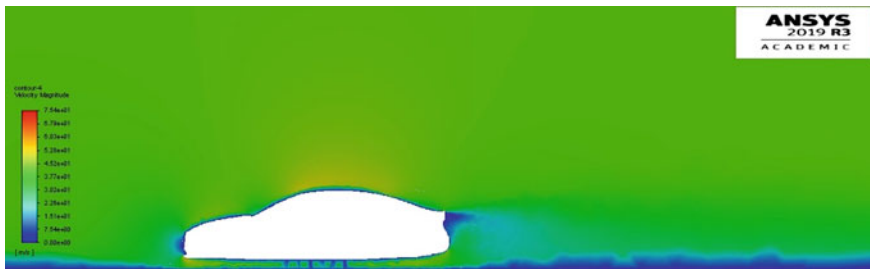


Fig. 6 Velocity distributions of Case 1

In this velocity cut plot distribution, we see stagnation points under the vehicle, and under the rear side of the vehicle we see the high wind speed, corresponding to a low pressure and hence contributing to the downforce. The low wind speed in the rear of the vehicle correlates to the high wind speed just under the rear body, and proceeds to push the vehicle down.

3.2 Case 2: The Vehicle with the Full-Sized Rear Wing

With the addition of the wing, we can clearly see that the air above the wing is moving much slower and the air below the wing is faster thus providing that extra downforce that was expected of it. The rest of the airflow does not change much around the vehicle and we can see the pattern remains the same more or less, just with the addition of the wing, we get some additional downforce at the rear end of the vehicle (Figs. 7 and 8).

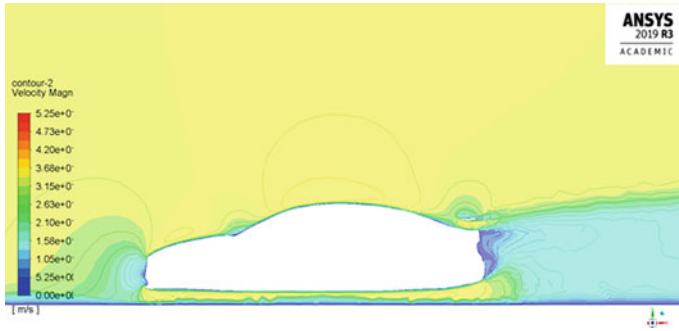


Fig. 7 Velocity distribution of Case 2

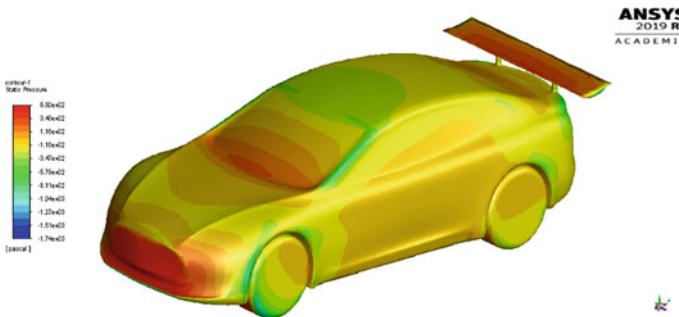


Fig. 8 Pressure distribution contours of Case 2

3.3 Case 3: The Vehicle with Quarter the Size of the Original Wing

Here, the size of the wing was changed and we see that as expected, the wing provides some downforce but still not enough as the full-sized wing given the fact that the surface area is significantly reduced in Case 3 (Figs. 9 and 10).

The velocity distribution is not changed much because the orientation of the wing remains the same and so do the boundary conditions and the angle of incidence and all remain the same. In this case we can see that the addition of the wing does more harm than good, as it significantly increases the value of the drag coefficient and the lift coefficient takes a hit for the worse. It is significantly less than the full wing or even C_{l1} in our Case 1.

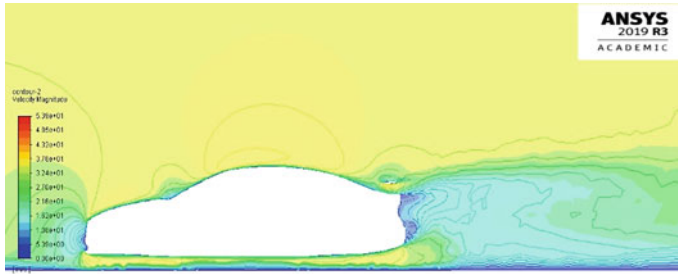


Fig. 9 Velocity distribution of Case 3

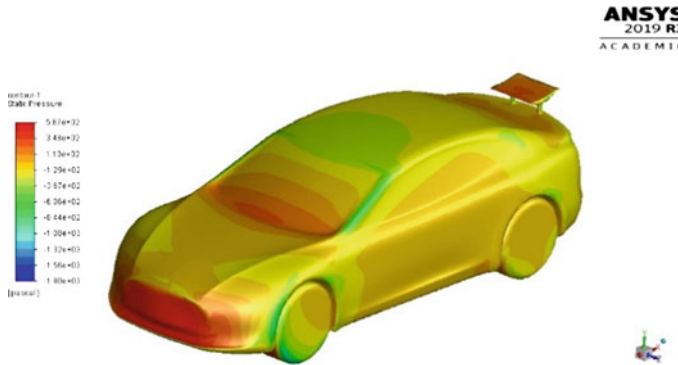


Fig. 10 Pressure distribution contours of Case 3

3.4 Case 4: The Vehicle with the Wing Half the Size of the Original Wing

Since the change in size was compared in Case 2, we change the orientation of the wing in this one by putting the wing horizontally symmetrically outwards (Fig. 11).

In this pressure contour distribution, we see the orientation of the wing, has been changed, it has been placed horizontally outwards from the vehicle. Where the flow over the wing is almost as it should be, we see that the fact that the total flow of the air over the vehicle is almost exact as the contours on the car without the wing attached (Fig. 12).

From the velocity cut plot distribution it seems clear that the change in orientation does not necessarily make any difference to the original, since the flow over the car remains the same, almost exact as in Case 1. So, we can say that changing the orientation of the wing, makes little to no difference, in fact we see that it increases the drag, without providing the compensating lift forces to go with it.

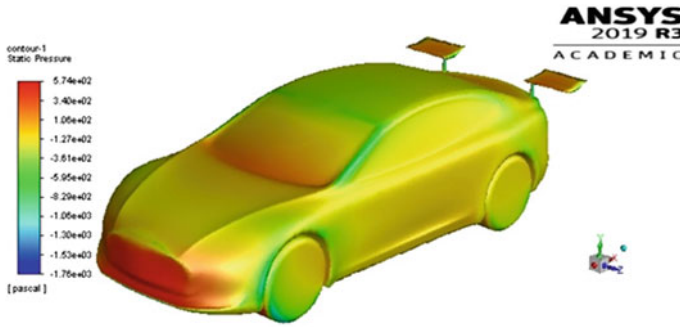


Fig. 11 Static pressure distribution contours Case 4

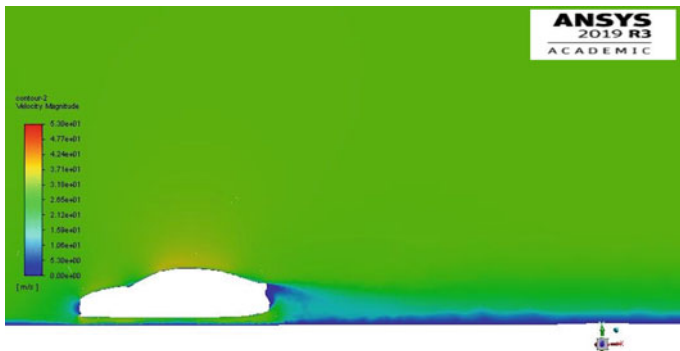


Fig. 12 Velocity magnitude distribution of Case 4

4 Conclusion

We can easily deduce the fact that the orientation of the wing matters, but not enough to overcome the effect of surface area. The full wing creates the most drag, but the lift is more than enough to compensate for that. The change in orientation of the wing in Case 4, is unable to make a difference because of its lack of surface area. Surprisingly the drag created is not as much as the drag created by Quarter wing, which is counter intuitive because in Case 4, the surface area is double the surface area of the wing in Case 3. The full wing creates the most drag, but the lift is more than enough to compensate for that. Surprisingly the drag created in half wing is not as much as the drag created by Quarter wing, which is counter intuitive because in the half wing model, the surface area is double the surface area of the wing in quarter wing (Table 2).

Table 2 Complied table of C_D and C_L from the four cases

Cases	C_D	C_L
Case 1 (Without rear wing)	0.29	-0.38
Case 2 (With the full rear wing)	0.38	-0.47
Case 3 (With the quarter sized rear wing)	0.34	-0.056
Case 4 (With half the size of the rear wing)	0.339	-0.222

Acknowledgements We would like to thank Professor Dr. Shyam Pandey and Prof. Narayan Khatri for their guidance and support. We would also like to express our gratitude towards them for showing confidence in us. It was a privilege to work with them. We are thankful to the University of Petroleum and Energy Studies, for providing us the opportunity of pursuing B. TECH in Automotive Design Engineering (ADE) in a peaceful environment with ample resources. We are thankful to our friends, our professors for guiding through this project, office staff. In the end, we would like to acknowledge our parents, family members without whose support, this work would not have been possible.

References

1. Ghaffar H, Yusoff H, Ibrahim D, Budin S, Razak M (2019) A simulation study of tubercles effect of aerodynamics performance on car rear spoiler. *J Phys Conf Ser* 1349(1)
2. McKay N, Gopalarathnam A (2002) The effects of wing aerodynamics on race vehicle performance. *SAE Tech Pap* 2022-01-3294
3. Hu X, Zhang R, Ye J, Yan X, Zhao Z (2011) Influence of different diffuser angle on Sedan's aerodynamic characteristics. *Phys Procedia* 22:239-245
4. Humnic A, Humnic G (2020) Aerodynamics of curved underbody diffusers using CFD. *J Wind Eng Ind Aerodyn* 205
5. Lanfrit M (2005) Best practice guidelines for handling automotive external aerodynamics with FLUENT. *Fluent Deutschland GmbH*, 64295 Darmstadt/Germany
6. Ganesh G, Vasudevan V (2015) Analysis of effects of rear spoiler in automobile using Ansys 6(6):762-766
7. Nawam M, Rosli M, Rosli N (2018) Simulation study on the effect of rear-wing spoiler on the open aerodynamic performance of sedan vehicle. *J Adv Res Fluid Mech Therm Sci* 49(2):146-154